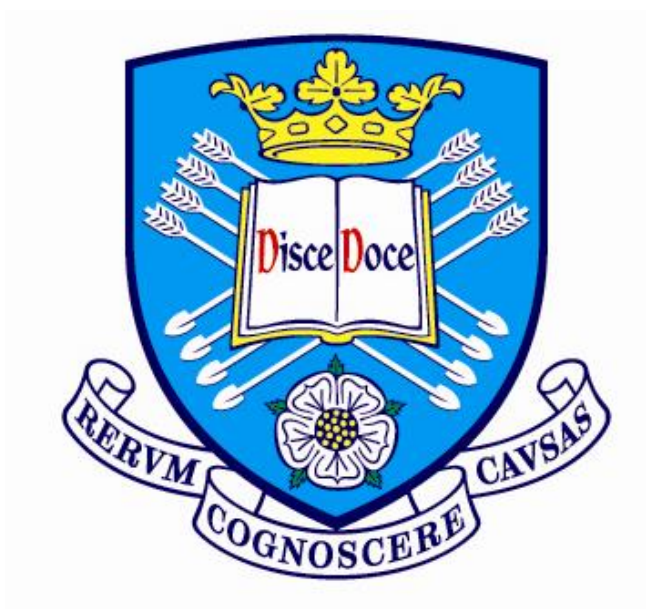


**Synthesis and reactivity of Rh(I) and Ir(I)
complexes and their application in catalytic
decarbonylative dehydration reactions**



Dean C Cocker

Supervisor: Dr. A. Haynes

A thesis submitted for the degree of doctor of
philosophy

Department of Chemistry

University Of Sheffield

August 2015

Summary

Chapter 1

This chapter introduces fundamental aspects of catalytic and organometallic chemistry such as ligand effects and pincer complexes. Renewable fuel sources are discussed and the catalytic decarbonylative dehydration of long chain fatty acids and anhydrides to give high value fuel feedstocks is reviewed, with particular emphasis on homogeneous metal catalysts. The aims of the project are outlined.

Chapter 2

Chapter two reports the synthesis and reactivity of iridium(I) phosphine carbonyl complexes of bidentate iminopyrrolyl ligands. These complexes have the general formulae $[\text{Ir}(\text{Ar-NN})(\text{CO})(\text{PR}_3)]$ and have been fully characterised by IR, NMR, mass spectroscopy, elemental analysis and in some cases X-ray crystallography. These complexes (except the most sterically hindered example) react rapidly with MeI to give Ir(III) complexes $[\text{Ir}(\text{Ar-NN})(\text{CO})(\text{PR}_3)(\text{Me})(\text{I})]$, for which NMR spectroscopy provides evidence for restricted rotation about the N-aryl bond. Methyl iodide oxidative addition kinetics for these complexes is reported, showing that *o*-anisyl substituted phosphine ligands give the highest reactivity.

Chapter 3

Chapter three extends the investigation of the iminopyrrolyl ligand backbone by incorporating an additional donor ligand to generate a terdentate pincer ligand with an NN X donor set ($X = \text{P}, \text{N}$ or C). All the ligands form stable Rh(I) carbonyl pincer complexes that react rapidly with MeI, the outcome depending upon the nature of the X donor. The NNP pincer complexes react with MeI to form Rh(III) methyl species, followed by slow migratory CO insertion to give Rh(III) acetyl products. The complexes with NNN and NNC pincer ligands also undergo facile oxidative addition, but do not undergo migratory insertion. Methyl iodide oxidative addition kinetics for the Rh complexes follows the order $\text{NNC} > \text{NNN} > \text{NNP}$, reflecting the electron donor strength of the pincer ligand. Ir(I) NNP complexes were also synthesised and found to undergo oxidative addition of MeI approximately 20 times faster than the rhodium analogues to give stable Ir(III) methyl products.

Chapter 4

Chapter four details the synthesis of a number of PNP pincer ligands based on a diaryl amido backbone and their associated Ir(I) carbonyl complexes. These complexes react

with methyl iodide to form stable Ir(III) methyl complexes with the general formula $[\text{Ir}(\text{CO})(\text{R-PNP})(\text{Me})(\text{I})]$, which were fully characterised, in some cases by X-ray crystallography. These complexes are an order of magnitude more reactive than their rhodium congeners, investigated previously. The *o*-anisyl substituted complex was the most reactive toward MeI and also activates the C-Cl bond of CH_2Cl_2 at room temperature. Kinetics for reactions of some known Rh(I) diaryl amido NNN pincer complexes with MeI were measured and rates were found to be approximately an order of magnitude faster than the Rh(I) PNP pincer complexes.

Chapter 5

Chapter five describes the catalytic decarbonylative dehydration of long chain carboxylic acids and anhydrides to give alkenes. An initial investigation into ligand and metal effects using Vaska type complexes $[\text{IrCl}(\text{CO})(\text{PR}_3)_2]$ as catalysts identified $[\text{IrCl}(\text{CO})(\text{PCy}_3)_2]$ as an efficient catalyst that gives high selectivity for internal alkenes. A number of multidentate Rh(I) and Ir(I) complexes were also screened to investigate ligand and metal effects on the reaction. The important role of an iodide co-catalyst implicates participation of acyl iodides that can undergo facile oxidative addition to Rh(I) and Ir(I). The second half of this chapter investigates catalytic decarbonylative dehydration using Rh(I) iminophosphine complexes. These complexes are efficient catalysts and analysis of the catalytic residues confirms the formation of stable Rh(III) complexes formed under catalytic conditions. These complexes were fully characterised including X-ray crystal structures for two examples, demonstrating N-acetylation of the iminophosphine ligand to give a tridentate PCO donor ligand. Notably these complexes remain active catalysts. Mechanistic studies indicate incorporation of deuterium from a $(\text{CD}_3\text{CO})_2\text{O}$ additive at the C-1 position of alkene products. A mechanism involving metal promoted ketene formation from acyl iodides is proposed.

Chapter 6

Chapter six provides general conclusions and suggestions for future work.

Chapter 7

Chapter seven gives full details of the experimental procedures used.

Chapter 8

Chapter eight gives supplementary spectroscopic and experimental details.

For Elizabeth

Acknowledgements

I am grateful to my supervisor Dr. A Haynes, for his support and guidance throughout my time in Sheffield and my industrial supervisor Dr Glenn Sunley for the many interesting discussions throughout the project.

I would like to thank all of the staff in the department who assisted me throughout my PhD. The list is endless, however I would like to give special thanks to Harry Adams, who unlike Daniel Radcliffe is an actual wizard and solved all of the structures reported in this thesis. Huge thanks also go to Sue Bradshaw for putting up with my persistent whining and doing me the odd sneaky NMR when requested. Many thanks to Louise and Denise for financing help (you know what I mean), Sharon, Simon and Jenny for all the analytical data and finally to Pete and Nick in stores who brought the bantz.

Many thanks to all of the members both past and present of the Haynes group especially Stephen Repper, Chris Parks and Dave Griffin for tea, laughs and .gif time.

A massive thank you goes out to all of the amazing friends I have made throughout my time in Sheffield, Liam Ratcliffe, Joe Lovett, Mark Latham, Alex Metherell, Esther Allen, Lizzy Jones, Sarah Canning, Rebecca Collins, all the guys from 10:15 and 3:00pm tea and everyone from football too.

Last but by no means least my biggest thanks goes to the family. Beth who has done nothing but constantly support me throughout this PhD, provided me with adequate amount of “tough love” when necessary and has given me a future I can look forward to (bunsters and Luna too obvs). Huge thanks goes to Adam and Laura for feeding, housing me and providing me with a beautiful nephew Archie. Finally to mum and dad, thanks for all the support, I hope I have done you proud.

I have had an amazing time doing this work (not so much writing it up), Sheffield is an amazing place and I have been very proud to be part of the University of Sheffield for the last 7 years and am extremely sad to be saying goodbye.

In memoriam: Jérôme. F. Vivat – Allez les bleus Jéjé.

Abbreviations

General

Ac	acetyl
Acac	acetylacetonate
Ar	aryl
atm	atmospheres
Bu	butyl
ⁿ BuLi	n-butyl lithium
^t Bu	tertiary-butyl
COD	1,5-cyclooctadiene
COE	cyclooctene
Cy	cyclohexyl
Cyp	cyclopentyl
DFT	density functional theory
DMSO	dimethylsulfoxide
DMPU	1,3-Dimethyl-3,4,5,6-tetrahydro-2(1H)-pyrimidinone
Et	ethyl
L	ligand
M	metal
Me	methyl
min	minutes
nbd	norbornadiene
Ph	phenyl
ⁱ Pr	iso-propyl
R	alkyl or aryl group
THF	tetrahydrofuran
<i>o</i> -Tol	ortho-tolyl
<i>o</i> -An	ortho-anisyl
Piv	^t BuCO

Dppe	1,2-bis(diphenylphosphino)ethane
Dppms	bis(diphenylphosphino)methane sulfide
Xantphos	4,5-bis(diphenylphosphino)-9,9-dimethylxanthene
Dpe-phos	Oxydi-2,1-phenylene-bis(diphenylphosphine)
Dpppent	1,5-Bis(diphenylphosphino)pentane

Infrared Spectroscopy

IR	infra-red
cm ⁻¹	wavenumbers
A	absorbance
ν	stretching frequency
$\nu(\text{CO})$	carbonyl stretching frequency

NMR Spectroscopy

NMR	nuclear magnetic resonance
δ	chemical shift
ppm	parts per million
s	singlet
d	doublet
dd	doublet of doublets
t	triplet
dt	doublet of triplets
ddt	doublet of doublets of triplets
dtd	doublet of triplets of doublets
br	broad
Sept	septet
m	multiplet
J	coupling constant (Hz)

HSQC heteronuclear single quantum coherence spectroscopy

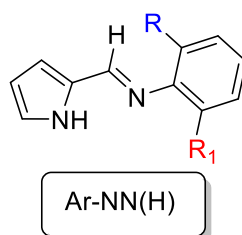
UV/Vis Spectroscopy

Uv/Vis ultraviolet/visible

λ_{\max} Uv/Vis absorbtion with largest ϵ

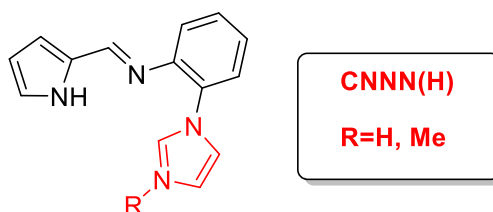
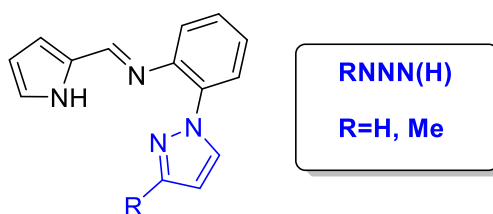
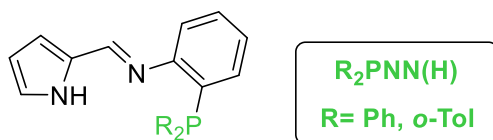
Ligand Precursors

Ar-NN(H)

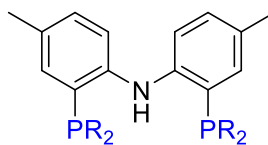


Ar	R	R ₁
Ph	H	H
2- ⁱ PrC ₆ H ₄	H	ⁱ Pr
2,6- ⁱ Pr ₂ C ₆ H ₃	ⁱ Pr	ⁱ Pr

RXNN(H)

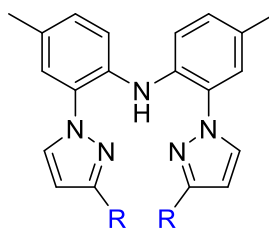


R-PNP(H)



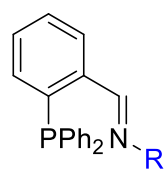
R=Ph, *o*-Tol, *o*-An, ^{*i*}Pr, Cy

R(NNN)(H)



R=H, Me

PN-R iminophosphine ligands



R

^{*t*}Bu

2-MeOC₆H₄

3,5-(CF₃)₂C₆H₃

2,6-Me₂C₆H₃

2,6-^{*i*}Pr₂C₆H₃

2,4,6-Me₃C₆H₂

Contents

Chapter 1-General Introduction	1
1.0 Catalysis	2
1.01 General definition and classification.	2
1.02 Transition metals in homogeneous catalysis.	3
1.1 Oil feedstock demands and renewable sources.	5
1.2 Transition metal catalysed deoxygenation of carboxylic acids	9
1.2.1 Heterogeneously catalysed decarboxylation of aliphatic acids	9
1.2.2 Homogeneously catalysed deoxygenation of fatty acids	9
1.2.3 Rhodium catalysed decarbonylative dehydration of fatty acids	10
1.2.4 Palladium catalysed decarbonylative dehydration of fatty acids	11
1.2.5 Iridium catalysed decarbonylative dehydration of fatty acids	14
1.2.6 Iron catalysed decarbonylative dehydration of fatty acids	15
1.2.7 Mechanistic steps	16
1.3 Ligand Effects	20
1.4 Pincer complexes	26
1.4.1 Reactions of pincer complexes toward MeI	27
1.4.2 Application of pincer complexes in catalysis	31
1.5 Project aims	32
1.6 References	34
Chapter 2- Synthesis and reactivity of Ir(I) iminopyrrolyl phosphine complexes	38
2.0 Introduction	39
2.1 Results and discussion	42
2.1.1 Pro-ligand synthesis	42
2.1.2 NMR analysis	42

2.1.3 Synthesis and characterisation of [Ir(Ar-NN)(CO) ₂] complexes	42
2.1.4 Reactivity of [Ir(Ph-NN)(CO) ₂] with MeI	44
2.1.5 MeI oxidative addition kinetics	44
2.1.6 Synthesis and characterisation of [Ir(Ar-NN)(CO)(L)] complexes	46
2.1.7 Spectroscopic characterisation	46
2.1.8 X-ray crystallography	49
2.2 Reaction of [Ir(Ar-NN)(CO)(PR₃)] complexes with MeI	50
2.2.1 Spectroscopic characterisation	50
2.2.2 NMR characterisation of complexes 4a-e	51
2.2.3 X-ray crystallography	52
2.2.4 Spectroscopic characterisation of complexes 4f-j	53
2.2.5 Spectroscopic characterisation of complexes 4k and 4m	54
2.2.6 MeI oxidative addition kinetics	57
2.2.7 Analysis of complexes 3a-e	60
2.2.8 Analysis of complexes 3d , 3g-3i and 3m	61
2.2.9 Effect of sequential incorporation of o-anisyl ligand substituents	61
2.3 Summary	63
2.4 References	64
Chapter 3- Synthesis and reactivity of Rh(I) and Ir(I) iminopyrrolyl pincer complexes	
3.0 Introduction	67
3.1 Results and discussion	69
3.1.1 Pro-ligand synthesis	69
3.1.2 Synthesis of Rh(I) iminopyrrolyl pincer complexes	71
3.1.3 Infrared spectroscopic analysis	71

3.1.4 NMR analysis	73
3.1.5 X-ray crystallography	73
3.1.6 Reactivity of Rh(I) iminopyrrolyl pincer complexes with MeI	74
3.1.7 Reaction of complexes 5c-f with MeI	78
3.1.8 X-ray crystallography	79
3.1.9 MeI oxidative addition kinetics	81
3.2 Synthesis and characterisation of Ir(I)PR₂NN pincer complexes	84
3.2.1 Reactivity of complexes 8a and 8b with MeI	85
3.2.2 X-ray crystallography	86
3.3 Summary	89
3.4 References	90
Chapter 4- Synthesis and reactivity of Rh and Ir diaryl amido pincer complexes	91
4.0 Introduction	92
4.1 Aims	96
4.2 Synthesis and reactivity of [Ir(CO)(R-PNP)] complexes	97
4.2.1 Synthesis of R-PNP(H) pro-ligands	97
4.2.2 Synthesis of [Ir(CO)(R-PNP)] complexes	97
4.2.3 IR and ³¹ P{ ¹ H} NMR analysis	98
4.2.4 X-ray crystallography	99
4.3 Reactivity of [Ir(CO)(R-PNP)] complexes with MeI	100
4.3.1 IR and NMR analysis	100
4.3.2 X-ray crystallography	103
4.3.3 MeI oxidative addition kinetics	106
4.4 Synthesis and reactivity of Rh(di(2-pyrazolyl)-<i>p</i>-tolyl) pincer complexes	109
4.4.1 Synthesis of RhNNN(CO) complexes 12a and 12b	109

4.4.2 Reactivity of 12a and 12b with MeI	110
4.4.3 UV-Vis kinetics	110
4.5 Summary	112
4.6 References	113
Chapter 5 - Rh and Ir catalysed decarbonylative dehydration of long chain acids	115
5.0 Introduction	116
5.1 Results and discussion	116
5.1.1 General method	116
5.1.2 Decarbonylative dehydration using [IrCl(CO)(L) ₂] complexes	117
5.1.3 Temperature and time dependence	118
5.1.4 Additive effect on reactivity	119
5.1.5 Ligand effects	121
5.1.6 Decarbonylative dehydration using Ir(I) multidentate complexes	123
5.1.7 Decarbonylative dehydration using Rh(I) complexes	124
5.2 Synthesis and catalytic activity of Rh(I) iminophosphine complexes –isolation of Rh(III) products	129
5.2.1 Decarbonylative dehydration of long chain acids using complexes 15d , 15f and 15g	138
5.2.2 Mechanistic studies	140
5.3 Summary	145
5.4 References	146
Chapter 6- Conclusions and future work	148
6.1 Conclusions	149
6.2 Future work	151
6.2.1 New complexes	151

6.2.2 Decarbonylative dehydration reactions	151
6.2.3 In-Situ reaction monitoring	152
6.3 References	153
Chapter 7- Experimental	154
7.0 Experimental	155
7.1 Solvents and reagents	155
7.2 Schlenk techniques	155
7.3 Instrumentation	156
7.4 X-ray crystallography	156
7.5 General procedures for Ultra Violet kinetic studies	156
7.6 General procedure for IR kinetic studies	157
7.7 Synthesis of Rh/Ir precursors	158
7.8 Synthesis of literature reported ligands	158
7.9 Synthesis of literature reported Rh/Ir complexes	158
7.10 Ligand synthesis	159
7.10.1 Synthesis of Ph-NN(H)	159
7.10.2 Synthesis of 2- ⁱ PrC ₆ H ₄ NN(H)	159
7.10.3 Synthesis of 2,6- ⁱ Pr ₂ C ₆ H ₃ NN(H)	160
7.10.4 Synthesis of 2-diphenylphosphino aniline	160
7.10.5 Synthesis of 2-di(<i>o</i> -tolyl)phosphino aniline	161
7.10.6 Synthesis of Ph ₂ PNN(H)	162
7.10.7 Synthesis of <i>o</i> -Tol ₂ PNN(H)	162
7.10.8 Synthesis of 2-Pyrazolyl aniline	163
7.10.9 Synthesis of 2-(3-methylpyrazolyl) aniline	164
7.10.10 Synthesis of H-NNN(H)	164

7.10.11 Synthesis of H-NNN(H)	165
7.10.12 Synthesis of CNN(H)	166
7.10.13 Synthesis of Me-CNN(H)	166
7.10.14 Synthesis of Et-CNN(H)	167
7.10.15 Synthesis of Cy-PNP(H)	167
7.10.16 Synthesis of <i>o</i> -Tol-PNP(H)	168
7.10.17 Synthesis of <i>o</i> -An-PNP(H)	169
7.10.18 Synthesis of 2,6-Et ₂ C ₆ H ₃ PN	170
7.10.19 Synthesis of 2,4,6-Me ₃ C ₆ H ₂ PN	170
7.11 Synthesis of Rh and Ir complexes	171
7.11.1 Synthesis of [Ir(Ph-NN)(CO) ₂] 1a	171
7.11.2 Synthesis of [Ir(Ph-NN)(CO) ₂ (Me)I] 2a	172
7.11.3 Synthesis of [Ir(Ar-NN)(CO)L] complexes	172
7.11.4 Synthesis of [Ir(Ph-NN)(CO)(PPh ₃)] 3a	173
7.11.5 Synthesis of [Ir(Ph-NN)(CO)(P <i>o</i> -Tol ₃)] 3b	174
7.11.6 Synthesis of [Ir(Ph-NN)(CO)(P <i>p</i> -Tol ₃)] 3c	174
7.11.7 Synthesis of [Ir(Ph-NN)(CO)(P <i>o</i> -An ₃)] 3d	175
7.11.8 Synthesis of [Ir(Ph-NN)(CO)(P(4-FC ₆ H ₄) ₃)] 3e	176
7.11.9 Synthesis of [Ir(2- <i>i</i> PrC ₆ H ₄ -NN)(CO)(PPh ₃)] 3f	177
7.11.10 Synthesis of [Ir(2- <i>i</i> PrC ₆ H ₄ -NN)(CO)(P <i>o</i> -Tol ₃)] 3g	178
7.11.11 Synthesis of [Ir(2- <i>i</i> PrC ₆ H ₄ -NN)(CO)(PPh ₂ <i>o</i> -An)] 3h	178
7.11.12 Synthesis of [Ir(2- <i>i</i> PrC ₆ H ₄ -NN)(CO)(PPh <i>o</i> -An ₂)] 3i	179
7.11.13 Synthesis of [Ir(2- <i>i</i> PrC ₆ H ₄ -NN)(CO)(P <i>o</i> -An ₃)] 3j	180
7.11.14 Synthesis of [Ir(2,6- <i>i</i> Pr ₂ C ₆ H ₃ -NN)(CO)(PPh ₃)] 3k	181

7.11.15 Synthesis of [Ir(2,6- <i>i</i> Pr ₂ C ₆ H ₄ -NN)(CO)(P- <i>o</i> -Tol ₃)] 3l	182
7.11.16 Synthesis of [Ir(2,6- <i>i</i> Pr ₂ C ₆ H ₄ -NN)(CO)(P(<i>o</i> -An) ₃)] 3m	182
7.11.17 Synthesis of [Ir(Ar-NN)(CO)L(Me)I] complexes 4a-k	183
7.11.18 Synthesis of [Ir(Ph-NN)(CO)(PPh ₃)(Me)I] 4a	183
7.11.19 Synthesis of [Ir(Ph-NN)(CO)(P- <i>o</i> -Tol ₃)(Me)I] 4b	184
7.11.20 Synthesis of [Ir(Ph-NN)(CO)(P- <i>p</i> -Tol ₃)(Me)I] 4c	185
7.11.21 Synthesis of [Ir(Ph-NN)(CO)(P- <i>o</i> -An ₃)(Me)I] 4d	186
7.11.22 Synthesis of [Ir(Ph-NN)(CO)(P(4-FC ₆ H ₄) ₃)(Me)I] 4e	186
7.11.23 Synthesis of [Ir(2- <i>i</i> PrC ₆ H ₄ -NN)(CO)(PPh ₃)(Me)I] 4f	187
7.11.24 Synthesis of [Ir(2- <i>i</i> PrC ₆ H ₄ -NN)(CO)(P- <i>o</i> -Tol ₃)(Me)I] 4g	188
7.11.25 Synthesis of [Ir(2- <i>i</i> PrC ₆ H ₄ -NN)(CO)(PPh ₂ - <i>o</i> -An)(Me)I] 4h	189
7.11.26 Synthesis of [Ir(2- <i>i</i> PrC ₆ H ₄ -NN)(CO)(PPh- <i>o</i> -An ₂)(Me)I] 4i	190
7.11.27 Synthesis of [Ir(2- <i>i</i> PrC ₆ H ₄ -NN)(CO)(P- <i>o</i> -An ₃)(Me)I] 4j	191
7.11.28 Synthesis of [Ir(2,6- <i>i</i> Pr ₂ C ₆ H ₄ -NN)(CO)(PPh ₃)(Me)I] 4k	192
7.11.29 Synthesis of [Ir(2,6- <i>i</i> Pr ₂ C ₆ H ₄ -NN)(CO)(P- <i>o</i> -An ₃)(Me)I] 4m	193
7.11.30 Synthesis of [Rh(Ph ₂ PNN)(CO)] 5a	193
7.11.31 Synthesis of [Rh(<i>o</i> -Tol ₂ PNN)(CO)] 5b	194
7.11.32 Synthesis of [Rh(H-NNN)(CO)] 5c	195
7.11.33 Synthesis of [Rh(Me-NNN)(CO)] 5d	196
7.11.34 Synthesis of [Rh(Me-CNN)(CO)] 5e	196
7.11.35 Synthesis of [Rh(EtCNN)(CO)] 5f	197
7.11.36 Synthesis of [Rh(<i>o</i> -Tol ₂ PNN)I(COMe)] 7b	198
7.11.37 Synthesis of [Rh(H-NNN)(CO)(Me)I] 6c	199
7.11.38 Synthesis of [Rh(Me-NNN)(CO)(Me)I] 6d	199
7.11.39 Synthesis of [Rh(Me-CNN)(CO)(Me)I] 6e	200

7.11.40 Synthesis of [Rh(Et-CNN)(CO)(Me)I] 6f	201
7.11.41 Synthesis of [Ir(Ph ₂ PNN)(CO)] 8a	201
7.11.42 Synthesis of [Ir(<i>o</i> -Tol ₂ PNN)(CO)] 8b	202
7.11.43 Synthesis of [Ir(Ph ₂ PNN)(CO)(Me)I] 9a	203
7.11.44 Synthesis of [Ir(<i>o</i> -Tol ₂ PNN)(CO)(Me)I] 9b	204
7.11.45 Synthesis of [Ir(CO)(R-PNP)] complexes	204
7.11.46 Synthesis of [Ir(CO)(Ph-PNP)] 10a	205
7.11.47 Synthesis of [Ir(CO)(<i>o</i> -Tol-PNP)] 10b	205
7.11.48 Synthesis of [Ir(CO)(<i>o</i> -An-PNP)] 10c	206
7.11.49 Synthesis of [Ir(CO)(^{<i>i</i>} Pr-PNP)] 10d	206
7.11.50 Synthesis of [Ir(CO)(Cy-PNP)] 10e	207
7.11.51 Synthesis of Ir(III) Methyl complexes 11 a-e	208
7.11.53 Synthesis of [Ir(CO)(<i>o</i> -Tol-PNP)I(Me)] 11b	208
7.11.54 Synthesis of [Ir(CO)(<i>o</i> -An-PNP)I(Me)] 11c	209
7.11.55 Synthesis of [Ir(CO)(^{<i>i</i>} Pr-PNP)I(Me)] 11d	210
7.11.56 Synthesis of [Ir(Cy-PNP)(CO)(Me)I] 11e	210
7.11.57 Synthesis of [Rh(R-PN)(CO)Cl] complexes	211
7.11.58 Synthesis of [Rh(^{<i>t</i>} Bu-PN)(CO)Cl] 14a	211
7.11.59 Synthesis of [Rh(<i>o</i> -An-PN)(CO)Cl] 14b	212
7.11.60 Synthesis of [Rh(2,5(CF ₃) ₂ C ₆ H ₃ -PN)(CO)Cl] 14c	212
7.11.61 Synthesis of [Rh(2,6Me ₂ -C ₆ H ₃ -PN)(CO)Cl] 14d	213
7.11.62 Synthesis of [Rh(2,6Et ₂ -C ₆ H ₃ -PN)(CO)Cl] 14e	213
7.11.63 Synthesis of [Rh(2,6Et ₂ -C ₆ H ₃ -PN)(CO)Cl] 14f	214
7.11.64 Synthesis of [Rh(2,4,6,Me ₃ -C ₆ H ₂ -PN)(CO)Cl] 14g	214
7.12 General method for catalytic decarbonylation reactions	215

7.12.1	Characterisation of alkene products	215
7.12.2	Undecenes (C ₁₁ H ₂₂) mixture of isomers isolated as a clear oil	215
7.12.3	Tridecenes (C ₁₃ H ₂₆) mixture of isomers isolated as a clear oil	216
7.12.4	Pentadecenes (C ₁₅ H ₃₀) mixture of isomers isolated as a clear oil	216
7.12.5	heptadecenes (C ₁₇ H ₃₄) mixture of isomers isolated as a clear oil	216
7.12.6	Synthesis of 15d	217
7.12.7	Synthesis of 15f	218
7.12.8	Synthesis of 15g	219
7.13	References	220
	Chapter 8- Appendix	222
8.1	Appendix 1- crystallographic data	223
8.2	Appendix 2 – tabulated rate constants	232
8.3	Appendix 3 – additional spectroscopic characterisation and information	238

Chapter 1

General Introduction

1	2	3	4	5	6	7	8	9	10	11	12	13	14	15	16	17	18
hydrogen 1 H 1.0079																	helium 2 He 4.0026
lithium 3 Li 6.941	beryllium 4 Be 9.0122											boron 5 B 10.811	carbon 6 C 12.011	nitrogen 7 N 14.007	oxygen 8 O 15.999	fluorine 9 F 18.998	neon 10 Ne 20.180
sodium 11 Na 22.990	magnesium 12 Mg 24.305											aluminum 13 Al 26.982	silicon 14 Si 28.086	phosphorus 15 P 30.974	sulfur 16 S 32.065	chlorine 17 Cl 35.453	argon 18 Ar 39.948
potassium 19 K 39.098	calcium 20 Ca 40.078											gallium 31 Ga 69.723	germanium 32 Ge 72.61	arsenic 33 As 74.922	seelenium 34 Se 78.96	bromine 35 Br 79.904	krypton 36 Kr 83.80
rubidium 37 Rb 85.468	strontium 38 Sr 87.62											indium 49 In 114.82	tin 50 Sn 118.71	antimony 51 Sb 121.75	tellurium 52 Te 127.60	iodine 53 I 126.90	xenon 54 Xe 131.29
cesium 55 Cs 132.91	barium 56 Ba 137.33	57-70 *										thallium 81 Tl 204.38	lead 82 Pb 207.2	bismuth 83 Bi 208.98	polonium 84 Po [209]	astatine 85 At [210]	radon 86 Rn [222]
francium 87 Fr [223]	radium 88 Ra [226]	89-102 **	lanthanum 57 La [227]	cerium 58 Ce 140.12	praseodymium 59 Pr 140.91	neodymium 60 Nd 144.24	promethium 61 Pm [145]	samarium 62 Sm 150.36	europlum 63 Eu 151.96	gadolinium 64 Gd 157.25	terbium 65 Tb 158.93	dysprosium 66 Dy 162.50	holmium 67 Ho 164.93	erbium 68 Er 167.26	thulium 69 Tm 168.93	ytterbium 70 Yb 173.04	
			actinium 89 Ac [227]	thorium 90 Th 232.04	protactinium 91 Pa 231.04	uranium 92 U 238.03	neptunium 93 Np [237]	plutonium 94 Pu [244]	americium 95 Am [243]	curium 96 Cm [247]	berkelium 97 Bk [247]	californium 98 Cf [251]	einsteinium 99 Es [252]	fermium 100 Fm [257]	mendelevium 101 Md [258]	nobelium 102 No [259]	

Key:

element name
atomic number
symbol
atomic weight (mean relative mass)

1.0 Catalysis

A catalyst is a chemical compound that has the ability to increase the rate of a chemical reaction without being consumed by the reaction. The catalyst does not change the overall standard Gibbs energy of reaction ΔG^\ominus , but provides a reaction pathway which has a lower Gibbs energy of activation ΔG^\ddagger (Figure 1.1).¹

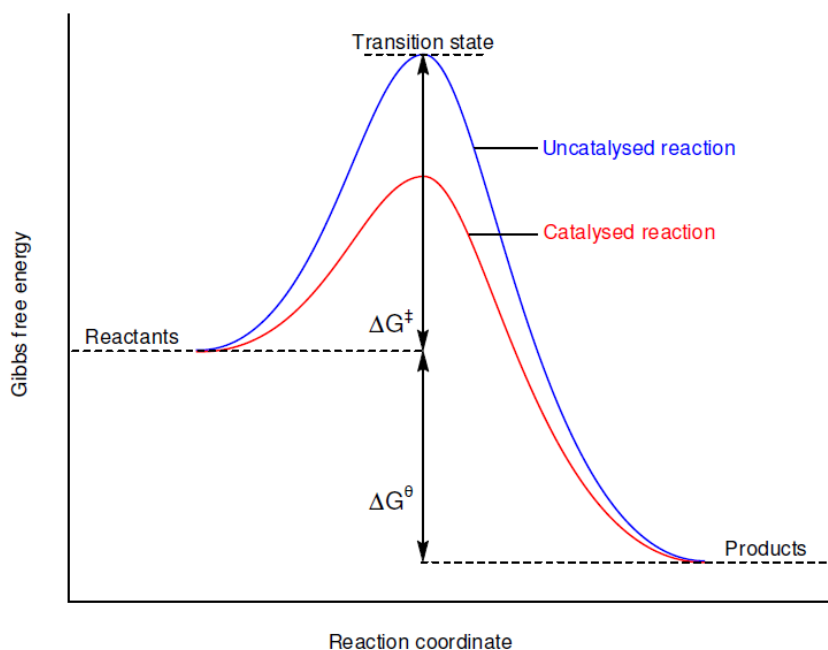


Figure 1.1: Gibbs free energy profiles for catalysed and uncatalysed reactions.

1.0.1 General definition and classification

The type of catalysis is dependent upon what phase the catalyst lies in compared to that of the substrate. Homogeneous catalysis occurs when both substrate and catalyst are in the same phase. Heterogeneous catalysis occurs when substrate and catalyst are in a different phase.²

Heterogeneous catalysts are usually metals on an inert solid support which provides a large surface area on which the reaction can take place. These catalysts allow easy product separation from reaction mixtures and are robust and recyclable, hence their use in industrial processes (Haber process, Fischer-Tropsch reaction and Ziegler-Natta polymerisation).³ Heterogeneous catalysts are less reactive than homogeneous catalysts and usually require harsh reaction conditions and have poor product selectivity.

Heterogeneous catalysts are easily poisoned and are harder to investigate using spectroscopic techniques, making obtaining mechanistic information very difficult.⁴

A homogeneous catalyst lies in the same phase as the reactant, and has notable advantages over a heterogeneous catalyst. It is possible to obtain a very high selectivity and can even be asymmetric, one of the main reasons for the commercial success of many homogeneous-catalysed industrial processes (e.g. alkene hydroformylation, methanol carbonylation and ethene methoxycarbonylation). Homogeneous catalysts usually have a much higher activity and often operate at much milder conditions, they are also less susceptible to poisoning e.g. by sulphur-containing compounds. Finally, in most situations, the activity of the catalyst can be explained and understood at a molecular level. This is because the active catalytic species in a homogeneously catalysed reaction is easier to identify than in a heterogeneously catalysed one. This enables careful ligand variation to optimise catalytic activity and selectivity, much more difficult to achieve in a heterogeneous system.⁵

A disadvantage of homogeneous catalysis is the difficulty in product separation. Distillation of products from the homogeneous mixture is an expensive undesirable step in the isolation of a pure product, costing both time and money. Catalyst degradation can also occur in the solution phase, decreasing the amount of active catalyst, leading to decreased yield and catalyst turnover.

To summarise, both heterogeneous and homogeneous catalysis play important roles in the chemical industry. Roughly 85% of all catalytic processes are based on heterogeneous catalysts. However homogeneous catalysts, due to their high selectivity and other advantages, are becoming increasingly important for the manufacture of tailor-made plastics, fine chemicals and pharmaceutical intermediates.⁶

1.0.2 Transition metals in homogeneous catalysis

Transition metals are utilised in homogeneous catalysis because they can increase the reactivity of inert molecules upon co-ordination to a metal centre, for example activation of CO and hydrocarbons are well reported within the literature.

Transition metals can also accommodate a wide variety of ligands due to their flexible oxidation states and co-ordination numbers.⁷ Having flexible co-ordination ability can often allow for ligand migration which produces a vacant site on the metal centre in which

another species can attack. The ability to accommodate a wide variety of ligands enables electronic and steric properties of a metal complex to be tuned to influence reactivity and selectivity.^{8,9}

The two most important characteristics of a catalyst are its selectivity and its activity. In a catalytic reaction there can be the potential for forming more than one product, this is where catalyst selectivity is key. By optimising the catalyst and process conditions it is possible to obtain high yields and selectivity for a catalytic reaction, vital in the production of fine chemicals. Table 1.1 displays some well known products from homogeneously catalysed reactions that are dependent upon a highly selective catalyst.¹⁰

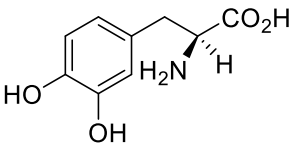
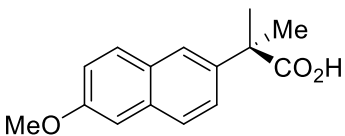
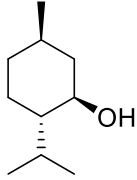
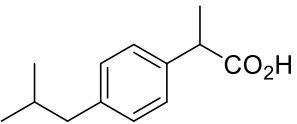
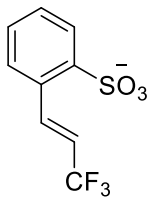
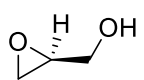
Structure	Name and use	Process
	L-Dopa Parkinsons disease	Asymmetric hydrogenation
	Naproxen© Anti inflammatory	Asymmetric hydroformylation
	L-Menthol Flavouring	Asymmetric isomerisation
	Ibuprofen Analgesic	Carbonylation
	Prosulferon herbicide intermediate	Heck reaction
	R-Glycidol Heart drug component	Asymmetric epoxidation

Table 1.1: Some selected chemicals synthesised by homogeneous catalysis.

Homogeneous catalysis has been applied to many organic transformations leading to a wide range of useful products. Examples include methanol carbonylation (Monsanto and Cativa® process),¹¹⁻¹³ alkene hydroformylation (Oxo process),¹⁴⁻¹⁹ alkene oxidation (Wacker process),²⁰ hydrogenation^{21,22} and alkene polymerisation²³ with a few selected examples being displayed in Table 1.2

Reaction	Example	Catalyst
Methanol Carbonylation	$\text{CH}_3\text{OH} + \text{CO} \rightarrow \text{CH}_3\text{COOH}$	Rh/I or Ir/I
Alkene Hydroformylation	$\text{RCH}=\text{CH}_2 + \text{CO} + \text{H}_2 \rightarrow \text{RCH}_2\text{CH}_2\text{CHO}$	Co/ PR_3 or Rh/ PPh_3
Hydrogenation	$\text{RCH}=\text{CH}_2 + \text{H}_2 \rightarrow \text{RCH}_2\text{CH}_3$	Rh/ PPh_3 or Co Ru/Phosphine
Alkene oxidation	$\text{C}_2\text{H}_4 + 0.5\text{O}_2 \rightarrow \text{CH}_3\text{CHO}$	$\text{PdCl}_2/\text{CuCl}_2$
Alkene Metathesis	$\text{RCH}=\text{CH}_2 + \text{R}'\text{CH}=\text{CH}_2 \rightarrow \text{RCH}=\text{CHR}' + \text{C}_2\text{H}_4$	$\text{RHC}=\text{RuCl}_2\text{L}_2$ L= PR_3 or NHC
Alkene polymerisation / oligomerisation	$n\text{CH}_2=\text{CH}_2 \rightarrow (\text{CH}_2\text{CH}_2)_n$	Ni, Ti, Zr and Cr

Table 1.2: Industrial relevant homogeneously catalysed transformations.

1.1 Oil feedstock demand and renewable sources.

Fossil fuels are non-renewable sources that take millions of years to form. The world supply is being depleted rapidly, therefore, renewable energy has seen a dramatic rise in research interest to try and deal with the global demands and increased energy needs.

Renewable energy comes from natural processes such as sunlight, wind, rain and biomass. About 16% of the world's energy comes from renewable sources, of the 16% 10% comes from biomass. Biomass is biological material from living or recently living organisms that can either be used directly or converted into other energy products such as bio-fuel. It has received considerable attention as a sustainable feedstock, especially for the transportation sector which is strongly dependent on petroleum, a non-renewable source.²⁴

In a market that is governed by preferences and habits that are based on widespread availability of liquid hydrocarbon fuels, bio-fuels are seen as the replacement of choice. They are similar in structure, meaning little change in the infrastructure of internal combustion engines is required when being used directly. For example bio-ethanol or biodiesel are currently being used commercially as blending agents in petroleum derived fuels.

Whilst bio-ethanol is a commonly used bio-fuel, fatty esters derived from renewable sources have attracted some interest as a transportation fuel. Fatty esters can be prepared easily by transesterification of vegetable oils with alcohols. However their reduced compatibility with internal combustion engines means that other routes to higher quality hydrocarbons are desired.²⁵

Fatty oils are made from one mole of glycerol and three moles of fatty acids and are commonly referred to as triglycerides, an example of which can be seen in Figure 1.2.

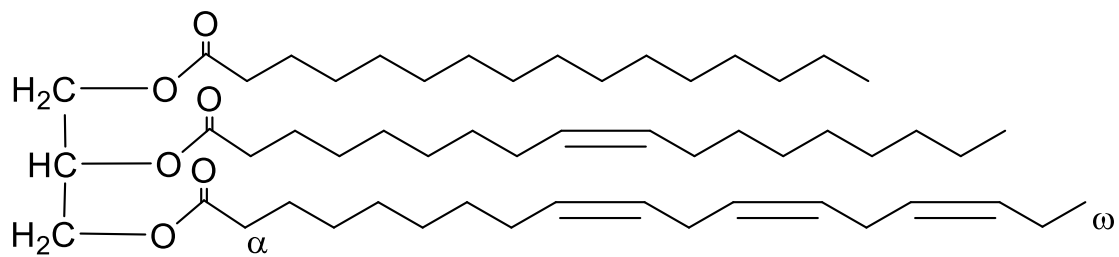


Figure 1.2: Example of an unsaturated triglyceride: Glycerol (left), attached to three fatty acid components.

Natural vegetable oils and animal fats are extracted or pressed to isolate the crude fat. Table 1.3 shows the percentage fatty acid composition of some common vegetable oils.²⁶⁻²⁸

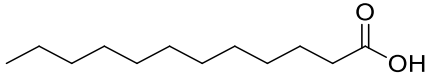
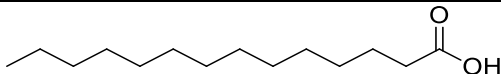
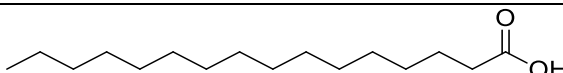
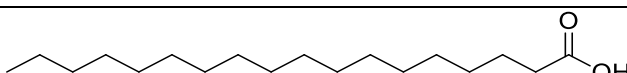
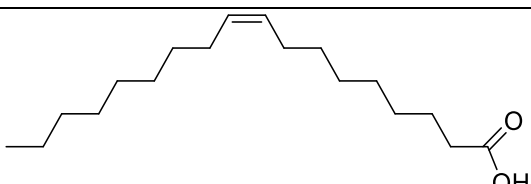
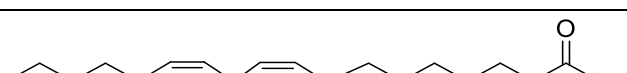
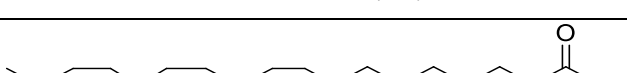
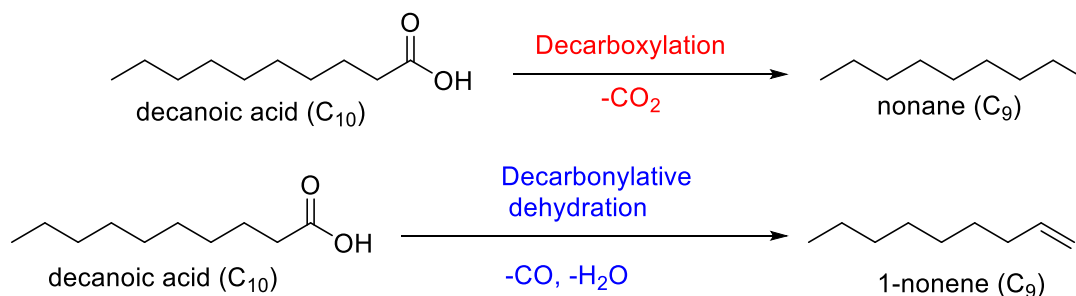
Fatty acid	Tallow	Soybean	Cottonseed	Palm
 <i>Lauric acid (C₁₂)</i>	0.1%	0.1%	0.1%	0.1%
 <i>Myristic acid (C₁₄)</i>	2.8%	0.1%	0.7%	1.0%
 <i>Palmitic acid (C₁₆)</i>	23.3%	10.2%	20.1%	42.8%
 <i>Stearic acid (C₁₈)</i>	19.4%	3.7%	2.6%	4.5%
 <i>Oleic acid (C₁₈)</i>	42.4%	22.8%	19.2%	40.5%
 <i>Linoleic acid (C₁₈)</i>	2.9%	53.7%	55.2%	10.1%
 <i>α-Linolenic acid (C₁₈)</i>	0.9%	8.6%	0.6%	0.2%

Table 1.3: Fatty acid composition of common vegetable oils.²⁹

Deoxygenation refers to chemical reactions that involve removal of oxygen from organic compounds. Oxygen can be removed from compounds containing oxygen as either H₂O, CO₂ or CO. Deoxygenation by dehydration (known as hydrodeoxygenation or HDO) involves an intramolecular or intramolecular source of H₂. Intramolecular dehydration does not involve any carbon consumption, however intermolecular dehydration requires H₂ produced from an external source, usually produced in an environment that consumes carbon and is thus less efficient.³⁰

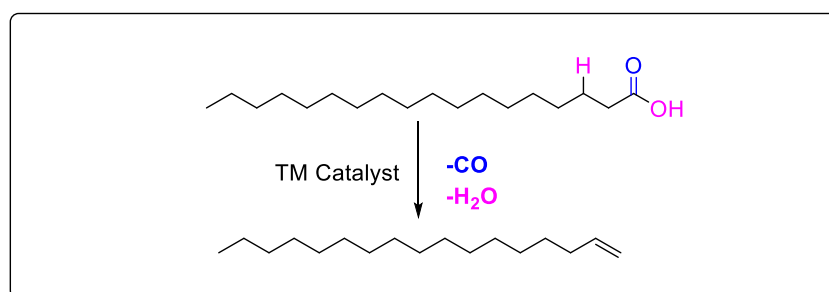
Carboxylic acids found in vegetable oils and animal fats can be readily converted to fuels and chemicals by decarbonylative dehydration and decarboxylation reactions.³¹

For example, linear acids are converted to linear alkanes and alkenes by decarboxylation and decarbonylative dehydration respectively, as shown for the reaction of decanoic acid in Scheme 1.1.



Scheme 1.1: Decarboxylation and decarbonylative dehydration of decanoic acid.

Terminal alkenes formed by decarbonylative dehydration are appealing organic materials because of their ability to be further functionalised and are important in the polymer sector. Therefore, an effective catalyst for decarbonylative dehydration prevents hydrogenation of the product α -olefin as well as double bond migration to form isomeric internal olefins. This would be an effective route to a much higher value chemical feedstock, as displayed in Scheme 1.2 for the conversion of stearic acid to 1-heptadecene.

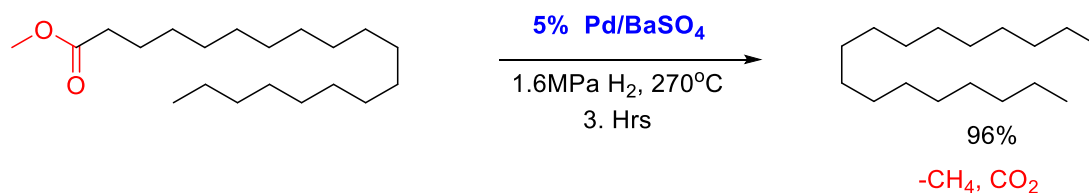


Scheme 1.2: Potential route to alkenes by decarbonylative dehydration of fatty acids (chemical prices taken from Sigma Aldrich July 2015).

1.2 Transition metal catalysed deoxygenation of carboxylic acids

1.2.1 Heterogenous catalysed decarboxylation of aliphatic acids

Although not the focus of this project, heterogeneously catalysed deoxygenation of long chain carboxylic acids has been investigated. A heterogeneous system is shown in Scheme 1.3 where palladium is used to decarboxylate higher aliphatic esters.²⁹



Scheme 1.3: Heterogeneous catalysed decarboxylation of aliphatic esters. ²⁹

Initial optimisation of catalyst and reaction conditions using methyl stearate as a model substrate was undertaken to identify the most active and selective catalyst. Palladium supported on barium sulphate showed the best activity and selectivity, affording the highest yields of heptadecanes with one carbon less than the fatty acid part of methyl stearate. It was also found that an appropriate pressure of H₂ was required to keep the heterogeneous Pd surface clean.

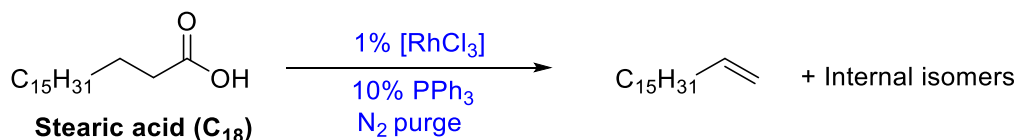
A large range of transition metals and solid supports have been tested in catalytic decarboxylation reactions. Carbonaceous supports are usually employed due to their amphoteric nature and minimal coke induced deactivation via large surface area. More interestingly metal performance has been investigated and the activity was found to follow the order Pd>Pt>Ni>Rh>Ir>Os, hence the most studied heterogeneous catalysts for decarboxylation are Pd and Pt.³²⁻³⁴ These results and more information on heterogeneous decarboxylation are summarised in a mini-review by Santillan-Jiminez et al.³⁵

1.2.2 Homogeneously catalysed deoxygenation of fatty acids

The homogeneously catalysed deoxygenation of long chain carboxylic acids had received very little consideration until publications by Foglia et al.³⁶ and Miller et al.³⁷. Since these seminal publications this area of research has grown in interest and is discussed in detail below.

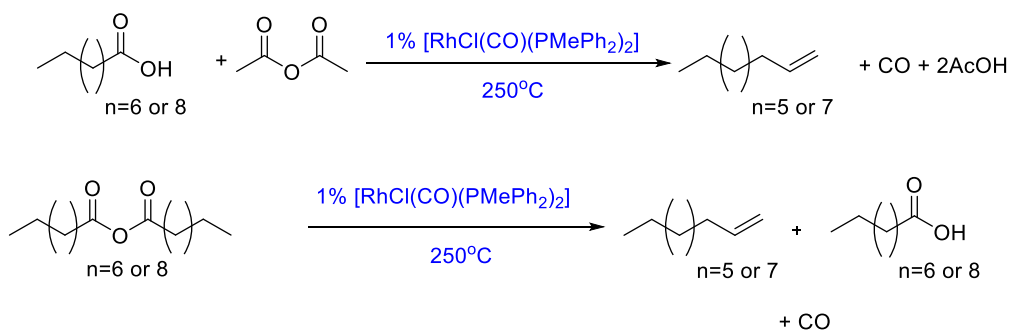
1.2.3 Rhodium catalysed decarbonylative dehydration of fatty acids.

Foglia et al.³⁶ reported the decarbonylative dehydration of stearic acid at 280°C using 1% loading of an RhCl₃ catalyst and 10% PPh₃ ligand, the reaction yielded heptadecenes in a 100% yield. Analysis of yellow crystals formed inside the reaction vessel revealed the presence of [Rh(CO)(Cl)(PPh₃)₂] which was formed during the reaction (Scheme 1.4).



Scheme 1.4: Decarbonylative dehydration of stearic acid using a rhodium catalyst.³⁶

Miller et al.³⁷ used 1% [RhCl(CO)(PMePh₂)₂] catalyst loading and either long chain anhydride or a equimolar amount of long chain carboxylic acid and an acetic anhydride additive both yielding alkene product (Scheme 1.5). Decarbonylation initiated when the reaction temperature reached 180-190 °C evidenced by rapid evolution of CO from the reaction vessel. Distillation of the olefin product from the reaction mixture was essential to ensure a high degree of terminal olefin selectivity.

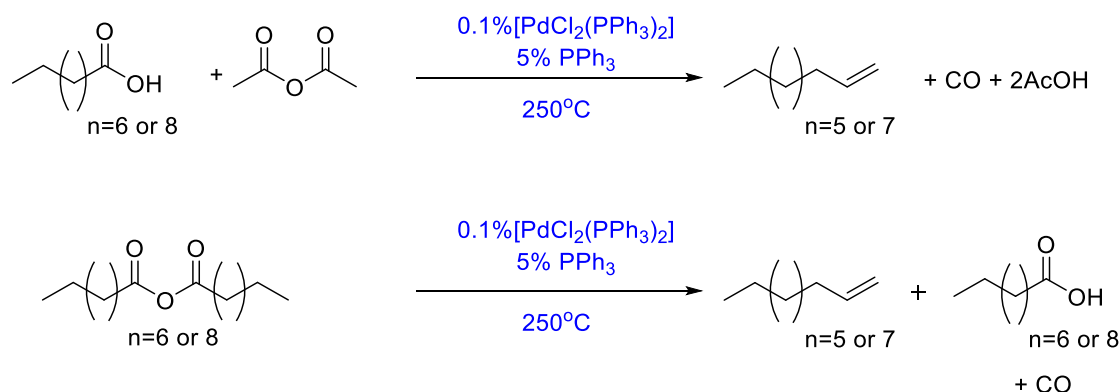


Scheme 1.5: Rhodium catalysed decarbonylative dehydration of long chain acids and anhydrides.³⁷

Varying the phosphine ligand of the rhodium catalyst had a very slight effect on selectivity toward 1-alkenes, but had a larger effect on catalyst turnover number with P(*o*-Tol)₃ > PMe₂Ph > PPh₃ and PCy₃.³⁷

1.2.4 Palladium catalysed decarbonylative dehydration of fatty acids

In the same publication, Miller et al.³⁷ also reported the decarbonylative dehydration of long chain carboxylic acids using a palladium catalyst. A lower loading of palladium (0.1% compared to acid) and a 50 fold excess of phosphine ligand resulted the formation of 1-alkenes in a high selectivity and turnover number (Scheme 1.6)

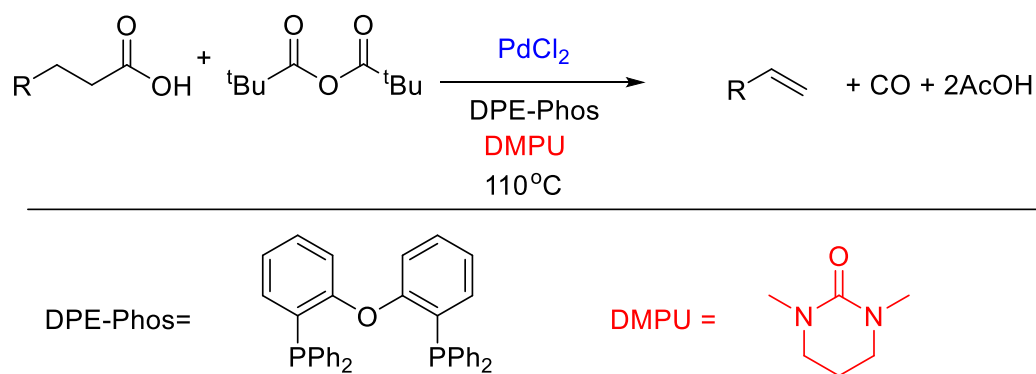


Scheme 1.6: Palladium catalysed decarbonylative dehydration of long chain acids and anhydrides.³⁷

Variation of the phosphine ligand had very little effect on the selectivity towards 1-alkenes, although the turnover number followed the order $\text{PCy}_3 > \text{PPh}_3 > \text{P}(o\text{-Tol})_3$.

Goößen and Rodriguez³⁸ reported the decarbonylative dehydration of phenyl butanoic acid using a pivalic anhydride additive, a $\text{PdCl}_2/\text{DPE-Phos}$ catalyst and a lower operating temperature of 110°C . No conversion occurred at room temperature, and only a small amount of the desired olefin product was observed at 110°C in toluene. However, on changing from toluene to a high polarity solvent (DMPU) the desired 1-alkene product was obtained in 83% yield when stopping the reaction at 85% conversion. Basic additives such as pyridine and K_2CO_3 were used in an attempt to improve selectivity but only had a negative effect on the yield and selectivity.

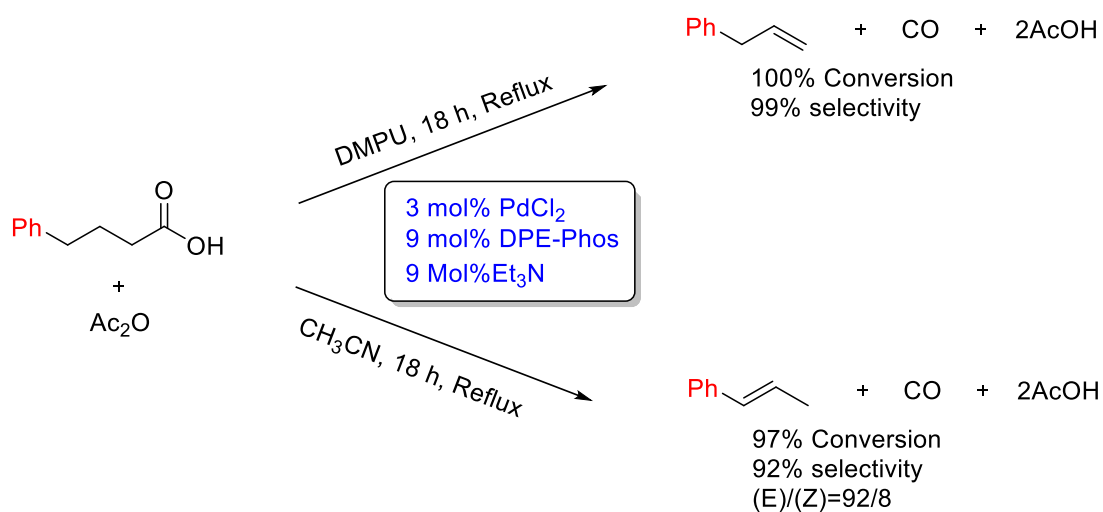
The optimised conditions obtained from the initial studies were then applied to the decarbonylative dehydration of an array of aliphatic and aromatic carboxylic acids (Scheme 1.7).



Scheme 1.7: Palladium catalysed system developed by Gooßen and Rodriguez. ³⁸

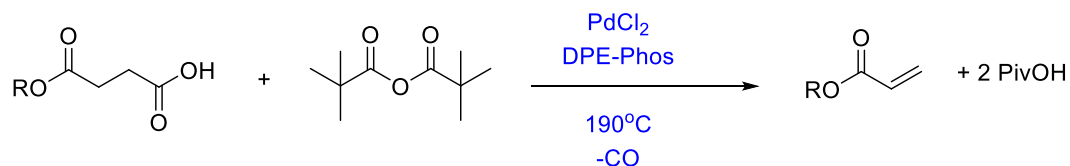
A palladium catalyst was also used by Le Notre et al.³⁹ who investigated the transformation of amino acids obtained from protein waste streams into more useful products by decarbonylative dehydration (Scheme 1.8).³⁹ Using similar conditions to those reported by Gooßen and Rodriguez,³⁸ (PdCl₂, DPE-Phos and DMPU solvent 110°C) a high yield and selectivity of 99:1 in favour of the terminal alkene was obtained when Et₃N was used as an additive. The Et₃N is proposed to stabilise cationic intermediates formed during the catalytic reaction.

Interestingly, when changing the solvent from DMPU to MeCN, not only were high yields obtained, but also high selectivity (92:8) toward the internal alkene. It is suggested that this is due to the formation of a highly efficient isomerisation catalyst such as [PdCl₂(NCMe)₂].



Scheme 1.8: Palladium catalysed system developed by Le Notre et al. ³⁹

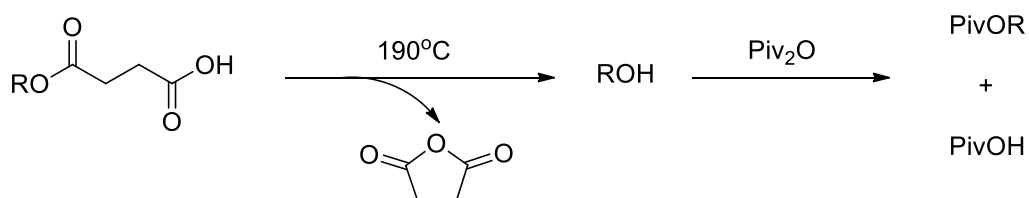
Miranda et al.⁴⁰ applied this chemistry to converting mono-alkyl succinates to the corresponding alkyl acrylates. These monomers are used extensively in the paint, coatings and textile industries and are examples of high volume petro-chemical derived commodity monomers. DPE-Phos was once again the best ligand, affording the highest yields of alkyl acrylate (Scheme 1.9).



R	Acrylate	PivOR	PivOH
Me	64%	12%	49%
<i>n</i> -Butyl	45%	21%	60%
<i>t</i> -Butyl	18%	10%	90%

Scheme 1.9: Palladium catalysed decarbonylative dehydration of mono alkyl succinates.⁴⁰

A substantial amount of a pivalic ester was formed during the reaction, however this was proven not to be part of the catalytic cycle using a controlled experiment. The mono alkyl succinate was heated to the same temperatures and an intramolecular cyclization was observed reforming the succinic anhydride and an alcohol. This could then react with the pivalic anhydride and form the pivalic ester and PivOH as displayed in Scheme 1.10.

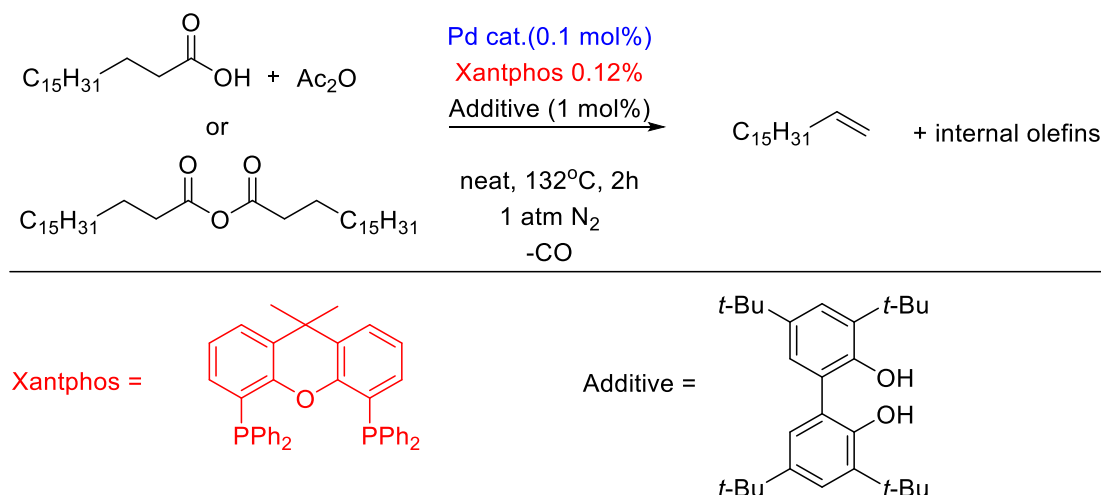


Scheme 1.10: Proposed route to formation of pivalic ester side product.

Liu et al.⁴¹ have recently reported a highly efficient palladium catalysed system which has low palladium loadings, is solvent free and runs under relatively mild conditions as displayed in Scheme 1.11.

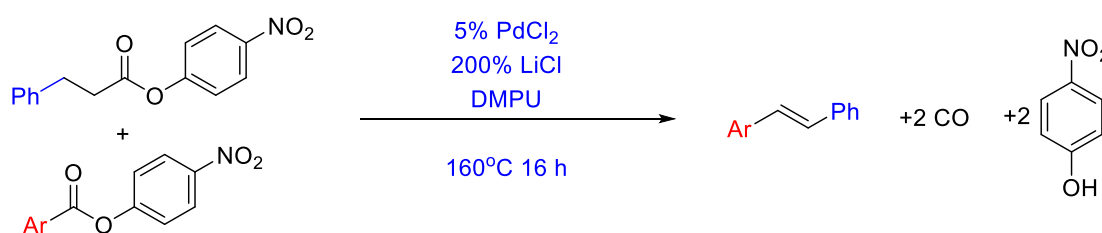
The most effective ligand was found to be xantphos with 1.5 equivalents of acetic anhydride additive (relative to acid substrate). Interestingly when only stearic anhydride was used a very poor yield of olefin was obtained, but upon addition of a protic additive, (*t*-Bu)₄biphenol, a dramatic increase in yield was observed, indicating that acid is playing

an important role in the reaction. The addition of acetic anhydride portion-wise resulted in higher terminal olefin selectivity by reducing the build-up of acetic acid in the reaction mixture. Adding the acetic anhydride in 6 portions over the course of the reaction enabled high terminal selectivity of olefins without distillation of the olefin from the reaction mixture.



Scheme 1.11: Palladium catalysed system developed by Liu et al.⁴¹

Recently John et al.⁴² developed a single pot tandem palladium catalysed decarbonylation and Heck coupling of p-nitrophenylesters. The reaction is catalysed by PdCl₂ in the absence of additional ligands and is promoted by metal halide additives and DMPU solvent. The reaction provides a new route to stilbenes, notable synthetic targets, in moderate yields (Scheme 1.12).

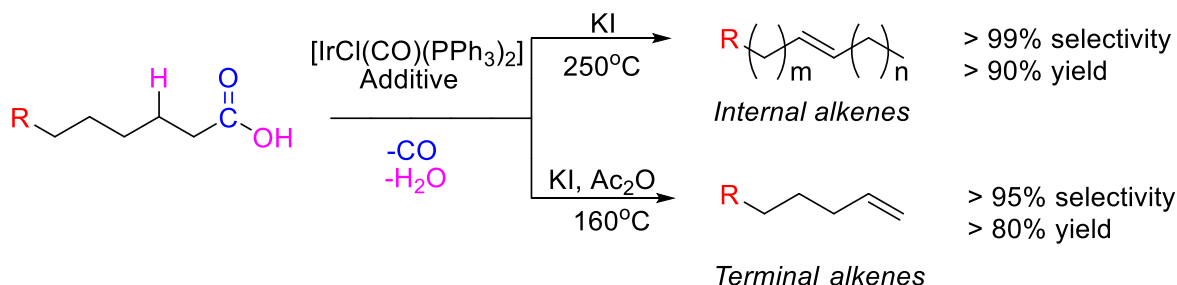


Scheme 1.12: Palladium catalysed tandem decarbonylative dehydration/Heck coupling reaction.⁴²

1.2.5 Iridium catalysed decarbonylative dehydration of fatty acids

Internal alkenes are not as sought after as terminal ones as they have a much lower commercial value. However internal alkenes are very useful and are used as paper sizing agents, lubricants and surfactants as well as many others. Vaska's complex has recently

been reported to decarbonylate carboxylic acids when combined with KI as an additive to give internal alkenes selectively.⁴³ On combining KI and Ac₂O as additives and lowering the temperature it was found that terminal alkenes could be formed selectively as displayed in Scheme 1.13.



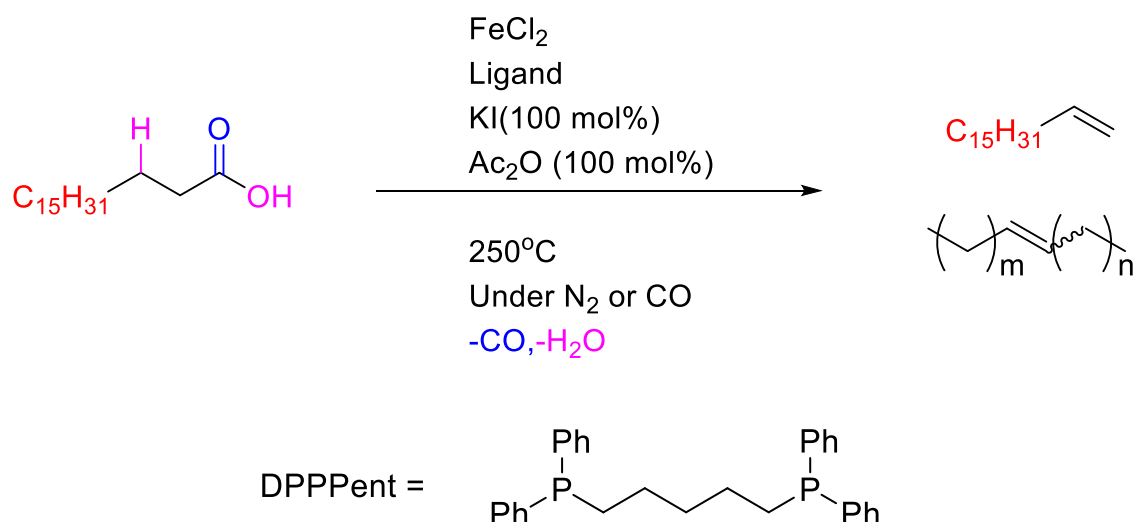
Scheme 1.13: Iridium catalysed decarbonylative dehydration of fatty acids.⁴³

The iridium catalysed reaction uses the combination of $[\text{IrCl}(\text{CO})(\text{PPh}_3)_2]$ and KI which is said to act as a halide exchange reagent at 250°C. These conditions were tested on numerous long chain carboxylic acids with a >84% yield and 99% selectivity of internal alkenes being formed. The double bond position of the products was also analysed, in all cases it was found that a mixture of alkenes was obtained.

1.2.6 Iron catalysed decarbonylative dehydration of fatty acids

With the catalytic synthesis of terminal olefins being dominated by expensive precious transition metal catalyst such as palladium, rhodium and iridium, iron was investigated by Maetani et al.⁴⁴ as it is an inexpensive and environmentally benign metal.⁴⁵

Using stearic acid as a model substrate with 10 mol % FeCl₂, 20% PPh₃ ligand, KI and Ac₂O as an additive, it was shown that decarbonylative dehydration of the fatty acid occurred, forming alkenes in 79% yield and 81% selectivity toward the 1-alkene, as shown in Scheme 1.14.



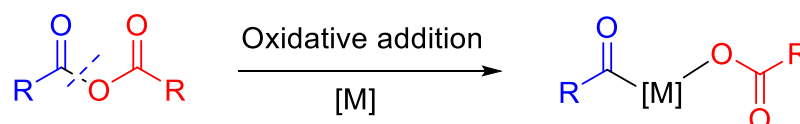
Scheme 1.14: Iron catalysed decarboxylation of long chain fatty acids. ⁴⁴

Optimisation of the reaction conditions found that the selectivity and the efficiency of the decarbonylation reaction could be improved by using DPPent, a flexible diphosphine ligand. A lower temperature of 240°C and a 20 bar atmosphere of CO was employed which afforded the terminal olefin in a 74% yield and 97% selectivity.

Detection of CO by GC indicated a decarbonylation step in the mechanism. The introduction of a radical scavenger (TEMPO) had no detrimental effect to the reaction, eliminating a radical pathway.

1.2.7 Mechanistic aspects

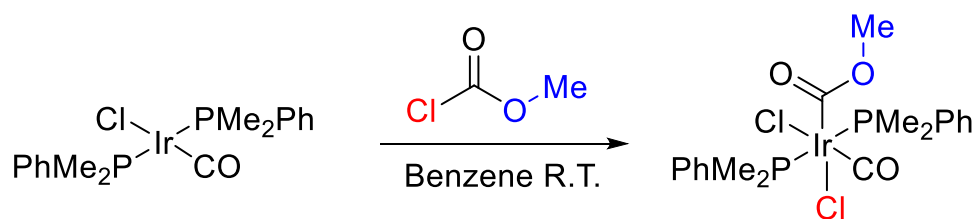
Miller et al.³⁷ and Foglia et al.³⁶ were the first to postulate a catalytic mechanism, suggesting that the first organometallic step was the oxidative addition of the C-O bond of an anhydride as shown in Scheme 1.15.



Scheme 1.15: Oxidative addition of a C-O bond of an anhydride.

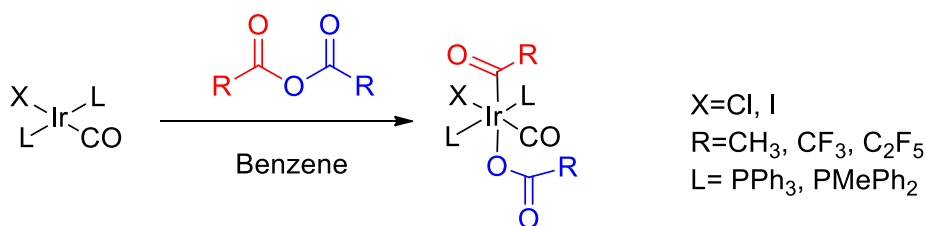
Oxidative addition of C-O bonds is less studied than that of carbon halogen bonds and tends to be far less facile. This was demonstrated by Deeming et al.⁴⁶ by reacting

$[\text{IrCl}(\text{CO})(\text{PMe}_2\text{Ph})_2]$ with methyl chloroformate, in which the C-Cl bond is broken exclusively over the C-O bond (Scheme 1.16).

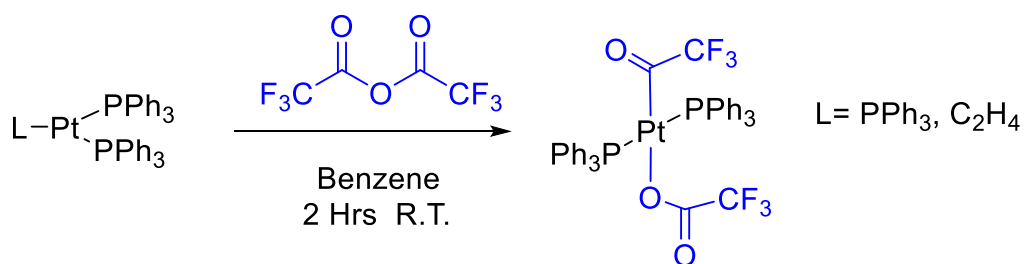


Scheme 1.16: Preference for C-Cl over C-O bond activation. ⁴⁶

However, examples of C-O bond activation are present within the literature. Blake et al.⁴⁷ reported reactions of carboxylic acid anhydrides with nucleophilic iridium (I) complexes (Scheme 1.17) and platinum (0) complexes (Scheme 1.18). These reactions give the Ir (III) and Pt(II) acyl complexes respectively, with the geometry of the final product being mutually trans confirmed by ¹H NMR spectroscopy.

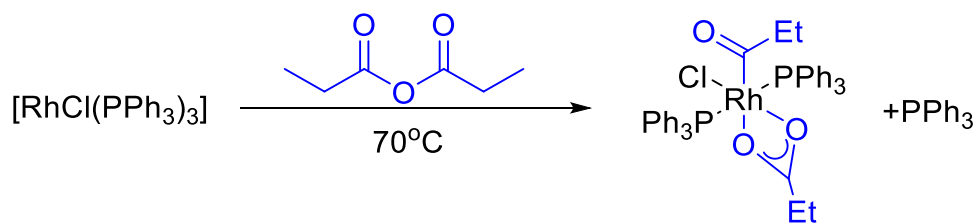


Scheme 1.17: Oxidative addition of anhydrides to form Ir(III) acyl complexes. ⁴⁷



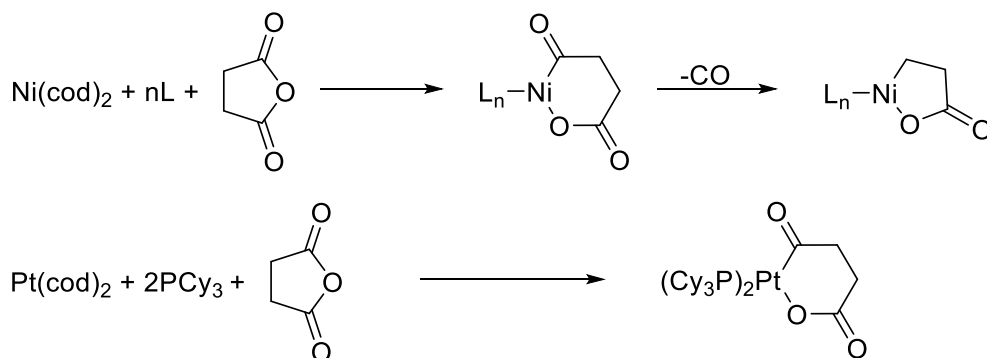
Scheme 1.18: Oxidative addition of trifluoroacetic anhydride to form a Pt(II) acyl. ⁴⁷

Miller et al.⁴⁸ also reported the oxidative addition of anhydrides to Rh(I) complexes in an earlier publication supporting the postulated mechanistic proposal as shown in Scheme 1.19.



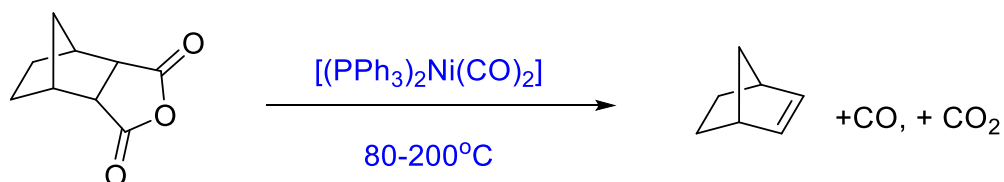
Scheme 1.19: C-O bond activation by a Rh(I) complex. ⁴⁸

Yamamoto et al.⁴⁹ described the synthesis of cyclic Ni and Pt containing esters by oxidative addition of cyclic carboxylic anhydrides (Scheme 1.20). The oxidative addition of the C-O bond by nickel is then followed by decarbonylation to form a nickel metallocycle with one less carbon atom. The analogous study using $[\text{Pt}(\text{cod})_2]$ with 2 equivalents of PCy_3 formed a 6 membered Pt acyl by oxidative addition of the anhydride. This complex however does not undergo the decarbonylation step.



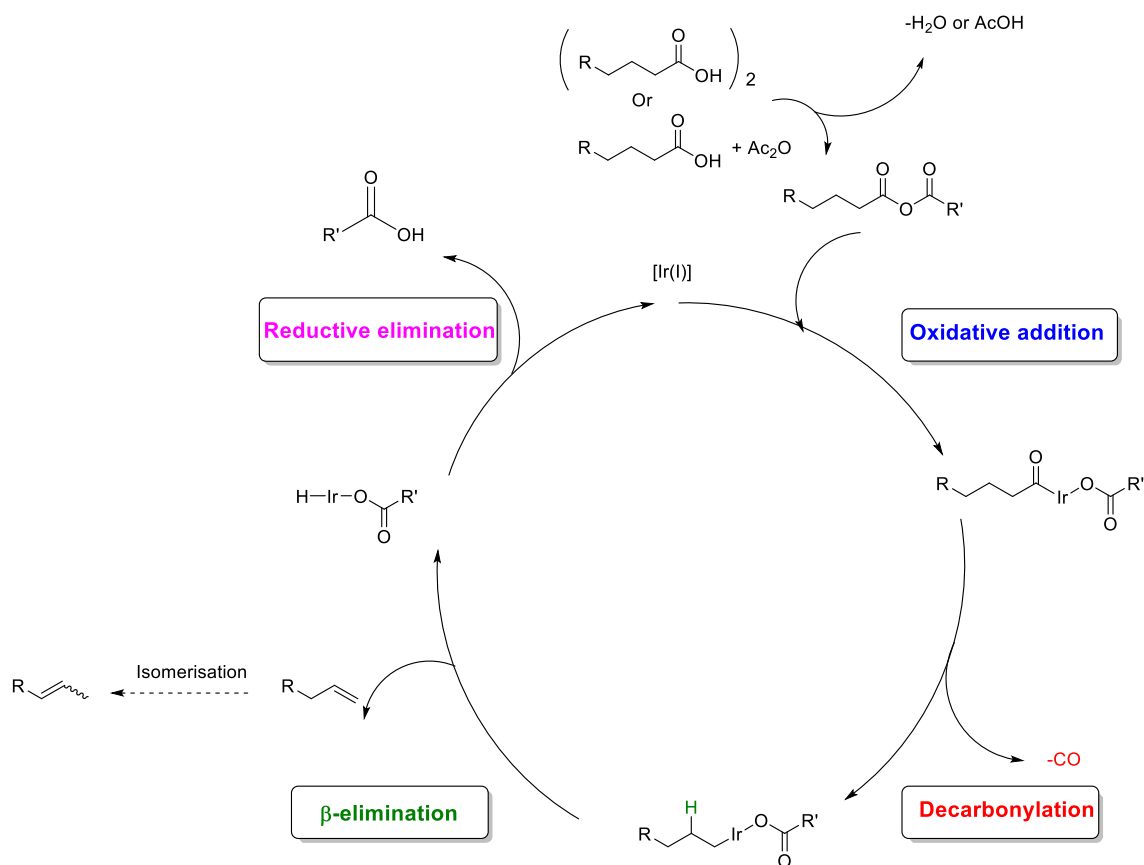
Scheme 1.20: Oxidative addition of succinic anhydride to form a cyclic Ni(II) ester by decarbonylation. ⁴⁹

Trost et al.⁵⁰ reported the oxidative addition and elimination of a cyclic anhydride using a nickel phosphine catalyst. Heating initially at 80°C and raising to 200°C generated the bicyclo heptene product which was constantly swept from the reaction mixture. The reactions of anhydrides with abstractable β -hydrogens resulted in complex reaction mixtures (Scheme 1.21).



Scheme 1.21: Oxidative addition and elimination of a cyclic anhydride using a nickel phosphine complex. ⁵⁰

Each postulated mechanism for the decarbonylative dehydration of long chain acids has included the oxidative addition of an anhydride. The proposed mechanism for the iridium catalysed decarbonylative dehydration and isomerisation of long chain aliphatic acids is shown in Scheme 1.22.

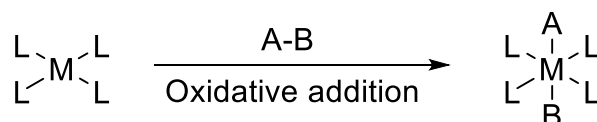


Scheme 1.22: Proposed mechanism for iridium catalysed decarbonylative dehydration (spectator ligands are omitted for clarity).

The first organometallic step of this proposed cycle is the oxidative addition of the anhydride C(O)-O bond which gives an iridium(III) acyl species. The acyl iridium complex then undergoes decarbonylation to form the alkyl iridium complex which can then undergo β - elimination to generate the 1-alkene product and an iridium(III) hydride. Reductive elimination of the acid regenerates the catalytically active Ir(I) species. Alkene isomerisation to the internal alkene is facilitated by the re-insertion of the terminal alkene and β - elimination to form the thermodynamically favoured internal alkenes and reform the Ir(III) hydride.

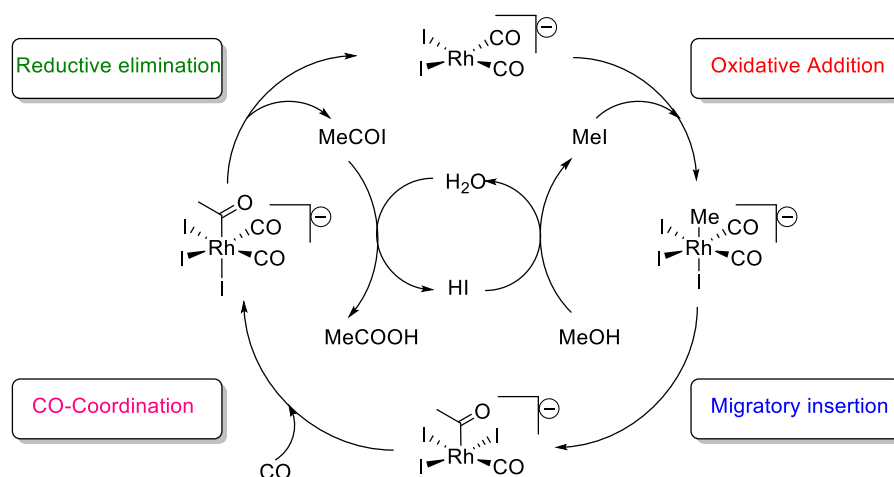
1.3 Ligand effects on oxidative addition

It is common for d^8 square planar metal complexes, for example rhodium(I), iridium(I) and platinum(II), to undergo oxidative addition reactions of various substrates, typically alkyl or aryl halides, H_2 and halogens. The metal is inserted into a substrate of general formula A-B, forming a bond to both A and B. The metal's oxidation state and coordination number increase by 2 (Scheme 1.23).⁵¹



Scheme 1.23: Oxidative addition of A-B to a ML_4 complex.

Oxidative addition is a vital step in many catalytic cycles, examples including rhodium and iridium catalysed methanol carbonylation.^{11,13,52-60} Methanol carbonylation is the insertion of CO into the C-O bond of methanol, however the transition metal catalyst is not reactive enough to activate this bond itself and relies on the conversion of methanol into methyl iodide by HI under catalytic conditions. The methyl iodide then undergoes carbonylation by the transition metal catalyst to give acetyl iodide which is hydrolysed to give acetic acid. A catalytic cycle for rhodium catalysed methanol carbonylation is displayed in Scheme 1.24.



Scheme 1.24: Catalytic cycle for rhodium catalysed methanol carbonylation.

Oxidative addition of MeI to $[Rh(CO)_2I]^-$ is the rate determining step (determined by kinetic measurements)⁶¹ and many attempts at improving the catalytic activity have been investigated by increasing the rate of the oxidative addition step.

There has been a large amount of research to develop transition metal complexes with increased nucleophilicity. By varying both metal and ligand properties the reactivity of a

metal complex can be tuned, these changes can be quantified using oxidative addition kinetics and compared to reported literature data.

Oxidative addition can be accelerated by the co-ordination of electron rich ligands such as phosphines. Phosphine ligands are good σ -donors meaning they can donate electron density resulting in a more electron rich metal centre.

The electronic properties of a phosphine ligand can be characterised by a parameter developed by Tolman⁶² called the electronic parameter (ν). Tolman studied the effect of phosphine ligands on simple $[\text{Ni}(\text{CO})_3\text{PR}_3]$ complexes by measuring the A_1 carbonyl stretching frequency displayed in Table 1.4.

PR_3	$\nu(\text{CO})/\text{cm}^{-1}$
PPh_3	2069
$\text{P}i\text{-Tol}_3$	2066
$\text{P}o\text{-Tol}_3$	2066
PMe_3	2064
PEt_3	2061
$\text{P}i\text{Pr}_3$	2059
$\text{P}t\text{Bu}_3$	2056

Table 1.4: $\nu(\text{CO})$ values (A_1 Vibrational mode) for $[\text{Ni}(\text{CO})_3\text{PR}_3]$ complexes.

As expected there is a direct correlation between the electron donating ability of the phosphine ligand and $\nu(\text{CO})$. Complexes containing a more donating phosphine ligand have lower $\nu(\text{CO})$ values (due to greater Ni-CO π -backbonding) compared to those containing a less donating phosphine ligand. This electronic parameter can be applied to other ligands and gives a good indication of how much electron density is situated upon a metal centre.

The steric properties of a simple phosphine ligand can be characterised by another parameter developed by Tolman called the cone angle (θ) (Figure 1.3).⁶² The cone angle is that which envelops all of the ligand and substituents, taken from a point 2.28 Å from the co-ordinated phosphorus atom and encloses the van der Waals radii of the outermost atoms of the ligand substituents. The cone angle is useful in predicting the reactivity of complexes containing a phosphine ligand, vital in shaping the reactivity of a homogeneous catalyst.

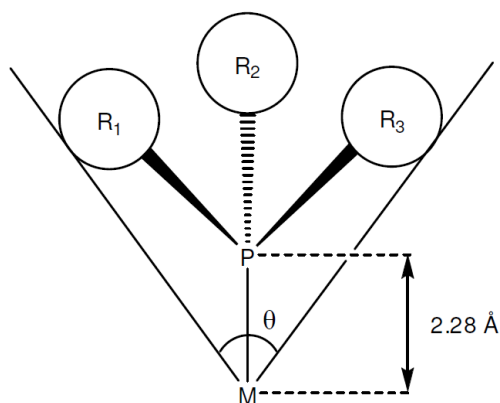
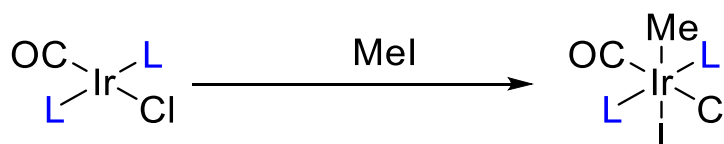


Figure 1.3: Tolmans cone angle (θ).

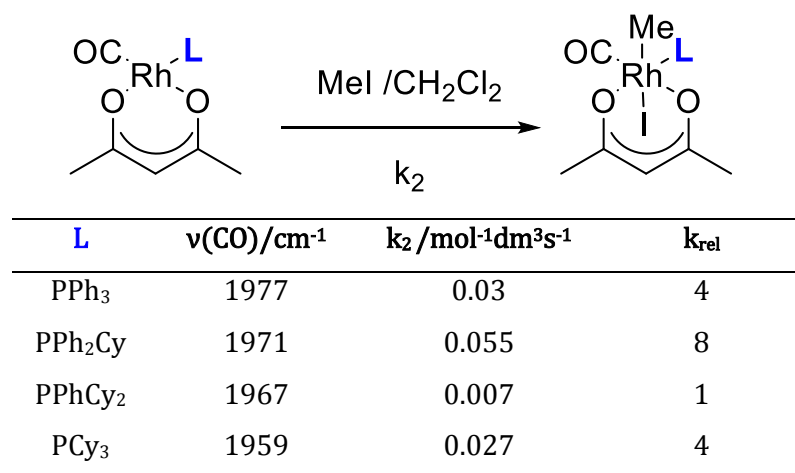
Wilson et al.⁶³ investigated the reactivity of a series of iridium Vaska type complexes $[\text{IrCl}(\text{CO})\text{L}_2]$ toward MeI (Scheme 1.25). Changing the phosphine ligand from PPh_3 to PMe_2Ph resulted in a shift to a lower $\nu(\text{CO})$ and a 14 fold increase in oxidative addition rate. Incorporating a methoxy group at the 4 position of the phosphine also results in a shift to a lower $\nu(\text{CO})$ and a 7 fold increase in rate was observed compared to PPh_3 . A fluorine atom at the 4-position has the opposite effect, resulting in a shift to a higher $\nu(\text{CO})$ and a large reduction in oxidative addition rate.



L	$\nu(\text{CO})$	$10^3 k_2 / \text{mol}^{-1} \text{dm}^3 \text{s}^{-1}$	k_{rel}
PPh_3	1964	3.5	1
PMe_2Ph	1954	50	14
$\text{P}(4\text{-OMeC}_6\text{H}_4)_3$	1960	25.3	7
$\text{P}(4\text{-FC}_6\text{H}_4)_3$	1968	0.08	0.02

Scheme 1.25: Oxidative addition of MeI to $[\text{Ir}(\text{CO})\text{Cl}(\text{PR}_3)_2]$ complexes.⁶³

The reactivity of a series of $[\text{Rh}(\text{acac})(\text{CO})\text{L}]$ towards MeI was investigated by Brink et al.⁶⁴ (Scheme 1.26). Stepwise interchange of phenyl to cyclohexyl groups of the phosphine has a large effect on $\nu(\text{CO})$ and the reactivity toward MeI. No correlation between reactivity and $\nu(\text{CO})$ was observed meaning steric effects are also playing a key role in the reaction.



Scheme 1.26: Oxidative addition of MeI to a series of [Rh(acac)(CO)L] complexes. ⁶⁴

Rankin et al. ^{65,66} modified the original Monsanto catalyst [Rh(CO)₂I₂]⁻ with donating trialkyl phosphine ligands PEt₃ forming [Rh(CO)I(PEt₃)₂] (Figure 1.4). The oxidative addition rate of MeI was 57 times faster for [Rh(CO)I(PEt₃)₂] compared to [Rh(CO)₂I₂]⁻.

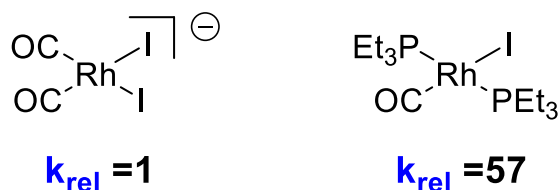


Figure 1.4: Relative rates of [Rh(CO)₂I₂]⁻ and [Rh(CO)I(PEt₃)₂]. ^{65,66}

N-heterocyclic carbene (NHC) ligands are seen as the replacement of choice for phosphine ligands due to their strong donating ability and poor back donating ability.⁶⁷ Replacement of the PEt₃ ligands of [Rh(CO)I(PEt₃)₂] with NHC ligands results in a shift in the $\nu(\text{CO})$ band by approximately 20 cm⁻¹. However, despite being more electron rich the [Rh(CO)I(L_{Me})₂] complex is 3.5 times less reactive toward MeI than [Rh(CO)I(PEt₃)₂] (Figure 1.5).

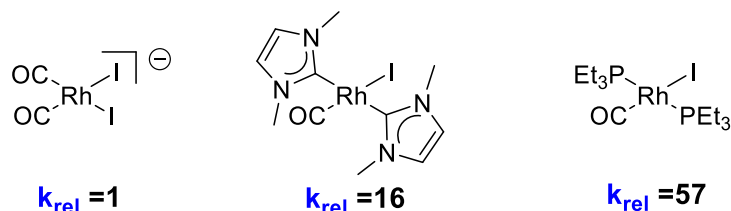
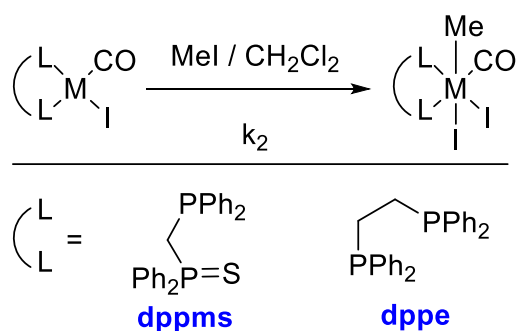


Figure 1.5: Relative rates of [Rh(CO)₂I₂]⁻ and [Rh(CO)I(PEt₃)₂] and [Rh(CO)I(L_{Me})₂]. ⁶⁷

The reduced reactivity of [Rh(CO)I(L_{Me})₂] toward MeI compared to [Rh(CO)I(PEt₃)₂] can be explained by steric effects. The [Rh(CO)I(L_{Me})₂] complex adopts a conformation where

the methyl groups of the NHC ligands are situated above and below the plane of the rhodium centre and cause significant steric congestion in the vacant axial co-ordination sites.

Gonsalvi et al.^{68,69} reported the steric and electronic effects on the reactivity of Rh and Ir complexes containing P-S, P-P and P-O chelate ligands (Scheme 1.27). The dppms, and dppe rhodium(I) complexes and [Rh(CO)I(PEt₃)₂] all have a very similar reactivity toward MeI despite the large difference in $\nu(\text{CO})$. The Rh(I)dppms complex enhances the rate of methanol carbonylation by approximately eight times. Changing the metal from rhodium to iridium resulted in acceleration of oxidative addition by approximately 40 times.



Complex	$\nu(\text{CO})/\text{cm}^{-1}$	$k_2 \text{ mol}^{-1}\text{dm}^3\text{s}^{-1}$	k_{rel}
[Rh(CO)I(dppms)]	1987	0.0012	1
[Rh(CO)I(dppe)]	2011	0.0014	1.1
[Ir(CO)I(dppms)]	1972	0.05	41
[Ir(CO)I(dppe)]	1994	0.051	42

Scheme 1.27: Oxidative addition to Rh(I) and Ir(I) dppms and dppe complexes.^{68,69}

McConnell et al.⁷⁰ reported a series of cyclopentadienyl phosphine complexes that incorporate a C₂H₄ linker leading from the cyclopentadienyl ligand to the phosphine ligand (Figure 1.6). The oxidative addition rate of one of the tethered complexes was much higher than related rhodium(I) Cp and Cp* complexes. Under catalytic methanol carbonylation conditions the tethered complex not only displayed the highest rate of methanol carbonylation but was also the most resistant to degradation by quaternisation and oxidation.

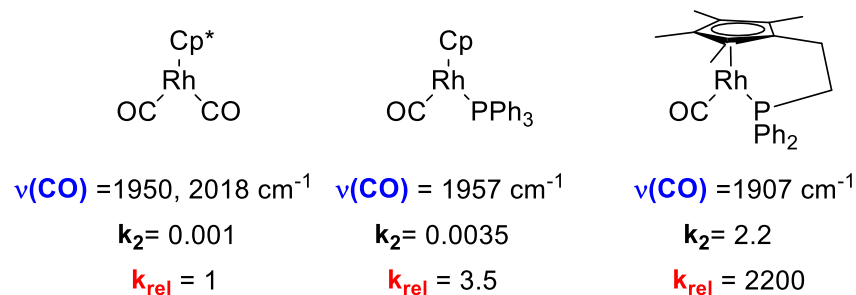


Figure 1.6: Oxidative addition to rhodium (I) Cp and Cp* complexes. ⁷⁰

Gaunt and Gonsalvi⁷¹ quantified the effect of sterics on the reactivity of some Rh(I) diimine complexes. The reactivity differs by an order of magnitude for the three complexes displayed in Figure 1.7. The least sterically hindered ligands resulted in a faster oxidative addition rate of MeI with the more bulky ligands facilitating migratory CO insertion. The least hindered complex in the series [Rh(CO)I(Bipy)] is approximately 7000 times more reactive toward MeI than [Rh(CO)₂I₂]:

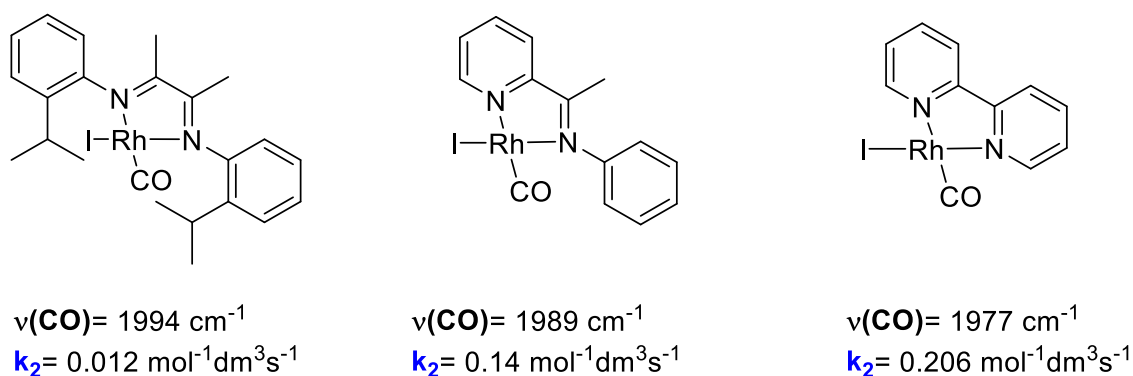
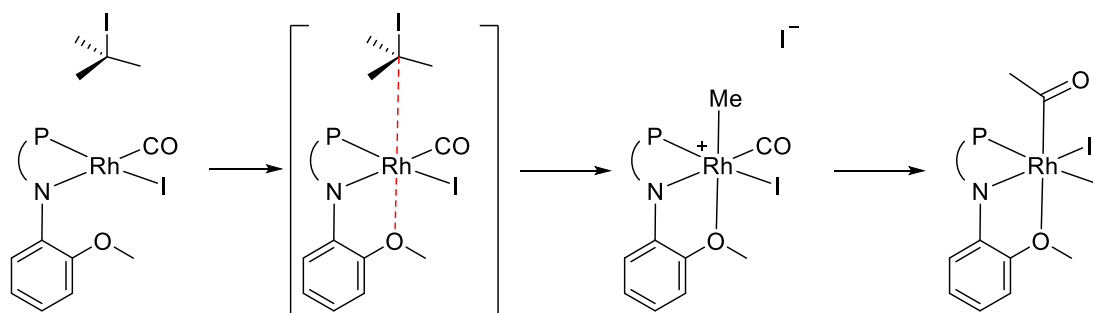


Figure 1.7: Oxidative addition of MeI to rhodium(I) diimine and Bipy complexes. ⁷¹

A series of rhodium iodo carbonyl complexes containing neutral bidentate iminophosphine ligands was investigated by Best et al.⁷² The reactivity of these complexes toward MeI is dependent upon both steric and electronic properties of the N-aryl substituent of the iminophosphine ligand. The most significant increase in both oxidative addition and CO migratory insertion was found for an *o*-methoxy aryl substituent which was proposed to have an intramolecular interaction with the rhodium centre (Scheme 1.28).

The *o*-methoxy substituted variant was an order of magnitude more reactive than the phenyl derivative. X-ray crystallography confirmed that the oxygen coordinates to rhodium in the migratory insertion product, thus stabilising acetyl species.



Scheme 1.28: Simplified mechanism of the reaction of rhodium (I) iminophosphine complexes with MeI.⁷²

1.4 Pincer Complexes

As the search for new ligands that can deliver specific electronic and steric effects upon a metal centre continues, pincer ligands have attracted particular attention due to their increased thermal and kinetic stabilities. In 1976 Moulton and Shaw synthesized the first pincer type complexes based on a terdentate PCP pincer ligand. A rhodium(I) carbonyl complex containing this ligand is shown in Figure 1.8.⁷³

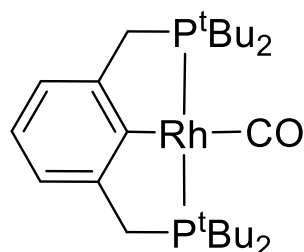


Figure 1.8: Rhodium (I) pincer complex synthesised by Moulton and Shaw.

A pincer ligand generally adopts a *mer* κ^3 co-ordination mode in which the ligand binds in a tridentate manner donating 6 electrons to the metal centre with the neutral donors “D” being trans to one another. Figure 1.9 shows how a pincer complex can be modified to influence reactivity. Steric influences can be varied by changing donor substituent size, however these changes will also effect the electronic environment of the metal centre. The size, rigidity and donating ability can be changed by modifications to the backbone and linker arms. The outcome enables the fine tuning of stereoelectronic properties of a pincer complex, and as a result pincer ligands are being designed to suit specific chemical transformation.⁷⁴

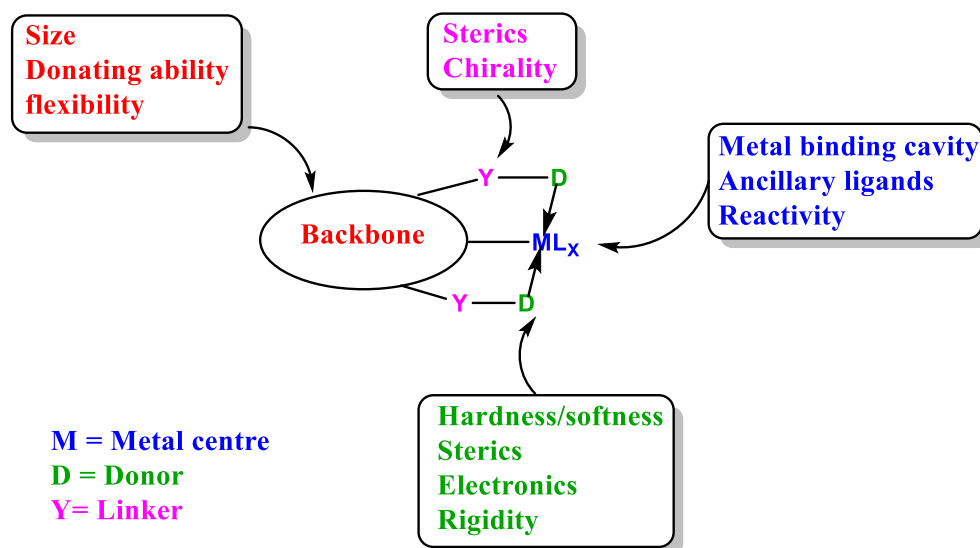


Figure 1.9: Typical pincer complex configuration.

Pincer complexes have been shown to have exceptional thermal stability which is due to the backbone metal σ bond strength. This deters dissociation of the metal from the ligand, making it harder for decomposition to occur. Varying the backbone enables the tuning of σ donors; a few selected examples are displayed in Figure 1.10.⁷⁵

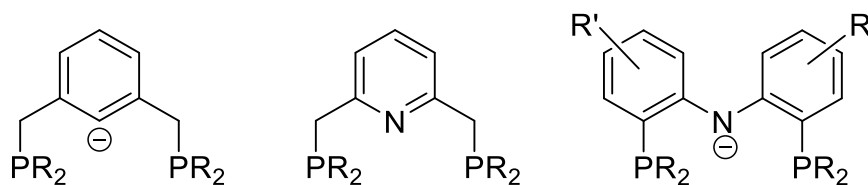


Figure 1.10: Examples of some common pincer ligand motifs

1.4.1 Reactivity of pincer complexes toward MeI

The reactivity of pincer complexes toward MeI has been investigated both within the Haynes group and elsewhere. Rhodium(I) bis(imino)carbazolide complexes were investigated in collaboration with the Gibson group at Imperial College London.⁷⁶ The nature of the R group of the imino substituent has a large impact on the reactivity of these complexes. The most reactive variant was found to be three orders of magnitude more reactive toward MeI than $[\text{Rh}(\text{CO})_2\text{I}_2]^-$ (Scheme 1.29).



Scheme 1.29: Rh (I) bis(imino)carbazolide carbonyl complex.⁷⁶

Moser et al.⁷⁷ found that replacing the imine donor arms with N-heterocyclic carbene donors had a huge effect on reactivity toward MeI. The $\nu(\text{CO})$ for the $[\text{Rh}(\text{CO})\text{CNC}]$ pincer complex was observed at 1921 cm^{-1} consistent with a very electron rich rhodium centre. The reactivity of $[\text{Rh}(\text{CO})\text{CNC}]$ complex towards MeI was found to have a second order rate constant of $3.4 \times 10^{-3} \text{ mol}^{-1} \text{ dm}^3 \text{ s}^{-1}$ at -78°C , approximately nine orders of magnitude more reactive than $[\text{Rh}(\text{CO})_2\text{I}_2]^-$ at the same temperature (Figure 1.11).

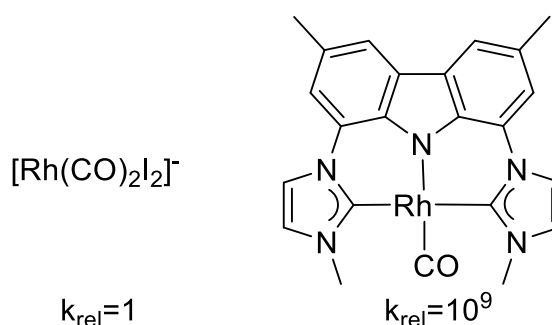


Figure 1.11: Relative reactivity of $[\text{Rh}(\text{CO})_2\text{I}_2]^-$ and $[\text{Rh}(\text{CO})\text{CNC}]$ towards MeI.

Wilson et al.⁷⁸ found that despite being cationic, rhodium(CO) pyridyl bis(carbene) complexes were reactive toward MeI. The most reactive variant was found to have a second order rate constant of $0.0927 \text{ mol}^{-1} \text{ dm}^3 \text{ s}^{-1}$. In contrast both a cationic SNS rhodium complex^{79,80} and a $[\text{Rh}(\text{CO})\text{Xantphos}]$ complex⁸¹ were found to be much less reactive (Figure 1.12).

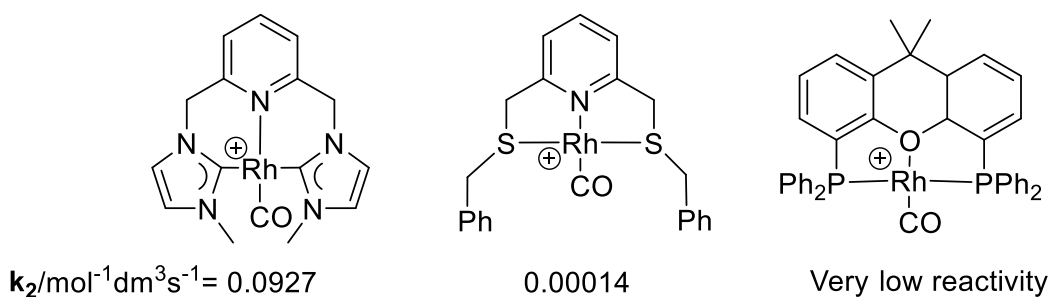


Figure 1.12: k_2 values for the oxidative addition of MeI to some cationic rhodium complexes.

Rigid PCP “anthrathos” complexes based on the anthracene backbone have also been investigated in collaboration with the University of Bristol.⁸² These complexes display very high reactivity toward MeI. More flexible PNP complexes based on a diaryl-amido backbone have also been synthesised by Wells⁸³, these are less rigid but also display high reactivity towards MeI. Both will be discussed in detail later in this thesis (Figure 1.13).

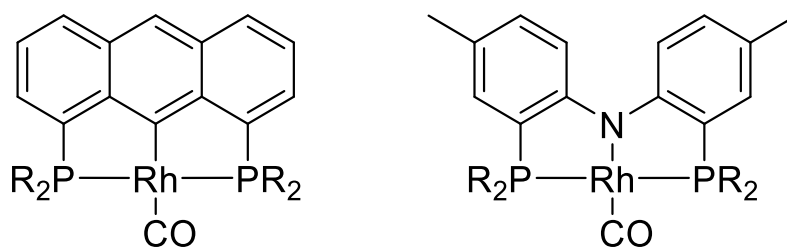
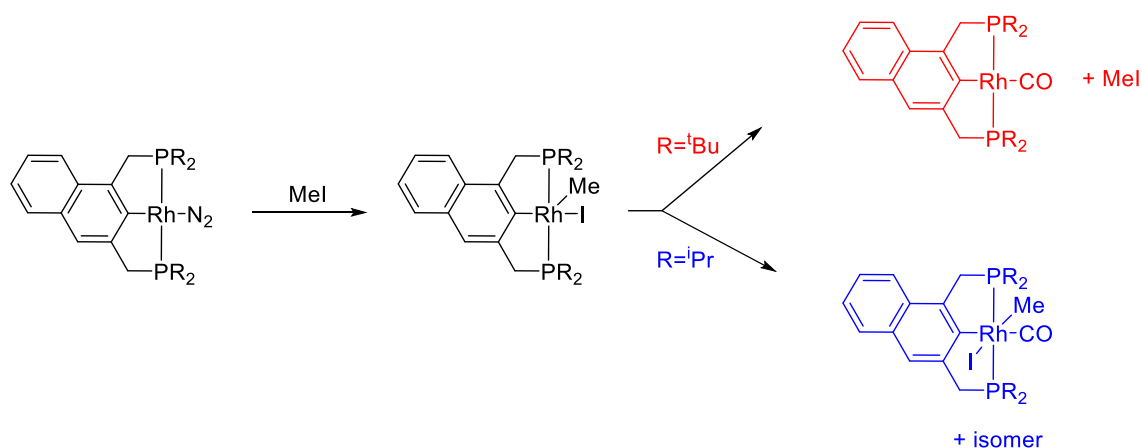


Figure 1.13: Rh (I) carbonyl anthrathos and PNP complexes.

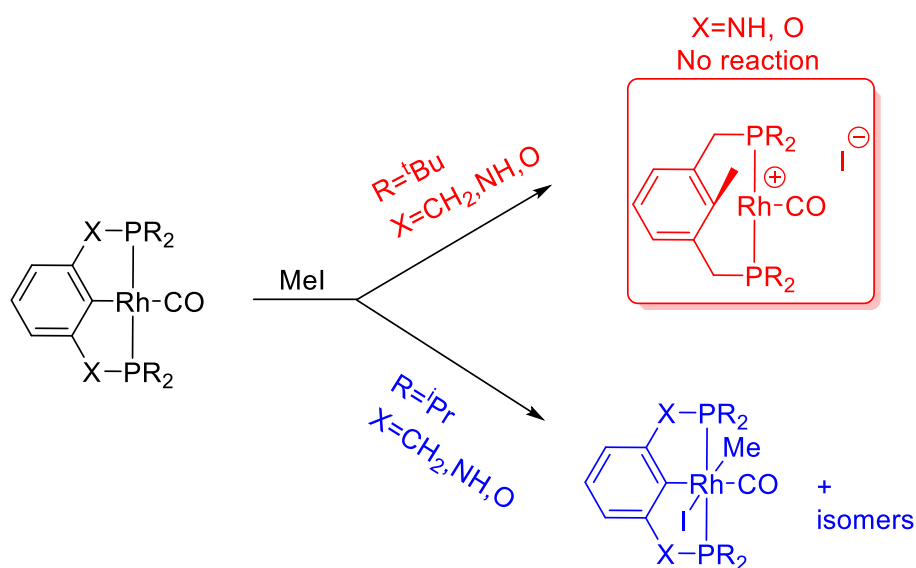
Milstein and Frech⁸⁴ reported oxidative addition of MeI to two different rhodium(I) PCP complexes with different steric properties. Both rhodium(I) complexes oxidatively added MeI, however upon treatment with CO the bulkier ^tBu substituted complex reductively eliminated MeI to yield solely the Rh(I) carbonyl complex. The ⁱPr substituted complex gave a mixture of two Rh(III) methyl isomers highlighting the importance of the steric environment around a metal centre (Scheme 1.30).



Scheme 1.30: Demonstration of steric effect in oxidative addition of MeI to Rh(I) complexes.⁸⁴

Recent work within the Haynes group by Wells⁸³ on [Rh(CO)PXCXP] complexes highlights the importance of both steric and electronic factors upon oxidative addition of MeI (Scheme 1.31). The bulky ^tBu substituted complexes do not undergo oxidative addition when the linker arm is NH or O, however when the linker arm is a CH₂ oxidative addition occurs but is followed by facile methyl migration to the ipso carbon. Similar Rh-Me interactions have been observed in related rhodium complexes.^{85,86}

In contrast the ⁱPr substituted complexes are less bulky and all undergo facile oxidative addition to form Rh(III) methyl products. Interestingly the linker arm has a large effect on oxidative addition rate. The reactivity correlates with the change in electron density on rhodium as the linker group in the pincer ligand changes from CH₂>NH>O and effectively demonstrates the importance of electronic effects on oxidative addition.

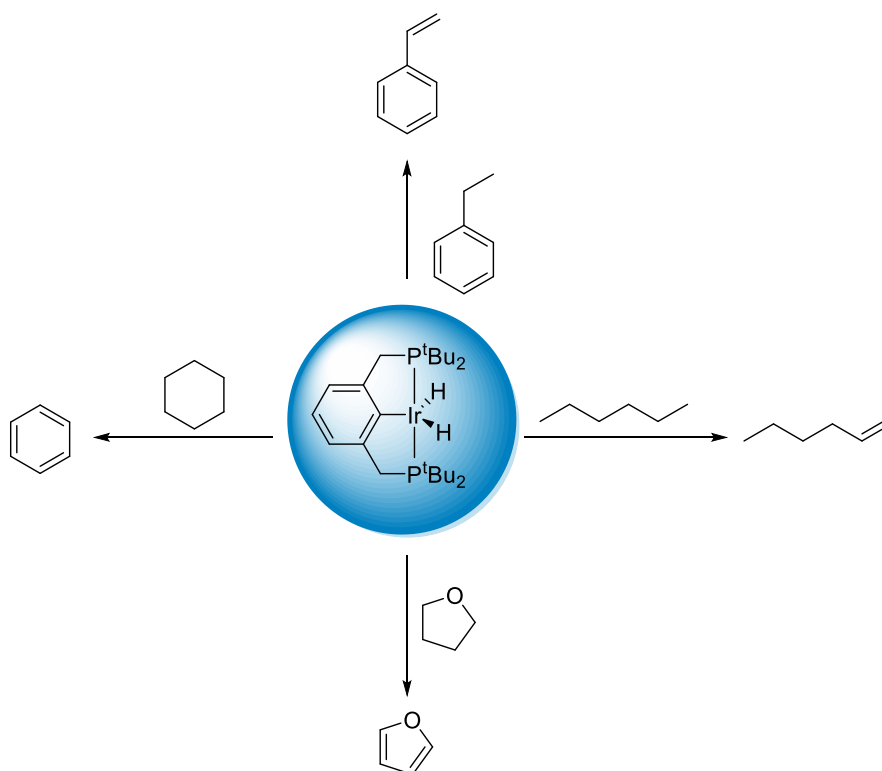


Scheme 1.31: Oxidative addition of MeI to Rh(I) PXCXP complexes.⁸³

1.4.2 Application of pincer complexes in catalysis.

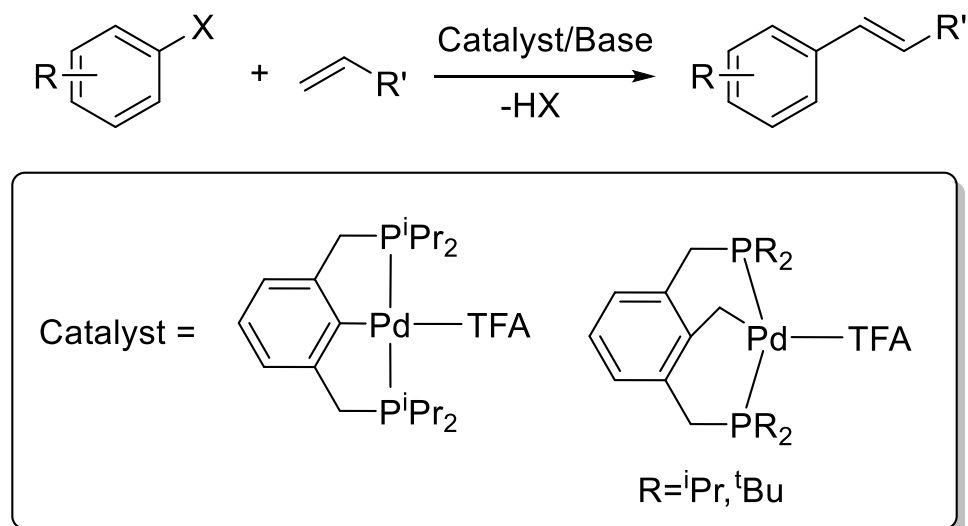
Pincer complexes have been applied to a wide range of chemical transformations due to their tunable properties, high reactivity and increased stability. The application of pincer complexes in catalysis is extensively covered in several review articles with a few selected reactions being covered below.^{75,87-90}

Scheme 1.32 shows dehydrogenation reactions catalysed by an iridium pincer complex. A notable example is the dehydrogenation of alkanes. Alkanes are readily available from fuel feedstocks, however conversion of alkanes into a more useful substance is very difficult due to their lack of reactivity. Using an iridium PCP pincer complex based on a xylene backbone, a wide range of hydrocarbons have been catalytically transformed into higher value terminal olefins via C-H activation.⁹¹⁻⁹³



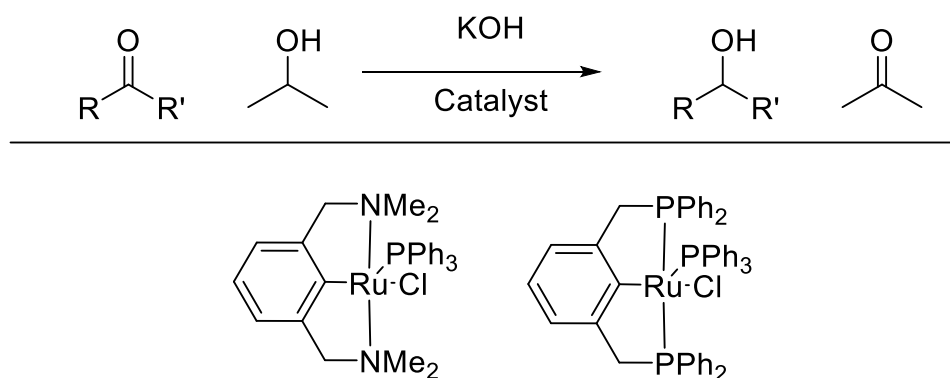
Scheme 1.32: Alkane dehydrogenation using a PCP pincer complex.

Cyclometalated d^8 palladium pincer complexes are particularly efficient catalysts for Heck olefination reactions. The first pincer type complexes reported to catalyse the Heck reaction were synthesised by Milstein⁹⁴ and are shown in Scheme 1.33. These complexes have turnover numbers $> 100,000$, achieve high yields when using unreactive aryl bromide starting materials and are resistant to catalyst degradation.



Scheme 1.33: Heck olefination reactions catalysed by palladium pincer complexes. ⁹⁴

Gupta et al. and Wang et al.^{95,96} have used ruthenium PCP and NCN pincer complexes to reduce ketones to their corresponding alcohols using ⁱPrOH as a hydrogen source and a KOH co-catalyst. The best yields and activity were obtained using PCP pincer complexes which are substantially better than those obtained for monodentate phosphine complexes such as [RuCl₂(PPh₃)₃] and [RuCl(H)(PPh₃)₃] (Scheme 1.34).



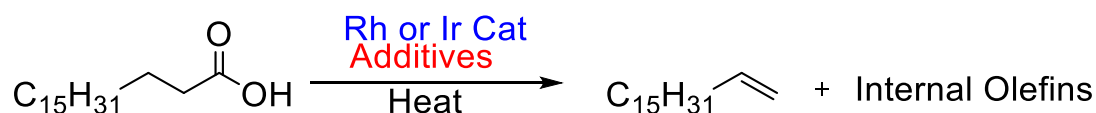
Scheme 1.34: Hydrogen transfer reaction catalysed by ruthenium pincer complexes. ^{95,96}

1.5 Project aims

The decarbonylative dehydration of long chain fatty acids has mainly focussed on palladium catalysts. However, other transition metals are known to catalyse the reaction, notably, rhodium and iridium Vaska type complexes ([M(CO)(Cl)L₂]). The literature

suggested mechanism for this reaction requires the oxidative addition of a C-O bond of an anhydride by the metal centre which requires a highly reactive metal complex.

The overall aim of this project is to investigate a range of transition metal catalysts for the decarbonylative dehydration of long chain fatty acids/ anhydrides (Scheme 1.35). An initial study using Ir(I) Vaska type complexes will build on the reported literature data.



Scheme 1.35: Catalytic decarbonylation of long chain acids using a rhodium or iridium catalyst

A range of electron rich rhodium and iridium complexes containing multidentate P, N and C donor ligands will be synthesised and their activity in the decarbonylative dehydration of long chain acids and anhydrides will be explored (Figure 1.14).

As an investigation into fundamental organometallic reactivity these novel multidentate complexes will be reacted with MeI. This is a well understood, cited and quantified reaction and enables a way of comparing their reactivity and stability with other complexes reported in the literature.

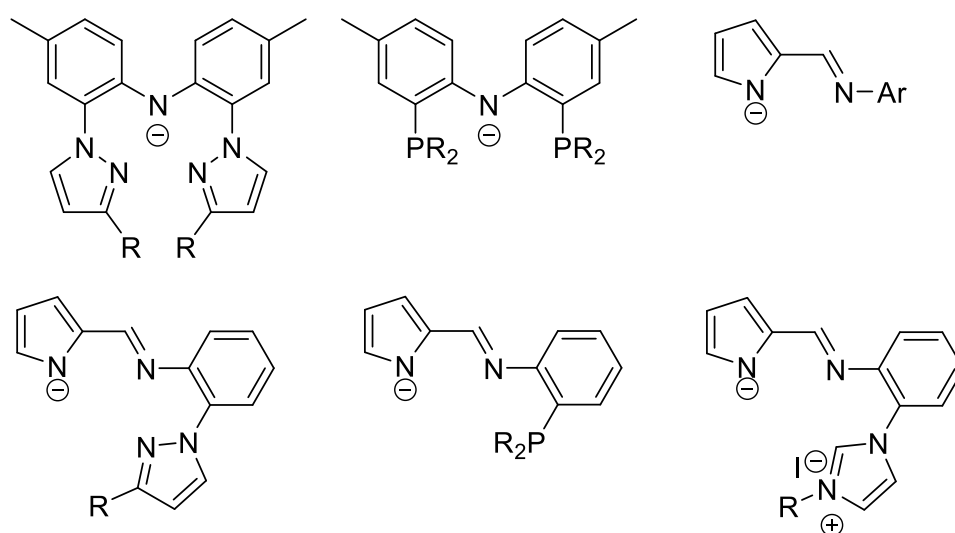


Figure 1.14: ligands used in this study

1.6 References

- (1) McNaught, A. D.; Wilkinson, A. In *The Gold Book*; RSC: Cambridge UK, **1997**.
- (2) Zapf, A. *Angew. Chem. Int. Ed. Engl.*, **2005**, *117*, 1321.
- (3) Thomas, J. M.; Thomas, W. J.; Anderson, J.; Boudart, M. *Principles and Practice of Heterogeneous Catalysis*; VCH Weinheim, **1997**.
- (4) Cornils, B.; Herrmann, W. A. *J. Catal.*, **2003**, *216*, 23.
- (5) Hagen, J. In *Industrial Catalysis*; Wiley-VCH Verlag GmbH & Co. KGaA: **2006**, p 59.
- (6) Gallei, E. F.; Hesse, M.; Schwab, E. In *Handbook of Heterogeneous Catalysis*; Wiley-VCH Verlag GmbH & Co. KGaA: **2008**.
- (7) Herrmann, W. A. *Comm. Inorg. Chem.*, **1988**, *7*, 73.
- (8) Bochmann, M. *Organometallics 1*; Oxford University Press, **1994**.
- (9) Winter, M. J. *d-block chemistry*; Oxford University Press **1994**.
- (10) Bhaduri, S.; Mukesh, D. In *Homogeneous Catalysis*; John Wiley & Sons, Inc.: **2002**.
- (11) Haynes, A. In *Catalytic Carbonylation Reactions*; Beller, M., Ed.; Springer Berlin Heidelberg: **2006**; Vol. 18, p 179.
- (12) Haynes, A. *Carbonylation reactions*; Elsevier: Oxford, **2013**; Vol. 6.
- (13) Haynes, A. In *Advances in Catalysis*; Gates, B., Ed.; Burlington: Academic press, **2010**; Vol. 53, p 1.
- (14) Brown, J. M.; Kent, A. G. *J. Chem. Soc. Perkin Trans 2*. **1987**, 1597.
- (15) Evans, D.; Osborn, J. A.; Wilkinson, G. *J. Chem. Soc. A*. **1968**, 3133.
- (16) Hebrard, F.; Kalck, P. *Chem. Rev.* **2009**, *109*, 4272.
- (17) Moasser, B.; Gladfelter, W. L.; Roe, D. C. *J. Organomet. Chem.*, **1995**, *14*, 3832.
- (18) Slauch, L. H.; Mullineaux, R. D. *J. Organomet. Chem.*, **1968**, *13*, 469.
- (19) Wender, I.; Sternberg, H. W.; Orchin, M. *J. Am. Chem. Soc.* **1953**, *75*, 3041.
- (20) Jira, R. *Angew. Chem. Int. Ed. Engl.*, **2009**, *48*, 9034.
- (21) Crabtree, R. H.; Felkin, H.; Morris, G. E. *J. Organomet. Chem.*, **1977**, *141*, 205.
- (22) Osborn, J. A.; Jardine, F. H.; Young, J. F.; Wilkinson, G. *J. Chem. Soc. A*. **1966**, 1711.
- (23) Mecking, S. *Angew. Chem. Int. Ed. Engl.*, **2001**, *40*, 534.
- (24) Savage, N. *Nature*, **2011**, *474*, S9.
- (25) Knothe, G. *Fuel Process. Technol.* **2005**, *86*, 1059.
- (26) Petrus, L.; Noordermeer, M. A. *Green Chem.* **2006**, *8*, 861.
- (27) Ma, F.; Hanna, M. A. *Bioresour. Technol.* **1999**, *70*, 1.
- (28) Miao, X.; Wu, Q. *Bioresour. Technol.* **2006**, *97*, 841.
- (29) Han, J.; Sun, H.; Ding, Y.; Lou, H.; Zheng, X. *Green Chem.* **2010**, *12*, 463.
- (30) Benson, T. J.; Daggolu, P. R.; Hernandez, R. A.; Liu, S.; White, M. G. In *Advances in Catalysis*; Bruce, C. G., Friederike, C. J., Eds.; Academic Press: **2013**; Volume 56, p 187.

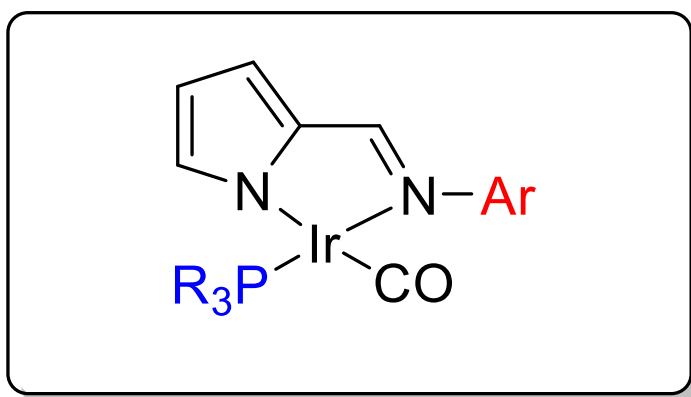
- (31) Lopez-Ruiz, J. A.; Davis, R. J. *Green Chem.* **2014**, *16*, 683.
- (32) Snåre, M.; Kubičková, I.; Mäki-Arvela, P.; Chichova, D.; Eränen, K.; Murzin, D. Y. *Fuel*. **2008**, *87*, 933.
- (33) Kubičková, I.; Snåre, M.; Eränen, K.; Mäki-Arvela, P.; Murzin, D. Y. *Catalysis Today* **2005**, *106*, 197.
- (34) Mäki-Arvela, P.; Kubickova, I.; Snåre, M.; Eränen, K.; Murzin, D. Y. *Energy & Fuels*. **2007**, *21*, 30.
- (35) Santillan-Jimenez, E.; Crocker, M. J. *Chem. Technol. Biotechnol.* **2012**, *87*, 1041.
- (36) Foglia, T. Barr, P. *J. Am. Oil Chem. Soc.* **1976**, *53*, 737.
- (37) Miller, J. A.; Nelson, J. A.; Byrne, M. P. *J. Org. Chem.*, **1993**, *58*, 20.
- (38) Gooßen, L.; Rodriguez, N. *Chem. Commun.*, **2004**, 724.
- (39) Le Nôtre, J.; Scott, E. L.; Franssen, M. C. R.; Sanders, J. P. M. *Tetrahedron Lett.* **2010**, *51*, 3712.
- (40) Miranda, M. O.; Pietrangelo, A.; Hillmyer, M. A.; Tolman, W. B. *Green Chem.* **2012**, *14*, 490.
- (41) Liu, Y.; Kim, K. E.; Herbert, M. B.; Fedorov, A.; Grubbs, R. H.; Stoltz, B. M. *Adv. Synth. Catal.* **2014**, *356*, 130.
- (42) John, A.; Hogan, L. T.; Hillmyer, M. A.; Tolman, W. B. *Chem. Commun.*, **2015**, *51*, 2731.
- (43) Maetani, S.; Fukuyama, T.; Suzuki, N.; Ishihara, D.; Ryu, I. *Organometallics*. **2011**, *30*, 1389.
- (44) Maetani, S.; Fukuyama, T.; Suzuki, N.; Ishihara, D.; Ryu, I. *Chem. Commun.*, **2012**, *48*, 2552.
- (45) Enthaler, S.; Junge, K.; Beller, M. *Angew. Chem. Int. Ed. Engl.*, **2008**, *47*, 3317.
- (46) Deeming, A. J.; Shaw, B. L. *J. Am. Chem. Soc.* **1969**, 443.
- (47) Blake, D. M.; Shields, S.; Wyman, L. *Inorg. Chem.*, **1974**, *13*, 1595.
- (48) Miller, J. A.; Nelson, J. A. *Organometallics*. **1991**, *10*, 2958.
- (49) Yamamoto, T.; Sanno, K.; Yamamoto, A. *Bull. Chem. Soc. Jpn* **1984**, *57*.
- (50) Trost, B. M.; Chen, F. *Tetrahedron Lett.* **1971**, *12*, 2603.
- (51) Crespo, M.; Puddephatt, R. J. *J. Organomet. Chem.*, **1987**, *6*, 2548.
- (52) Haynes, A.; Maitlis, P. M.; Morris, G. E.; Sunley, G. J.; Adams, H.; Badger, P. W.; Bowers, C. M.; Cook, D. B.; Elliott, P. I. P.; Ghaffar, T.; Green, H.; Griffin, T. R.; Payne, M.; Pearson, J. M.; Taylor, M. J.; Vickers, P. W.; Watt, R. J. *J. Am. Chem. Soc.* **2004**, *126*, 2847.
- (53) Wilson, J. M. PhD Thesis, University Of Sheffield. **2006**.
- (54) Paulik, F. E.; Roth, J. F. *Chem. Commun.*, **1968**, 1578a.

- (55) Forster, D. In *Adv. Organomet. Chem.*; Stone, F. G. A., Robert, W., Eds.; Academic Press: **1979**; Vol. Volume 17, p 255.
- (56) Maitlis, P. M.; Haynes, A.; Sunley, G. J.; Howard, M. J. *J. Chem. Soc. Dalton Trans.* **1996**, 2187.
- (57) Thomas, C. M.; Süss-Fink, G. *Coord. Chem. Rev.*, **2003**, *243*, 125.
- (58) Haynes, A.; Mann, B. E.; Gulliver, D. J.; Morris, G. E.; Maitlis, P. M. *J. Am. Chem. Soc.* **1991**, *113*, 8567.
- (59) Sunley, G. J.; Watson, D. J. *Catalysis Today*, **2000**, *58*, 293.
- (60) Dilworth, J. R.; Miller, J. R.; Wheatley, N.; Baker, M. J.; Sunley, J. G. *Chem. Commun.*, **1995**, 1579.
- (61) Forster, D.; Ann, N. Y. *Acad.Sci.* **1977**, *295*, 79.
- (62) Tolman, C. A. *Chem. Rev.* **1977**, *77*, 313.
- (63) Wilson, M. R.; Liu, H.; Prock, A.; Giering, W. P. *Organometallics.* **1993**, *12*, 2044.
- (64) Brink, A.; Roodt, A.; Steyl, G.; Visser, H. G. *Dalton Trans.* **2010**, *39*, 5572.
- (65) Rankin, J.; C. Benyei, A.; J. Cole-Hamilton, D.; Poole, A. D. *Chem. Commun.*, **1997**, 1835.
- (66) Rankin, J.; C. Benyei, A.; Poole, A. D.; J. Cole-Hamilton, D. *J. Chem. Soc. Dalton Trans.* **1999**, 3771.
- (67) Herrmann, W. A.; Köcher, C. *Angew. Chem. Int. Ed. Engl.*, **1997**, *36*, 2162.
- (68) Gonsalvi, L.; Adams, H.; Sunley, G. J.; Ditzel, E.; Haynes, A. *J. Am. Chem. Soc.* **1999**, *121*, 11233.
- (69) Gonsalvi, L.; Adams, H.; Sunley, G. J.; Ditzel, E.; Haynes, A. *J. Am. Chem. Soc.* **2002**, *124*, 13597.
- (70) McConnell, A. C.; Pogorzelec, P. J.; Slawin, A. M. Z.; Williams, G. L.; Elliott, P. I. P.; Haynes, A.; Marr, A. C.; Cole-Hamilton, D. J. *Dalton Trans.* **2006**, 91.
- (71) Gonsalvi, L.; Gaunt, J. A.; Adams, H.; Castro, A.; Sunley, G. J.; Haynes, A. *Organometallics.* **2003**, *22*, 1047.
- (72) Best, J.; Wilson, J. M.; Adams, H.; Gonsalvi, L.; Peruzzini, M.; Haynes, A. *Organometallics.* **2007**, *26*, 1960.
- (73) Moulton, C. J.; Shaw, B. L. *J. Am. Chem. Soc., Dalton Trans.*, **1976**, 1020.
- (74) Morales, D. M. *Rev. Soc. Quim. Mex.*, **2004**, *48*, 338.
- (75) Albrecht, M.; van Koten, G. *Angew. Chem. Int. Ed. Engl.*, **2001**, *40*, 3750.
- (76) Gaunt, J. A.; Gibson, V. C.; Haynes, A.; Spitzmesser, S. K.; White, A. J. P.; Williams, D. J. *J. Organomet. Chem.*, **2004**, *23*, 1015.
- (77) Moser, M.; Wucher, B.; Kunz, D.; Rominger, F. *Organometallics.* **2007**, *26*, 1024.
- (78) Wilson, J. M.; Sunley, G. J.; Adams, H.; Haynes, A. *J. Organomet. Chem.*, **2005**, *690*, 6089.

- (79) Bassetti, M.; Capone, A.; Salamone, M. *Organometallics*. **2004**, *23*, 247.
- (80) Bassetti, M.; Capone, A.; Mastrofrancesco, L.; Salamone, M. *Organometallics*. **2003**, *22*, 2535.
- (81) Williams, G. L.; Parks, C. M.; Smith, C. R.; Adams, H.; Haynes, A.; Meijer, A. J. H. M.; Sunley, G. J.; Gaemers, S. *Organometallics*. **2011**, *30*, 6166.
- (82) Reynolds, T. J. PhD Thesis, University Of Bristol. **2011**.
- (83) Wells, J. PhD Thesis, University Of Sheffield. **2011**.
- (84) Frech, C. M.; Milstein, D. *J. Am. Chem. Soc.* **2006**, *128*, 12434.
- (85) Gandelman, M.; Shimon, L. J. W.; Milstein, D. *Chem. Eur. J.* **2003**, *9*, 4295.
- (86) Montag, M.; Efremenko, I.; Leitun, G.; Ben-David, Y.; Martin, J. M. L.; Milstein, D. *Organometallics*. **2013**, *32*, 7163.
- (87) van der Boom, M.; Milstein, D. *Chem. Rev.* **2003**, *103*, 1759.
- (88) Bedford, R. B.; Draper, S. M.; Noelle Scully, P.; Welch, S. L. *New. J. Chem.* **2000**, *24*, 745.
- (89) Benito-Garagorri, D.; Kirchner, K. *Acc. Chem. Res.* **2008**, *41*, 201.
- (90) Selander, N.; J. Szabó, K. *Chem. Rev.* **2011**, *111*, 2048.
- (91) Morales-Morales, D.; Jensen, C. *The Chemistry of Pincer Compounds*, Elsevier Science, **2007**.
- (92) Morales-Morales, D. *Mini-Rev. Org. Chem.*, **2008** *5*, 141.
- (93) Singleton, J. *Tetrahedron Lett.* **2003**, *59*, 1837.
- (94) Ohff, M.; Ohff, A.; van der Boom, M. E.; Milstein, D. *J. Am. Chem. Soc.* **1997**, *119*, 11687.
- (95) Gupta, M.; Hagen, C.; Flesher, R. J.; Kaska, W. C.; Jensen, C. M. *Chem. Commun.*, **1996**, 2083.
- (96) Wang, K.; Goldman, M. E.; Emge, T. J.; Goldman, A. S. *J. Organomet. Chem.*, **1996**, *518*, 55.

Chapter 2

Synthesis and Reactivity of Iridium (I) Iminopyrrolyl Phosphine Carbonyl Complexes



2.0 Introduction

Ligand effects on the reactivity of transition metal complexes have been studied in great detail over the last couple of decades. An area that has been widely investigated is methanol carbonylation. An important step in this catalytic cycle is the oxidative addition of MeI formed *in-situ* from methanol and HI under catalytic conditions.¹ This step is modelled in order to investigate both quantitatively and qualitatively the effects of varying ligand properties. Recent work within the Haynes group has shown that increasing the steric bulk of Rh(I)-diimine complexes not only has a large effect on the rate of oxidative addition but also the kinetics and thermodynamics of migratory CO insertion.² A series of rhodium iodo carbonyl complexes containing neutral bidentate iminophosphine ligands has also been investigated.³ The reactivity of these complexes toward MeI is dependent upon both steric and electronic properties of the N-aryl substituent of the iminophosphine ligand. The most significant increase in both oxidative addition and CO migratory insertion was promoted by an *o*-methoxy aryl substituent which was proposed to have an intramolecular interaction with the rhodium centre.

Recent work both in the literature and the Haynes group has focussed on monoanionic bidentate ligands and associated rhodium complexes such as [Rh(acac)(CO)L]⁴⁻⁷ and [Rh(Nacac)(CO)L]⁸ complexes (Figure 2.1). This chapter will discuss the synthesis and reactivity of iminopyrrolyl phosphine carbonyl complexes (Figure 2.1) where the iminopyrrolyl and the phosphine substituents can be varied easily.

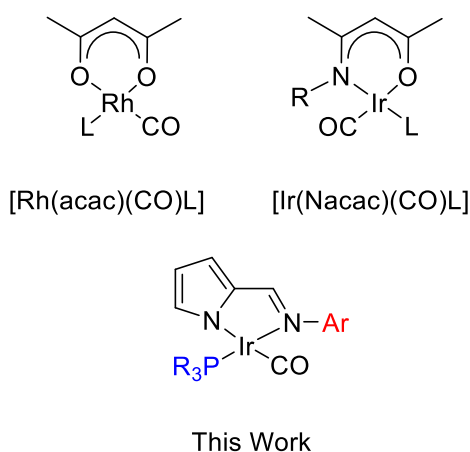


Figure 2.1: [Rh(acac)(CO)L], [Rh(Nacac)(CO)L] and [Rh(Ar-NN)(CO)(L)] complexes.⁴⁻⁸

Transition metal complexes that incorporate an iminopyrrolyl ligand are well documented in the literature. Gibson et al.⁹ demonstrated that Cr(II) and Cr(III) iminopyrrolyl complexes (Figure 2.2) are efficient ethene polymerisation catalysts when combined with alkylaluminium promoters.

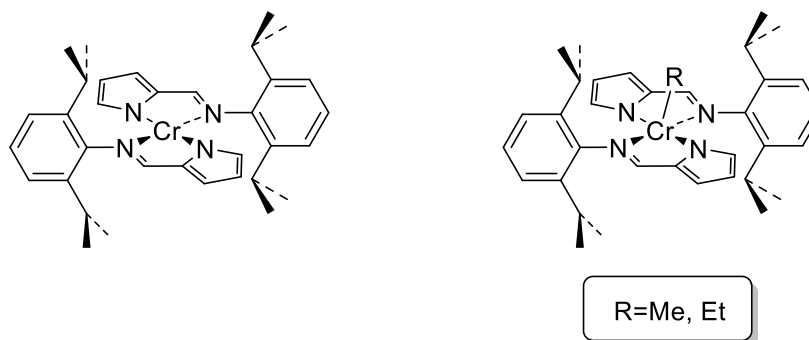


Figure 2.2: Cr(II) and Cr(III) ethene polymerisation catalysts developed by Gibson et al.⁹

In addition to ethene polymerisation catalysis, of which there are numerous examples,⁹⁻¹⁶ iminopyrrolyl complexes are active in the copolymerisation of ethene and norbornene¹⁷ as well as the polymerisation of methyl methacrylate¹⁸ and 1-hexene.¹⁹ The polymerisation of cyclic esters and lactams is more challenging but recently the research groups of Phomphrai²⁰ and Hormnirun²¹ were able to catalyse this reaction using 5-coordinate aluminium alkyl iminopyrrolyl catalysts shown in Figure 2.3.

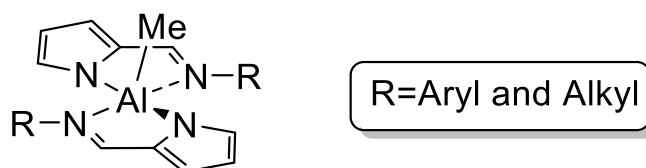


Figure 2.3: Al(III) iminopyrrolyl ring opening polymerisation catalysts.^{20, 21}

Carabineiro et al.²² reported the synthesis and characterisation of Co(II) bis(iminopyrrolyl) complexes shown in Figure 2.4. The majority of these complexes were tetrahedral, but a complex containing a sterically demanding ligand adopted a square planar geometry due to a combination of stereochemical interligand repulsion and electronic factors.

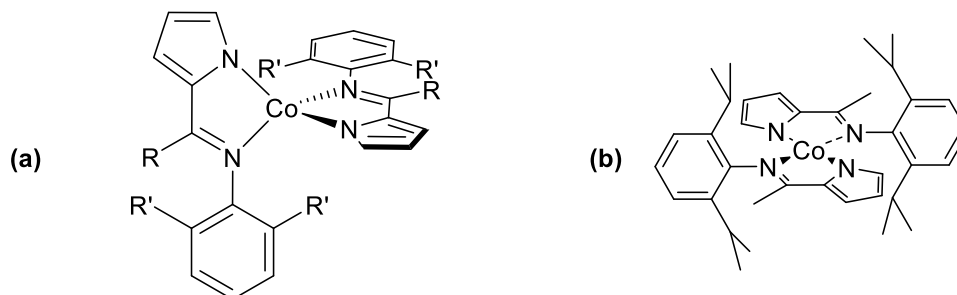


Figure 2.4: Tetrahedral (a) and a square planar (b) Co(II) bis(iminopyrrolyl) complexes.²²

The synthesis of Co(II) bis(iminopyrrolyl)phosphine complexes has also been reported by Carabineiro et al.²³ Treatment of $\text{CoCl}_2(\text{PMe}_3)_2$ or CoCl_2 and PMe_3 with an iminopyrrolyle ligand afforded the phosphine containing complex (Figure 2.5).

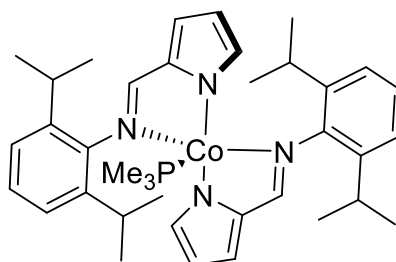
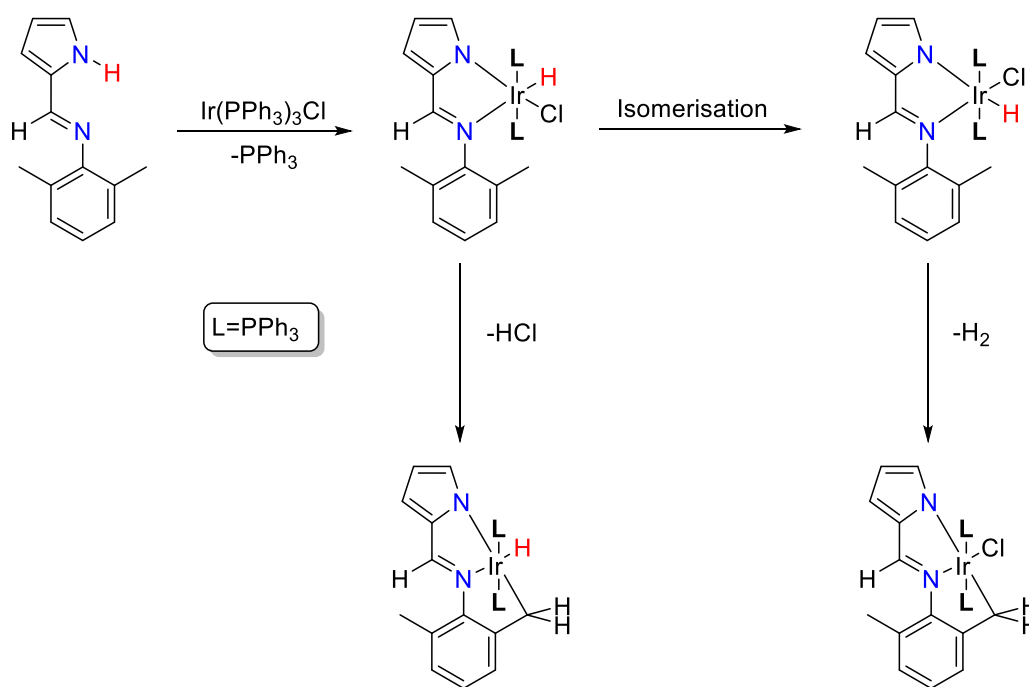


Figure 2.5: Cobalt(II) iminopyrrolyl phosphine complexes.²³

A recent publication by Paul et al.²⁴ reported the reaction of a 2,6- $\text{Me}_2\text{C}_6\text{H}_3$ iminopyrrolyle ligand with $[\text{Ir}(\text{PPh}_3)_3\text{Cl}]$ in refluxing toluene shown in Scheme 2.1. Co-ordination occurs via initial N-H activation of the iminopyrrolyle followed by C-H activation of an ortho methyl substituent and reductive elimination of HCl . An alternative product is formed by isomerisation and reductive elimination of H_2 .



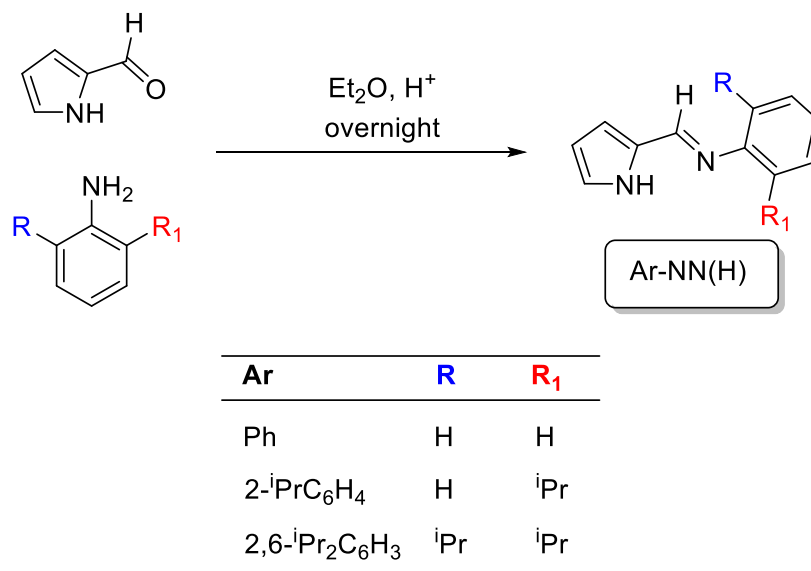
Scheme 2.1: Synthesis of Iridium(III) iminopyrrolyl complexes.²⁴

Iridium iminopyrrolyl complexes containing CO and phosphine ligands have not been reported previously. This chapter will discuss the synthesis of a small series of this class of complexes, followed by a study of the effect that systematic variation of iminopyrrolyl and phosphine ligand has on the reactivity toward MeI .²⁴

2.1 Results and discussion

2.1.1 Pro-ligand synthesis

The iminopyrrole pro-ligands Ar-NN(H) were prepared by condensation of 2-pyrrolicarboxaldehyde and the appropriate aniline (Scheme 2.2) and were used without further purification.



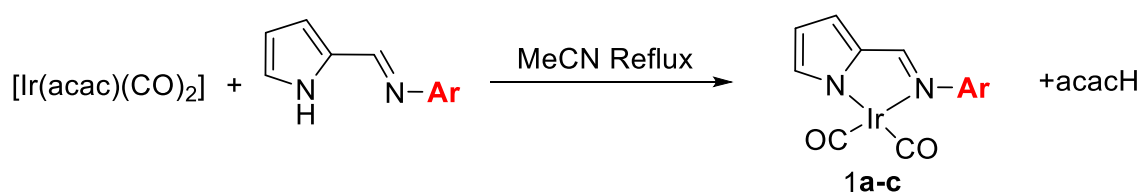
Scheme 2.2: Synthesis of iminopyrrole pro-ligands used in this study.

2.1.2 NMR Analysis

The ¹H NMR spectra of the 3 iminopyrroles are consistent with data reported in the literature.^{22,23} The N-H proton signal is broad and appears in the region of δ 10.5-11.5. The imine proton appears as a singlet in the region of ca. δ 8.25-7.9 and moves to a lower chemical shift with substitution of the aryl group. Both 2-ⁱPrC₆H₄ and 2,6-ⁱPr₂C₆H₃ substituted ligands show a septet for the methine proton at ca. δ 3.1 and a doublet for the methyl protons at ca. δ 1.1, indicating that there is free rotation around the N-aryl bond.

2.1.3 Synthesis and characterisation of [Ir(Ar-NN)(CO)₂] complexes

Synthesis of the corresponding Ir(I) dicarbonyl complexes was achieved by refluxing [Ir(acac)(CO)₂] with an equimolar amount of iminopyrrole ligand in MeCN (Scheme 2.3).



Scheme 2.3: Synthesis of [Ir(Ar-NN)(CO)₂] complexes **1a-c**

The reactions were monitored by IR spectroscopy, which displayed a clear change upon ligand displacement. A shift to a lower $\nu(\text{CO})$ was observed due to the increased donating ability of the iminopyrrolyl ligand compared to acetylacetonate. Overlaid IR spectra of reactant and product **1a** are displayed in Figure 2.6 with $\nu(\text{CO})$ values for **1a-c** reported in Table 2.1.

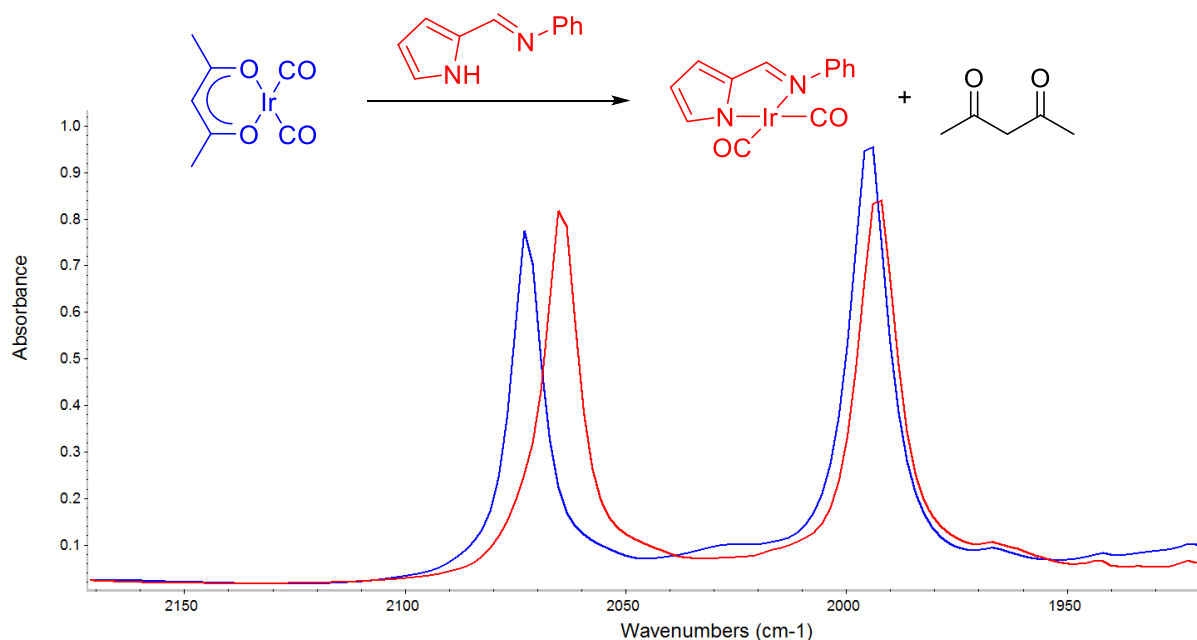


Figure 2.6: Overlaid IR spectra of $[\text{Ir}(\text{acac})(\text{CO})_2]$ and **1a** in MeCN.

Complex	Ar	$\nu(\text{CO})/\text{cm}^{-1}$ (MeCN)
1a	Ph	2064, 1993
1b	2- <i>i</i> PrC ₆ H ₄	2064, 1993
1c	2,6- <i>i</i> Pr ₂ C ₆ H ₃	2063, 1993

Table 2.1: $\nu(\text{CO})$ of complexes **1a-c**.

The complex $[\text{Ir}(\text{Ph-NN})(\text{CO})_2]$ (**1a**) was isolated as a dark brown solid and was fully characterised by ^1H and ^{13}C NMR spectroscopy, mass spectrometry, and elemental analysis.

The ^1H NMR spectrum of complex **1a** shows that the N-H proton has been lost and other signals are shifted slightly relative to the free iminopyrrole. Complexes **1b,c** were not isolated as solids but were generated *in situ* and used in subsequent reactions with phosphines (*vide infra*).

2.1.4 Reactivity of [Ir(Ph-NN)(CO)₂] with MeI

The reactivity of complex **1a** with MeI in CH₂Cl₂ was monitored by *in-situ* IR spectroscopy, a series of overlaid IR spectra obtained during the reaction is displayed in Figure 2.7. Two new metal carbonyl bands grow at a higher wavenumber consistent with the oxidative addition of MeI to form an Ir(III) methyl species **2a**. Several other lower intensity $\nu(\text{CO})$ bands are also formed during the reaction at a lower frequency than those of **2a**. A change in the $\nu(\text{C}=\text{N})$ from 1560 to 1580 cm⁻¹ is also observed upon oxidative addition of MeI.

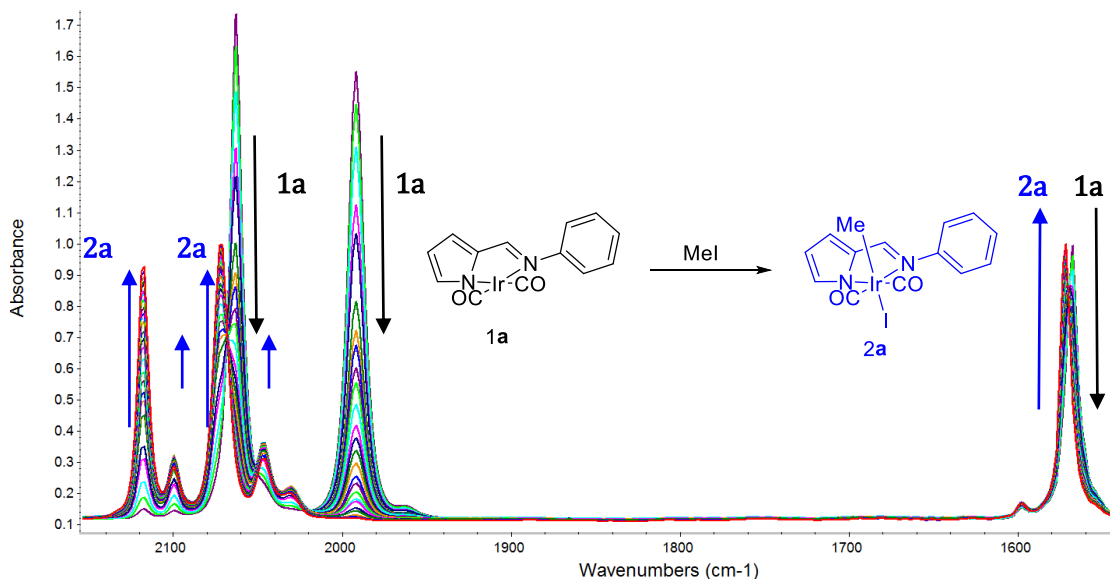


Figure 2.7: Series of overlaid IR spectra for complex **1a** reacting with MeI (1.6M, 23°C in CH₂Cl₂).

Several products were observed in the ¹H NMR spectrum after reaction of **1a** with MeI. A major Ir(III) methyl peak was observed at δ 1.19 corresponding to **2a** with lower intensity Ir(III) methyl peaks also present. High resolution mass spectroscopy indicated that the only detectable product was the Ir(III) methyl species (m/z 561) and therefore the smaller species can be tentatively assigned to isomeric forms of **2a**.

2.1.5 MeI oxidative addition kinetics

The reactivity of complex **1a** towards MeI was quantified by IR spectroscopy under pseudo first order conditions. Plots of absorbance vs. time for the band of **1a** at 1993 cm⁻¹ are well fitted to a 1st order exponential decay indicating that the reaction is first order in Ir(I) complex. A plot of k_{obs} vs. [MeI] (Figure 2.8) is linear, indicating that the reaction is first order in [MeI] and thus second order overall. From the gradient of this plot a second order rate constant k_2 can be obtained which is displayed in Table 2.2 along with comparative data for related iridium dicarbonyl complexes.

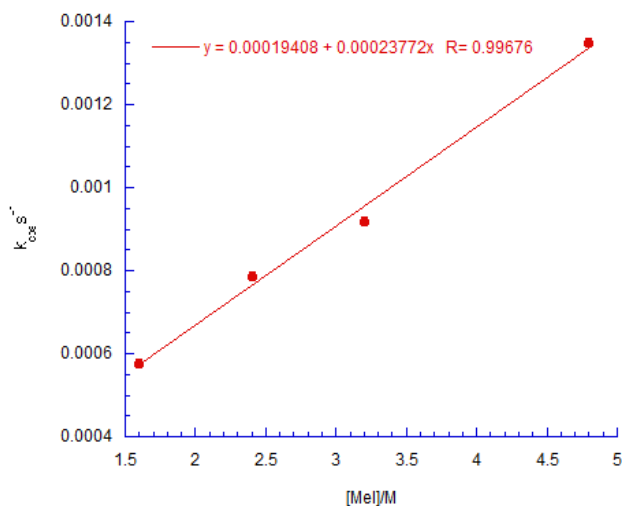


Figure 2.8: Plot of k_{obs} vs $[\text{MeI}]$ for reaction of **1a** reacting with MeI (23°C, CH_2Cl_2).

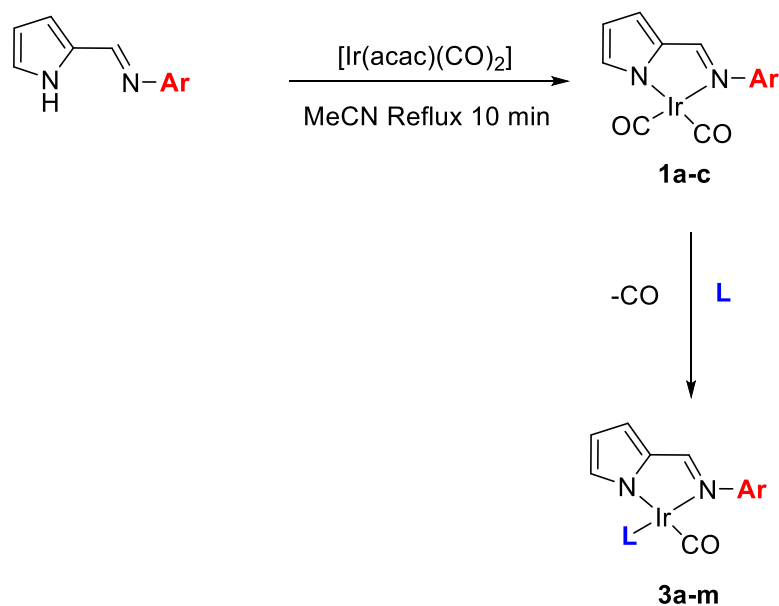
Complex	$\nu(\text{CO})/\text{cm}^{-1}$	$k_2 \cdot 10^5 / \text{dm}^3 \text{mol}^{-1} \text{s}^{-1}$	k_{rel}	Ref
	2072,1994	6.3	1	25
	2064,1993	23.7	4	
	2061,1985	50.9	8	26
	2049,1976	408	65	26

Table 2.2: Second order rate constants for reactions of Ir(I) dicarbonyl complexes with MeI.^{25,26}

Table 2.2 shows that **1a** is ca. 4 times more reactive toward MeI than $[\text{Ir}(\text{acac})(\text{CO})_2]$.²⁵ The increase in rate is attributed to the greater electron donating ability of the iminopyrrolyl ligand, and is consistent with lower $\nu(\text{CO})$ values for **1a**. However, related bidentate iridium(I) diiminate and ketoiminate complexes synthesised recently by Singer-Hobbs²⁶ have even lower $\nu(\text{CO})$ values and higher MeI oxidative addition rates.

2.1.6 Synthesis and characterisation of [Ir(Ar-NN)(CO)L] complexes

The phosphine substituted [Ir(Ar-NN)(CO)L] complexes **3a-m** were synthesised by the route shown in Scheme 2.4.



Scheme 2.4: Synthesis of [Ir(Ar-NN)(CO)L] complexes **3a-m**.

Refluxing equimolar amounts of [Ir(acac)(CO)₂] and iminopyrrole ligand in MeCN gives the [Ir(Ar-NN)(CO)₂] complexes **1a-c** as described above. Addition of one equivalent of a tri-aryl phosphine resulted in rapid evolution of CO. The solution was further refluxed and monitored by IR spectroscopy until the reactant complex was no longer present.

The [Ir(Ar-NN)(CO)L] complexes **3a-m** were isolated as orange/red powders by removal of MeCN under vacuum when soluble in MeCN, or by vacuum filtration in cases where the product precipitated out of solution upon cooling. No further purification was required, the products were characterised using ¹H, ³¹P and ¹³C NMR spectroscopy, IR spectroscopy, mass spectrometry and elemental analysis.

2.1.7 Spectroscopic characterisation

Complexes **3a-m** all show a single ν(CO) absorption in the region of 1957-1968 cm⁻¹ as listed in Table 2.3.

Complex	Ar	L	Yield %	$\nu(\text{CO}) / \text{cm}^{-1}(\text{MeCN})$	$\delta^{31}\text{P}(\text{CDCl}_3)$
3a	Ph	PPh ₃	73	1965	17.5
3b	Ph	P <i>o</i> -Tol ₃	82	1962	11.2
3c	Ph	P <i>p</i> -Tol ₃	65	1962	15.3
3d	Ph	P <i>o</i> -An ₃	85	1957	0.3
3e	Ph	P(4-FC ₆ H ₄) ₃	72	1968	15.5
3f	2- ⁱ PrC ₆ H ₄	PPh ₃	74	1965	17.9
3g	2- ⁱ PrC ₆ H ₄	P <i>o</i> -Tol ₃	70	1963	11.0, 11.5
3h	2- ⁱ PrC ₆ H ₄	P <i>o</i> -AnPh ₂	72	1964	11.3
3i	2- ⁱ PrC ₆ H ₄	P <i>o</i> -An ₂ Ph	69	1961	6.1
3j	2- ⁱ PrC ₆ H ₄	P <i>o</i> -An ₃	78	1957	0.25
3k	2,6- ⁱ Pr ₂ C ₆ H ₃	PPh ₃	79	1965	18.3
3l	2,6- ⁱ Pr ₂ C ₆ H ₃	P <i>o</i> -Tol ₃	91	1962	11.3
3m	2,6- ⁱ Pr ₂ C ₆ H ₃	P <i>o</i> -An ₃	68	1957	0.13

Table 2.3: Selected spectroscopic data for complexes **3a-m**.

The $\nu(\text{CO})$ gives a good indication of the amount of electron density situated on the metal centre. Substitution at the 2, or both 2 and 6 positions of the aromatic ring of the iminopyrrole ligand with electron donating ⁱPr groups has little effect on $\nu(\text{CO})$, illustrated by complexes **3a,f** and **3k** which have the same $\nu(\text{CO})$ value (1965 cm⁻¹).

However, changing the phosphine ligand has a greater effect on $\nu(\text{CO})$. The complex containing the most electron withdrawing phosphine ligand P(4-FC₆H₄)₃ (**3e**) has the highest $\nu(\text{CO})$ value as expected. Conversely complexes **3d,j** and **3m** which all incorporate a P(*o*-An)₃ ligand have the lowest $\nu(\text{CO})$ due to the increased donating ability of the P(*o*-An)₃ phosphine ligand substituents.

The carbonyl stretching frequency of **3a** is very similar to that for Vaska's complex,²⁷ (1964 cm⁻¹), but lower than values reported by Gonsalvi for [Ir(CO)(I)(dppms)] (1972 cm⁻¹) and [Ir(CO)(I)(dppe)] (1995 cm⁻¹).²⁸

All complexes excluding **3g** show a single resonance in the ³¹P{¹H} NMR spectra between ca. δ 18.5 and 0 consistent with a single isomer. However, complex **3g** displays two broad resonances which potentially arise from a steric interaction between the 2-substituted iminopyrrole ligand and the P(*o*-Tol)₃ ligand. If rotation around the N-aryl or Ir-P bond is slowed two different conformers may exist, leading to two ³¹P{¹H} NMR signals. Upon

heating a sample of **3g** in d^8 toluene the two peaks at δ 12.1 and 11.7 firstly coalesce to a broad resonance at δ 11.9 at 60°C as shown in Figure 2.9. This then sharpens at 80°C indicating that exchange between the two conformers has become rapid on the NMR timescale.

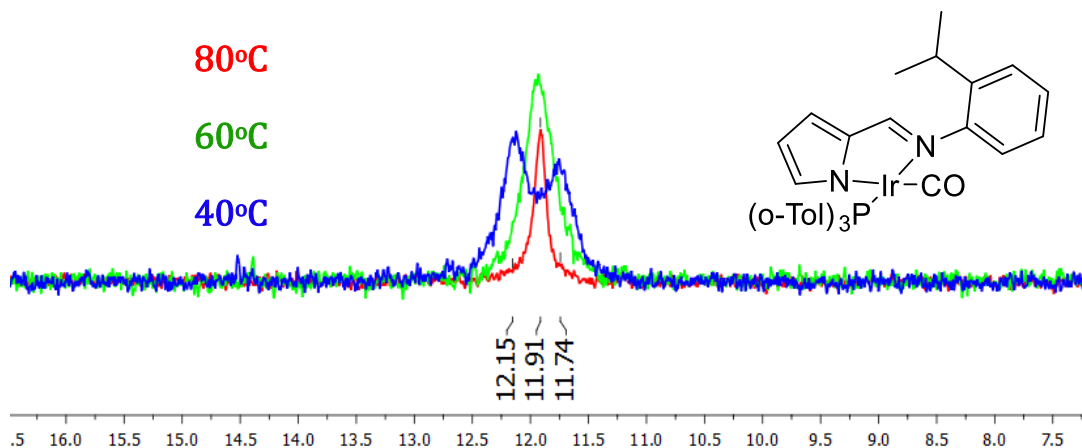


Figure 2.9: Overlaid $^{31}\text{P}\{^1\text{H}\}$ NMR spectra of complex **3g** from 40-80°C in d^8 toluene 101MHz.

For all the square planar Ir(I) iminopyrrolyl complexes, two geometrical isomers are possible, however only one is observed by $^{31}\text{P}\{^1\text{H}\}$ and ^1H NMR spectroscopy. The coordination of phosphine *trans* to the imino nitrogen donor was confirmed by X-ray crystallography (shown below). Complexes **3c,g** and **3h** all show broad ^1H NMR signals which sharpen at increased temperature. Complexes **3a-m** display a signal between ca. δ 7.9 and 8.0 for the imine proton which appears as a doublet (ca. 7 Hz) from $^4J_{\text{P-H}}$ coupling. In the ^1H NMR spectra of complexes **3f-m** two doublets at ca. δ 1.2 and 1.4 are observed. This indicates inequivalence of the methyls of the isopropyl groups due to restricted rotation around the N-aryl bond. This results in “front-back” asymmetry illustrated in Figure 2.10. A similar observation was reported for related $[\text{RhI}(\text{CO})(\text{di-imine})]$ and $[\text{RhI}(\text{CO})(\text{pyridyl imine})]$ complexes studied by Gaunt and Gonsalvi.² Selected ^1H NMR data for complexes **3f** and **3k** are displayed in Table 2.4.

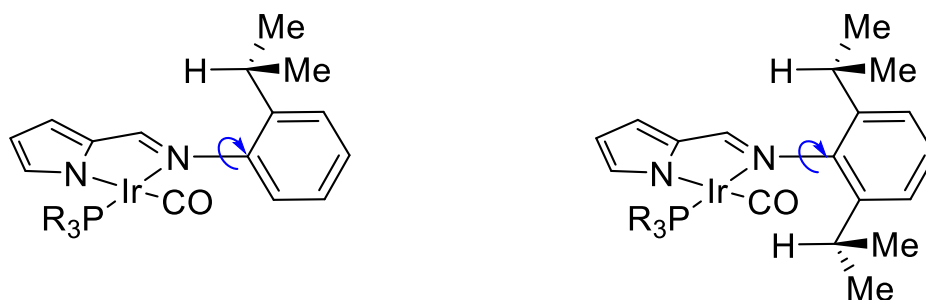


Figure 2.10: Illustration to show inequivalence.

Complex	HC=Nar	Pyrrole	R / R ₁
3f	δ 7.91, d, J = 7.0Hz, 1H	δ 6.63, d, J = 3.0Hz 1H	δ 3.85, sept, J = 6.6Hz, 1H
		δ 5.87, s, 1H	δ 1.27, d, J =6.7Hz, 3H
		δ 5.81, s, 1H	δ 1.11, d, J = 6.7Hz, 3H
3k	δ 7.9, d, J = 7.3Hz, 1H	δ 6.72 dd, J = 3.4, 1.3Hz, 1H	δ 3.76, sept J =6.8Hz, 2H
		δ 5.91, m, 2H	δ 1.36 d, J = 6.8Hz, 6H
			δ 1.23 d, J = 6.9Hz, 6H

Table 2.4: Selected ^1H NMR data for complexes **3f** and **3k** (CDCl_3 , 400MHz, 298K).

2.1.8 X-Ray crystallography

Crystals of complexes **3g,k** and **3m** suitable for single crystal X-ray crystallography were obtained by slow evaporation from concentrated MeCN solutions. The structures are shown in Figure 2.11, with selected bond lengths and angles given in Table 2.5.

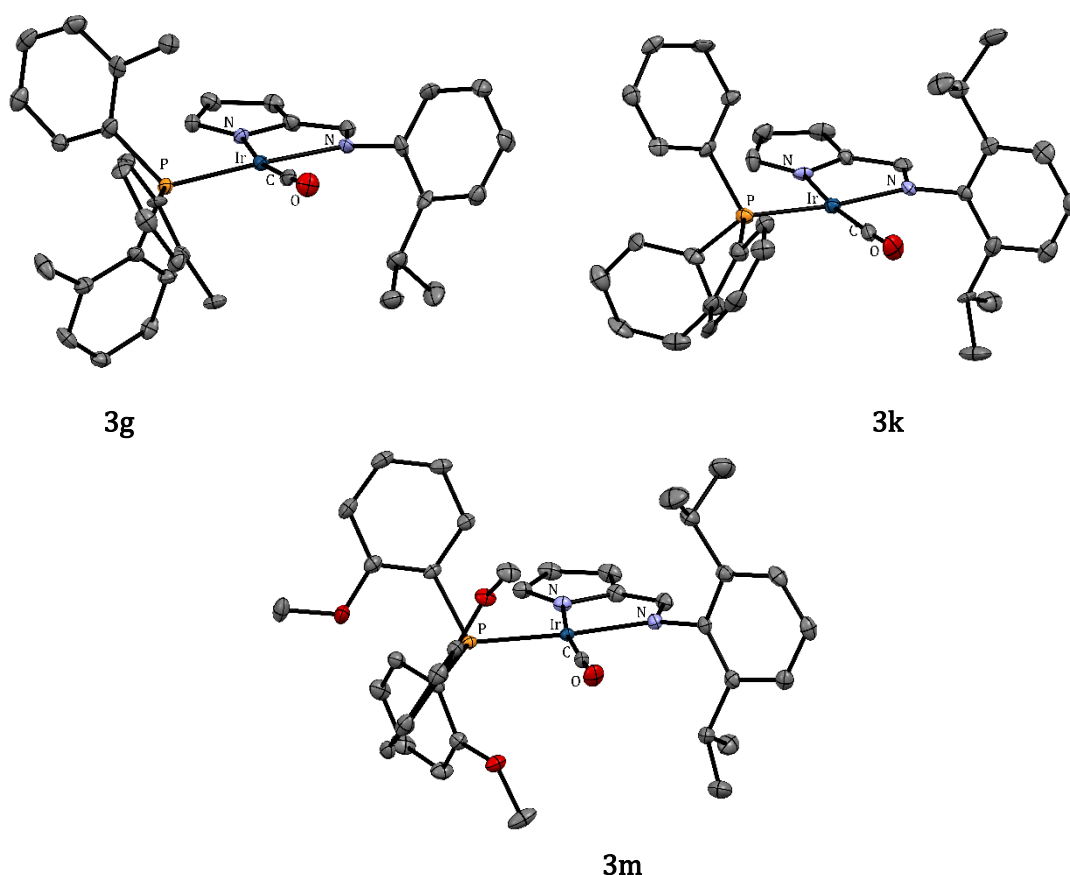


Figure 2.11: X-ray crystal structures of complexes **3g,k** and **3m** with thermal ellipsoids shown at 50% probability level. Hydrogen atoms and MeCN solvent molecule for **3k** are omitted for clarity.

	3g	3k	3m
Ir-CO	1.823(7)	1.852(8)	1.819(2)
Ir-N _{pyrrole}	2.075(5)	2.062(6)	2.0797(16)
Ir-N _{imine}	2.106(5)	2.092(6)	2.0896(16)
Ir-P	2.2719(16)	2.250(2)	2.2671(5)
N=C	1.299(7)	1.305(9)	1.303(3)
N-Ar	1.442(7)	1.429(9)	1.442(3)
OC-Ir-N _{pyrrole}	170.3(2)	171.9(3)	172.19(8)
OC-Ir-N _{imine}	94.2(2)	94.0(3)	94.19(8)
N-Ir-N	77.64(18)	77.9(2)	78.01(7)

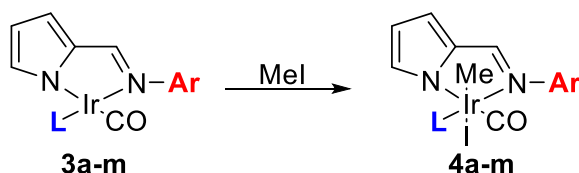
Table 2.5: Selected bond lengths (Å) and angles (deg) for complex **3g**, **3k** and **3m**.

All three structures show that an approximate square planar geometry is adopted by the iridium centre with an NN chelate bite angle of ca. 78°. The iridium pyrrolyl nitrogen bond length is slightly shorter than the iridium imine nitrogen bond which may arise from the anionic nature of the pyrrole nitrogen. The phosphine ligand is coordinated *trans* to the imine nitrogen donor atom to minimise steric interaction with the Ir-P bond length being shorter in **3k** than **3g** and **3m** due the increased bulk of the phosphine ligand in **3g** and **3m**. The N=C bond length is shorter than the N-Ar bond length consistent with double bond character and is similar in length to other reported iminopyrrolyl containing complexes.^{15,22,23} Interestingly the N-aryl group in **3g**, **3k** and **3m** is oriented approximately perpendicular to the plane of the molecule to minimise the steric interactions within the complexes.

2.2. Reaction of [Ir(Ar-NN)(CO)(PR₃)] complexes with MeI

2.2.1 Spectroscopic characterisation

Complexes **3a-k** and **3m** all react rapidly with MeI in CH₂Cl₂ yielding Ir(III) methyl complexes **4a-k** and **4m** (Scheme 2.5), However, **3l** does not react with even neat MeI. Reaction with MeI results in a shift of the carbonyl stretching frequency by approximately 80 cm⁻¹ to a higher frequency indicative of oxidative addition. Each product shows a single $\nu(\text{CO})$ at ca. 2045cm⁻¹ except **4m** which displays two $\nu(\text{CO})$ bands at a slightly lower frequency. No spectroscopic evidence for formation of Ir(III) acyl species was observed. Selected spectroscopic data for complexes **4a-m** are displayed in Table 2.6.


Scheme 2.5: Oxidative addition of MeI to complexes **3a-m**.

Complex	Ar	L	$\nu(\text{CO}) / \text{cm}^{-1}$	$\delta^{31}\text{P}$	Ratio	Yield %
4a	Ph	PPh_3	2046	-8.4	-	82
4b	Ph	$P\text{-}o\text{-Tol}_3$	2042	-10.7	-	83
4c	Ph	$P\text{-}p\text{-Tol}_3$	2044	-10.4	-	74
4d	Ph	$P\text{-}o\text{-An}_3$	2044	-21.5	-	72
4e	Ph	$\text{P}(4\text{-FC}_6\text{H}_4)_3$	2043	-10.6	-	81
4f	$2\text{-}^i\text{PrC}_6\text{H}_4$	PPh_3	2045	-8.1,-9.4	1:2	81
4g	$2\text{-}^i\text{PrC}_6\text{H}_4$	$P\text{-}o\text{-Tol}_3$	2043	-10.9,-13.3	1:3	82
4h	$2\text{-}^i\text{PrC}_6\text{H}_4$	$P\text{-}o\text{-AnPh}_2$	2045	-12.1, -14.8	1:2	79
4i	$2\text{-}^i\text{PrC}_6\text{H}_4$	$P\text{-}o\text{-An}_2\text{Ph}$	2044	-14.0, -16.1	1:1.75	76
4j	$2\text{-}^i\text{PrC}_6\text{H}_4$	$P\text{-}o\text{-An}_3$	2043	-20.7, -22.7	1:3.5	71
4k	$2,6\text{-}^i\text{Pr}_2\text{C}_6\text{H}_3$	PPh_3	2045	-9.0	-	89
4m	$2,6\text{-}^i\text{Pr}_2\text{C}_6\text{H}_3$	$P\text{-}o\text{-An}_3$	2039,2020	14.3,-6.1	9:1	71

Table 2.6: Selected spectroscopic data for complexes **4a-m** ($\nu(\text{CO})$ recorded in CH_2Cl_2 , $^{31}\text{P}\{^1\text{H}\}$ NMR recorded in CDCl_3 , 162MHz, 298K).

2.2.2 NMR characterisation of complexes **4a-e**

The $^{31}\text{P}\{^1\text{H}\}$ NMR spectra of complexes **4a-e** show a single resonance in the region of -8 to -25 ppm, indicative of a single isomer.

The ^1H NMR spectra of complexes **4a-e** and **4k** each display a single doublet between ca. δ 7.5 and 7.7 ppm with a $^4\text{J}_{\text{P-H}}$ coupling constant of ca. 9Hz for the imine proton. The methyl

ligand for these complexes appears as a doublet in the region of δ 0.6-1.3 with a $^3J_{\text{H-P}}$ coupling constant of ca. 3Hz.

2.2.3 X-ray crystallography

A single crystal of **4d** suitable for X-ray crystallography was obtained by slow evaporation of CH_2Cl_2 from a concentrated solution of the complex. The structure is displayed in Figure 2.12; selected bond angles and lengths are displayed in Table 2.7.

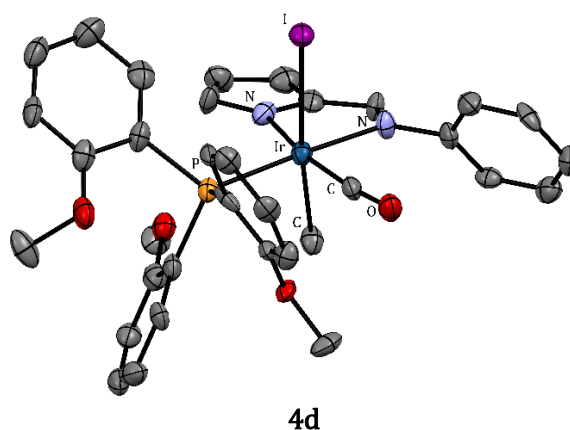


Figure 2.12: X-Ray crystal structure of complex **4d** with thermal ellipsoids set at 50% probability level. Hydrogen atoms and CH_2Cl_2 molecule omitted for clarity.

Bond	length (Å)	Angle	Degrees
Ir-CO	1.837(12)	OC-Ir-N _{pyrrole}	167.1(4)
Ir-N _{pyrrole}	2.089(9)	OC-Ir-N _{imine}	89.0(4)
Ir-N _{imine}	2.114(8)	N-Ir-N	78.5(3)
Ir-CH ₃	2.124(10)	Me-Ir-I	174.0(3)
Ir-I	2.8259(9)	P-Ir-N _{pyrrole}	177.3(2)
Ir-P	2.368(3)		
N=C	1.308(12)		
N-Ar	1.413(13)		

Table 2.7: Selected bond lengths (Å) and angles (deg) for complex **4d**.

The structure assumes a distorted octahedral geometry in which the methyl and the iodide ligand are mutually *trans*. The phenyl group of the iminopyrrolyl ligand lies approximately perpendicular to the plane to minimise interaction with the metal centre with the phosphine ligand remaining *trans* to the imine nitrogen donor ligand. The

methoxy groups of the phosphine are oriented away from the centre of the molecule to minimise the steric congestion around the metal centre.

2.2.4 Spectroscopic characterisation of complexes 4f-j

The $^{31}\text{P}\{^1\text{H}\}$ NMR spectra of complexes **4f-j** each show two broad signals with closely separated chemical shifts that appear in the range of -8 to -24 ppm. A $^{31}\text{P}\{^1\text{H}\}$ NMR spectrum of complex **4g** is displayed in Figure 2.13.

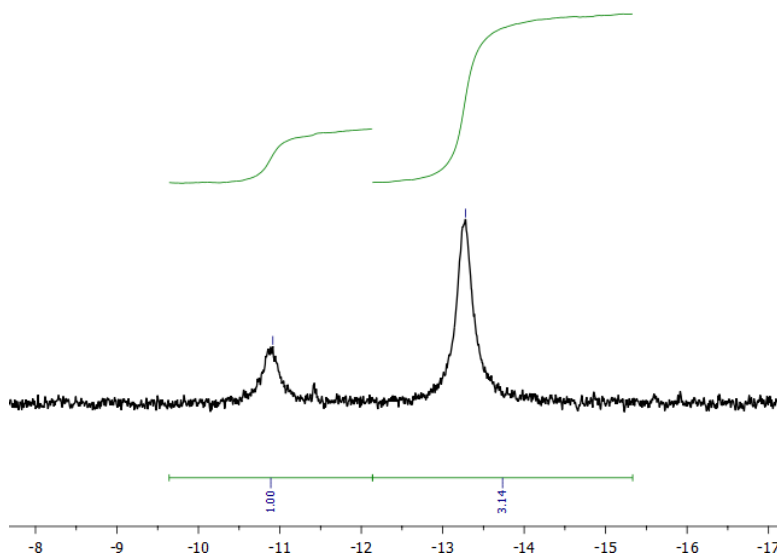


Figure 2.13: The $^{31}\text{P}\{^1\text{H}\}$ NMR spectrum of complex **4g** (298K, CDCl_3 , 162MHz).

Similarly, the ^1H NMR spectra of complexes **4f-j** show a mirroring of all the resonances consistent with the presence of major and minor species. A ^1H NMR spectrum of **4g** shown in Figure 2.14 illustrates the mirroring of the Ir-methyl and ligand isopropyl peaks. Selected ^1H NMR data for complex **4g** are displayed in Table 2.8.

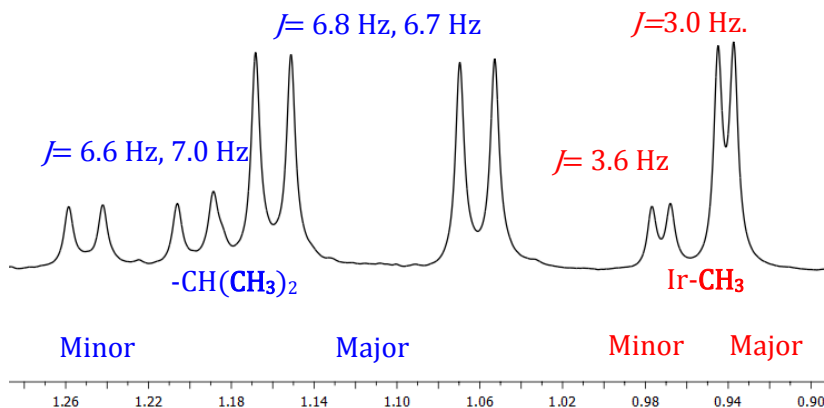


Figure 2.14: Partial ^1H NMR spectrum of complex **4g** (CDCl_3 , 298K, 400MHz) displaying isomeric species.

Complex	HC=ArN	Ir-CH ₃	ArCH(CH ₃) ₂	ArCH(CH ₃) ₂
4g	7.37, d, J=10.5 Hz	0.94 d, J =3.0 Hz	3.04, sept J=7.8Hz	1.16, d, J = 6.8 Hz
Major				1.06, d, J = 6.7 Hz
4g	7.35, d, J=9.8 Hz	0.97 d, J=3.6 Hz	3.74, sept J=7.8Hz	1.19, d, J = 7.0 Hz
Minor				1.25, d, J = 6.6 Hz

Table 2.8: Selected ¹H NMR data for complex **4g** (CDCl₃, 400MHz, 298K).

The closely separated ³¹P{¹H} and ¹H NMR chemical shifts and a single ν(CO) absorption indicates rotameric isomers are present from restricted rotation around the N-aryl bond. Upon oxidative addition the isopropyl group can direct toward the methyl or iodide ligand giving two rotational isomers as displayed in Figure 2.15. Unlike complex **3g** heating a NMR sample of **4f-j** (d⁸ toluene 100°C) does not cause the two broad peaks to coalesce, suggesting a higher barrier of rotation in the Ir(III) octahedral complexes.

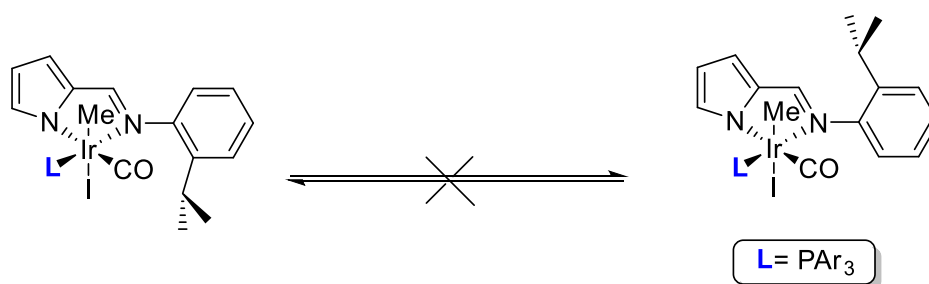


Figure 2.15: Schematic showing rotameric isomers for **4f-j**.

2.2.5 Spectroscopic characterisation of complexes **4k** and **4m**

The ³¹P{¹H} NMR spectrum of **4k** displays a single chemical shift and is consistent with a single geometrical isomer.

¹H NMR displays a doublet at δ 7.6 with a ⁴J_{P-H} coupling constant of 9.2 Hz for the imine proton. A partial NMR spectrum of **4k** (Figure 2.16) displaying from δ 5.0 – 0 shows a doublet at δ 0.65 with a ³J_{H-P} coupling constant of 3.1 Hz for the methyl ligand. Four doublets and two septets are also observed, consistent with “front-back” and “top-bottom” asymmetry from restricted rotation about the N-aryl bond.

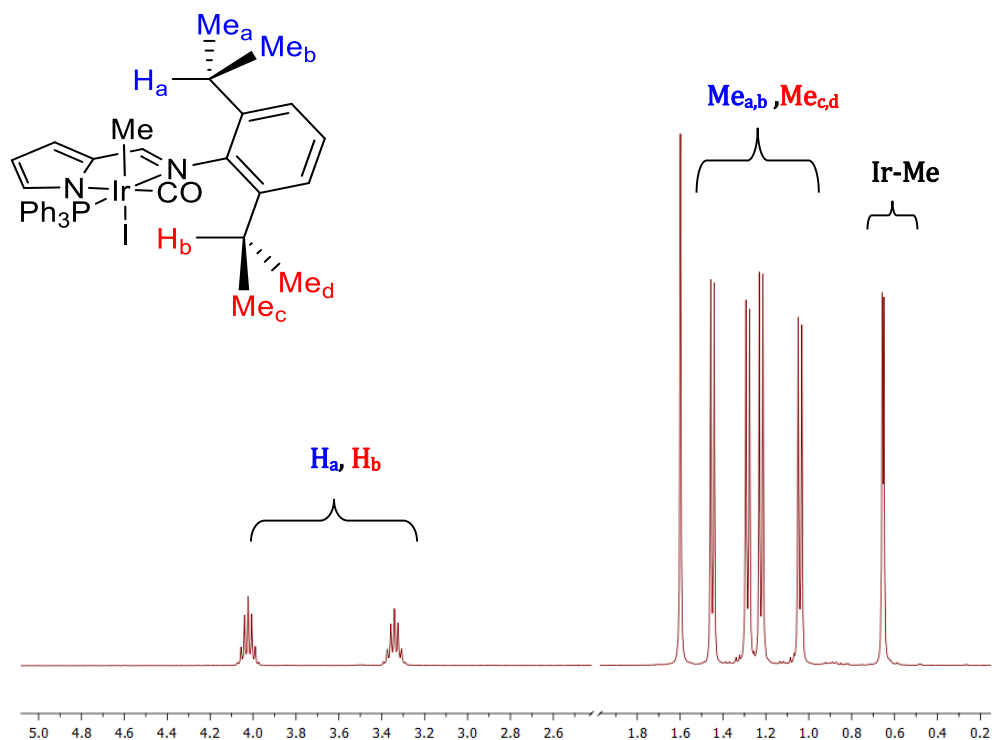


Figure 2.16: A partial ^1H NMR spectrum of complex **4k** showing “front,back” and “top, bottom” asymmetry, residual MeI peak omitted for clarity (CDCl_3 , 298K, 400MHz).

A single crystal of **4k** suitable for X-ray crystallography was obtained by slow diffusion of hexanes into a concentrated CH_2Cl_2 solution of the complex. The structure is displayed in Figure 2.17; selected bond angles and lengths are displayed in Table 2.9.

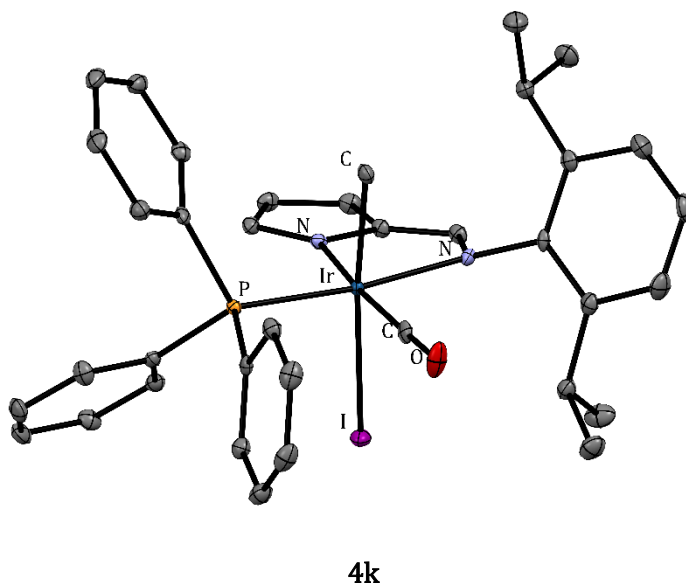


Figure 2.17: X-ray crystal structure of complex **4k** with thermal ellipsoids set at 50% probability level. Hydrogen atoms and CH_2Cl_2 solvent molecule omitted for clarity.

Bonds	length (Å)	Angle	Degrees
Ir-CO	1.862(2)	OC-Ir-N _{pyrrole}	171.93(8)
Ir-N _{pyrrole}	2.0792(17)	OC-Ir-N _{imine}	92.60(7)
Ir-N _{imine}	2.1514(18)	N-Ir-N	78.33(7)
Ir-CH ₃	2.120(2)	Me-Ir-I	174.72(6)
Ir-I	2.8060(2)	P-Ir-N _{pyrrole}	98.51(5)
Ir-P	2.3245(5)		
N=C	1.307(3)		
N-Ar	1.447(3)		

Table 2.9: Selected bond lengths (Å) and angles (deg) for complex **4k**.

The structure assumes a distorted octahedral geometry in which the methyl and the iodide ligand are mutually *trans*. The 2,6-*i*Pr₂C₆H₃ group of the iminopyrrole ligand is aligned in such a way to avoid the steric congestion generated by the methyl and iodide ligands. The phosphine ligand remains *trans* to the imine nitrogen donor ligand minimising steric interactions.

The ³¹P{¹H} NMR spectrum of complex **4m** shows two signals separated by 20 ppm in a 9:1 ratio. These two signals are in a different region of the spectrum to the other Ir(III) *P**o*-An₃ phosphine containing complexes **4d** and **4j** which appear in the δ -22 to -21 region. The large difference in chemical shifts, ratio and position in the ³¹P{¹H} NMR spectrum indicates that **4m** is likely a mixture of two geometrical isomers formed upon oxidative addition of MeI.

Similarly the ¹H NMR spectrum of complex **4m** also displays two sets of chemical shifts with ca. 9:1 difference in intensity. This is best illustrated by the chemical shifts for the methyl ligands, a major resonance with a low chemical shift at δ 0.07 with a coupling constant of 3.3 Hz and a minor resonance at δ 1.03 with a coupling constant of 1.7 Hz. The large difference in position and coupling constants for the two methyl ligands is indicative of two different ligand arrangements around the metal centre and is also consistent with ν(CO) and ³¹P{¹H} NMR spectroscopy. However, without further evidence, definitive structures for these isomers cannot be assigned.

2.2.6 MeI oxidative addition kinetics

Kinetic experiments were carried out using at least a tenfold excess of MeI to ensure pseudo first order conditions. In the case of less reactive complexes, IR spectroscopy was used to monitor the reactivity. For complexes that had high reactivity toward MeI, UV-vis spectroscopy was used, the sensitivity of which allows a lower concentration of complex, hence lower [MeI] to give convenient measurable rates whilst maintaining pseudo first order conditions.

In the case of **3b,g** and **3k** infrared spectroscopy was used an example of a series of spectra recorded during a typical experiment reacting **3g** with MeI is shown in Figure 2.18.

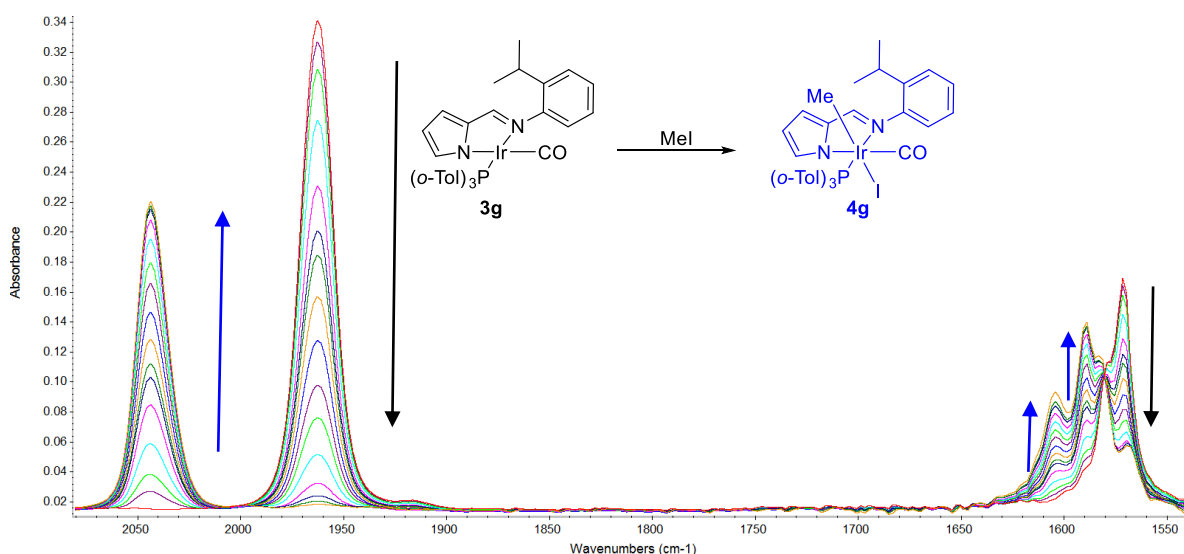


Figure 2.18: Series of IR spectra during the reaction of **3g** with MeI (0.04 M in CH₂Cl₂ at 23°C).

The decay of the carbonyl band for the Ir(I) starting material at 1963 cm⁻¹ for **3g** is mirrored by the growth of a carbonyl band at 2043 cm⁻¹ indicative of oxidative addition of MeI and the formation of an Ir(III) methyl species **4g**. Changes in the $\nu(\text{C}=\text{N})$ at 1565, 1580 and 1610 cm⁻¹ is also observed upon oxidative addition of MeI. Analogous observations were made for complexes **3b** and **3k**.

For the remainder of the complexes UV-vis spectroscopy was used to monitor the reaction. A series of difference spectra was taken in order to determine a wavelength suitable to measure in the kinetic assessment. An example set of difference spectra for the reaction of complex **3f** with MeI is displayed in Figure 2.19.

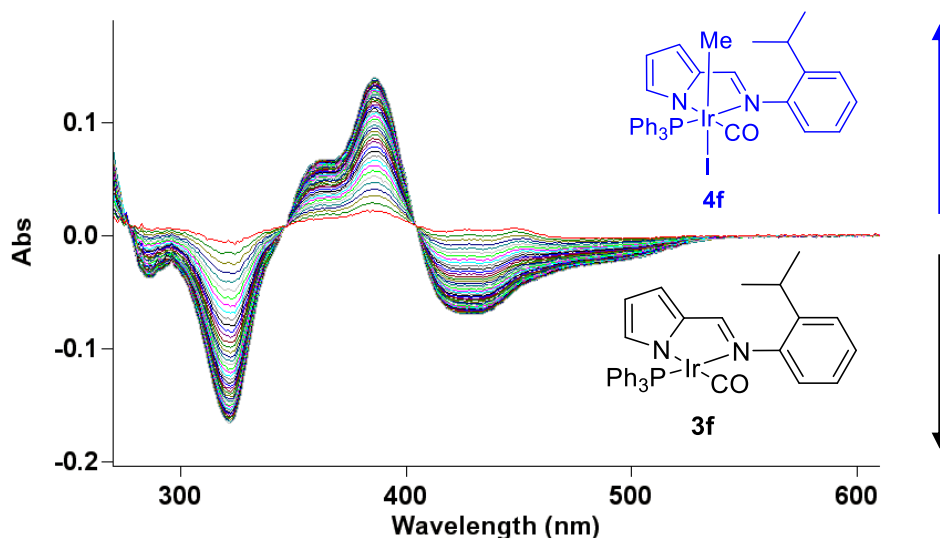


Figure 2.19: Series of UV-vis difference spectra for the reaction of **3f** with MeI (0.0064M in CH_2Cl_2 at 23°C).

Bands with a negative absorbance are associated with the decay of the reactant, whilst those with a positive absorbance are associated with the product. The absorbance at wavelengths of ca.320 nm and 425 nm for the starting Ir(I) complex **3f** decreases with time mirrored by the growth in absorbance at wavelengths of ca 350 and 380 nm for the Ir-methyl complex, **4f**.

The decay of the identified IR or UV-vis absorbance was analysed to obtain a pseudo first order rate constant (k_{obs}). Plots of absorbance vs. time were well fitted to an exponential decay curve (an example for complex **3f** is shown in Figure 2.20), indicating that the reaction was first order in Ir(I) complex

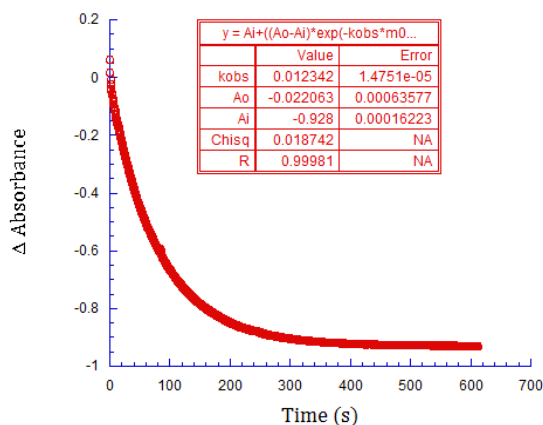


Figure 2.20: Plot of absorbance at 320 nm Vs time for reaction of complex **3f** with MeI (0.00192M in CH_2Cl_2 at 23°C).

Plots of k_{obs} vs. $[\text{MeI}]$ are linear indicating that the reactions are first order in $[\text{MeI}]$ and therefore second order overall. Plots for complexes **3a-c** and **3e** are shown in Figure 2.21. Second order rate constants k_2 can be obtained from the gradient of such plots which are displayed in Table 2.10 for complexes **3a-m**.

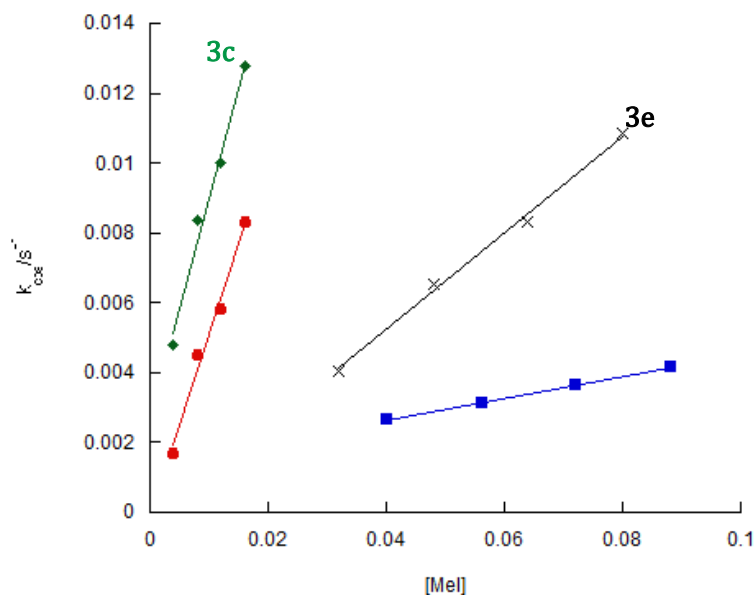


Figure 2.21: Plot of k_{obs} vs. $[\text{MeI}]$ for reaction of **3a-c** and **3e** with MeI (23°C in CH_2Cl_2).

Complex	Ar	L	$\nu(\text{CO}) / \text{cm}^{-1}$	Technique	$k_2 / \text{dm}^3 \text{mol}^{-1} \text{s}^{-1}$
3a	Ph	PPh_3	1965	UV-Vis	0.52
3b	Ph	$\text{P-}o\text{-Tol}_3$	1962	IR	0.03
3c	Ph	$\text{P-}p\text{-Tol}_3$	1962	UV-Vis	0.64
3d	Ph	$\text{P-}o\text{-An}_3$	1957	UV-Vis	32.3
3e	Ph	$\text{P(4-FC}_6\text{H}_4)_3$	1968	UV-Vis	0.13
3f	$2\text{-}^i\text{PrC}_6\text{H}_4$	PPh_3	1965	UV-Vis	0.31
3g	$2\text{-}^i\text{PrC}_6\text{H}_4$	$\text{P-}o\text{-Tol}_3$	1963	IR	0.05
3h	$2\text{-}^i\text{PrC}_6\text{H}_4$	$\text{P-}o\text{-AnPh}_2$	1961	UV-Vis	9.1
3i	$2\text{-}^i\text{PrC}_6\text{H}_4$	$\text{P-}o\text{-An}_2\text{Ph}$	1959	UV-Vis	25.1
3j	$2\text{-}^i\text{PrC}_6\text{H}_4$	$\text{P-}o\text{-An}_3$	1957	UV-Vis	42.1
3k	$2,6\text{-}^i\text{PrC}_6\text{H}_3$	PPh_3	1965	IR	0.03
3m	$2,6\text{-}^i\text{PrC}_6\text{H}_3$	$\text{P-}o\text{-An}_3$	1957	UV-Vis	3.1

Table 2.10: Second order rate constant (k_2) values for reaction of complexes **3a-m** with MeI measured in CH_2Cl_2 at 23°C.

2.2.7 Analysis of complexes 3a-e

The observed reactivity towards iodomethane varies over three orders of magnitude dependent upon the iminopyrrolyl and phosphine ligand substituents. The reactivity of complexes **3a-e** is dramatically changed upon variation of the phosphine ligand. Changing the phosphine ligand from PPh_3 (**3a**) to $\text{P-}o\text{-Tol}_3$ (**3b**) results in a 17 fold reduction in rate due to increased steric congestion. However, changing the phosphine ligand to $\text{P-}p\text{-Tol}_3$ (**3c**) results in a slight increase in reactivity from the increased donating ability of the phosphine and very little change in steric environment. Conversely changing to an electron withdrawing phosphine ligand $\text{P(4-FC}_6\text{H}_4)_3$ (**3e**) results in a four-fold reduction in reactivity toward MeI compared to **3a**.

Increasing the steric bulk of the iminopyrrolyl ligand also has a large effect on the oxidative addition rate. An isopropyl group at the 2 position of the ligand decreases the rate by almost a half and when both the 2 and 6 positions of the ligand are substituted, a 14 fold reduction in rate is observed as illustrated in Figure 2.22.

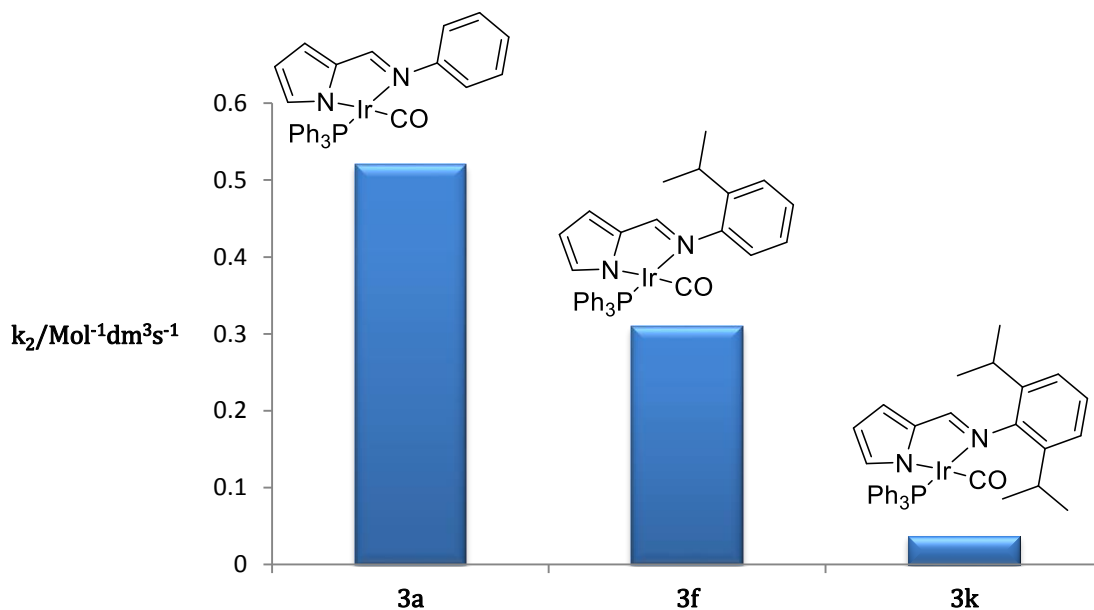


Figure 2.22: Graph showing the effect of iminopyrrolyl backbone substitution on reactivity toward MeI in complexes **3a,f** and **3k**.

Surprisingly, when comparing **3b** with **3g** (both contain a $\text{P-}o\text{-Tol}_3$ ligand) the opposite effect occurs. An increase in rate is observed when the iminopyrrolyl ligand is substituted at the 2-position with an isopropyl group. Substitution at both the 2 and 6 positions of the ligand results in reactivity toward MeI to cease altogether.

2.2.8 Analysis of complexes **3d**, **3g-i** and **3m**

The complexes with the highest oxidative addition rates are **3d**, **3g-i** and **3m** all of which incorporate *o*-anisyl substituents on the phosphine ligand.

Incorporating a P(*o*-An)₃ ligand results in a large rate enhancement, the MeI oxidative addition rate of **3d** is 32.2 M⁻¹s⁻¹ an increase in reactivity of approximately 60 times compared to **3a** and approximately 1000 times faster than complex **3b** that has a P(*o*-Tol)₃ ligand which has a similar steric bulk.

Surprisingly, again, an initial increase in rate is observed when the iminopyrrolyl ligand is substituted at the 2-position with an isopropyl group to 42.1 M⁻¹s⁻¹ for complex **3j**. Substitution at both 2 and 6 position results in a large reduction in rate to 2.9 M⁻¹s⁻¹ for complex **3m**.

2.2.9 Effect of sequential incorporation of *o*-anisyl ligand substituents

Figure 2.23 shows what effect sequentially replacing phenyl ligand substituents to *o*-anisyl substituents has on oxidative addition rate. A single *o*-anisyl group (**3h**) increases the rate ca. 30 times compared to PPh₃ (**3f**), a second 80 times (**3i**) and full substitution (**3j**) increases the rate ca. 135 times.

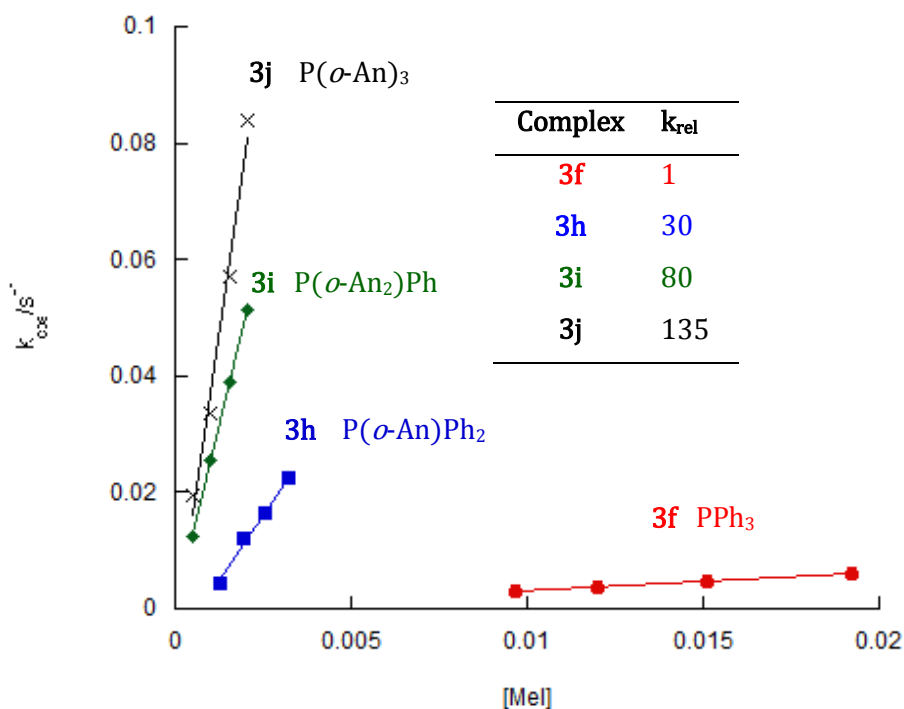
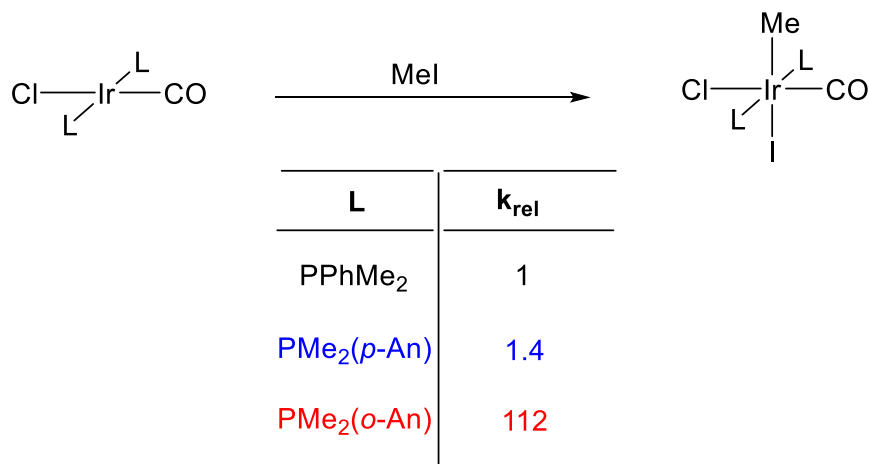


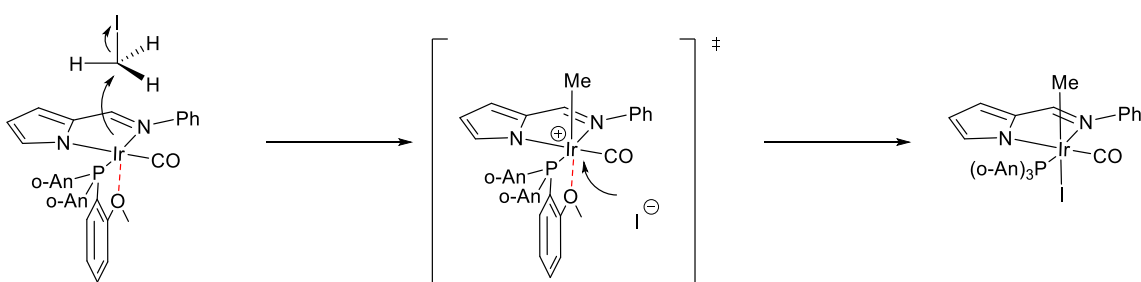
Figure 2.23: Plots of k_{obs} vs. [MeI] for complexes **3f** and **3h-j** (23°C CH₂Cl₂).

Miller and Shaw^{29,30} were the first to observe the effect of *o*-anisyl containing phosphine complexes on reactivity. They observed that the oxidative addition reaction of complexes $[\text{Ir}(\text{CO})(\text{Cl})(\text{PMe}_2(\textit{o}\text{-An}))_2]$ with MeI was approximately 100 times faster than the corresponding $[\text{IrCl}(\text{CO})(\text{PMe}_2(\textit{p}\text{-An}))_2]$ and $[\text{IrCl}(\text{CO})(\text{PMe}_2\text{Ph})_2]$ at 25°C (Scheme 2.6).



Scheme 2.6: Dramatic rate enhancement observed by Miller and Shaw for reaction of complexes $[\text{IrCl}(\text{CO})(\text{PMe}_2(\textit{o}\text{-An}))_2]$ with MeI.^{29,30}

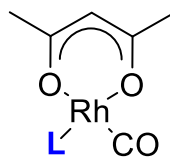
The large rate enhancement was attributed to an electronic interaction between the iridium metal centre and the lone pair of electrons on the pendent methoxy oxygen of the $\text{P}(\text{Me}_2\textit{o}\text{-An})$ ligand, which helps to stabilise the $\text{S}_{\text{N}}2$ transition state and increase reactivity. The same interaction can occur in complexes **3d**, **3g-i** and **3m** and would account for the large rate enhancement observed for complexes incorporating *o*-anisyl containing phosphine ligand. A schematic representation of this effect for complex **3d** is displayed in Scheme 2.7.



Scheme 2.7: Proposed mechanism for the oxidative addition of MeI to complex **3d**.

Recent research within the Haynes group on $[\text{Rh}(\text{acac})(\text{CO})\text{L}]$ systems³¹ also observed rate enhancement when incorporating phosphine ligands with *o*-anisyl substituents, as shown in Figure 2.24. An initial 15 fold rate enhancement is observed by substitution of 1 phenyl group, this continues to increase with further substitution, these findings are consistent with those observed for the iridium iminopyrrolyl complexes reported in this

chapter, which are approximately 15-20 fold more reactive toward MeI than the [Rh(acac)(CO)L] complexes.



L=	PPh ₃	PPh ₂ (<i>o</i> -An)	PPh(<i>o</i> -An) ₂	P(<i>o</i> -An) ₃
k _{rel} =	1	15	40	63

Figure 2.24: Effect of *o*-An substituents on reactivity toward MeI in [Rh(acac)(CO)L] complexes.³¹

2.3 Summary

A series of iridium iminopyrrolyl phosphine carbonyl complexes has been synthesised. These complexes have been fully characterised by IR, NMR, mass spectroscopy, elemental analysis and in some cases X-Ray crystallography and were found to be a single isomer with the phosphine displacing the CO trans to the imino nitrogen donor ligand.

These complexes (excluding the very bulky [2,6-ⁱPr₂C₆H₃NNIr(CO)(P-*o*-Tol₃)] **3l**) react with MeI forming Ir(III) methyl species. Rotameric isomers were obtained in the cases of **4f-j** which contain a 2-ⁱPrC₆H₄NN ligand. [2,6-ⁱPrC₆H₃NNIr(CO)(P-*o*-An₃)] complex **4m** forms two different geometrical isomers tentatively assigned by ¹H, ³¹P and ν(CO) analysis.

The oxidative addition rate of these complexes has been measured using IR or UV-vis kinetics, complexes that incorporate *o*-anisyl substituted phosphine ligands show the highest MeI oxidative addition rates, for example [2-ⁱPrC₆H₄NNIr(CO)(P-*o*-An₃)] complex **3j** reacts 135 times faster toward MeI than [2-ⁱPrC₆H₄NNIr(CO)(PPh₃)] complex **3i** which has no *o*-anisyl functionality and is attributed to the neighbouring group effect.

In the following chapter, the iminopyrrolyl ligand backbone is modified to incorporate an additional donor. These terdentate ligands will be complexed to rhodium and iridium and will then be reacted with MeI to investigate their reactivity.

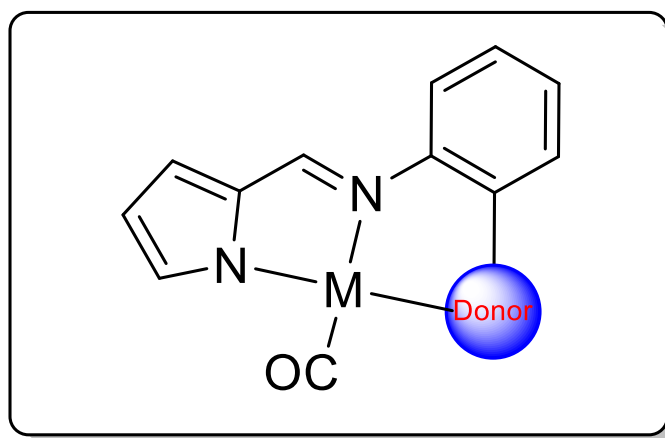
2.4 References

- (1) Haynes, A. In *Advances in Catalysis*; Bruce, C. G., Helmut, K., Eds.; Academic Press: **2010**; Volume 53, p 1.
- (2) Gonsalvi, L.; Gaunt, J. A.; Adams, H.; Castro, A.; Sunley, G. J.; Haynes, A. *Organometallics*. **2003**, *22*, 1047.
- (3) Best, J.; Wilson, J. M.; Adams, H.; Gonsalvi, L.; Peruzzini, M.; Haynes, A. *Organometallics*. **2007**, *26*, 1960.
- (4) Basson, S. S.; Leipoldt, J. G.; Nel, J. T. *Inorg. Chim. Acta*. **1984**, *84*, 167.
- (5) Basson, S. S.; Leipoldt, J. G.; Roodt, A.; Venter, J. A.; van der Walt, T. J. *Inorg. Chim. Acta*. **1986**, *119*, 35.
- (6) Brink, A.; Roodt, A.; Steyl, G.; Visser, H. G. *Dalton. Trans.* **2010**, *39*, 5572.
- (7) Conradie, M. M.; Conradie, J. *Dalton. Trans.* **2011**, *40*, 8226.
- (8) Clinton, A. MChem Thesis, University Of Sheffield, **2015**.
- (9) Gibson, V. C.; V.; Newton, C.; Redshaw, C.; A. Solan, G.; J. P. White, A.; J. Williams, D.; J. Maddox, P. *Chem. Commun.* **1998**, 1651.
- (10) Gibson, V. C.; Newton, C.; Redshaw, C.; Solan, G. A.; White, A. J. P.; Williams, D. J. *J. Chem. Soc., Dalton Trans.* **2002**, 4017.
- (11) Matsui, S.; Yoshida, Y.; Takagi, Y.; Spaniol, T. P.; Okuda, J. *J. Organomet. Chem.* **2004**, *689*, 1155.
- (12) Pennington, D. A.; Coles, S. J.; Hursthouse, M. B.; Bochmann, M.; Lancaster, S. J. *Chem. Commun.* **2005**, 3150.
- (13) Yoshida, Y.; Matsui, S.; Takagi, Y.; Mitani, M.; Nakano, T.; Tanaka, H.; Kashiwa, N.; Fujita, T. *Organometallics*. **2001**, *20*, 4793.
- (14) Matsui, S.; Spaniol, T. P.; Takagi, Y.; Yoshida, Y.; Okuda, J. *J. Chem. Soc., Dalton Trans.* **2002**, 4529.
- (15) Bellabarba, R. M.; Gomes, P. T.; Pascu, S. I. *Dalton. Trans.* **2003**, 4431.
- (16) Vanka, K.; Xu, Z.; Ziegler, T. *Organometallics*. **2004**, *23*, 2900.
- (17) Li, Y.-S.; Li, Y.-R.; Li, X.-F. *J. Organomet. Chem.* **2003**, *667*, 185.
- (18) Cui, C.; Shafir, A.; Reeder, C. L.; Arnold, J. *Organometallics*. **2003**, *22*, 3357.
- (19) Yasumoto, T.; Yamagata, T.; Mashima, K. *Organometallics*. **2005**, *24*, 3375.
- (20) Pracha, S.; Praban, S.; Niewpung, A.; Kotpisan, G.; Kongsaree, P.; Saithong, S.; Khamnaen, T.; Phiriyawirut, P.; Charoenchaidet, S.; Phomphrai, K. *Dalton. Trans.* **2013**, *42*, 15191.
- (21) Tabthong, S.; Nanok, T.; Kongsaree, P.; Prabpai, S.; Hormnirun, P. *Dalton. Trans.* **2014**, *43*, 1348.

- (22) Carabineiro, S. A.; Silva, L. C.; Gomes, P. T.; Pereira, L. C. J.; Veiros, L. F.; Pascu, S. I.; Duarte, M. T.; Namorado, S.; Henriques, R. T. *Inorg. Chem.* **2007**, *46*, 6880.
- (23) Carabineiro, S. A.; Bellabarba, R. M.; Gomes, P. T.; Pascu, S. I.; Veiros, L. F.; Freire, C.; Pereira, L. C. J.; Henriques, R. T.; Oliveira, M. C.; Warren, J. E. *Inorg. Chem.* **2008**, *47*, 8896.
- (24) Paul, P.; Richmond, M. G.; Bhattacharya, S. *J. Organomet. Chem.* **2014**, *751*, 760.
- (25) Cottrerill, B. MChem Thesis, University Of Sheffield, **2012**.
- (26) Singer-Hobbs, M. MChem Thesis, University Of Sheffield, **2013**.
- (27) Vaska, L.; DiLuzio, J. W. *J. Am. Chem. Soc.* **1961**, *83*, 2784.
- (28) Gonsalvi, L.; Adams, H.; Sunley, G. J.; Ditzel, E.; Haynes, A. *J. Am. Chem. Soc.* **2002**, *124*, 13597.
- (29) Miller, E. M.; Shaw, B. L. *J. Chem. Soc., Dalton Trans.* **1974**, 480.
- (30) Empsall, H. D.; Hyde, E. M.; Jones, C. E.; Shaw, B. L. *J. Chem. Soc., Dalton Trans.* **1974**, 1980.
- (31) John, C. MChem Thesis, University Of Sheffield, **2011**.

Chapter 3

Synthesis and reactivity of Rh(I) and Ir(I) iminopyrrolyl pincer complexes



3.0 Introduction

The search for new ligands that can direct specific electronic and steric effects upon a metal centre is one that attracts intense interest. Pincer ligands with a wide variety of donor sets are now available with Figure 3.1 displaying a very small selection.¹

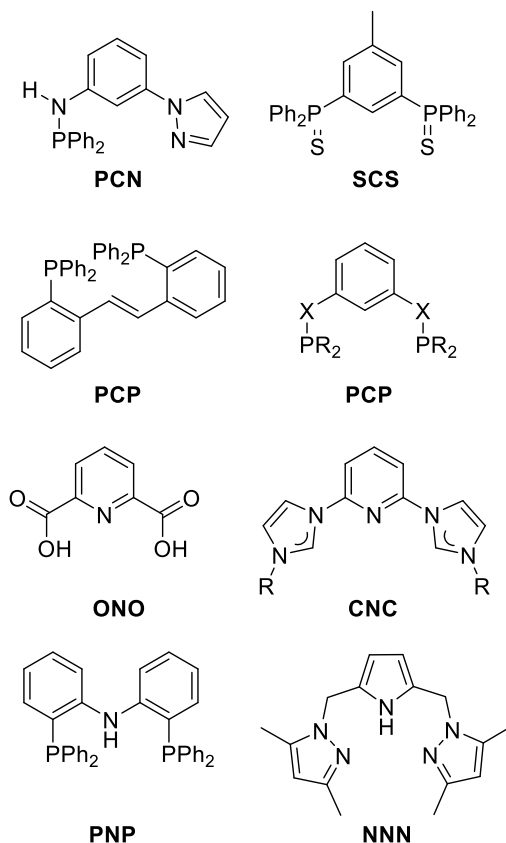
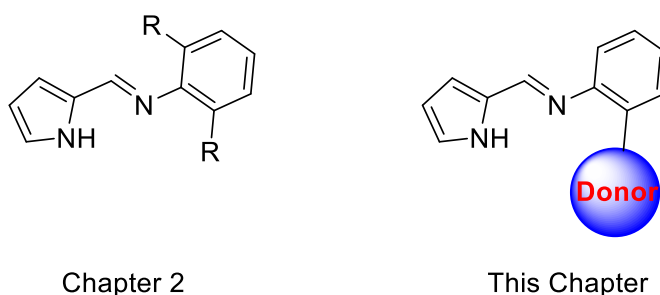


Figure 3.1: Examples of some different pincer ligands.¹

NNN and PNP donating pincer ligands based on a diaryl-amido backbone will be discussed in detail in the next chapter. Chapter two described the synthesis and reactivity of iridium carbonyl complexes containing an iminopyrrolyl ligand. By incorporating a donor at the two position of the aromatic substituent a terdentate pincer ligand can be accessed (Figure 3.2).



Chapter 2

This Chapter

Figure 3.2: Bidentate and terdentate iminopyrrolyl ligands.

This chapter introduces rhodium and iridium complexes that contain iminopyrrolyl pincer ligands with NNP, NNN and NNC donors (Figure 3.3).

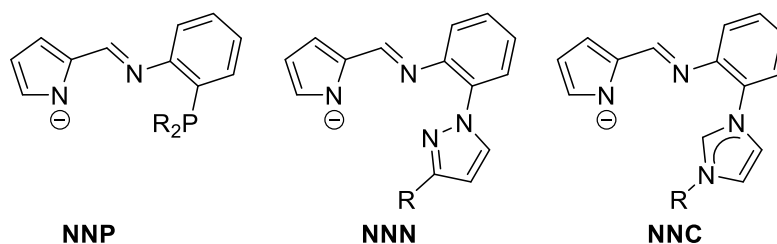


Figure 3.3: Iminopyrrolyl pincer ligands used in this study.

Paul et al.² described the synthesis of Ir(III) NNC iminopyrrolyl pincer complexes formed by N-H and C-H activation using an Ir(I) precursor. Hang et al.³ have reported the synthesis and characterisation of nickel and palladium (II) iminopyrrolyl NNP pincer complexes shown in Figure 3.4.

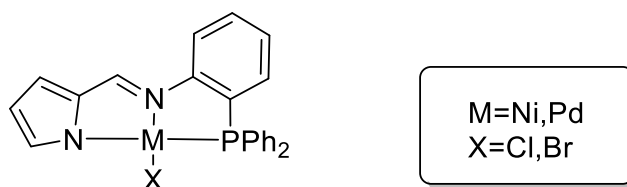


Figure 3.4: Group 10 Iminopyrrolyl pincer complexes.³

Yang et al.⁴ have recently described the synthesis and reactivity of mono and binuclear nickel (II) complexes containing iminopyrrolyl pincer ligands (Figure 3.5). These complexes were shown to be active in cross coupling reactions.

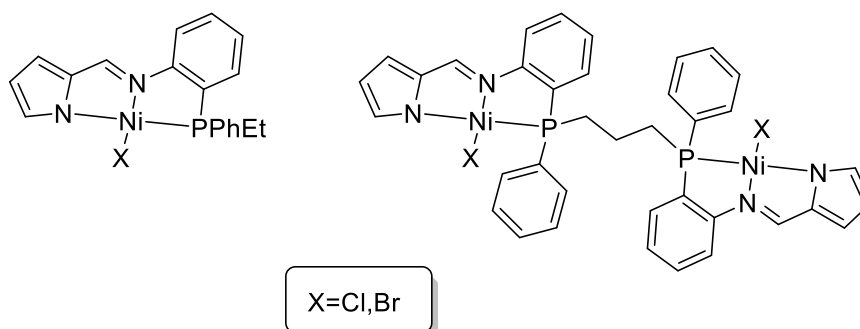


Figure 3.5: Mono and binuclear nickel iminopyrrolyl pincer complexes.⁴

Qiao et al.⁵ have also reported the synthesis and characterisation of aluminium and zinc complexes supported by iminopyrrolyl NNN pincer ligands, an example is displayed in Figure 3.6. The aluminium complexes were found to be active in the polymerisation of ϵ -caprolactone.

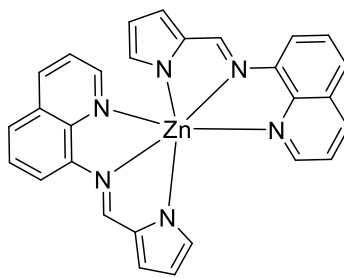


Figure 3.6: Zinc iminopyrrolyl pincer complex. ⁵

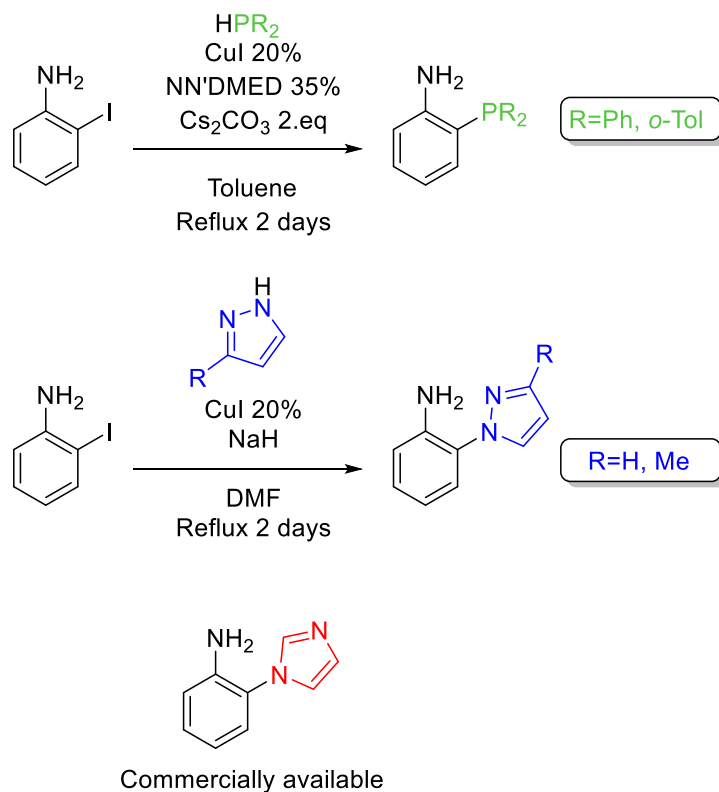
To our knowledge, currently there are no reported rhodium or iridium carbonyl complexes containing an iminopyrrolyl pincer ligand. This chapter will discuss the synthesis and reactivity of a number of such complexes where the donor is modified to change the electronic and steric environment of the metal centre.

3.1 Results and discussion

3.1.1 Pro-ligand synthesis

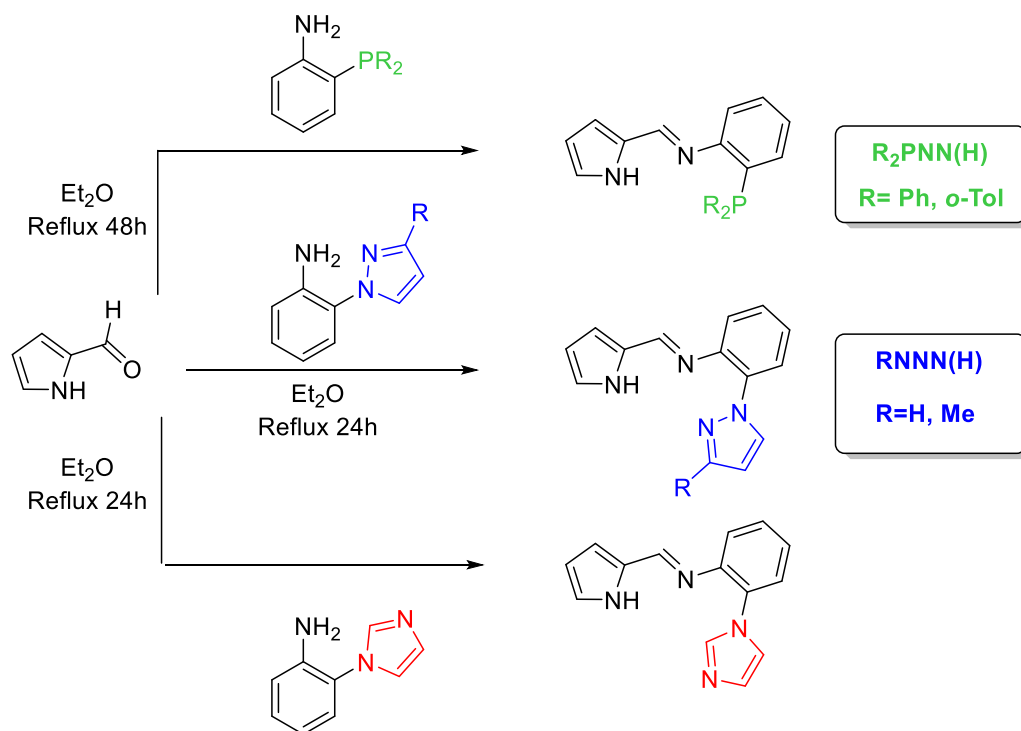
Synthesis of the iminopyrrole pro-ligands utilised a condensation reaction between 2-pyrrole carboxaldehyde and 2-substituted anilines.

The synthesis of the 2-substituted anilines (if not commercially available) utilises modified Ullmann coupling conditions similar to those reported by Wanniarachchi et al.⁶⁻⁹ as illustrated in Scheme 3.1.



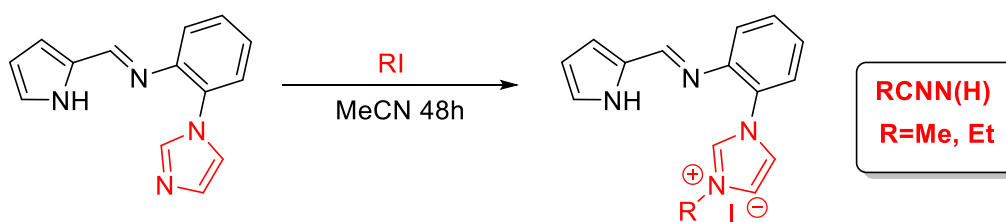
Scheme 3.1: Synthesis of 2-substituted anilines.

Three iminopyrrolyl pincer ligand variants were synthesised containing phosphine, pyrazole and imidazole donor arms, as shown in Scheme 3.2.



Scheme 3.2: Synthesis of iminopyrrolyl pincer ligands.

The imidazole pincer ligand precursor needs to be further functionalised with an alkyl halide to obtain the carbene pro-ligands (Scheme 3.3). This was performed using an excess of methyl or ethyl iodide in acetonitrile at room temperature.



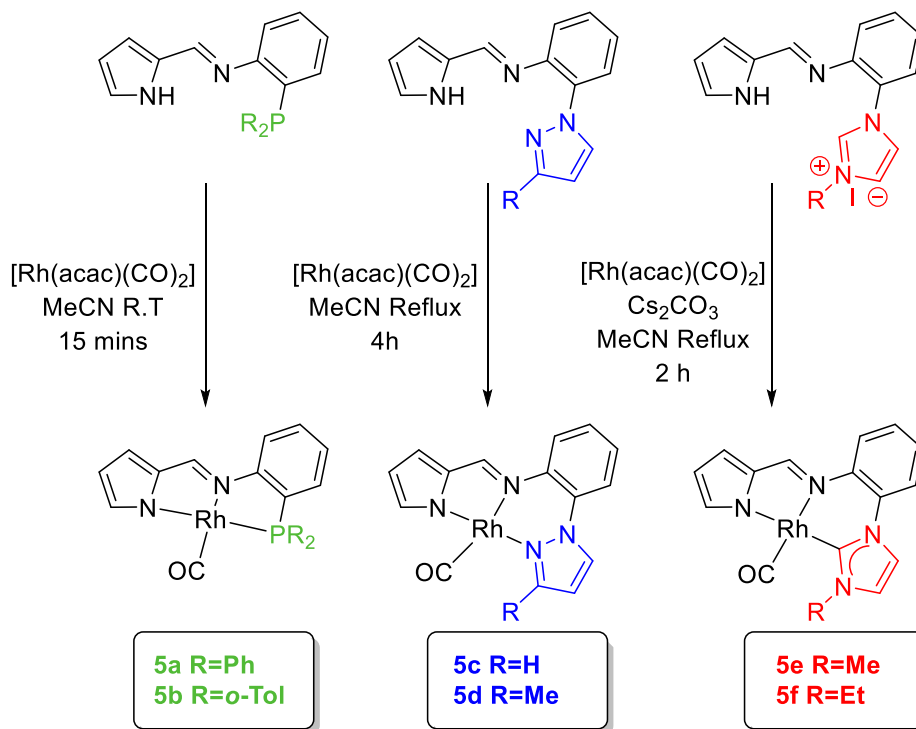
Scheme 3.3: Synthesis of imidazolium pro-ligand.

Each pro-ligand was characterised by NMR spectroscopy and mass spectrometry. A singlet is observed in the $^{31}\text{P}\{^1\text{H}\}$ NMR spectra of the $\text{R}_2\text{PNN(H)}$ pro-ligands appearing at δ -13.6 and δ -30.0 for the PPh_2 and $\text{P}(o\text{-Tol})_2$ products respectively.

The ^1H NMR spectra of the pro-ligands each display a broad peak between δ 9.0 and 11.5 for the N-H proton. A singlet is also observed corresponding to the imine proton between δ 8.0 and 8.3. The chemical shifts for ligand substituents appear in their expected regions, details of which can be found in the Experimental chapter.

3.1.2 Synthesis of Rh(I) iminopyrrole pincer complexes

The rhodium carbonyl complexes **5a-d** were synthesised by reacting equimolar amounts of pro-ligand and $[\text{Rh}(\text{acac})(\text{CO})_2]$ (Scheme 3.4). The synthesis of **5e** and **5f** requires an additional equivalent of base to deprotonate the imidazolium ring to generate the NHC donor.



Scheme 3.4: Synthesis of Rh(I) iminopyrrolyl phosphine complexes.

3.1.3 Infrared spectroscopic analysis

Complexes **5a-f** all display a single $\nu(\text{CO})$ band between 1950 to 1980 cm^{-1} as displayed in Table 3.1.

Complex	R	$\nu(\text{CO})/\text{cm}^{-1}$ (MeCN)	Yield %
5a	Ph	1977	72
5b	<i>o</i> -Tol	1973	81
5c	H	1967	74
5d	Me	1961	77
5e	Me	1955	69
5f	Et	1952	70

Table 3.1: Selected spectroscopic data for complexes **5a-f**

Figure 3.7 displays the $\nu(\text{CO})$ bands for **5a,c** and **5e** in MeCN. The large variation in the $\nu(\text{CO})$ value is due to the different electronic properties of the donor substituents. Phosphines are good π acceptors, accepting electron density from filled metal d-orbitals into the σ^* orbital of the phosphine, hence complexes **5a** and **5b** have the highest $\nu(\text{CO})$. Conversely **5e** and **5f** have the lowest $\nu(\text{CO})$ values because the carbene donors are excellent σ -donors but are poor π acceptors due to the p_π orbital of the carbon donor accepting electron density from the two adjacent nitrogen donors as shown in Figure 3.8.¹⁰

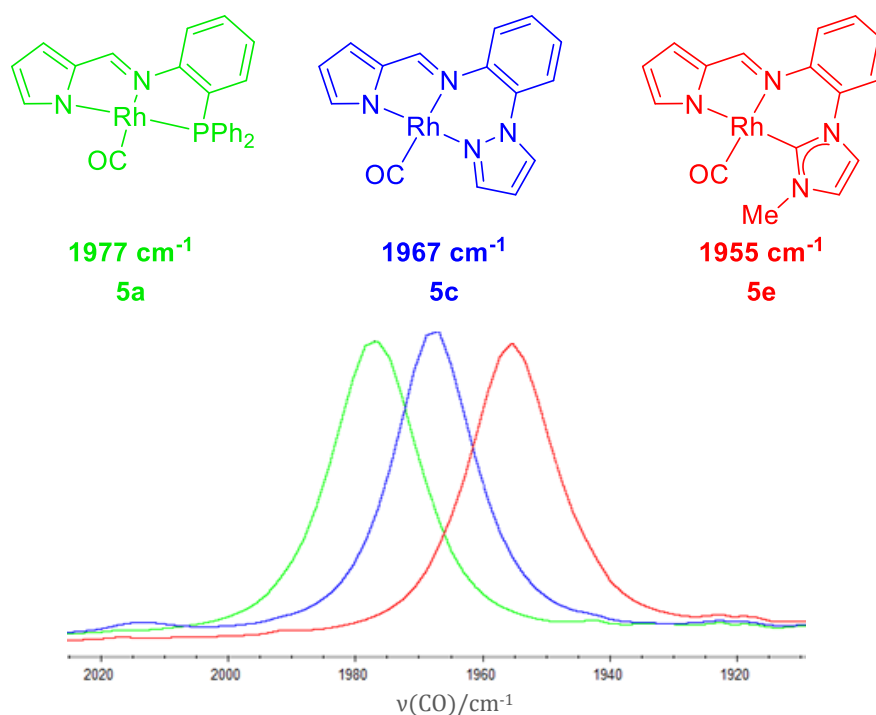


Figure 3.7: Overlaid IR spectra of complexes **5a**, **5c** and **5e** in MeCN.

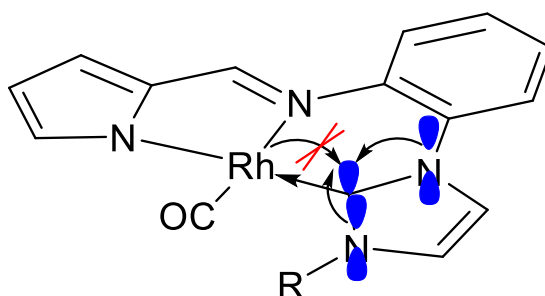


Figure 3.8: Schematic showing π interactions of the carbene ligand.

Figure 3.9 compares the $\nu(\text{CO})$ values for complexes **5a**, **5c** and **5e** with other reported Rh(I) pincer complexes. **5a-f** have $\nu(\text{CO})$ values similar to reported rhodium pincer complexes with PNP^{11,12}, PNN⁹ and NNN^{8,13} donor sets but higher than a rhodium complex with a CNC donor set.¹⁴

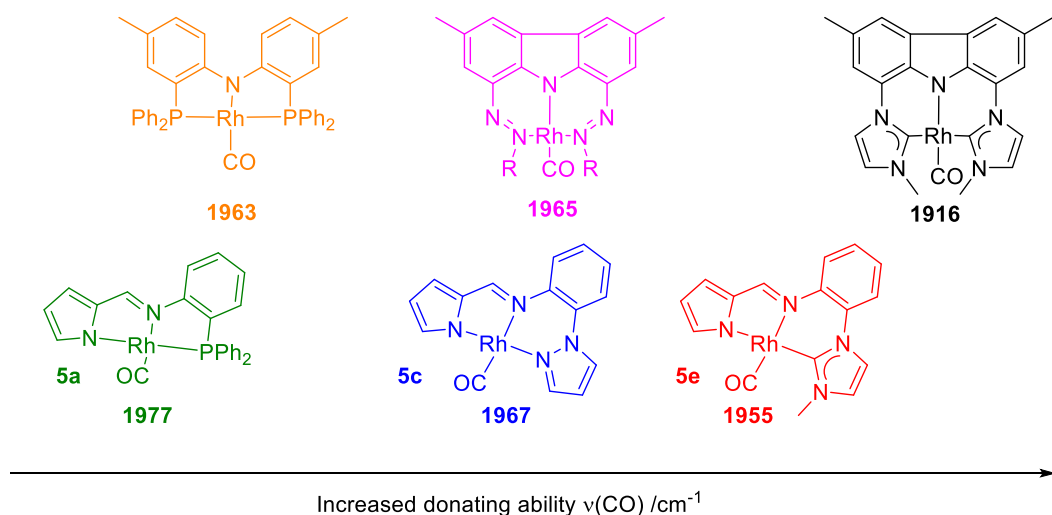


Figure 3.9: Comparison of $\nu(\text{CO})$ for some Rh(I) carbonyl complexes.

3.1.4 NMR analysis

Complexes **5a** and **5b** both display a doublet in their $^{31}\text{P}\{^1\text{H}\}$ NMR spectra with $J_{\text{Rh-P}}$ coupling, as displayed in Table 3.2.

Complex	$\delta^{31}\text{P}(J_{\text{Rh-P}})$
5a	δ 56.47 (d, 148 Hz)
5b	δ 40.67 (d, 148 Hz)

Table 3.2: $^{31}\text{P}\{^1\text{H}\}$ NMR data for complexes **5a** and **5b** (162 MHz CDCl_3).

Complexes **5a-f** all display a singlet in their ^1H NMR spectra at ca. δ 8.1-8.4 for the imine proton. Unlike the $[\text{Ir}(\text{Ar-NN})(\text{CO})\text{PR}_3]$ complexes discussed in chapter two, complexes **5a** and **5b** do not display $^4J_{\text{H-P}}$ coupling. This is because the pincer co-ordination geometry forces the phosphine ligand *cis* to the imine ligand. The pyrrole N-H resonance is no longer present in the ^1H NMR spectra of complexes **5a-f** and no imidazolium proton at the 2 position is observed for complexes **5e** and **5f** indicating complexation of the NHC ligands. Complex **5b** has two very broad resonances at δ 2.3-3.2 for the *o*-tolyl groups, suggesting restricted rotation around the P-aryl bond. The chemical shifts for the remaining protons of **5a-f** appear in the expected regions, as detailed in the Experimental chapter.

3.1.5 X-ray Crystallography

Single crystals of **5b** suitable for X-ray crystallography were obtained by slow evaporation of CH_2Cl_2 from a saturated solution of the complex. The structure is shown in Figure 3.10 and selected bond lengths and angles are given in Table 3.3.

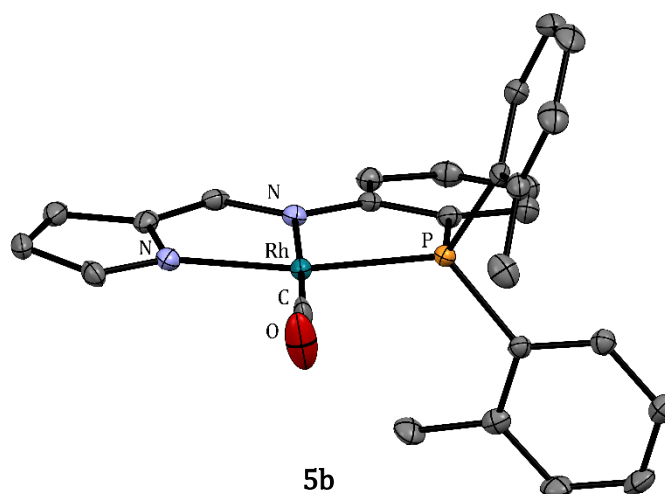


Figure 3.10: X-ray crystal structure of complex **5b** with thermal ellipsoids shown at 50% probability level. Hydrogen atoms are omitted for clarity.

Bonds	length (Å)	Angle	Degrees
Rh-CO	1.822(3)	N _{pyrrole} -Rh-P	162.58(8)
Rh-N _{pyrrole}	2.072(3)	CO-Rh-N _{Imine}	177.60(13)
Rh-N _{imine}	2.064(2)	CO-Rh-P	97.98(16)
Rh-P	2.2473	N _{imine} -Rh-P	83.84(11)
N=C	1.318(5)	N _{imine} -Rh-N _{pyrrole}	78.97(14)
N-Ar	1.419(5)		

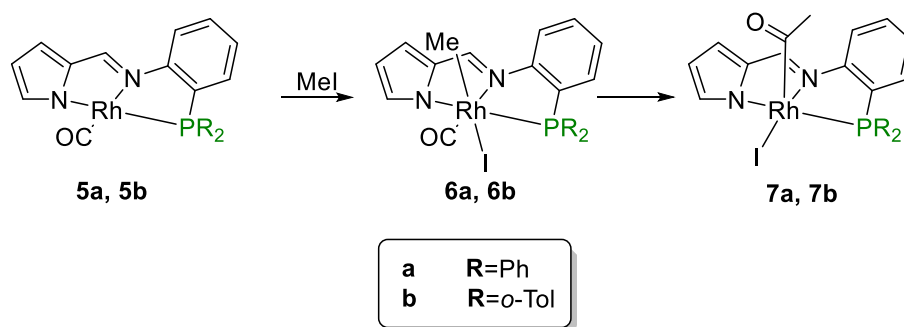
Table 3.3: Selected bond lengths (Å) and angles (deg) for complex **5b**.

The crystal structure of **5b** confirms that an approximate square planar geometry is adopted by the rhodium centre with the pyrrole and phosphine donors co-ordinated *trans* to one another. The P-Rh-N_{pyrrole} pincer bite angle is 162°. This is smaller than other corresponding angles reported for iminopyrrolyl pincer complexes which were found to be 170° and 169° for Ni(II) complexes (Figure 3.4) and 165° for a Pd(II) complex (Figure 3.5).

3.1.6 Reactivity of Rh(I) iminopyrrolyl pincer complexes with MeI

Complexes **5a-f** all react rapidly with MeI in CH₂Cl₂, the outcome of the reaction depending upon the nature of the donor ligand.

The reactions of complexes **5a** and **5b** with MeI were initially followed by IR spectroscopy. The growth of a $\nu(\text{CO})$ band at a higher frequency was observed in each case, indicative of oxidative addition of MeI to give a Rh(III) methyl product $[\text{Rh}(\text{R}_2\text{PNN})(\text{CO})\text{Me}(\text{I})]$ **6a** and **6b**. This is followed by slow growth of a $\nu(\text{CO})$ band at 1720 cm^{-1} consistent with the formation of Rh(III) acetyl species **7a** and **7b** formed by migratory insertion (Scheme 3.5). A series of spectra recorded for the reaction of **5b** with MeI is displayed in Figure 3.11.



Scheme 3.5: Oxidative addition of MeI to **5a** and **5b** and subsequent migratory insertion.

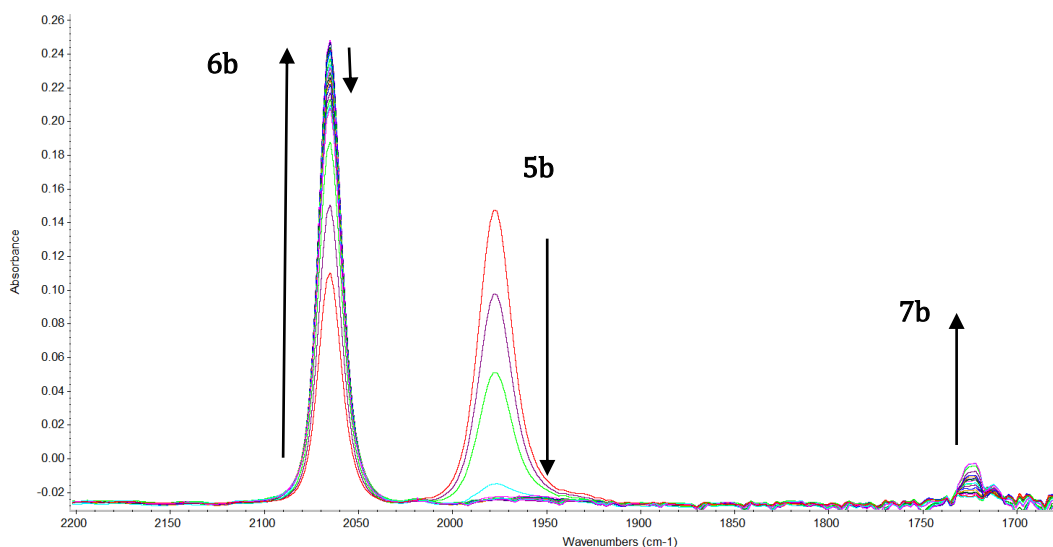


Figure 3.11: Series of IR spectra during the reaction of **5b** with MeI (0.04 M in CH_2Cl_2 at 23°C)

The oxidative addition reactions of **5a** and **5b** were also monitored by $^{31}\text{P}\{^1\text{H}\}$ and ^1H NMR spectroscopy. Figure 3.12 shows spectra for the reaction of **5a** with MeI over a period of 8 days. The oxidative addition reaction was too fast to observe the disappearance of the starting Rh(I) complex **5a** however the presence of new doublet in the $^{31}\text{P}\{^1\text{H}\}$ NMR for the Rh(III) methyl complex **6a** was observed at δ 50.1 (107 Hz).

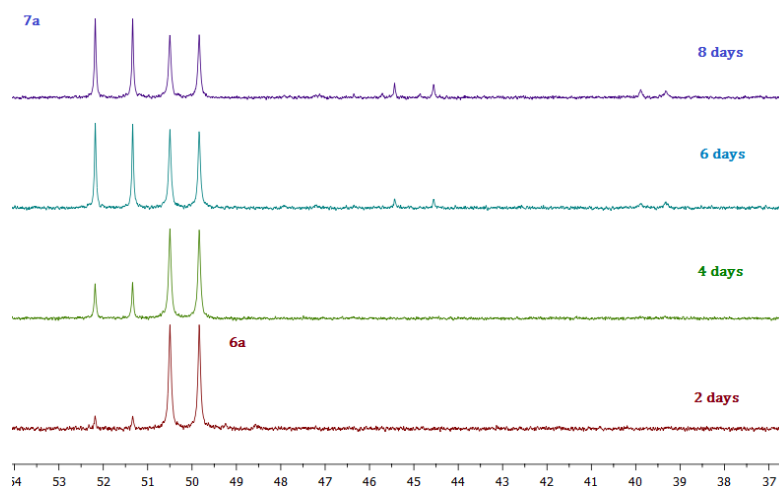


Figure 3.12: Series of spectra obtained after reacting **5a** with MeI (excess) over 8 days in CDCl_3 .

Over time the doublet at δ 50.1 decays and a doublet at δ 51.5 attributed to a Rh(III) acetyl **7a** formed by migratory insertion grows in intensity. This is accompanied by the growth of other minor doublets at δ 45.0 (142Hz) and δ 39.6 (90.4 Hz). A selected region of the ^1H NMR spectrum for the same reaction obtained after 8 days is displayed in Figure 3.13. A doublet of doublets at δ 0.49 and a singlet at δ 2.65 are assigned to methyl and acetyl products **6a** and **7a** respectively. The presence of additional minor Rh(III) methyl and acetyl species is indicated by the other weak signals apparent in Figure 3.13, these species have not been identified. After 8 days the methyl and acetyl species **6a** and **7a** appear to have reached equilibrium.

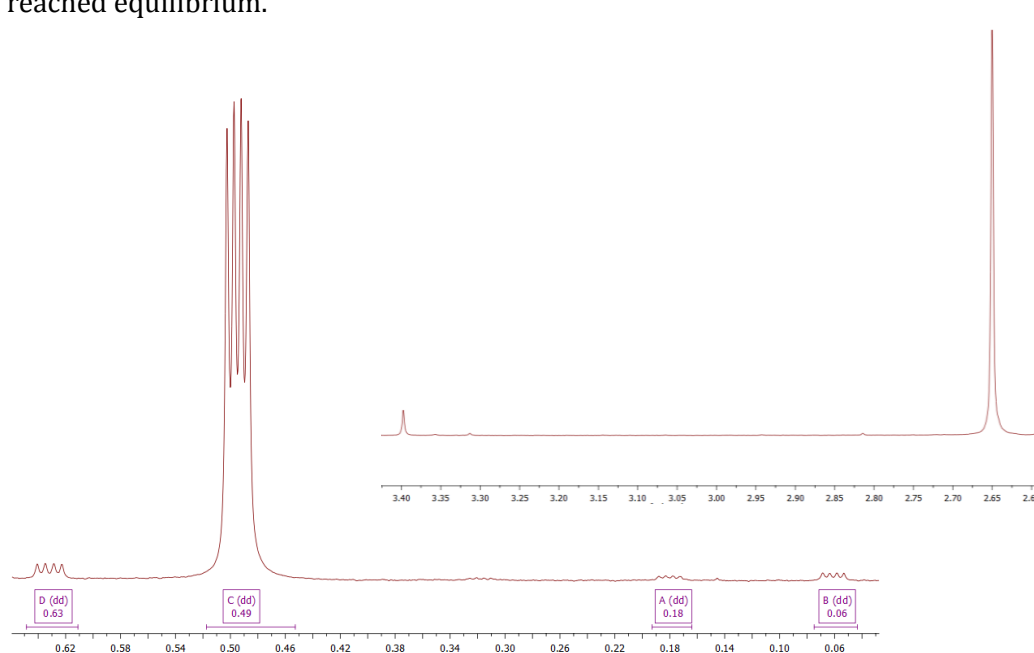


Figure 3.13: Selected region of the ^1H NMR spectrum obtained after reacting **5a** with MeI (excess) over 8 days in CDCl_3 .

The oxidative addition of MeI to **5b** was also monitored by $^{31}\text{P}\{^1\text{H}\}$ and ^1H NMR spectroscopy. The oxidative addition reaction was too fast to observe the disappearance of the starting Rh(I) complex however the presence of a new doublet at δ 49.5 (109 Hz) was observed for the Rh(III) methyl complex **6b**. This slowly decays and a doublet at δ 46.0 (146 Hz) corresponding to the Rh(III) acyl product **7b** grows in intensity (Figure 3.14).

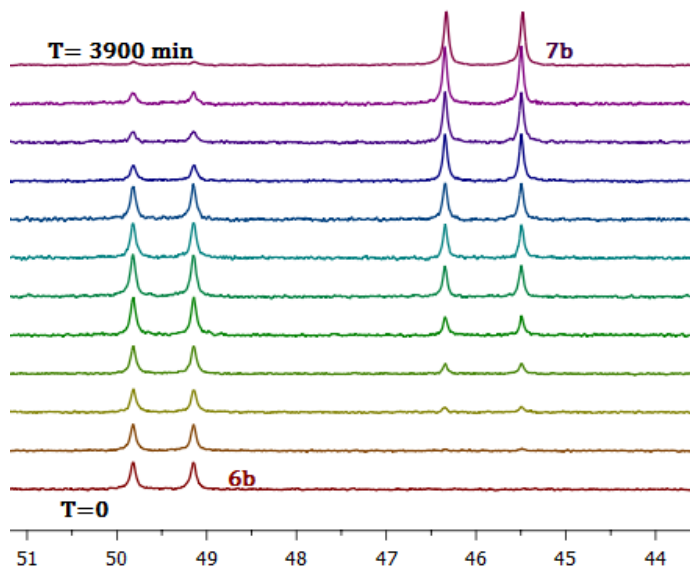


Figure 3.14: Overlaid $^{31}\text{P}\{^1\text{H}\}$ NMR spectra of **6b** undergoing migratory insertion over 3900 min at room temp in CDCl_3 .

A plot of % integrated intensity of the ^{31}P NMR doublet of **6b** vs time (Figure 3.15) gives the observed rate constant for migratory insertion (k_{obs}), which is 0.0013 min^{-1} at room temperature in CDCl_3 equating to a $t_{1/2}$ of 520 minutes.

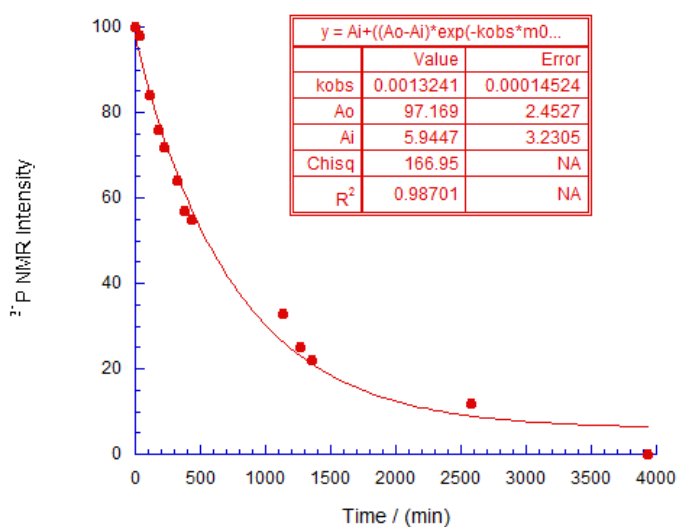


Figure 3.15: Plot of % $^{31}\text{P}\{^1\text{H}\}$ NMR intensity of **6b** Vs time.

Table 3.4 displays all the $^{31}\text{P}\{^1\text{H}\}$ NMR data and $\nu(\text{CO})$ values of the products obtained after reactions of **5a** and **5b** with MeI.

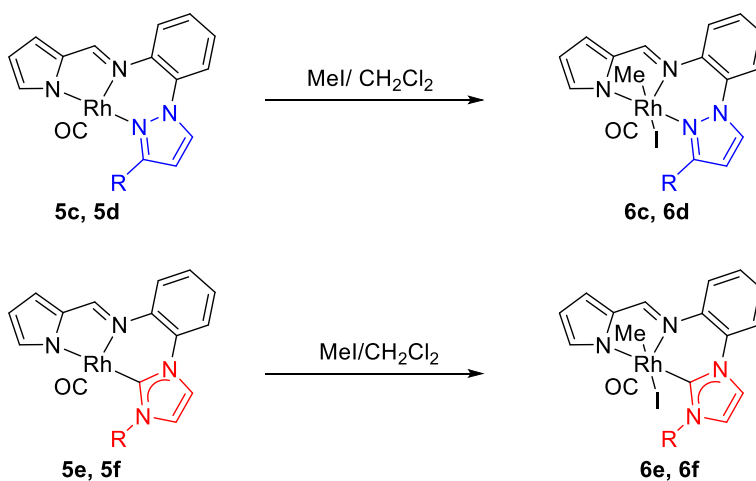
Reactant	$\delta^{31}\text{P Rh(III)Me}$ ($J_{\text{Rh-P}}$)	$\nu(\text{CO})/\text{cm}^{-1}$	$\delta^{31}\text{P Rh(III)acyl}$ ($J_{\text{Rh-P}}$)	$\nu(\text{CO})/\text{cm}^{-1}$
5a	50.17 (107Hz)	2066 (6a)	51.76 (136 Hz)	1725 (7a)
	48.90 (109 Hz)*		45.0 (142 Hz)*	
	39.6 (90.4 Hz)*			
5b	49.5 (109 Hz)	2065 (6b)	46.0 (138 Hz)	1724 (7b)

Table 3.4: $^{31}\text{P}\{^1\text{H}\}$ NMR chemical shifts and $\nu(\text{CO})$ values obtained after reaction of **5a** and **5b** with MeI (* denotes minor species).

In summary, complexes **5a** and **5b** both react rapidly with MeI to form Rh(III) methyl species **6a** and **6b**. Complex **6a** undergoes slow migratory insertion reaching equilibrium with a Rh(III) acetyl complex **7a**. Complex **6b** undergoes a faster migratory insertion than **6a** to form a single acetyl product **7b**. The rate increase for migratory insertion of complex **6b** is facilitated by the additional steric bulk of the *o*-Tol substituents on the phosphine. Similar observations have been made for related systems.¹⁵⁻¹⁹

3.1.7 Reactivity of complexes **5c-f** with MeI

Complexes **5c-f** react rapidly with iodomethane in CH_2Cl_2 to form Rh(III) methyl species **6c-6f** with a red to yellow colour change observed in solution (Scheme 3.6). The reactions result in a shift of $\nu(\text{CO})$ approximately $70\text{-}80\text{ cm}^{-1}$ to a higher wavenumber indicative of an oxidative addition of MeI. Selected spectroscopic data for complexes **6c-f** are displayed in Table 6.



Scheme 3.6: Oxidative addition of MeI to complex **5c-f**.

In contrast to the reactions of **5a** and **5b** there is no spectroscopic evidence for migratory insertion to give Rh(III) acetyl species. Complexes **6c-f** were isolated as solids and characterised by ^1H and ^{13}C NMR spectroscopy, IR spectroscopy and mass spectrometry. Selected spectroscopic data for **6c-f** are displayed in Table 3.5.

Complex	R	$\nu(\text{CO})/\text{cm}^{-1}$ (CH_2Cl_2)	Yield %	$\delta^1\text{H}$ Rh- CH_3 ($J_{\text{H-Rh}}$)
6c	H	2075	72	1.19 (d, $J = 1.9$ Hz)
6d	Me	2073	78	1.14 (d, $J = 1.9$ Hz)
6e	Me	2057	77	0.95 (d, $J = 2.1$ Hz)
6f	Et	2055, 2079	82	0.93 (d, $J = 2.1$ Hz)

Table 3.5: Selected spectroscopic data for complexes **6c-f**.

Complexes **6c-f** each display a doublet in their ^1H NMR spectra for the methyl ligand. Both the chemical shifts and coupling constants of methyl ligand are comparable to similar Rh(III) methyl complexes.^{8,13,14}

Over time in solution **6c** decomposes slightly to unidentifiable insoluble products. A similar observation was observed by Wanniarachchi et al.⁸ for related Rh(III) pincer complexes. Over time the growth of a second $\nu(\text{CO})$ band 20 cm^{-1} to a higher frequency is observed for **6f**, attributed to an isomeric Rh(III)-methyl product.

3.1.8 X-ray crystallography

Single crystals of **6d** and **6e** suitable for single crystal X-ray crystallography were obtained by slow vapour diffusion of hexanes into concentrated CH_2Cl_2 solutions. The structures are shown in Figure 3.16 and Figure 3.17 and selected bond lengths and angles are given in Tables 3.6 and 3.7.

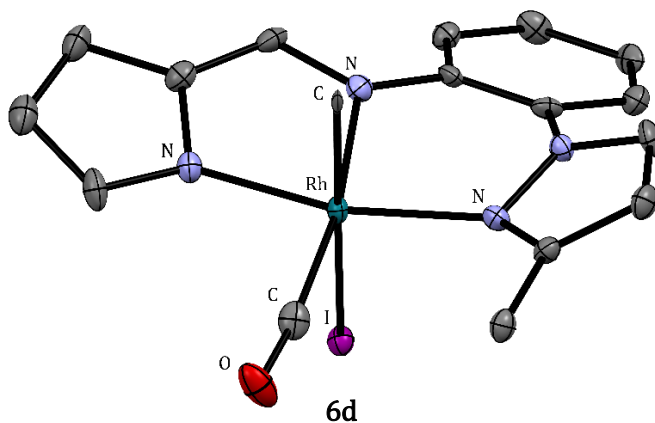


Figure 3.16: X-ray crystal structure of complex **6d** with thermal ellipsoids shown at 50% probability level. Hydrogen atoms are omitted for clarity.

Bond	length (Å)	Angle	Degrees
Rh-CO	1.873(4)	N _{pyrrole} -Rh-N _{Pyrazole}	167.1(1)
Rh-N _{pyrrole}	2.004(3)	N _{imine} -Rh-CO	170.0(2)
Rh-N _{imine}	2.059(3)	CH ₃ -Rh-I	177.0(1)
Rh-N _{Pyrazole}	2.074(3)	N _{imine} -Rh-N _{pyrrole}	91.0(1)
Rh-CH ₃	2.163(5)	N _{pyrrole} -Rh-N _{imine}	80.2(1)
Rh-I	2.8096(9)		

Table 3.6: Selected bond lengths (Å) and angles (deg) for complex **6d**.

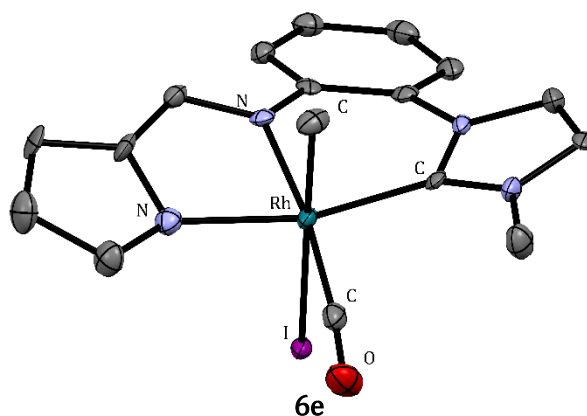


Figure 3.17: X-ray crystal structure of complex **6e** with thermal ellipsoids shown at 50% probability level. Hydrogen atoms and CH₂Cl₂ solvent molecule are omitted for clarity.

Bond	length (Å)	Angle	Degrees
Rh-CO	1.883(9)	N _{pyrrole} -Rh-C _{imidazole}	165.3(3)
Rh-N _{pyrrole}	2.075(6)	N _{imine} -Rh-CO	173.0(3)
Rh-N _{imine}	2.068(7)	CH ₃ -Rh-I	179.4(2)
Rh-C _{imidazole}	1.998(7)	N _{imine} -Rh-C _{imidazole}	88.9(3)
Rh-CH ₃	2.095(7)	N _{pyrrole} -Rh-N _{imine}	80.1(3)
Rh-I	2.8164(7)		

Table 3.7: Selected bond angles (deg) and lengths (Å) for complex **6e**

A distorted octahedral geometry is adopted by the rhodium centre in both **6d** and **6e** with the methyl and iodide ligands being mutually *trans*. The CH₃-Rh-I bond angles are 177° and 179° respectively, approaching linearity for **6e**. The N_{pyrrole}-Rh-Donor bite angles are 167° and 165° respectively, the bite angle being slightly smaller in **6e** than in **6d** due to the change from nitrogen to a carbon donor.

3.1.9 MeI oxidative addition kinetics

Kinetic experiments were carried out using at least a tenfold excess of MeI to ensure pseudo first order conditions. Since complexes **5a-f** display high reactivity toward MeI UV-vis spectroscopy was used.

A series of difference spectra were taken in order to obtain a wavelength suitable to monitor in the kinetic assessment. An example set of difference spectra for the reaction of complex **5d** with MeI is displayed in Figure 3.18. The five isosbestic points indicate a clean transformation is occurring with no side reactions. Wavelengths with a negative absorbance are associated with the decay of the Rh(I) complex **5d**, whilst those with a positive absorbance are associated with the Rh(III) methyl product **6d**.

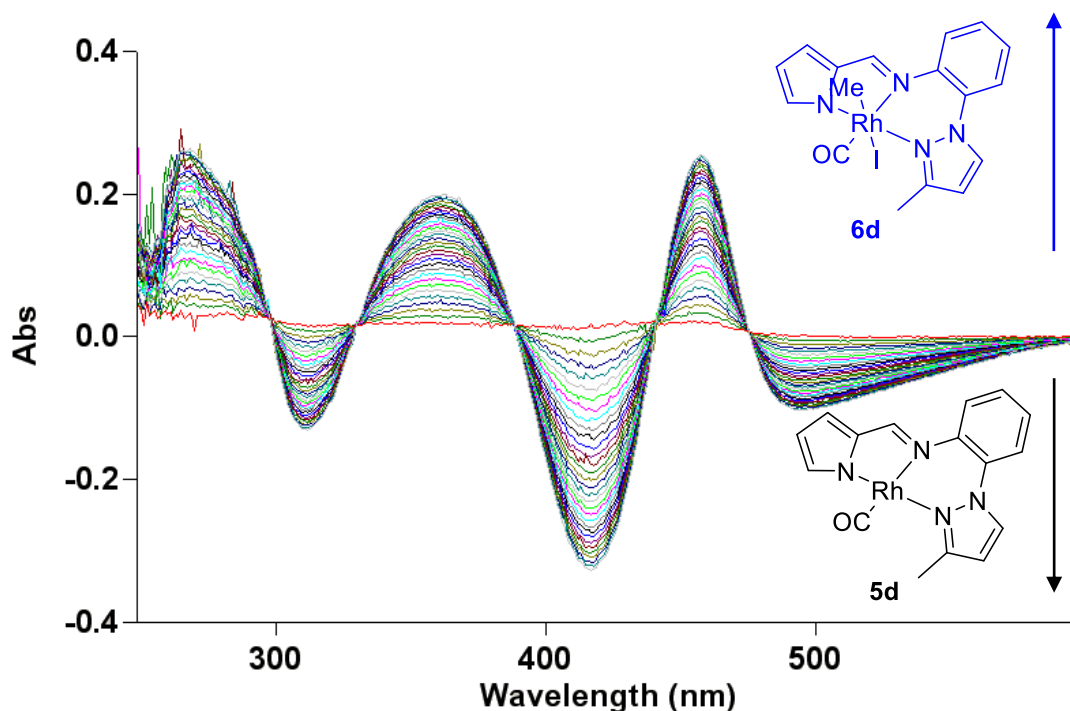


Figure 3.18: Series of UV-vis difference spectra for the reaction of **5d** with MeI (0.0032 M in CH₂Cl₂ at 23°C).

The decay of the identified UV-vis absorption was analysed to obtain a k_{obs} value for each experiment. Plots of absorbance vs. time are well fitted to an exponential decay curve (an example for complex **5d** is shown in Figure 3.19, indicating that the reactions are first order in Rh(I) complex.

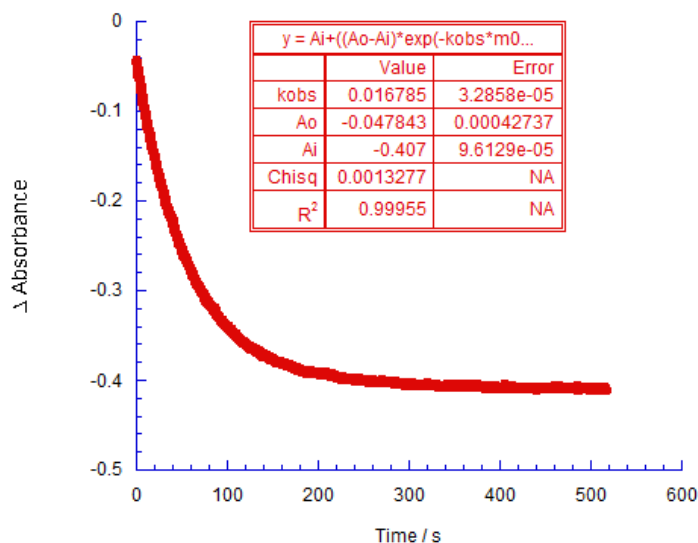


Figure 3.19: Kinetic profile for **5d** reacting with MeI at 0.0064 M MeI in CH_2Cl_2 at 23°C (423nm).

Plots of k_{obs} vs. $[\text{MeI}]$ are linear (Figure 3.20) indicating that the reactions are first order in $[\text{MeI}]$ and therefore second order overall. From the gradient of these plots values for second order rate constants (k_2) can be obtained which are displayed in Table 3.8.

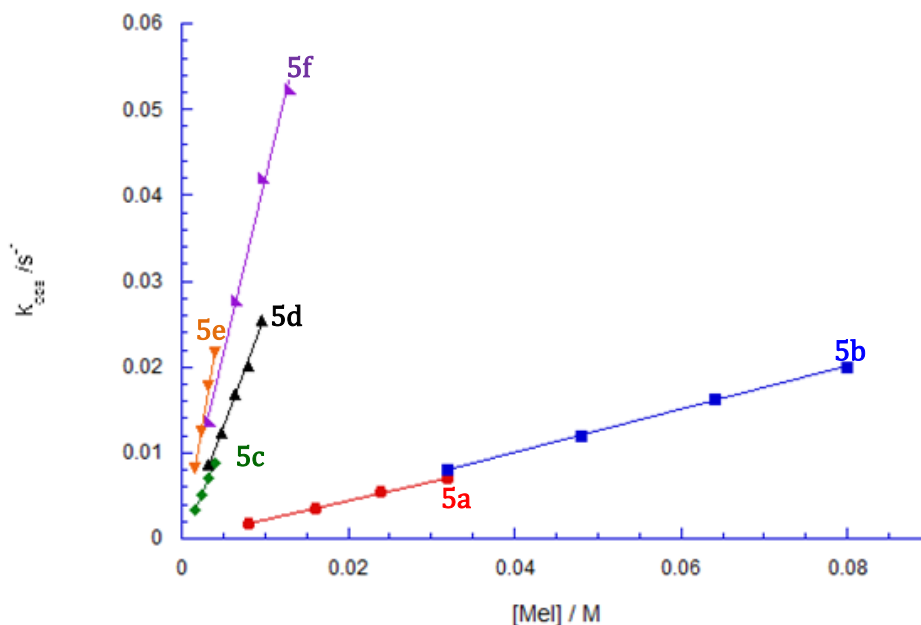


Figure 3.20: Plot of k_{obs} Vs $[\text{MeI}]$ for complexes **5a-f** at 23°C in CH_2Cl_2 .

Complex	$\nu(\text{CO})/\text{cm}^{-1}(\text{MeCN})$	$k_2/\text{mol}^{-1}\text{dm}^3\text{s}^{-1}$
5a	1977	0.22
5b	1973	0.25
5c	1967	2.31
5d	1961	2.59
5e	1955	5.66
5f	1952	4.07

Table 3.8: Second order rate constants (k_2) for oxidative addition of MeI to complexes **5a-f** in CH_2Cl_2 at 23°C .

The observed reactivity towards iodomethane varies over an order of magnitude dependent upon the donor arm of the pincer ligand. Complexes **5a** and **5b** are the least reactive, with **5b** having a slightly higher k_2 value than **5a** despite having bulkier phosphine substituents.

Figure 3.21 compares the reactivity of **5a** with some Rh(I) carbonyl complexes reported by Wells.¹¹ **5a** is ca 2 times more reactive toward MeI than $[\text{Rh}(\text{CO})(\text{Ph-PNP})]$ but approximately half as reactive as $[\text{Rh}(\text{CO})(i\text{Pr-PCP})]$ and $[\text{Rh}(\text{CO})(\text{Cyp-anthraphos})]$.¹¹

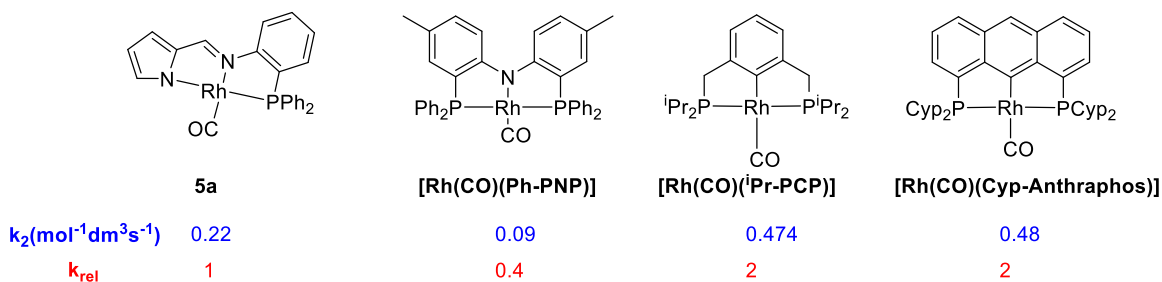


Figure 3.21: Comparison of reactivity of **5a** toward MeI with some rhodium pincer complexes.¹¹

The NNN pincer complexes **5c,d** are an order of magnitude more reactive toward MeI than the NNP pincer complexes **5a,b**. The increase in reactivity is due to a combination of steric and electronic factors; the pyrazole donor ligands are better donors (observed in the $\nu(\text{CO})$) and are also less sterically demanding.

Figure 3.22 compares the second order rate constants (k_2) obtained for **5d** with a related [Rh(CO)bis(imino)carbazolide] complex reported by Gaunt et al.¹³ Complex **5d** has similar reactivity, being only slightly more reactive toward MeI.

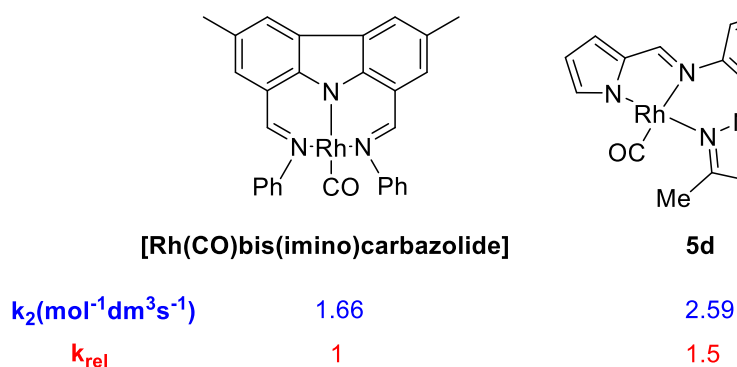
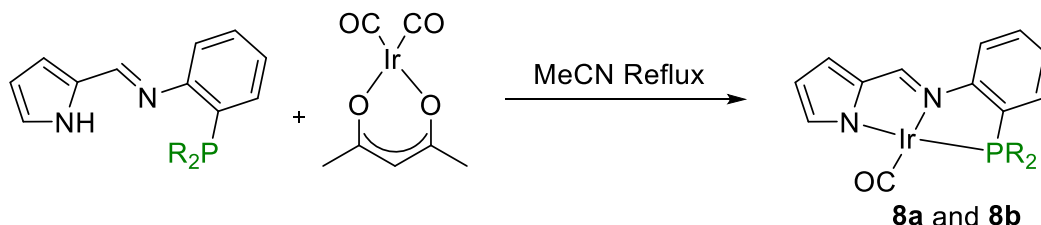


Figure 3.22: Comparison of reactivity of **5d** toward MeI with [Rh(CO)bis(imino)carbazolide].¹³

The NNC pincer complexes **5e,f** display the highest reactivity toward MeI, being approximately 20 times more reactive than the NNP complexes and twice more reactive than the NNN complexes. The increase in rate compared to the NNN pincer complexes is an electronic effect as the carbene ligands are better donor ligands than the pyrazole ligands (as shown by the lower $\nu(\text{CO})$) and are sterically very similar.

3.2 Synthesis and characterisation of iridium(I) PR_2NN pincer complexes

Iridium PR_2NN pincer complexes **8a** and **8b** were synthesised by reaction of equimolar amounts of $[\text{Ir}(\text{acac})(\text{CO})_2]$ and $\text{PR}_2\text{NN}(\text{H})$ pro ligand (Scheme 3.7) and were isolated as red microcrystalline powders. Selected characterisation data for complexes **8a** and **8b** are displayed in Table 3.9.



Scheme 3.7: Synthesis of complexes **8a** and **8b**

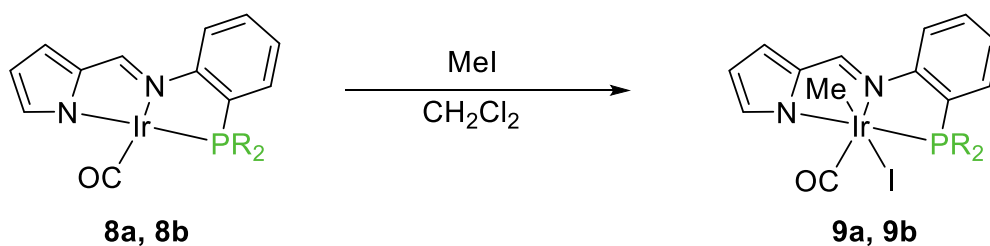
Complex	R	$\nu(\text{CO})/\text{cm}^{-1}$ (MeCN)	$\delta^{31\text{P}}$	Yield %
8a	Ph	1962	31.2	72
8b	<i>o</i> -Tol	1961	17.4	79

Table 3.9: Selected characterisation data for complexes **8a** and **8b**.

The $\nu(\text{CO})$ absorptions are shifted by approximately 10 cm^{-1} compared to the rhodium analogues **5a** and **5b**, indicating stronger back donation from iridium. Both **8a** and **8b** display a singlet in the $^{31\text{P}}\{^1\text{H}\}$ NMR spectrum in the expected region.

3.2.1 Reactivity of complexes **8a** and **8b** with MeI

Complexes **8a** and **8b** both react rapidly with MeI in CH_2Cl_2 yielding Ir(III) methyl species **9a** and **9b** (Scheme 3.8). Reaction with MeI results in a shift of the $\nu(\text{CO})$ by approximately 80 cm^{-1} to a higher frequency indicative of oxidative addition. No spectroscopic evidence for formation of Ir(III) acetyl species was observed. Selected spectroscopic data for complexes **9a** and **9b** are displayed in Table 3.10.



Scheme 3.8: Oxidative addition of MeI to complexes **8a** and **8b**.

Complex	R	$\nu(\text{CO})/\text{cm}^{-1}$ (CH_2Cl_2)	$\delta^{31\text{P}}$	Yield %
9a	Ph	2038	11.4	81
9b	<i>o</i> -Tol	2038	13.4	72

Table 3.10: Selected characterisation data for complexes **9a** and **9b**

The $^{31\text{P}}\{^1\text{H}\}$ NMR spectra of complexes **9a** and **9b** both display a single resonance indicative of a single product. The ^1H NMR spectra display an Ir-methyl resonance at δ 0.26 and δ 0.15 respectively. Coupling to $^{31\text{P}}$ is observed in **9a** with a $J_{\text{H-P}}$ coupling constant of 4 Hz, however this coupling is not resolved for **9b** which gives a broad peak.

3.2.2 X-ray crystallography

Single crystals of **9a** and **9b** suitable for single crystal X-ray crystallography were obtained by slow evaporation of CH_2Cl_2 from saturated solutions of the complexes. The structures of **9a** and **9b** are displayed in Figures 3.23 and 3.24 and selected bond lengths and angles are given in Table 3.11.

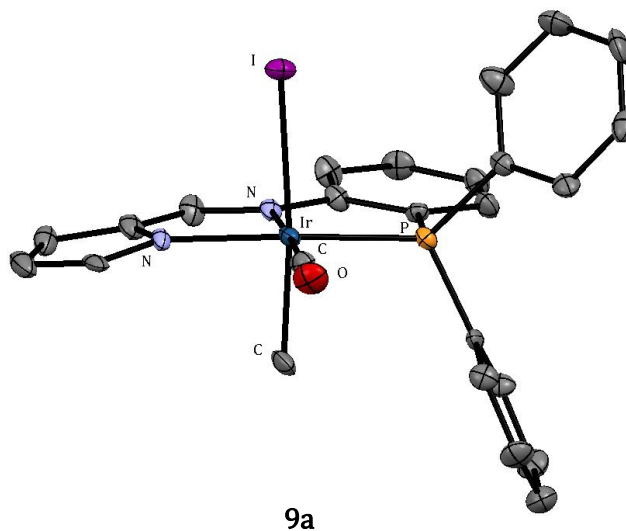


Figure 3.23: X-ray crystal structure of complex **9a** with thermal ellipsoids shown at 50% probability level. Hydrogen atoms are omitted for clarity.

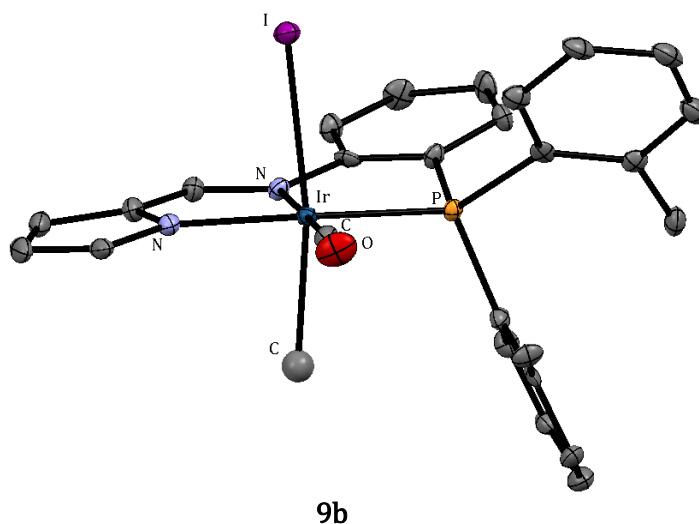


Figure 3.24: X-ray crystal structure of complex **9b** with thermal ellipsoids shown at 50% probability level. Hydrogen atoms are omitted for clarity.

	9a	9b
Ir-CO	1.86(1)	1.854(6)
Ir-N _{imine}	2.064(8)	2.078(5)
Ir-N _{pyrrole}	2.070(6)	2.074(5)
Ir-P	2.282(2)	2.313(2)
Ir-CH ₃	2.108(5)	2.284(8)
Ir-I	2.7758(4)	2.7827(5)
OC-Ir-N _{imine}	177.8(3)	177.0(2)
P-Ir-N _{pyrrole}	161.0(2)	161.0(1)
CH ₃ -Ir-I	174.2(2)	170.3(2)

Table 3.11: Selected bond lengths (Å) and bond angles (deg) for complexes **9a** and **9b**

The crystal structures of both **9a** and **9b** show that a distorted octahedral geometry is adopted by the iridium centre with the methyl ligand *trans* to the iodide ligand. The Ir-P bond length in complex **9b** is longer than in complex **9a** presumably due to the additional steric bulk preventing the phosphorus ligand getting as close to the iridium centre. The CH₃-Ir-I bond angle in **9b** deviates more from linearity than in **9a**, again because of the added steric bulk of the *o*-tolyl substituted phosphine ligand.

3.2.3 MeI oxidative addition kinetics

The reactivity of complexes **8a** and **8b** was also quantified using UV-vis kinetics. A series of difference spectra was taken in order to obtain a wavelength suitable to measure in the kinetic assessment. An example set of difference spectra for the reaction of complex **8a** with MeI is displayed in Figure 3.25.

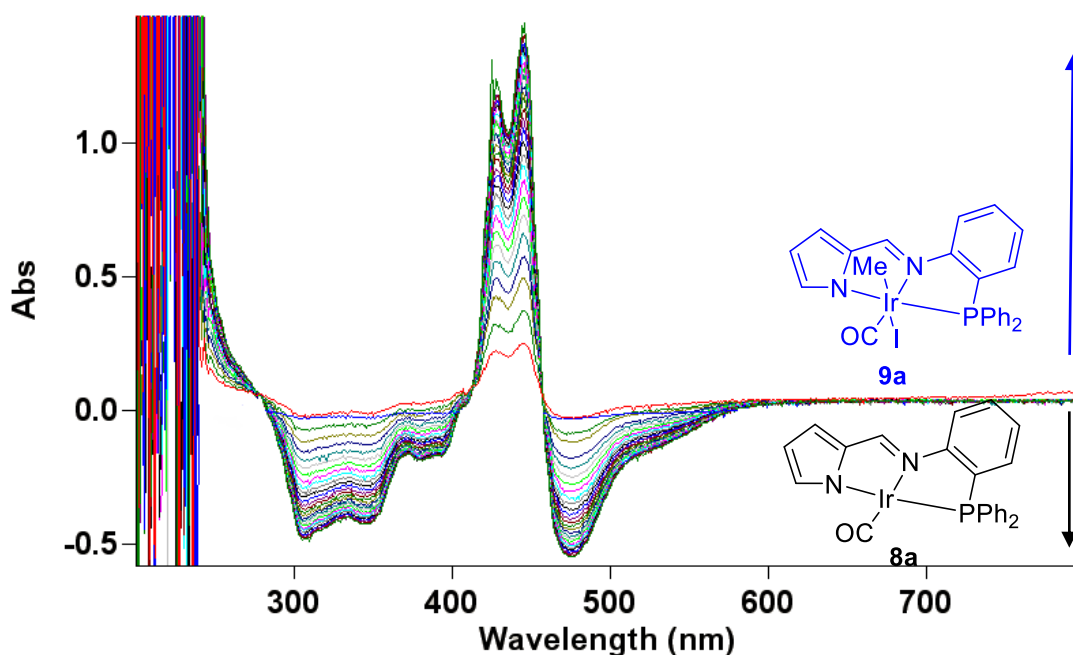


Figure 3.25: Series of UV-vis difference spectra for the reaction of **8a** with MeI (0.00064 M in CH_2Cl_2 at 23°C).

The decays in absorbance at 475nm for **8a** and 480 nm for **8b** were analysed to obtain k_{obs} values. Plots of absorbance vs. time were well fitted to an exponential decay curve, indicating that the reactions are first order in Ir(I) complex.

Plots of k_{obs} vs. [MeI] are linear indicating that the reactions are first order in [MeI] and therefore second order overall. From the gradient of the plots displayed in Figure 3.26 values for the second order rate constants (k_2) for complexes **8a** and **8b** are displayed in Table 3.12.

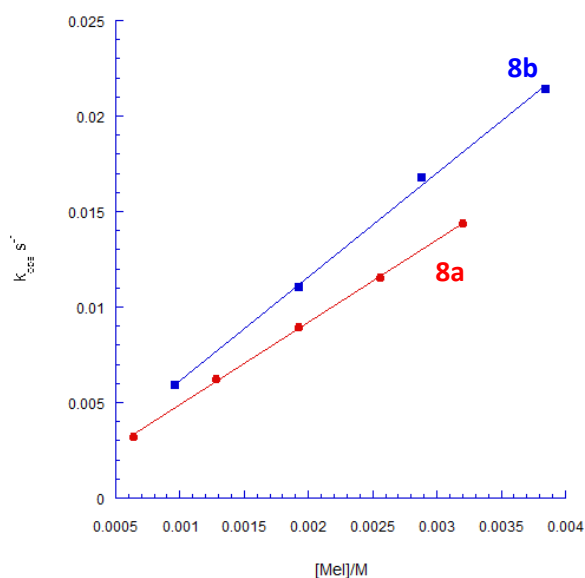


Figure 3.26: Plot of k_{obs} Vs [MeI] for complexes **8a** and **8b** at 23°C in CH_2Cl_2 .

Complex	$k_2 / \text{mol}^{-1} \text{dm}^3 \text{s}^{-1}$
8a	4.31
8b	5.44

Table 3.12: Second order rate constants (k_2) for oxidative addition of MeI to complexes **8a** and **8b** at 23°C in CH_2Cl_2 .

The iridium complexes **8a** and **8b** are approximately 20 times more reactive toward MeI than their rhodium analogues **5a** and **5b**. This is comparable to observations made by Gonsalvi et al.²⁰ when comparing reactivity of some rhodium and iridium complexes containing bidentate P,P or P,S donor ligands.

Figure 3.27 compares the reactivity of the **8a** with that of an iridium iminopyrrolyl phosphine complex **3a** reported in chapter two. Complexes **3a** and **8a** contain the same donor sets, however it is noteworthy the pincer complex **8a** is seven times more reactive toward MeI than **3a**.

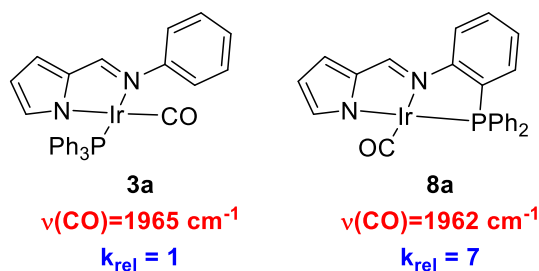


Figure 3.27: Comparison of reactivity of complexes **8a** and **3a** toward MeI.

3.3 Summary

A series of rhodium and iridium carbonyl complexes containing iminopyrrolyl pincer ligands has been synthesised. These complexes have been fully characterised by IR, NMR, mass spectroscopy, and in some cases X-ray crystallography.

Rhodium complexes **5a-f** react rapidly with MeI in CH_2Cl_2 , the outcome of the reaction depending upon the nature of the donor ligand. The NNP pincer complexes react with MeI and form Rh(III) methyl species, however over time these complexes undergo migratory insertion. The less bulky $[\text{PPh}_2\text{NNRh}(\text{CO})]$ pincer complex **5a** reaches equilibrium between Rh(III) acyl and Rh(III) methyl complexes, whilst the more bulky $[\text{o-Tol}_2\text{PNNRh}(\text{CO})]$ pincer complex **5b** yields solely the Rh(III) acetyl complex. Complexes **5c-f** react rapidly and form Rh(III) methyl products **6c-6f** with no spectroscopic evidence of migratory insertion.

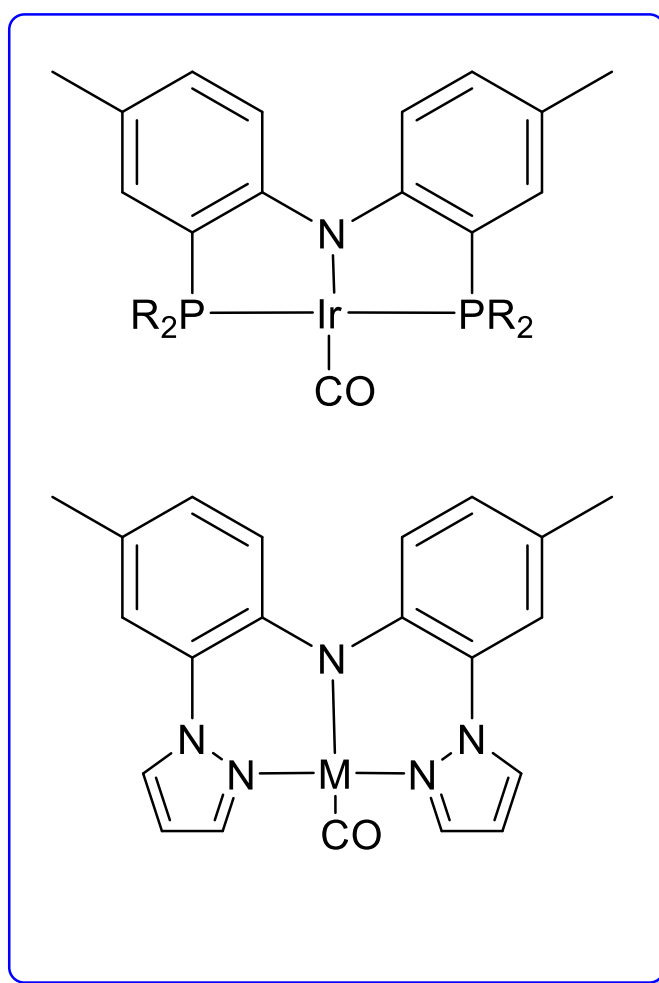
The reactivity of these complexes toward MeI was quantified using UV-vis kinetics, and follows the order NNC > NNN > NNP donor set which mirrors the trend in $\nu(\text{CO})$. The iridium complexes **8a** and **8b** are approximately 20 times more reactive toward MeI than rhodium congeners **5a** and **5b**.

3.4 References

- (1) Morales, D. M.; Jensen, C. *The Chemistry of Pincer Compounds*; Elsevier, **2007**.
- (2) Paul, P.; Richmond, M. G.; Bhattacharya, S. *J. Organomet. Chem.* **2014**, *751*, 760.
- (3) Han, F.-B.; Zhang, Y.-L.; Sun, X.-L.; Li, B.-G.; Guo, Y.-H.; Tang, Y. *Organometallics.* **2008**, *27*, 1924.
- (4) Yang, X.; Wang, Z.-X. *Organometallics.* **2014**, *33*, 5863.
- (5) Qiao, S.; Ma, W.-A.; Wang, Z.-X. *J. Organomet. Chem.* **2011**, *696*, 2746.
- (6) Wanniarachchi, S.; Liddle, B. J.; Toussaint, J.; Lindeman, S. V.; Bennett, B.; Gardinier, J. R. *Dalton. Trans.* **2010**, *39*, 3167.
- (7) Wanniarachchi, S.; Liddle, B. J.; Toussaint, J.; Lindeman, S. V.; Bennett, B.; Gardinier, J. R. *Dalton. Trans.* **2011**, *40*, 8776.
- (8) Wanniarachchi, S.; Liddle, B. J.; Lindeman, S. V.; Gardinier, J. R. *J. Organomet. Chem.* **2011**, *696*, 3623.
- (9) Wanniarachchi, S.; Hewage, J. S.; Lindeman, S. V.; Gardinier, J. R. *Organometallics.* **2013**, *32*, 2885.
- (10) Herrmann, W. A.; Köcher, C. *Angew. Chem. Int. Ed. Engl.*, **1997**, *36*, 2162.
- (11) Wells, J. PhD Thesis, University Of Sheffield, **2010**.
- (12) Winter, A. M.; Eichele, K.; Mack, H.-G.; Potuznik, S.; Mayer, H. A.; Kaska, W. C. *J. Organomet. Chem.* **2003**, *682*, 149.
- (13) Gaunt, J. A.; Gibson, V. C.; Haynes, A.; Spitzmesser, S. K.; White, A. J. P.; Williams, D. J. *Organometallics.* **2004**, *23*, 1015.
- (14) Moser, M.; Wucher, B.; Kunz, D.; Rominger, F. *Organometallics.* **2007**, *26*, 1024.
- (15) Brink, A.; Roodt, A.; Steyl, G.; Visser, H. G. *Dalton. Trans.* **2010**, *39*, 5572.
- (16) Basson, S. S.; Leipoldt, J. G.; Roodt, A.; Venter, J. A.; van der Walt, T. J. *Inorg. Chim. Acta.* **1986**, *119*, 35.
- (17) Best, J.; Wilson, J. M.; Adams, H.; Gonsalvi, L.; Peruzzini, M.; Haynes, A. *Organometallics.* **2007**, *26*, 1960.
- (18) Gonsalvi, L.; Gaunt, J. A.; Adams, H.; Castro, A.; Sunley, G. J.; Haynes, A. *Organometallics.* **2003**, *22*, 1047.
- (19) Clinton, A. MChem Thesis, University Of Sheffield, **2015**.
- (20) Gonsalvi, L.; Adams, H.; Sunley, G. J.; Ditzel, E.; Haynes, A. *J. Am. Chem. Soc.* **2002**, *124*, 13597.

Chapter 4

Synthesis and reactivity of Rh and Ir diaryl-amido pincer complexes.



4.0 Introduction

This chapter describes the synthesis and characterisation of Rh and Ir (I) complexes containing pincer ligands with a diaryl-amido backbone. Transition metal complexes containing this ligand skeleton have great thermal stability and interesting chemical behaviour.¹ Figure 4.1 displays examples of some reported diaryl-amido pincer ligands with PNP¹, NNP² and NNN³⁻⁵ donor sets.

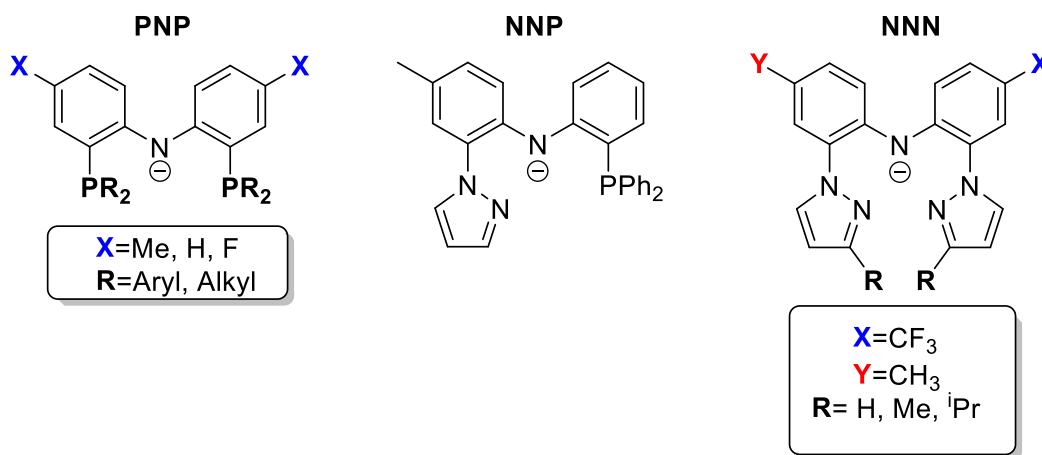
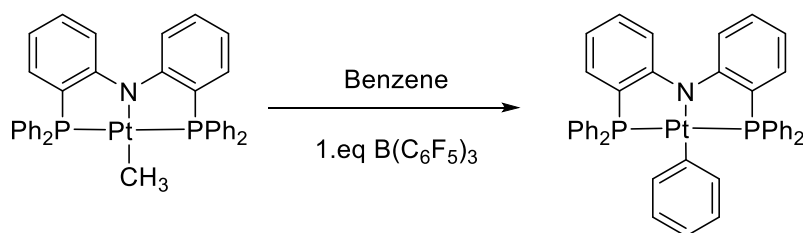


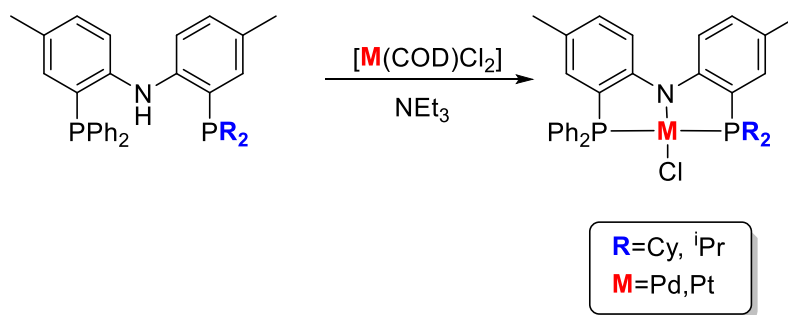
Figure 4.1: Chemical structures of some reported diaryl-amido pincer ligands.¹⁻⁵

Platinum (II) PNP pincer complexes have been prepared by Liang et al.⁶ and applied to the C-H activation of benzene (Scheme 4.1). Liang et al. have also reported the synthesis of symmetrical and unsymmetrical nickel(II) PNP complexes and their application in olefin insertion chemistry.⁷



Scheme 4.1: C-H activation of benzene by $[\text{Pt}(\text{Me})\text{PNP}]$.⁶

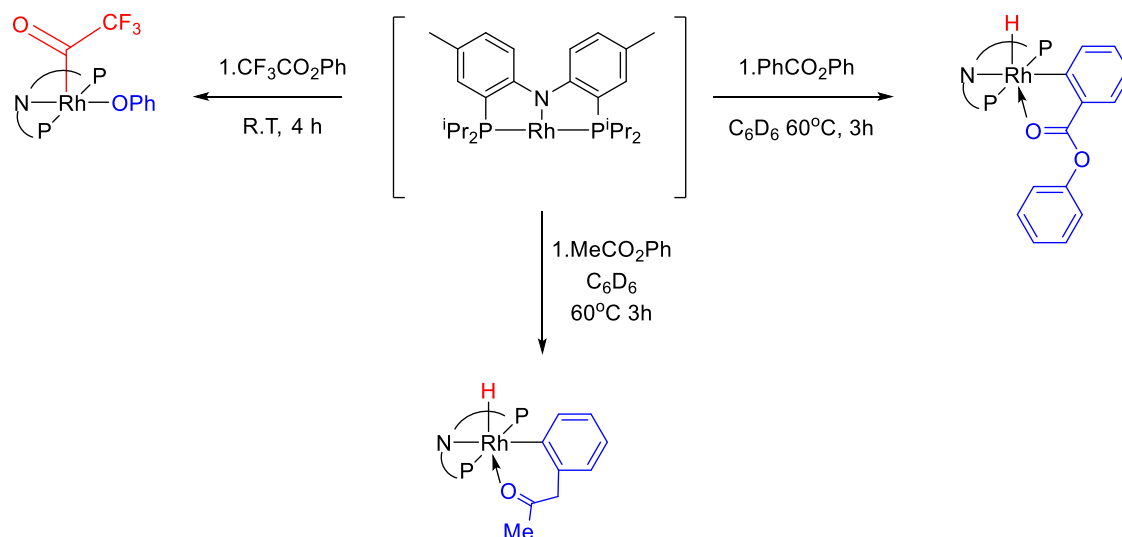
Lancing, Kemp and Goldberg⁸ reported the synthesis and reactivity of unsymmetrical PNP pincer ligands and their corresponding group 10 complexes as shown in Scheme 4.2.



Scheme 4.2: Synthesis of unsymmetrical group 10 pincer complexes.⁸

Tilley and Calimano⁹ demonstrated that the hydrosilation of alkenes can be successfully catalysed by iridium PNP silyl and silylene complexes. Cavaliere et al.¹⁰ have reported the dehydrogenation of ethane to ethylene utilising a titanium alkylidyne PNP complex. These two examples showcase the interesting chemical reactivity promoted by diaryl-amido pincer ligands.

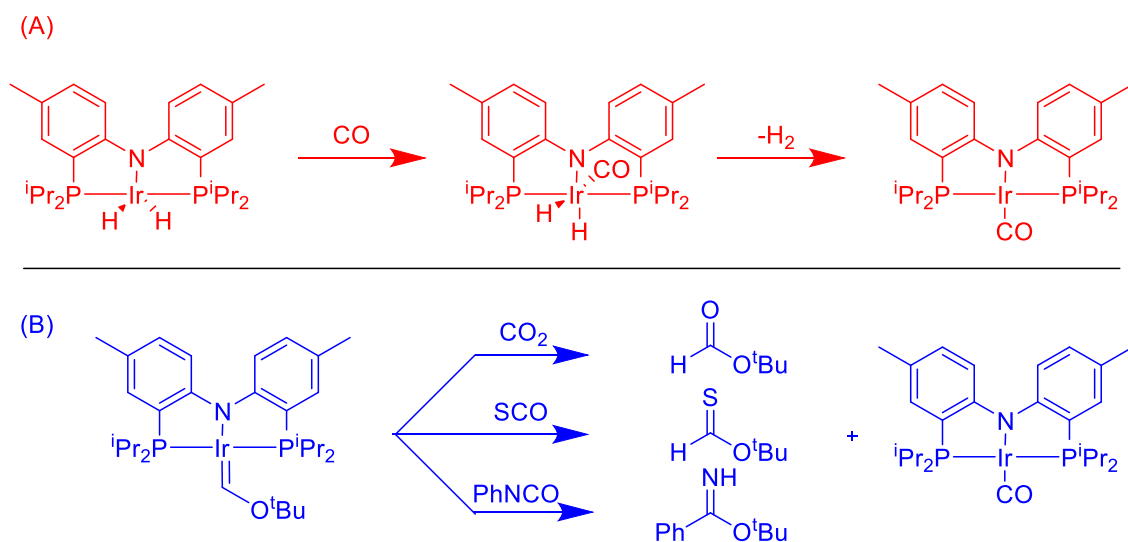
Ozerov et al. have demonstrated the ability of Rh and Ir PNP pincer fragments to perform C-X bond activation.^{11,12} The example displayed in Scheme 4.3 demonstrates the activation of C-O and C-H bonds by rhodium at ambient temperatures.¹³ The key 14 electron rhodium(I) PNP fragment used in these reactions cannot be isolated or observed due to its extremely high reactivity, but is generated in situ via reductive elimination from a Rh(III) precursor.



Scheme 4.3: C-O and C-H bond activation by a reactive rhodium PNP fragment.^{11,12}

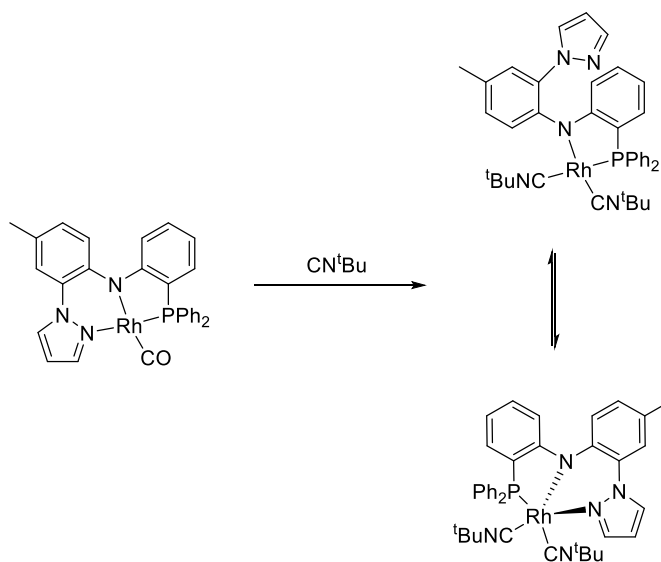
In several publications Grubbs and Whited et al.^{12,14-18} have showcased the ability of Ir(I) fragments to perform C-H bond activation with ethers to form Fischer carbenes. Interestingly, during these investigations an Ir(I) carbonyl complex has been synthesised

(Scheme 4.4). $[\text{Ir}(\text{iPr-PNP})(\text{CO})]$ was synthesised from either addition of CO to $[\text{Ir}(\text{iPr-PNP})(\text{H})_2]$ (A) or decarbonylation of CO containing electrophiles (B) and has been fully characterised including X-Ray crystallography.



Scheme 4.4: Two synthetic routes toward $[\text{Ir}(\text{iPr-PNP})(\text{CO})]$.^{12,14-18}

A recent publication by Wanniarachchi et al.² describes the synthesis of a Rh(I) carbonyl complex containing a PNN pincer ligand that shows hemilabile properties in solution. Its reaction with CN^tBu shown in Scheme 4.5 demonstrates the hemilabile character and flexible co-ordination of the NNP pincer ligand.



Scheme 4.5: Reaction of CN^tBu with a PNN pincer complex.²

The synthesis and reactivity of Rh(I)carbonyl complexes containing a NNN pincer ligand have been investigated by Wanniarachchi et al. (Figure 4.2).⁵ Both symmetrical and unsymmetrical variants of the pincer ligand have been synthesised and co-ordinated to rhodium.

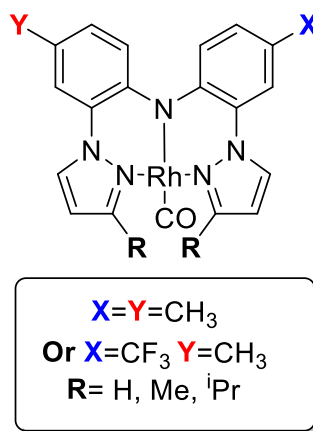
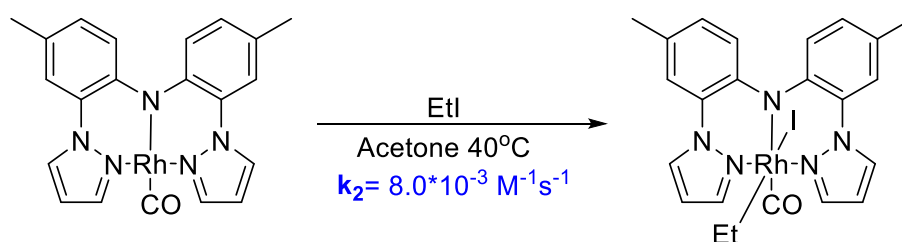


Figure 4.2: Chemical structure of the [Rh(CO)NNN] complexes.

The oxidative addition of iodomethane to these complexes proceeds rapidly to form the *trans*-[Rh(CO)(NNN)(Me)(I)] complexes. Due to the high reactivity of these complexes kinetic measurements could not be obtained for iodomethane, however the oxidative addition of iodoethane proceeds at a convenient measurable rate. The second order rate constant (k_2) for oxidative addition of to the most reactive complex (Scheme 4.6) was approximately three orders of magnitude higher than for those reported for [Rh(CO)₂I₂]⁻ and [CpRh(CO)(PPh₃)].^{5,19}



Scheme 4.6: Second order rate constant (k_2) for oxidative addition of iodoethane to [Rh(CO)NNN].

Recent work within the Haynes group by Wells²⁰ described the synthesis of rhodium carbonyl complexes incorporating a PNP pincer ligand (Figure 4.3). These complexes undergo rapid oxidative addition of MeI with the reactivity being heavily dependent on the nature of the phosphine ligand substituents.

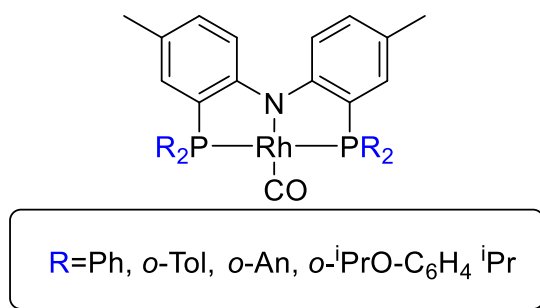


Figure 4.3: Chemical structure of $[\text{Rh}(\text{CO})(\text{R-PNP})]$ complexes.

4.1 Aims

This chapter will describe the synthesis of iridium carbonyl complexes that incorporate PNP pincer ligands (Figure 4.4). This is followed by an investigation of the effect that changing the phosphine substituent has on reactivity toward MeI.

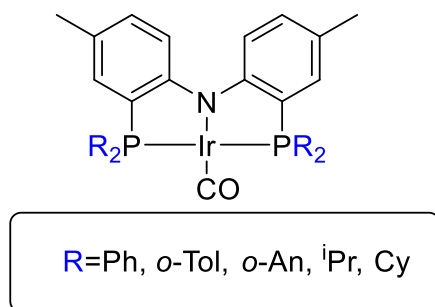


Figure 4.4: Chemical structure of $[\text{Ir}(\text{CO})(\text{R-PNP})]$ complexes.

Using Uv-vis spectroscopy the reactivity of the two most reactive complexes reported by Wanniarachchi et al.⁵ toward MeI is quantified (Figure 4.5) and compared with those obtained for related Rh(I) pincer complexes.

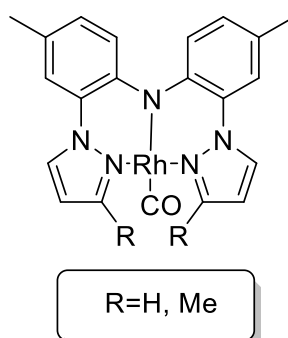
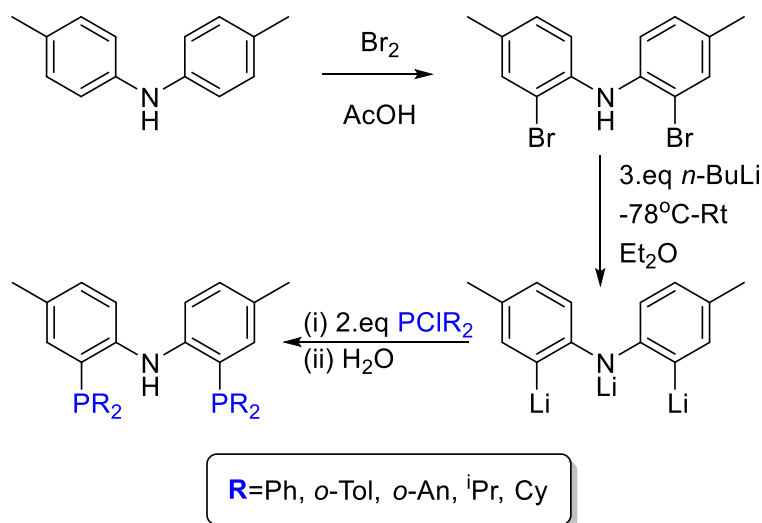


Figure 4.5: Structure of the $[\text{Rh}(\text{CO})(\text{R-NNN})]$ complexes reported by Wanniarachchi et al.

4.2 Synthesis and reactivity of [Ir(CO)(R-PNP)] complexes

4.2.1 Synthesis of R-PNP(H) pro-ligands

The R-PNP(H) pro-ligands were synthesised using a method developed by Fan et al.²¹ displayed in Scheme 4.7. One pot deprotonation and lithium halogen exchange of brominated amine starting material is followed by phosphination using PR_2Cl to provide R-PNP(H) ligands upon hydrolysis.



Scheme 4.7: Synthesis of R-PNP(H) ligands.

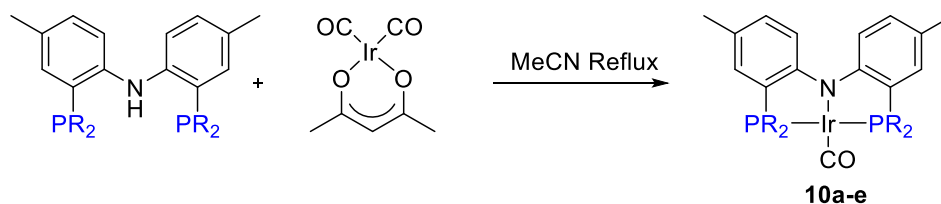
Five different R-PNP(H) pro-ligands were synthesised by this method and were characterised by ^1H , ^{31}P , ^{13}C NMR spectroscopy and mass spectrometry. Selected spectroscopic data for the R-PNP(H) pro-ligands are displayed in Table 4.1.

R	$\delta^{31}\text{P}$	Yield %
Ph	-19.8	68
<i>o</i> -Tol	-36.5	55
<i>o</i> -An	-40.1	64
<i>i</i> Pr	-11.8	71
Cy	-19 (br)	56

Table 4.1: Selected data for the R-PNP(H) pro-ligands.

4.2.2 Synthesis and characterisation of [Ir(CO)(R-PNP)] complexes

The [Ir(CO)(R-PNP)] complexes **10a-e** were synthesised using the route displayed in Scheme 4.8.



Scheme 4.8: Synthesis of [Ir(CO)(R-PNP)] complexes.

Refluxing equimolar amounts of [Ir(acac)(CO)₂] and pro-ligand in MeCN yielded a yellow/orange precipitate, which was filtered and washed with MeCN to give pure [Ir(R-PNP)(CO)] complexes **10a-e**.

4.2.3 IR and ³¹P{¹H} NMR analysis

Some selected spectroscopic data for complexes **10a-e** are displayed in Table 4.2. The products were characterised using ¹H, ³¹P and ¹³C NMR spectroscopy, IR spectroscopy, mass spectrometry and elemental analysis.

Complex	R	δ ³¹ P	ν(CO)/cm ⁻¹	Yield %
10a	Ph	36.4	1944	80
10b	<i>o</i> -Tol	24.9	1941	88
10c	<i>o</i> -An	24.5	1945	75
10d	ⁱ Pr	53.5	1924	77
10e	Cy	47.7	1923	70

Table 4.2: Summary of spectroscopic data for the [Ir(CO)(R-PNP)] complexes **10a-e**.

Complexes **10d** and **10e** have the lowest ν(CO) due to the increased donating ability of the basic alkyl phosphine substituents. The ν(CO) values of **10d** and **10e** are ca. 20 cm⁻¹ lower than the aryl phosphine containing complexes **10a,b** and **10c**. The ν(CO) values for complexes **10a-e** are approximately 15-20 cm⁻¹ lower than those of the equivalent [Rh(CO)(R-PNP)] congeners reported by Wells²⁰ and a related rhodium complex reported by Winter et al.²² indicating they are more electron rich.

The ³¹P{¹H} NMR spectra of complexes **10a-e** each display a single resonance in the region of ca. δ20-55, consistent with equivalent phosphorus atoms and approximate C₂ symmetry.

4.2.4 X-ray crystallography

Crystals of complex **10b** suitable for single crystal X-ray crystallography were obtained by slow vapour diffusion of hexanes into a concentrated toluene solution of the complex. The structure is shown in Figure 4.6, with selected bond lengths and angles given in Table 4.3.

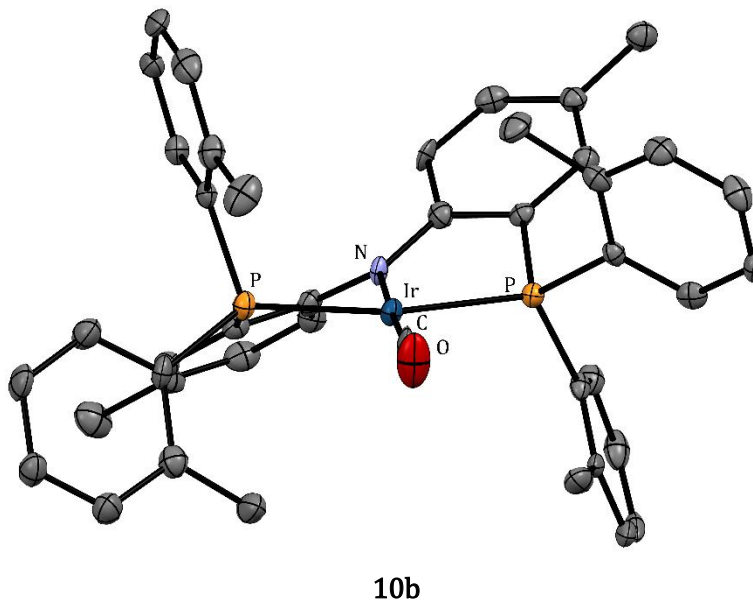


Figure 4.6: X-ray crystal structure of complex **10b** with thermal ellipsoids set at 50% probability level. Hydrogen atoms are omitted for clarity.

Bonds	length Å	Angle	Degrees
Ir-CO	1.836(5)	P-Ir-P	160.46(4)
Ir-N	2.077(3)	N-Ir-CO	177.10(18)
Ir-P	2.2921(11)/2.3088(12)		

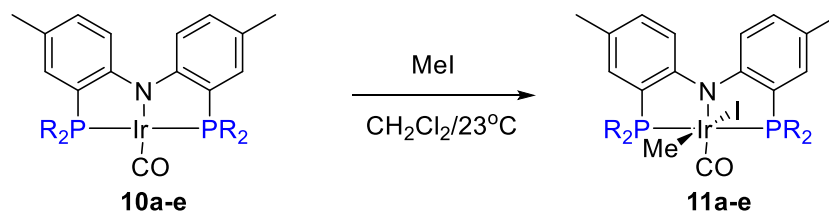
Table 4.3: Selected bond lengths (Å) and angles (deg) for complex **10b**.

Complex **10b** possesses approximate C_2 symmetry with a slightly distorted square planar geometry around the iridium centre. The two phosphorus atoms are coordinated *trans* to one another in a pincer geometry with a P-Ir-P bite angle of 160.5°, approximately 3° shallower than the corresponding [Rh(CO)(*o*-Tol-PNP)] complex reported by Wells.²⁰ The aromatic rings of the PNP backbone are twisted relative to one another, this removes the steric interaction between the two hydrogen atoms at the six position of the PNP ligand backbone. The twisting of the backbone aromatic rings is illustrated by the P-Ir-N-C torsion angle of 25.7°, similar to the corresponding rhodium analogue reported by Wells.²⁰

4.3 Reactivity of [Ir(CO)(R-PNP)] complexes with MeI

4.3.1 IR and NMR analysis

Complexes **10a-e** react rapidly with iodomethane in CH₂Cl₂ to yield Ir(III) methyl species **11a-e** with an orange to yellow colour change observed in solution (Scheme 4.9). Selected spectroscopic data for complexes **11a-e** are displayed in Table 4.4.



Scheme 4.9: Oxidative addition of MeI by [Ir(CO)(R-PNP)] complexes.

Complex	R	$\delta^{31\text{P}}$	$\nu(\text{CO})/\text{cm}^{-1}$	Yield %
11a	Ph	17.4	2018	75
11b	<i>o</i> -Tol	21.96, 18.63 ($J_{\text{p-p}}=363\text{Hz}$)*	2012	69
11c	<i>o</i> -An	15.3	2018	76
11d	<i>i</i> Pr	23.5	2011	81
11e	Cy	16.6	2008	71

Table 4.4: Selected spectroscopic data for complexes **11a-e** (* denotes AB splitting pattern).

The reaction of **10a-e** with MeI results in a shift of the $\nu(\text{CO})$ approximately 70-80 cm⁻¹ to a higher wavenumber indicative of an oxidative addition of MeI. There is no spectroscopic evidence for the formation of Ir(III) acyl species formed by migratory insertion. Complexes **11a-e** were isolated as stable solids.

The ¹H NMR spectra of complexes **11a-e** all display a triplet in the region of δ 0-1.0 for the Ir-methyl with ³J_{P-H} coupling of ca. 5.0 Hz. A singlet is also observed in the ¹H NMR spectra of complexes **11a-e**, corresponding to the diaryl-amido backbone methyl protons and is consistent with a single isomer in each case.

The ambient temperature ³¹P{¹H} NMR spectra of complexes **11a** and **11c-e** each display a singlet in the region of δ 15-25 consistent with the presence of a single Ir-methyl product. Interestingly, complex **11b** displays an AB splitting pattern at ambient temperature, indicating magnetically inequivalent phosphorus atoms (δ 21.96 and 18.63, ³J_{PP} 363 Hz).

On increasing the temperature from 298 to 373 K in d^8 toluene, the AB multiplet collapses into a singlet, as shown in Figure 4.7. Coalescence occurs at a temperature of ca. 358 K.

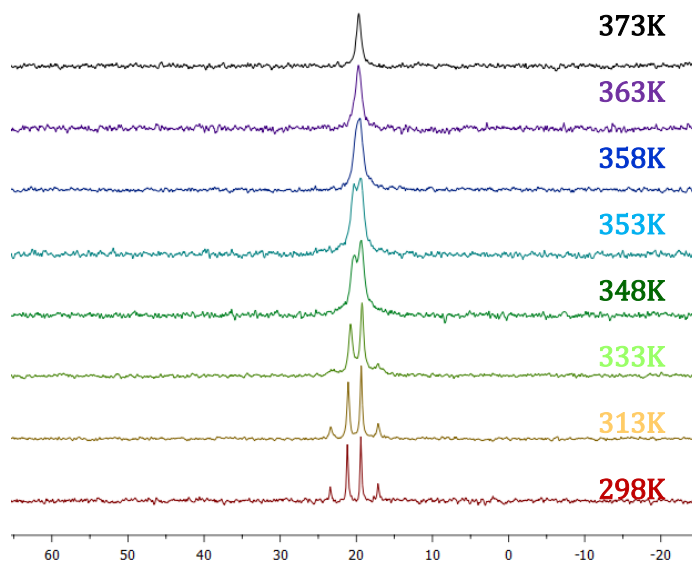
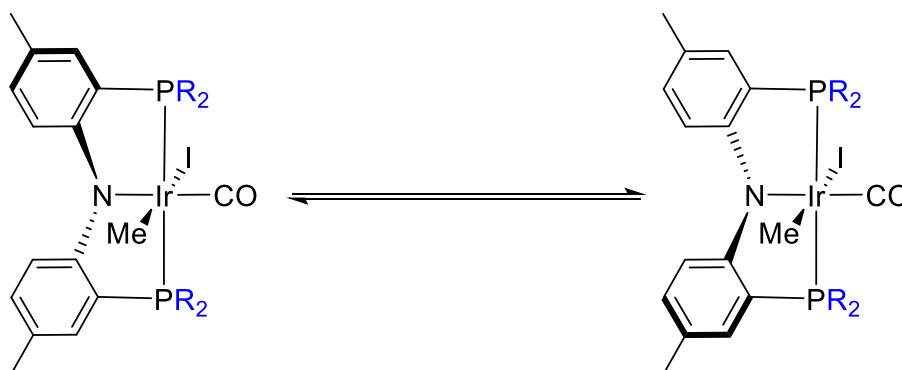


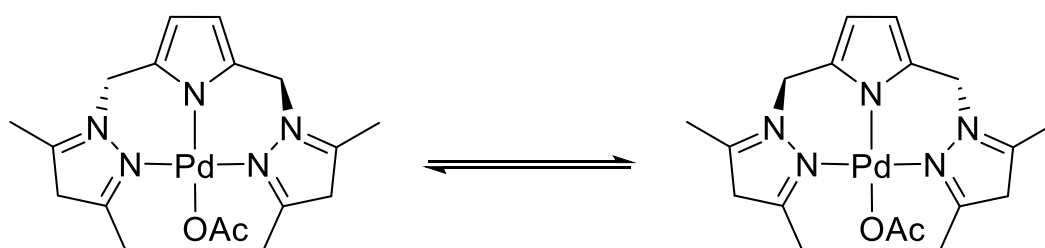
Figure 4.7: Variable temperature $^{31}\text{P}\{^1\text{H}\}$ NMR spectra (162MHz) of **11b** in d^8 toluene.

This behaviour can be explained by the restricted interconversion of two atropisomeric forms of the complex arising from the twisted conformation of the diaryl amido pincer ligand backbone, as illustrated in Scheme 4.10. Addition of MeI to the Ir(I) precursor results in the loss of C_2 symmetry, making the two phosphorus atoms inequivalent if the backbone conformation remains static. However, if the process shown in Scheme 4.10 is fast relative to the NMR timescale then a singlet will result in the $^{31}\text{P}\{^1\text{H}\}$ NMR spectrum due to time-averaged equivalence (as observed for **11a** and **11c-e**). If the interconversion is slower, then inequivalent phosphorus environments will be observed, as indicated by the AB pattern observed for **11b** at room temperature. The rate constant for the exchange process for **11b** was estimated as $k_{\text{ex}} = 1200 \text{ s}^{-1}$ at the coalescence temperature (using the expression $k_{\text{ex}} = \pi\Delta\nu/\sqrt{2}$)²³ corresponding to an activation barrier $\Delta G^\ddagger \sim 67 \text{ kJ mol}^{-1}$.



Scheme 4.10: Schematic to illustrate the conformational freedom of the PNP backbone.

For two of the complexes that showed singlets at ambient temperature, $^{31}\text{P}\{^1\text{H}\}$ NMR spectra were recorded at low temperature in CDCl_3 to determine whether the interconversion between atropisomers could be slowed sufficiently to observe inequivalent phosphorus atoms. For **11a** a singlet was observed on cooling to 223 K but for **11c** the singlet resolved into AB pattern (δ 16.63 and 15.58, $^3J_{\text{PP}}$ 368 Hz) with de-coalescence being attained at ca. 253 K. A value of $k_{\text{ex}} = 375 \text{ s}^{-1}$ at the coalescence temperature was estimated for **11c** corresponding to an activation barrier $\Delta G^\ddagger \sim 49 \text{ kJ mol}^{-1}$. Similar observations were made in the ^1H NMR spectrum of **11c** which at room temperature showed two signals for the methoxy protons of the ligand substituents. These broaden into a single broad resonance at 253K to give a broad signal, below this temperature the signal is resolved into four singlets. Both variable ^1H and $^{31}\text{P}\{^1\text{H}\}$ NMR spectra for **11c** are displayed in the Appendix of this Thesis.



Scheme 4.11: Schematic representation of the dynamic interconversion process between two conformers.

DFT modelling (*Gaussian09*, B3LYP, SDD) of the interconversion process (using a simplified model with $\text{R} = \text{Me}$) identified a transition state with an activation barrier of $\sim 37 \text{ kJ mol}^{-1}$,²⁴ broadly consistent with the experimental observations. Related complexes that display atropisomerism are reported within the literature,²⁵⁻²⁸ an example is shown in Scheme 4.11.²⁹ The variable-temperature NMR spectrum of this palladium pincer complex shows that the methylene protons are involved in a dynamic process. The up and down movement of the two chelate rings about the central Pd-N bond causes two chiral twisted conformers, observed in both NMR and X-ray crystallography. The coalescence temperature for this complex is 50°C corresponding to a Gibbs free energy of activation for interconversion (ΔG^\ddagger) of $\sim 63 \text{ kJ mol}^{-1}$.

4.3.2 X-ray Crystallography

Single crystals of **11b** and **11c** suitable for X-ray crystallography were obtained by slow vapour diffusion of n-hexane into concentrated CH_2Cl_2 solutions of complexes **11b** and **11c**. The structures are displayed in Figure 4.8 and Figure 4.9; selected bond lengths and angles are displayed in Table 4.5.

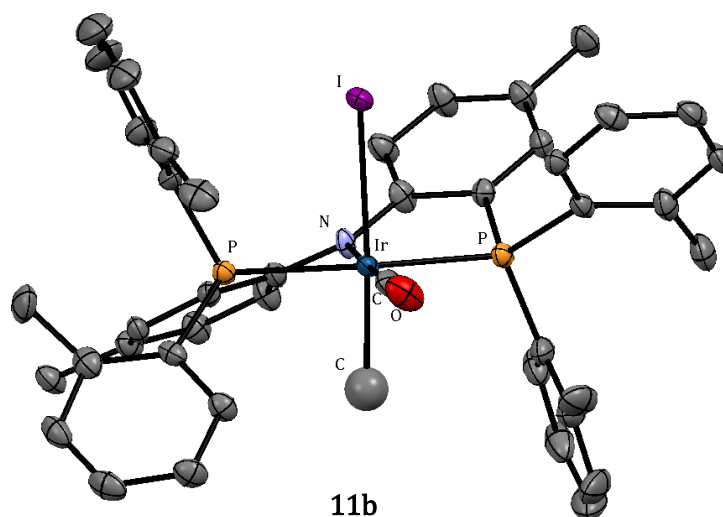


Figure 4.8: X-ray crystal structure of complex **11b** with thermal ellipsoids set at 50% probability level. Hydrogen and additional disordered methyl and iodide ligands have been omitted for clarity.

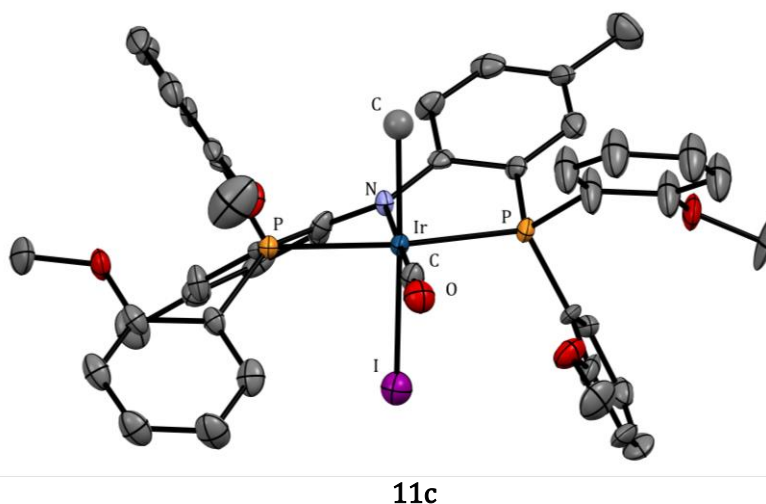


Figure 4.9: X-ray crystal structure of complex **11c** with thermal ellipsoids set at 50% probability level. Hydrogen atoms and n-hexane/ CH_2Cl_2 molecules are omitted for clarity.

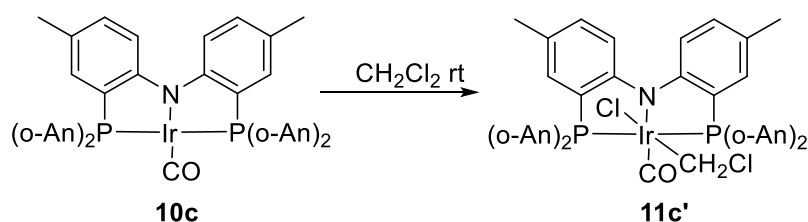
	11b	11c
Ir-CO	1.856(5)	1.849(13)
Ir-N	2.078(3)	2.066(9)
Ir-CH ₃	2.075(10)	2.246(13)
Ir-P	2.3516(12)/2.3536(12)	2.331(3)/2.342(3)
Ir-I	2.7189(16)/2.7594(4)	2.7823(10)
OC-Ir-N	178.00(18)	177.1(5)
P-Ir-P	161.11(4)	162.39(11)
CH ₃ -Ir-I	173.7(10)/172.7(3)	174.4(3)

Table 4.5: Selected bond lengths (Å) and angles (deg) for complex **11b** and **11c**.

The crystal structure of **11b** is modelled with the methyl and iodide ligands disordered between two trans coordination sites (79.5:20.5 respectively). This means that the Ir-Me and Ir-I bond lengths are not accurately resolved.

Both structures show that a distorted octahedral geometry is adopted by the iridium centre with the I and CH₃ ligands being mutually *trans*. The I-Ir-CH₃ bond angles for **10a** and **11b** deviate from 180° due to the steric bulk of the *o*-tolyl and *o*-anisyl substituted pincer ligand. The pincer ligands have bite angles of 161.1° and 162.3° respectively and are similar to a related [Rh(CO)I₂(*i*Pr-PNP)] complex reported by Wells.²⁰ The aromatic rings of the PNP backbone are twisted relative to each other to relieve the steric interaction between the C_{aromatic}-H atoms in the backbone. The P-Ir-N-C torsion angles are 24° and 29° respectively with **11c** having a larger torsion angle due to the greater steric bulk of the *o*-anisyl phosphine substituents.

Upon attempting to grow crystals of **10c** suitable for X-ray crystallography it was found that **10c** reacts with CH₂Cl₂ at room temperature to afford the oxidative addition product **11c'** shown in Scheme 4.12. The structure of **11c'** is displayed in Figure 4.10 with selected bond angles and lengths being displayed in Table 4.6.



Scheme 4.12: Oxidative addition of CH₂Cl₂ to **10c**.

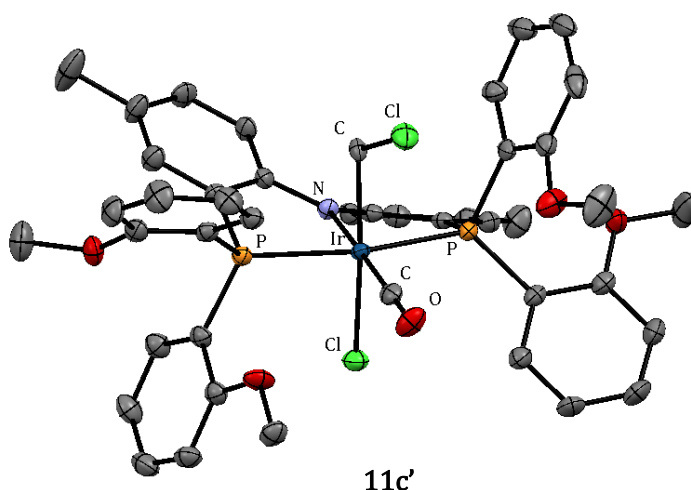


Figure 4.10: X-ray crystal structure of complex **11c'** with thermal ellipsoids set at 50% probability level. Hydrogen atoms and CH₂Cl₂ molecule are omitted for clarity.

Bonds	length Å	Angle	Degrees
Ir-CO	1.872(4)	P-Ir-P	163.67(3)
Ir-N	2.078(3)	N-Ir-CO	176.85(12)
Ir-P	2.3491(8)/2.3481(7)	CH ₂ Cl-Ir-Cl	171.69(9)
Ir-CH ₂ Cl	2.141(3)		
Ir-Cl	2.4501(8)		

Table 4.6: Selected bond lengths (Å) and angles (deg) for complex **10c'**

Oxidative addition of CH₂Cl₂ has been observed for a related [Rh(CO)(*o*-An-anthraphos)] complex by Reynolds.³⁰ Sieh et al.³¹ characterised the oxidative addition of CH₂Cl₂ to Rh and Ir pincer complexes and obtained crystal structures of both rhodium and iridium congeners. Complex **11c'** is only the second reported crystal structure for CH₂Cl₂ oxidative addition to an iridium pincer complex.

The crystal structure of **11c'** shows a distorted octahedral geometry is adopted by the iridium centre with the Cl and CH₂Cl ligands being mutually *trans*. The Cl-Ir-CHCl₂ bond angle is 171° and is distorted due to the steric bulk of the *o*-anisyl substituted pincer ligand. The pincer ligand has a bite angle of 163°, similar to **11c**. The aromatic rings of the PNP backbone are twisted relative to each other to relieve the steric interaction between the C_{aromatic}-H atoms in the backbone, with a P-Ir-N-C torsion angle of 23°.

4.3.3 MeI oxidative addition kinetics

Kinetic experiments were carried out using at least a tenfold excess of MeI to ensure pseudo first order conditions. For complex **10d**, IR spectroscopy was used to monitor the reactivity. For the remainder of the complexes, UV-vis spectroscopy was used, the sensitivity of which allows a lower concentration of complex, hence lower [MeI] to give convenient measurable rates whilst maintaining pseudo first order conditions.

An example of a series of IR spectra recorded during a typical experiment reacting **10d** with MeI is shown in Figure 4.11.

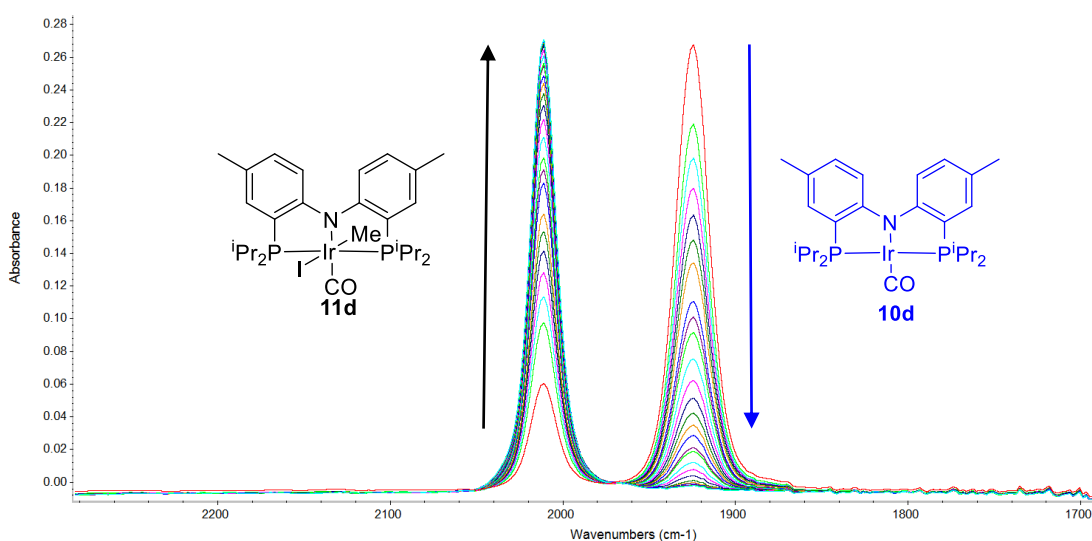


Figure 4.11: Series of IR spectra recorded during the reaction of **10d** with MeI (0.04 M in CH₂Cl₂ at 23°C)

The decay of the carbonyl band at 1923 cm⁻¹ for **10d** is mirrored by the growth of a carbonyl band at ca. 2011 cm⁻¹ for the Ir-methyl product **11d**.

When UV-vis spectroscopy was used a series of difference spectra were taken in order to obtain a wavelength suitable to measure in the kinetic assessment. An example set of difference spectra for the reaction of complex **10a** with MeI is displayed in Figure 4.12.

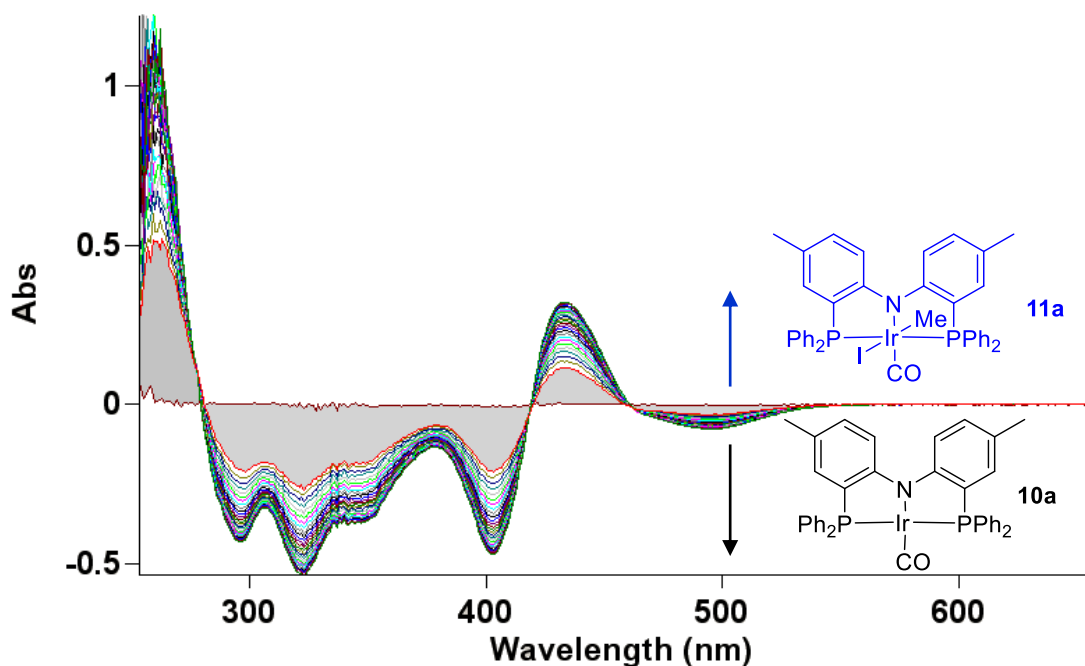


Figure 4.12: Series of UV-visible spectrum for reaction of **10a** with MeI (23°C, 0.00128 M in CH₂Cl₂).

Absorbances due to **10a** at 280 - 402 and 480 nm decay with time whilst a growth in absorbance at 250 and 440 nm is observed for the Ir(III) methyl complex **11a**.

The decay in absorbance of the chosen wavelength or $\nu(\text{CO})$ was then analysed to obtain a value of the pseudo first order rate constant k_{obs} . A kinetic profile for **10d** reacting with MeI is shown in Figure 4.13. Plots of absorbance vs. time were well fitted to a 1st order exponential decay indicating that the reaction is first order in Ir(I) complex.

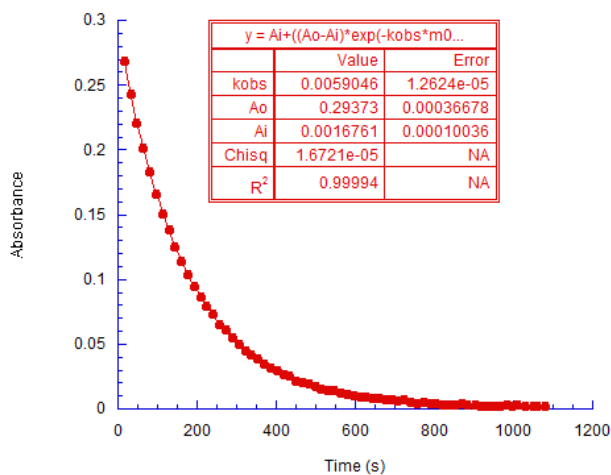


Figure 4.13: Plot of absorbance at 1923 cm⁻¹ Vs time for the reaction of **10d** with MeI at 0.032 M MeI at 23°C in CH₂Cl₂.

Plots of k_{obs} vs. $[\text{MeI}]$ are linear (Figure 4.14) indicating that the reactions are first order in $[\text{MeI}]$ and therefore second order overall. From the gradient of these plots second order rate constants (k_2) can be obtained.

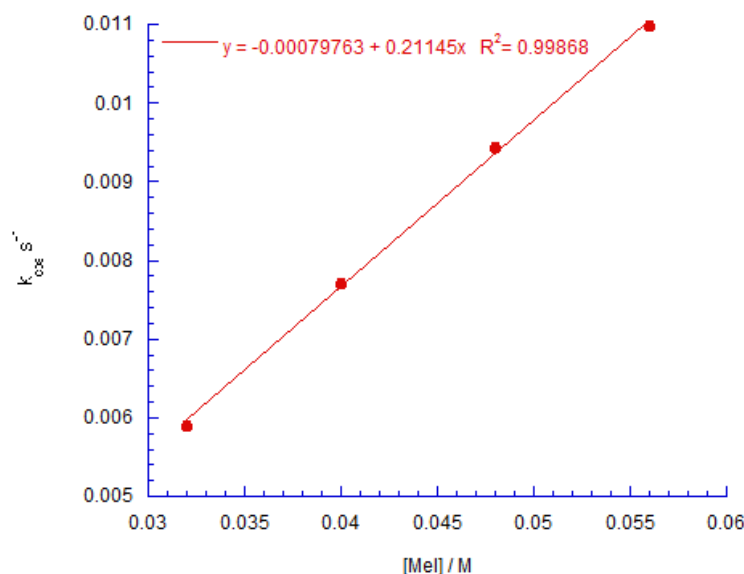


Figure 4.14: Plot of k_{obs} Vs $[\text{MeI}]$ for complex **10d** to determine the second order rate constant (k_2) at 23°C in CH_2Cl_2 .

Table 4.7 displays the second order rate constants (k_2) for reactions of complexes **10a-e** with MeI at 23°C in CH_2Cl_2 . Comparative data for the corresponding $[\text{Rh}(\text{CO})(\text{R-PNP})]$ complexes synthesised by Wells²⁰ are also given.

Complex	R	$k_2 / \text{M}^{-1}\text{s}^{-1}$ (Ir)	$k_2 / \text{M}^{-1}\text{s}^{-1}$ (Rh)	$k_{\text{Ir vs } k_{\text{Rh}}}$
10a	Ph	2.47	0.092	28
10b	<i>o</i> -Tol	0.58	0.021	28
10c	<i>o</i> -An	397	23.1	17
10d	<i>i</i> Pr	0.21	0.014	15
10e	Cy	0.36	-	-

Table 4.7: Second order rate constants (k_2) for oxidative addition of MeI to complexes **10a-e** in CH_2Cl_2 at 23°C.

Interestingly, complexes **10d** and **10e** were found to be least reactive toward MeI, presumably because of the bulky *i*Pr and Cy phosphine substituents.

Despite being the least electron rich, **10a** has the second highest MeI oxidative addition rate. Complex **10b** contains an *o*-tolyl substituted pincer ligand, this increases the electron

density on the metal centre but also decreases the rate of reaction by increasing the steric bulk around the metal centre.

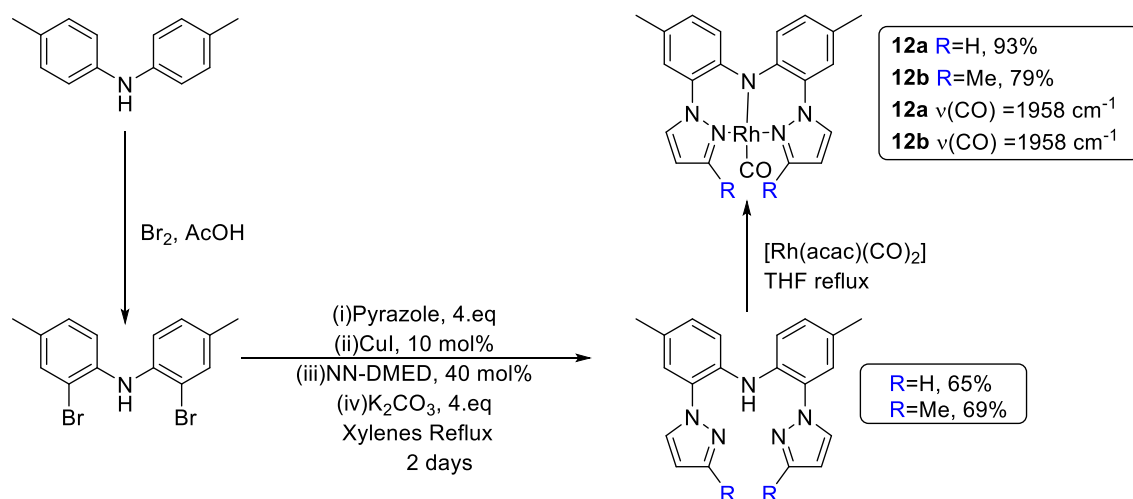
Complex **10c** has the highest MeI oxidative addition rate and contains a PNP ligand with pendant ortho alkoxy substituents. Wells²⁰ found that the corresponding [Rh(CO)(*o*-An-PNP)] and a related [Rh(CO)(*o*-An-Anthraphos)] complex had the fastest MeI oxidative addition rates reported to date. Complex **10c** is an order of magnitude more reactive than these two related complexes and has to my knowledge, the fastest MeI oxidative addition rate for any iridium(I) carbonyl complex.

4.4 Synthesis and reactivity of Rh di(2-Pyrazolyl-*p*-tolyl)amine pincer complexes

As mentioned in the introduction to this chapter Wanniarachchi et al.⁵ reported that [Rh(NNN)(CO)] pincer complexes react rapidly with MeI but only reported kinetics for the slower reaction with EtI. To make a direct comparison of PNP and NNN ligands it was of interest to measure the kinetics for MeI oxidative addition to the [Rh(NNN)(CO)] pincer complexes.

4.4.1 Synthesis of [Rh(NNN)(CO)] complexes **12a** and **12b**

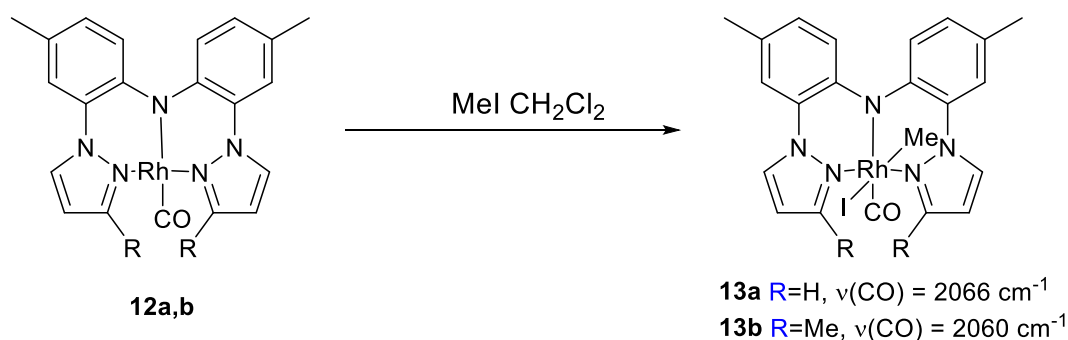
Scheme 4.13 shows the route used to synthesise the two pincer ligands and their corresponding Rh(I) complexes.



Scheme 4.13: Synthesis of Rh(R-NNN)(CO) complexes **12a** and **12b**.

4.4.2 Reactivity of **12a** and **12b** with MeI

Wanniarachchi et al.⁵ have shown that both **12a** and **12b** react rapidly with MeI forming the Rh(III) methyl species **13a** and **13b** as shown in Scheme 4.14.



Scheme 4.14: Oxidative addition of MeI by **12a** and **12b** forming Rh(III) methyl species **13a** and **13b**

4.4.3 UV-Vis kinetics

MeI oxidative addition kinetic experiments were carried out using at least a tenfold excess of MeI to ensure pseudo first order conditions.

The decay in absorbance at 360 nm for both **12a** and **12b** was measured with time to obtain values of k_{obs} . A kinetic profile for the reaction of **12a** with MeI is shown in Figure 4.15. Plots of absorbance vs. time are well fitted to a 1st order exponential decay indicating that the reactions are first order in Rh(I) complex.

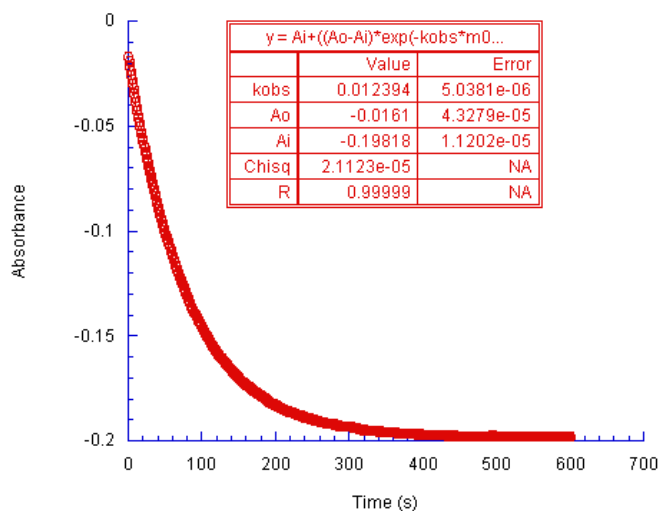


Figure 4.15: Kinetic profile for the reaction of **12a** with MeI at (0.00256 M in CH₂Cl₂ at 23°C).

Plots of k_{obs} vs. $[\text{MeI}]$ are linear (Figure 4.16) indicating that the reactions are also first order in $[\text{MeI}]$ and therefore second order overall. From the gradient of these plots second order rate constants (k_2) can be obtained which are displayed in Table 4.8.

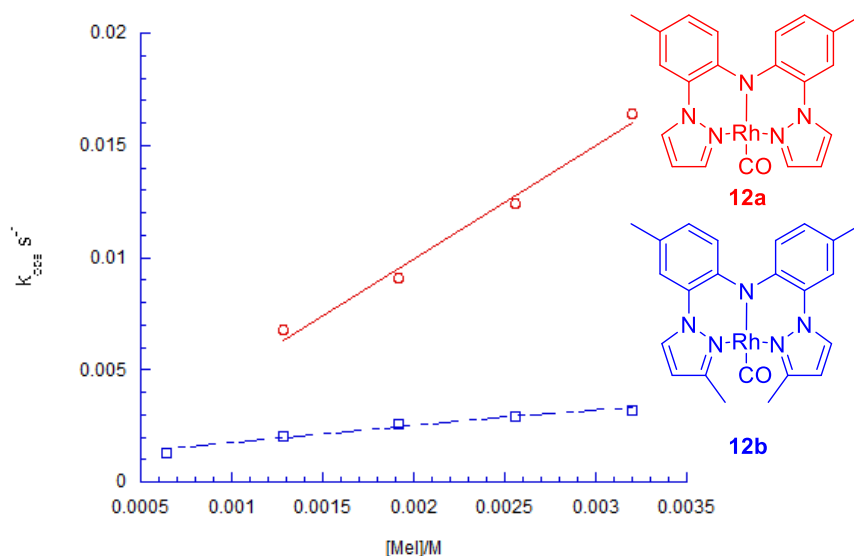


Figure 4.16: Plot of k_{obs} vs $[\text{MeI}]$ to determine the second order rate constants k_2 at 23°C in CH_2Cl_2 .

Complex	R	$k_{2(\text{MeI})}/\text{M}^{-1}\text{s}^{-1}$	$k_{2(\text{EtI})}/\text{M}^{-1}\text{s}^{-1}$
12a	H	5.04	0.008
12b	Me	0.73	0.0016

Table 4.8: Second order rate constants for oxidative addition of MeI in CH_2Cl_2 at 23°C. and EtI at 45°C in acetone.⁵

Complex **12a** is approximately seven times more reactive than **12b** toward MeI due to increased steric congestion caused by the 3-methyl substituents of the pyrazole donor in **12b**. The oxidative addition rate of MeI is approximately 600 times faster than with EtI at 40°C.⁵

Figure 4.17 compares the reactivity of complex **12a** to some related Rh(I) pincer complexes. Complex **12a** is approximately 55 times more reactive than $[\text{Rh}(\text{CO})(\text{Ph-PNP})]$ complex reported by Wells²⁰, three times more reactive toward MeI than $[\text{Rh}(\text{CO})\text{bis}(\text{imino})\text{carbazolide}]$ reported by Gibson et al.³² and two times more reactive than **5c** reported in Chapter 3.

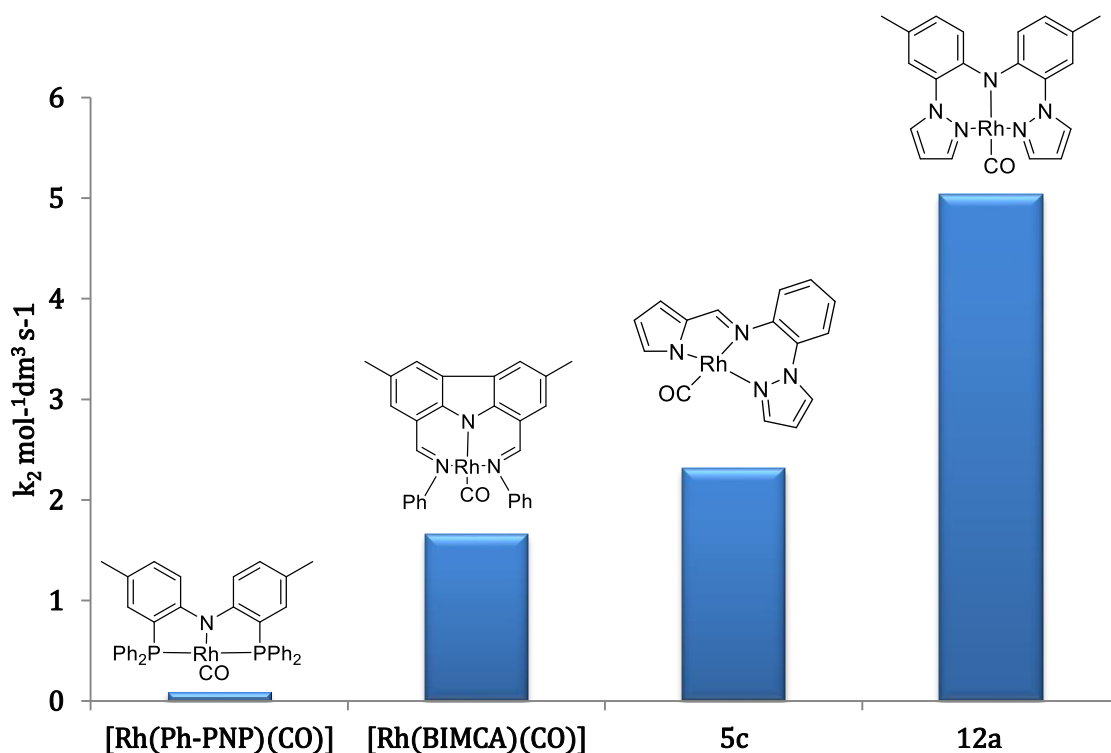


Figure 4.17: Comparison of k_2 values obtained for oxidative addition of MeI to **12a** and related Rh(I) complexes.

4.5 Summary

The synthesis and reactivity of a series of iridium PNP pincer complexes has been investigated. These complexes have been fully characterised by ^{31}P , ^{13}C and ^1H NMR spectroscopy, IR spectroscopy, mass spectrometry, elemental analysis and in some cases X-ray crystallography.

[Ir(R-PNP)(CO)] complexes **10a-e** react rapidly toward MeI, each forming a single Ir(III) methyl species [Ir(R-PNP)(CO)Me(I)] **11a-e**. The oxidative addition rates of these complexes have been obtained using IR and UV-vis spectroscopy and were found to be an order of magnitude more reactive than the corresponding [Rh(R-PNP)(CO)] complexes reported by Wells.²⁰ Complex **10c** incorporates an *o*-anisyl substituted pincer ligand and displays the highest MeI oxidative addition rate reported for any iridium(I) carbonyl complex.

Oxidative addition product [Ir(*o*-Tol-PNP)(CO)(Me)I] (**11b**) displays an AB splitting pattern at ambient temperature, indicating magnetically inequivalent phosphorus atoms and two atropisomeric forms of the complex. Upon heating **11b** to 358K coalescence is observed indicating that interconversion between the atropisomers is facile on the NMR timescale. Cooling a sample of [Ir(Ph-PNP)(CO)(Me)I] (**11a**) does not result in an AB

pattern in the ^{31}P NMR spectrum, however cooling $[\text{Ir}(o\text{-An-PNP}(\text{CO})(\text{Me})(\text{I}))]$ (**11c**) to 223K results in an AB pattern in the ^{31}P NMR spectrum indicative of two atropisomeric forms of the final octahedral complex, distinguishable at this temperature.

The reactivity of some reported NNN pincer complexes has been investigated. The most reactive complex $[\text{Rh}(\text{NNN})(\text{CO})]$ (**12a**) is approximately 55 times more reactive toward MeI than the $[\text{Rh}(\text{CO})(\text{Ph-PNP})]$ complex reported by Wells²². These complexes were found to react approximately 400-600 times faster toward MeI than EtI.

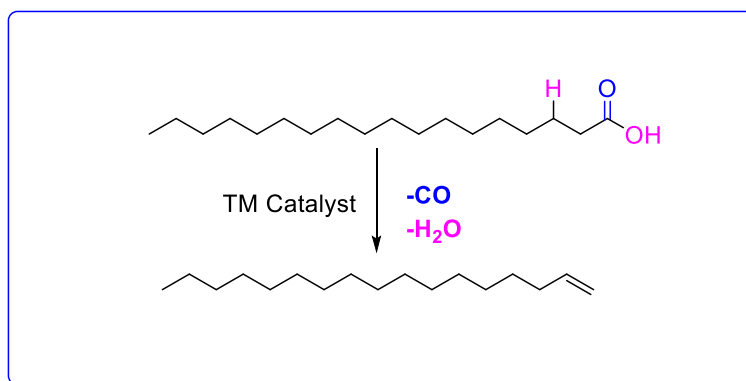
4.6 References

- (1) Liang, L.-C. *Coord. Chem. Rev.* **2006**, *250*, 1152.
- (2) Wanniarachchi, S.; Hewage, J. S.; Lindeman, S. V.; Gardinier, J. R. *Organometallics*. **2013**, *32*, 2885.
- (3) Wanniarachchi, S.; Liddle, B. J.; Toussaint, J.; Lindeman, S. V.; Bennett, B.; Gardinier, J. R. *Dalton Trans.* **2010**, *39*, 3167.
- (4) Wanniarachchi, S.; Liddle, B. J.; Toussaint, J.; Lindeman, S. V.; Bennett, B.; Gardinier, J. R. *Dalton Trans.* **2011**, *40*, 8776.
- (5) Wanniarachchi, S.; Liddle, B. J.; Lindeman, S. V.; Gardinier, J. R. *J. Organomet. Chem.* **2011**, *696*, 3623.
- (6) Liang, L.-C.; Lin, J.-M.; Lee, W.-Y. *Chem. Commun.* **2005**, 2462.
- (7) Liang, L.-C.; Chien, P.-S.; Lee, P.-Y. *Organometallics*. **2008**, *27*, 3082.
- (8) Lansing, R. B.; Goldberg, K. I.; Kemp, R. A. *Dalton Trans.* **2011**, *40*, 8950.
- (9) Calimano, E.; Tilley, T. D. *J. Am. Chem. Soc.* **2009**, *131*, 11161.
- (10) Cavaliere, V. N.; Crestani, M. G.; Pinter, B.; Pink, M.; Chen, C.-H.; Baik, M.-H.; Mindiola, D. J. *J. Am. Chem. Soc.* **2011**, *133*, 10700.
- (11) Fan, L.; Parkin, S.; Ozerov, O. V. *J. Am. Chem. Soc.* **2005**, *127*, 16772.
- (12) Whited, M. T.; Zhu, Y.; Timpa, S. D.; Chen, C.-H.; Foxman, B. M.; Ozerov, O. V.; Grubbs, R. H. *Organometallics*. **2009**, *28*, 4560.
- (13) Zhu, Y.; Smith, D. A.; Herbert, D. E.; Gatard, S.; Ozerov, O. V. *Chem. Commun.* **2012**, *48*, 218.
- (14) Romero, P. E.; Whited, M. T.; Grubbs, R. H. *Organometallics*. **2008**, *27*, 3422.
- (15) Whited, M. T.; Grubbs, R. H. *J. Am. Chem. Soc.* **2008**, *130*, 5874.
- (16) Whited, M. T.; Grubbs, R. H. *J. Am. Chem. Soc.* **2008**, *130*, 16476.
- (17) Whited, M. T.; Grubbs, R. H. *Organometallics*. **2008**, *27*, 5737.
- (18) Whited, M. T.; Grubbs, R. H. *Organometallics* **2009**, *28*, 161.
- (19) McConnell, A. C.; Pogorzelec, P. J.; Slawin, A. M. Z.; Williams, G. L.; Elliott, P. I. P.; Haynes, A.; Marr, A. C.; Cole-Hamilton, D. J. *Dalton Trans.* **2006**, 91.

- (20) Wells, J. PhD Thesis, University Of Sheffield, **2010**.
- (21) Fan, L.; Foxman, B. M.; Ozerov, O. V. *Organometallics*. **2004**, *23*, 326.
- (22) Winter, A. M.; Eichele, K.; Mack, H.-G.; Potuznik, S.; Mayer, H. A.; Kaska, W. C. *J. Organomet. Chem.* **2003**, *682*, 149.
- (23) Gutowsky, H.; Holm, C. *J. Chem. Phys.* **1956**, *25*, 1228.
- (24) Haynes, A. Personal Communication. **2015**.
- (25) Gründemann, S.; Albrecht, M.; Loch, J. A.; Faller, J. W.; Crabtree, R. H. *Organometallics*. **2001**, *20*, 5485.
- (26) Herbert, D. E.; Ozerov, O. V. *Organometallics*. **2011**, *30*, 6641.
- (27) Miecznikowski, J. R.; Grundemann, S.; Albrecht, M.; Megret, C.; Clot, E.; Faller, J. W.; Eisenstein, O.; Crabtree, R. H. *Dalton Trans.* **2003**, 831.
- (28) Danopoulos, A. A.; Tulloch, A. A. D.; Winston, S.; Eastham, G.; Hursthouse, M. B. *Dalton Trans.* **2003**, 1009.
- (29) Ghorai, D.; Kumar, S.; Mani, G. *Dalton Trans.* **2012**, *41*, 9503.
- (30) Reynolds, T. J. PhD Thesis, Bristol University, **2011**.
- (31) Sieh, D.; Schoffel, J.; Burger, P. *Dalton Trans.* **2011**, *40*, 9512.
- (32) Gaunt, J. A.; Gibson, V. C.; Haynes, A.; Spitzmesser, S. K.; White, A. J. P.; Williams, D. J. *Organometallics*. **2004**, *23*, 1015.

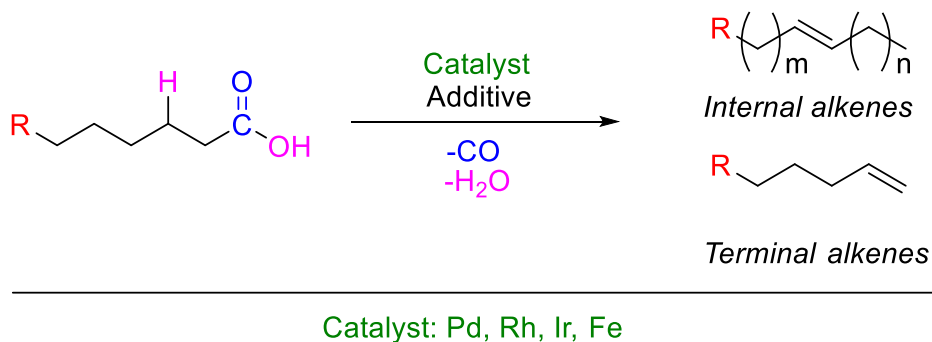
Chapter 5

Rh and Ir catalysed decarbonylative dehydration of long chain acids.



5.0 Introduction

Decarbonylative dehydration and renewable feedstocks were both introduced in Chapter 1 to which the reader is referred for a review of the literature on this topic. The decarbonylative dehydration of long chain carboxylic acids has been reported several times using a variety of transition metal catalysts (Scheme 5.1).¹⁻⁹



Scheme 5.1: Decarbonylative dehydration of fatty acids using a transition metal catalyst (Pd, Rh, Ir, Fe).¹⁻⁹

This chapter will firstly discuss the investigation of iridium catalysed decarbonylative dehydration. This is followed by an investigation into what effect changing the metal centre, ancillary ligands and additives has on selectivity, yield and longevity of the transition metal catalyst.

5.1 Results and discussion

5.1.1 General method

The reactions reported in this chapter were performed using the standard method outlined in the Experimental section of this thesis using either a microwave reactor or an oil bath for heating. Microwave heating was an attractive source due to potential reaction acceleration by factors known as the “specific microwave effect”, a topic reviewed by de la Hoz, Díaz-Ortiz and Moreno.¹⁰ All the data from these experiments are compiled in the Appendix of this thesis.

On completion of each catalytic experiment, the crude reaction mixture was analysed spectroscopically to identify the reaction products and the fate of the catalyst. The crude reaction mixture was then purified by column chromatography on silica, eluting with hexanes to remove the polar substrates and inorganic residues. The alkene products have

a high boiling point and were isolated by the removal of hexanes under vacuum and weighed to obtain a yield.

The product selectivity was measured by comparing the integrated intensities of the terminal (H_a & H_b) and internal (H_c) alkene peaks in the 1H NMR spectrum as a percentage. An example 1H NMR spectrum of $C_{15}H_{30}$ alkene products is shown in Figure 5.1 with an example calculation given in the Appendix.

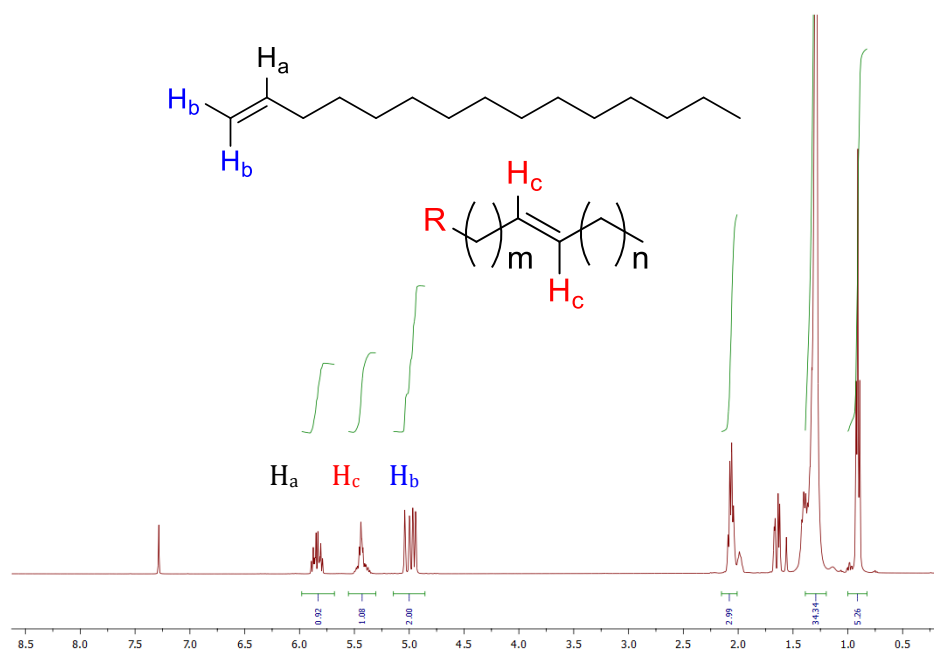
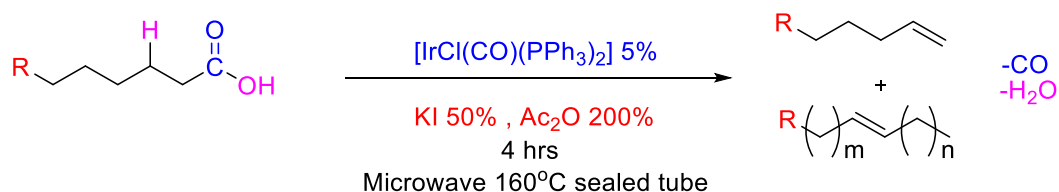


Figure 5.1: 1H NMR spectrum of $C_{15}H_{30}$ alkenes obtained after column chromatography.

5.1.2 Decarbonylative dehydration using $[IrCl(CO)(L)_2]$ Vaska type complexes

Preliminary experiments were performed using $[IrCl(CO)(PPh_3)_2]$ as a catalyst and the reaction conditions developed by Maetani et al. (KI additive is a proposed halide exchange reagent and the Ac_2O additive is a proposed dehydrating agent to aid the thermodynamics of the reaction).⁶ Four different chain length acids were decarbonylated using conditions shown in Scheme 5.2. Table 5.1 contains the results obtained from these experiments.

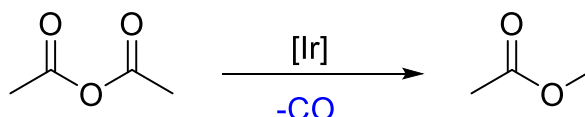


Scheme 5.2: Conditions used to decarbonylate C_{12} - C_{18} carboxylic acids.

Acid	Yield %	Terminal %	Internal %
Dodecanoic acid (C ₁₂)	43	64	36
Myristic acid (C ₁₄)	95	85	15
Palmitic acid (C ₁₆)	99	82	18
Stearic acid (C ₁₈)	95	93	7

Table 5.1: Yields and selectivity of alkene obtained from preliminary reactions.

¹H NMR analysis of the crude reaction mixtures confirmed that the reaction produces alkenes. Interestingly, a singlet at δ 3.6 is observed corresponding to MeOAc which is formed by the decarbonylation of acetic anhydride as shown in Scheme 5.3. Also present in the ¹H NMR spectra of the crude reaction mixtures are singlet peaks corresponding to acetic anhydride and acetic acid as well as trace amounts of acid starting material.

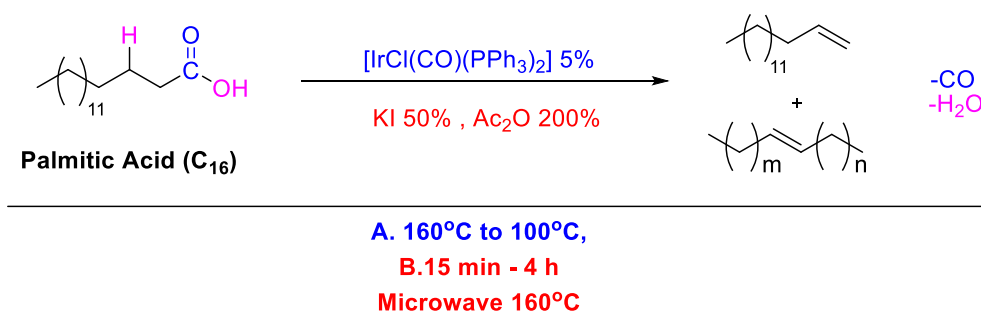


Scheme 5.3: Formation of methyl acetate via decarbonylation of acetic anhydride.

Encouragingly both isolated yields and selectivity are similar to those reported by Maetani et al.⁶ The low yield obtained using dodecanoic acid can possibly be explained by the lower boiling point of the undecene products which could be lost accidentally during removal of solvent under vacuum.

5.1.3 Temperature and time dependence

The effect of reaction duration and temperature was investigated as shown in Scheme 5.4. Reducing reaction temperature from 160°C in 20°C increments had a large effect on the overall yield of alkenes (Figure 5.2).



Scheme 5.4: Conditions used during the time and temperature dependant reactions

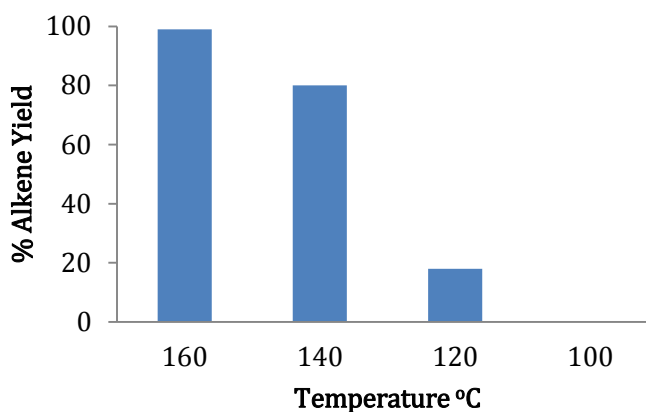


Figure 5.2: Effect of temperature on alkene yield.

The highest yield of alkene was obtained at 160°C and lowering the temperature reduces the overall yield. No decarbonylative dehydration was observed at 100°C.

The timescale of the reaction was investigated by performing multiple reactions with different durations (Figure 5.3). The reaction is 80% complete after 1 hour with the last 10-15% of the carboxylic acid being converted in the last 3 hours.

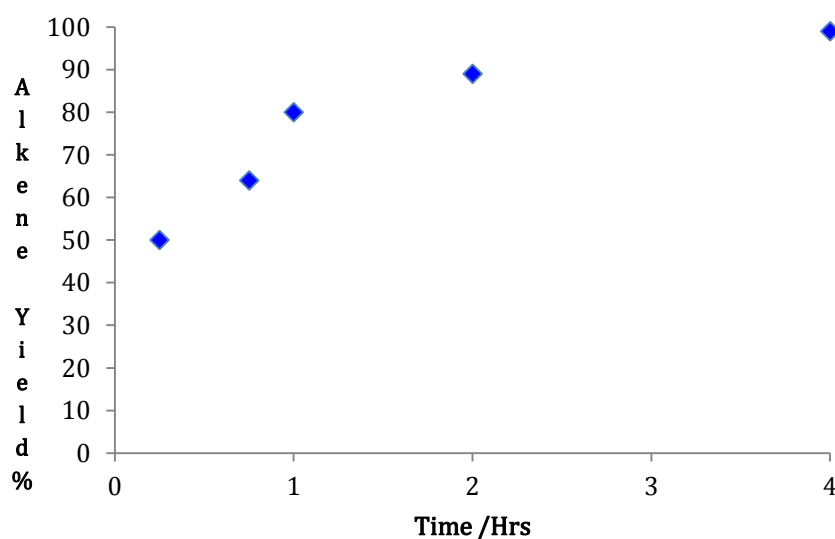


Figure 5.3: Plot of alkene yield Vs time.

5.1.4 Additive effect on reactivity

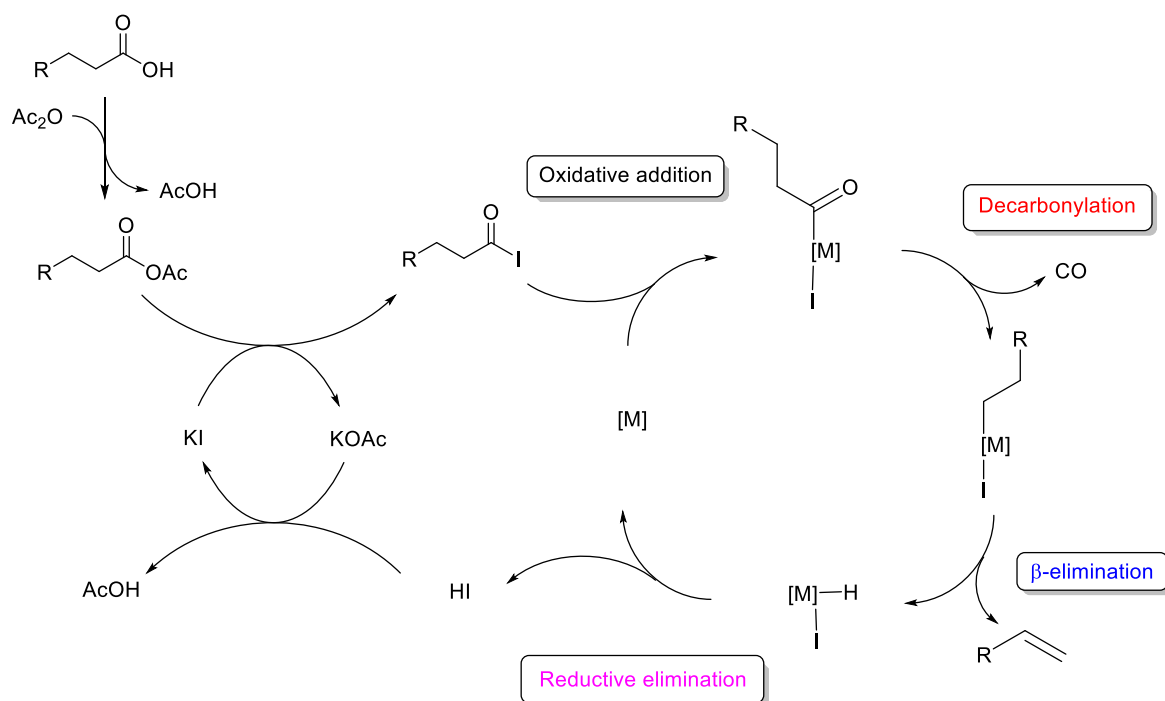
Reducing the amount of KI from 50% down to 5% (mol % compared to carboxylic acid) reduced the reaction yield to 23 % as shown in Table 5.2. Changing the halide of the potassium salt also has a detrimental effect on the yield of alkenes. Addition of KCl or KBr

reduced the yield to 14% and 8% respectively at the original loading of 50% KI (Table 5.2).

Additive	Yield %	Terminal %	Internal %
KI 50%	99	82	18
KI 25%	81	85	15
KI 5%	23	80	20
KBr 50%	14	77	23
KCl 50%	8	79	21

Table 5.2: Yield and selectivity of alkenes obtained with various additives.

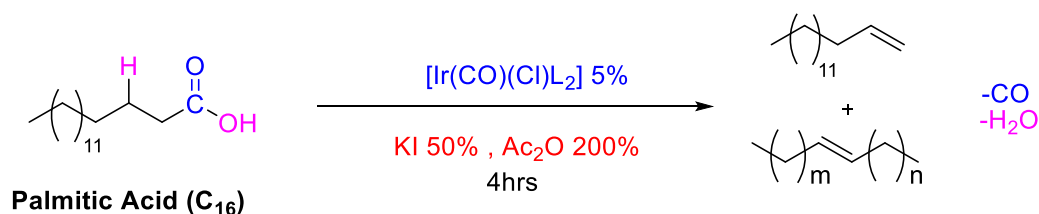
These results clearly show that KI plays a vital role in this reaction. The mechanism proposed by Maetani et al.⁶ included oxidative addition of a C-O bond of an anhydride as the first metal containing step. However the observed effect of iodide suggests an alternative mechanism that starts with the oxidative addition of a long chain acyl iodide, formed by reaction of a long chain carboxylic acid/anhydride with KI (Scheme 5.5). The acyl iodide is much more reactive and will undergo facile oxidative addition.



Scheme 5.5: Proposed mechanism (additional ligands omitted for clarity).

5.1.5 Ligand effects

A series of Vaska type complexes were synthesized using a method developed by Burk and Crabtree.¹¹ Scheme 5.6 shows the conditions used and Table 5.3 shows the yields and alkene selectivity obtained when using these catalysts.



Scheme 5.6: Reaction conditions used in the ligand variation experiments.

L	Yield %	Terminal %	Internal %
PPh ₃	99	82	18
PPh ₂ Et	92	56	44
PPhEt ₂	90	40	60
PCy ₃	93	7	93
P(<i>o</i> -Tol) ₃	-	-	-
P(<i>o</i> -An) ₃	-	-	-

Table 5.3: Ligand effect on alkene yield and selectivity.

A high yield of alkenes was obtained for all catalysts apart from [IrCl(CO)(P*o*-Tol₃)₂] and [IrCl(CO)(P*o*-An₃)₂] which did not catalyse the reaction. These two complexes are very insoluble even in highly polar solvents which could account for the lack of activity.

Increasing the number of alkyl substituents on the phosphine ligand increases the selectivity towards internal alkenes in the order of PPh₃ < PPh₂Et < PPhEt₂ < PCy₃. The behaviour of the [IrCl(CO)(PCy₃)₂] catalyst was investigated by reducing the reaction time incrementally from 4 hours to 1 min. Surprisingly, the reaction was 45% complete after 1 min yielding alkenes with 90% terminal selectivity. After 10 mins the reaction is 93% complete and favours internal alkenes (61%). After 2 hours the selectivity has increased to 93% internal alkenes (Figure 5.4). These results indicates that the PCy₃ complex promotes facile alkene isomerisation as well as decarbonylation. This observation is contrast to Strohmeier et al.¹² who reported that [IrCl(CO)(PPh₃)₂] was the least active alkene isomerisation catalyst from a selection of [IrCl(CO)(L)₂] complexes.

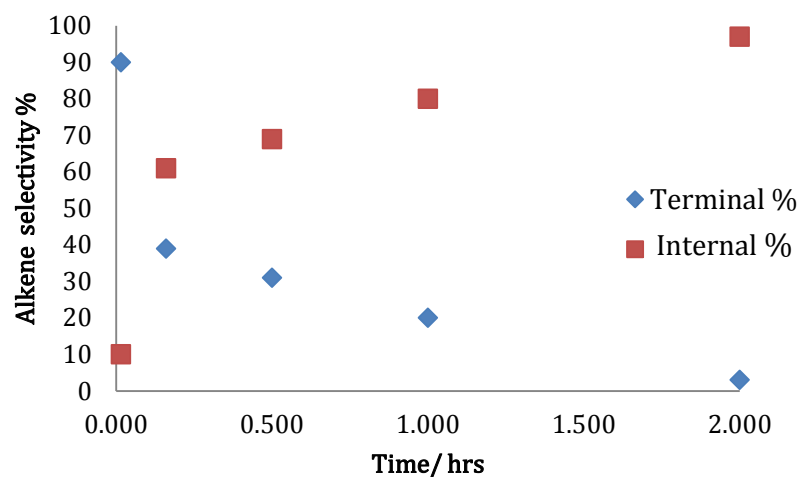


Figure 5.4: Alkene isomerisation vs. reaction time.

At this point it was discovered that some of the reactions had begun to coat the surface of the vial with metal, and in some extreme cases causing localised heating, shattering the vial under elevated pressure and temperature. For the longevity of the microwave instrument and safety, it was decided that conventional heating methods should be used instead.

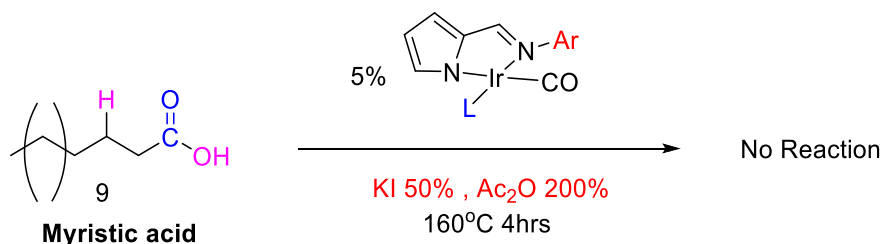
A control reaction was set up to compare the results obtained using microwave and standard heating methods. Using $[\text{IrCl}(\text{CO})(\text{PPh}_3)_2]$ as a catalyst but using an oil bath as the heating source a similar yield of alkene product was obtained. However, the reaction was more selective toward the 1-alkene product compared to using microwave heating (Table 5.4). As the yields are comparable, conventional heating methods were used for all subsequent reactions unless otherwise stated.

Heating source	Yield	Terminal %	Internal %
Microwave	99	82	18
Oil Bath	91	95	5

Table 5.4: Yield and selectivity of alkene obtained from the control experiment.

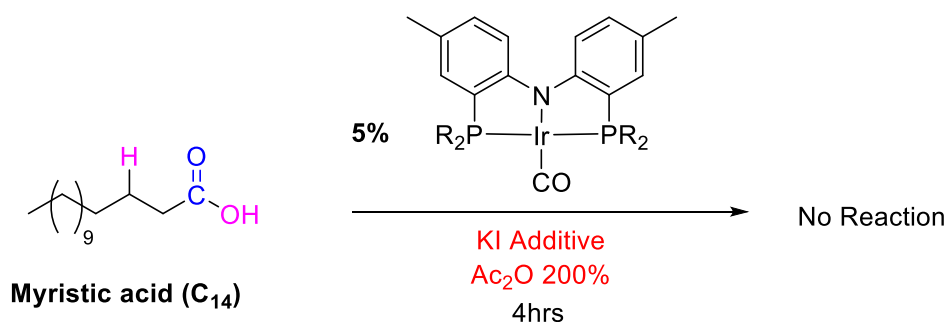
5.1.6 Decarbonylative dehydration using Ir(I) multidentate complexes

The iridium(I)iminopyrrolyl carbonyl phosphine complexes **3a-m** investigated in Chapter 2 were tested as catalysts. A range of these iridium complexes were tested both with and without KI. Unfortunately, these complexes did not catalyse the reaction and yielded no alkenes (Scheme 5.7). IR analysis of the crude reaction mixture shows a $\nu(\text{CO})$ in the Ir(III) region of the spectrum in each case with $^{31}\text{P}\{^1\text{H}\}$ NMR showing multiple singlet peaks.



Scheme 5.7: Catalytic conditions used with $[\text{Ir}(\text{Ar-NN})(\text{CO})\text{L}]$ catalysts.

The catalytic activity of the $[\text{Ir}(\text{R-PNP})(\text{CO})]$ pincer complexes (**10a-e**) was also investigated both with and without the KI additive (Scheme 5.8).



Scheme 5.8: Catalytic decarbonylation of myristic acid using $[\text{Ir}(\text{R-PNP})(\text{CO})]$ complexes **10a-e**.

Both with and without KI no alkene product was observed. The $^{31}\text{P}\{^1\text{H}\}$ NMR spectra of the crude reaction mixtures show only one major peak and IR analysis shows $\nu(\text{CO})$ bands that indicate formation of Ir(III) species.

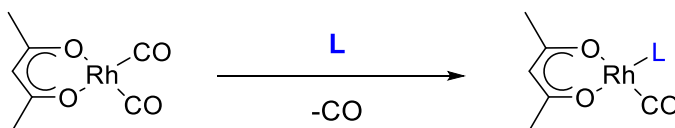
Interestingly, of all the iridium complexes tested, only the Vaska type complexes $[\text{IrCl}(\text{CO})(\text{PR}_3)_2]$ efficiently catalyse the reaction, however they do not survive the harsh reaction conditions. IR and $^{31}\text{P}\{^1\text{H}\}$ NMR spectra of the crude reaction mixture show multiple $\nu(\text{CO})$ bands and multiple ^{31}P resonances and unfortunately it cannot be said with

any certainty if the phosphine ligand remains co-ordinated to the metal centre. An alternative is to use rhodium based phosphine complexes, since, if phosphorus is coordinated to rhodium it will give a doublet in the $^{31}\text{P}\{^1\text{H}\}$ NMR spectrum due to ^{103}Rh - ^{31}P coupling.

Using the corresponding rhodium Vaska complex as a catalyst ($[\text{RhCl}(\text{CO})(\text{PPh}_3)_2]$) the decarbonylation of palmitic acid smoothly yielded alkenes in a 79% yield. However a singlet at δ 31.05 in the $^{31}\text{P}\{^1\text{H}\}$ NMR spectra indicated that the phosphine ligand is no longer co-ordinated to the metal centre.

5.1.7 Decarbonylative dehydration reactions using Rh(I) (CO) complexes

A number of $[\text{Rh}(\text{acac})(\text{CO})\text{L}]$ complexes with different phosphine ligands, (L) have been reported.¹³⁻¹⁶ Synthesis of these complexes is achieved by reacting one equivalent of a phosphine with $[\text{Rh}(\text{acac})(\text{CO})_2]$ (Scheme 5.9).



Scheme 5.9: Synthesis of $[\text{Rh}(\text{acac})(\text{CO})\text{PR}_3]$ complexes

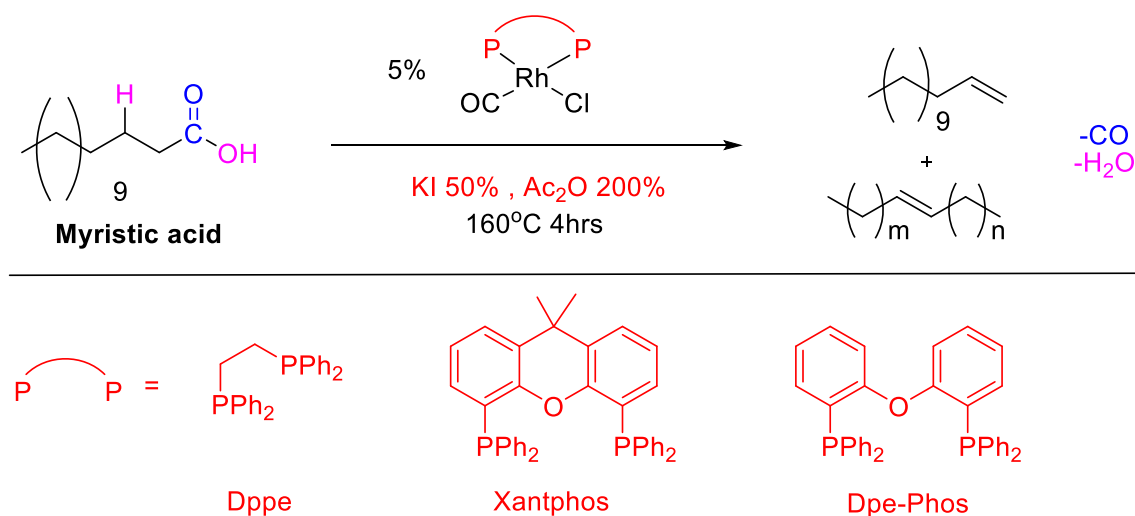
Using the conditions reported by Maetani et al.⁶ but changing the catalyst to a $[\text{Rh}(\text{acac})(\text{CO})\text{L}]$ complex still yielded alkenes in above an 89% yield (Table 5.5). The selectivity in these reactions is more moderate with the alkenes produced being closer to a 50/50 mixture of 1-alkene and internal alkenes. Interestingly, the unsubstituted $[\text{Rh}(\text{acac})(\text{CO})_2]$ catalyst resulted in a 94 % yield of alkene.

Unfortunately in each case the $[\text{Rh}(\text{acac})(\text{CO})(\text{PR}_3)]$ complex does not survive the catalytic conditions. The $^{31}\text{P}\{^1\text{H}\}$ NMR spectra of the crude reaction mixtures display a number of singlets indicating loss of the phosphine ligand from the rhodium centre.

L	Yield %	Terminal %	Internal%
<i>Pp</i> -An ₃	96	56	44
PCy ₃	92	70	30
<i>Po</i> -An ₃	92	55	46
P(4-ClC ₆ H ₄) ₃	94	56	44
P(<i>o</i> -Tol) ₃	98	62	38
PPh ₃	89	58	42
CO	94	52	48

Table 5.5: Yield and selectivities of alkenes obtained using [Rh(acac)(CO)L] complexes as catalysts (microwave heating).

Some rhodium (I) diphosphine complexes were also tested as catalysts (Scheme 5.10). The decarbonylative dehydration of myristic acid was successful in all three cases yielding alkenes in over 85% yield (Table 5.6). The highest selectivity toward the 1-alkene product was obtained for the [RhCl(CO)(dppe)] catalyst. In the ³¹P{¹H} NMR spectra of the crude reaction mixtures using all three catalysts no *J*_{Rh-P} coupling was observed indicating that the phosphine ligand is no longer co-ordinated to the metal centre.



Scheme 5.10: Bidentate phosphine catalysts used and reaction conditions.

P-P	Yield	Terminal %	Internal %
Dppe	85	88	12
Xantphos	95	50	50
Dpe-Phos	85	65	35

Table 5.6: Yield and selectivity of alkenes obtained when using [P-PRh(CO)Cl] catalysts.

Due to their greater thermal stability and interesting reactivity, pincer complexes were the next class of rhodium complex investigated as catalysts for the decarbonylative dehydration of long chain fatty acids. The rhodium(I) pincer complexes investigated in this study are shown in Figure 5.5.

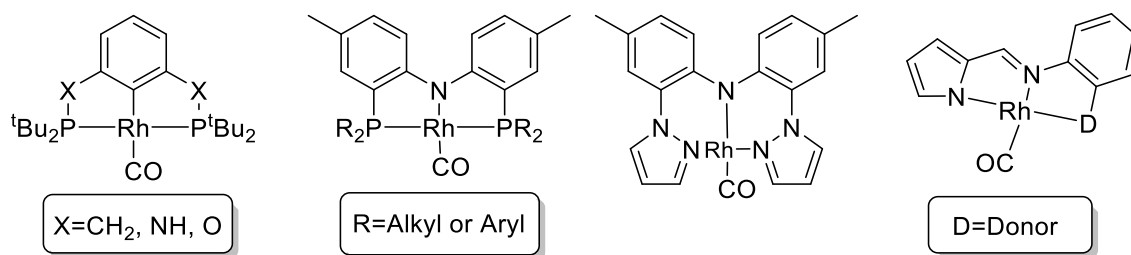
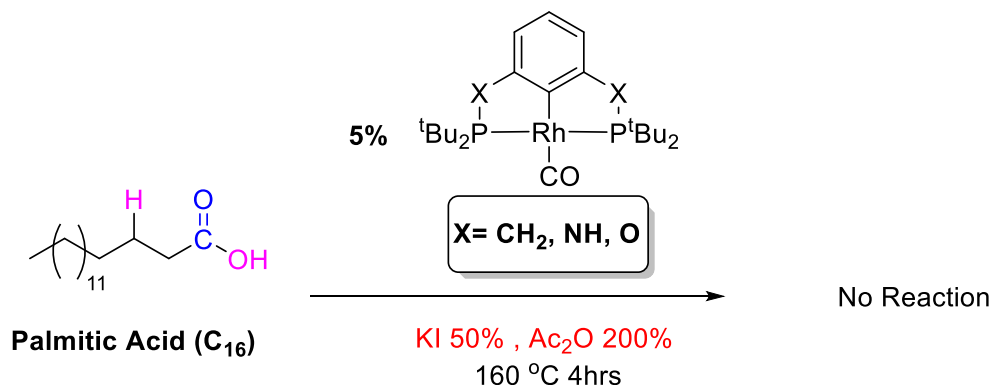


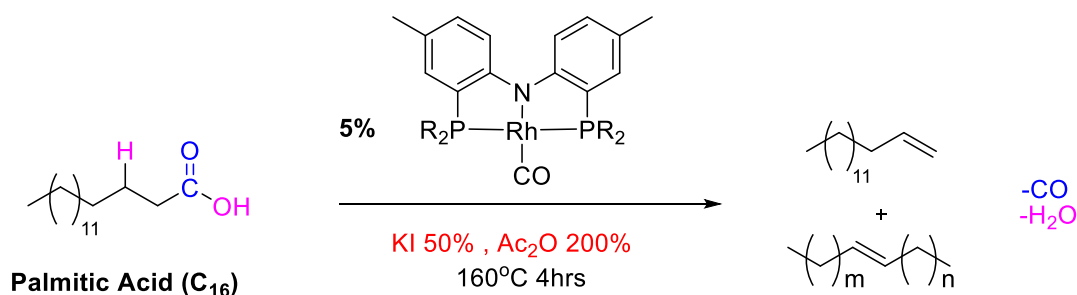
Figure 5.5: Structure of Rh(I) pincer complexes used in this study.

The PXCXP pincer complexes were the first class of pincer complex to be tested under catalytic conditions (Scheme 5.11). These Rh(I) catalysts did not produce any alkenes, palmitic acid starting material was seen in all cases and the Rh(I) complexes were intact showing a clean Rh(I) doublet in the $^{31}\text{P}\{^1\text{H}\}$ NMR spectra corresponding to the starting complex. The lack of reactivity of these complexes could be caused by the steric bulk of the ^tBu phosphine substituents.



Scheme 5.11: Catalytic conditions when using $[\text{Rh}(\text{CO})\text{PXCXP}]$ catalysts.

A selection of $[\text{Rh}(\text{R-PNP})(\text{CO})]$ complexes were tested toward the decarbonylative dehydration of palmitic acid (C_{16}) using the conditions shown in Scheme 5.12. The results and selected spectroscopic data for the reactions are displayed in Table 5.7.



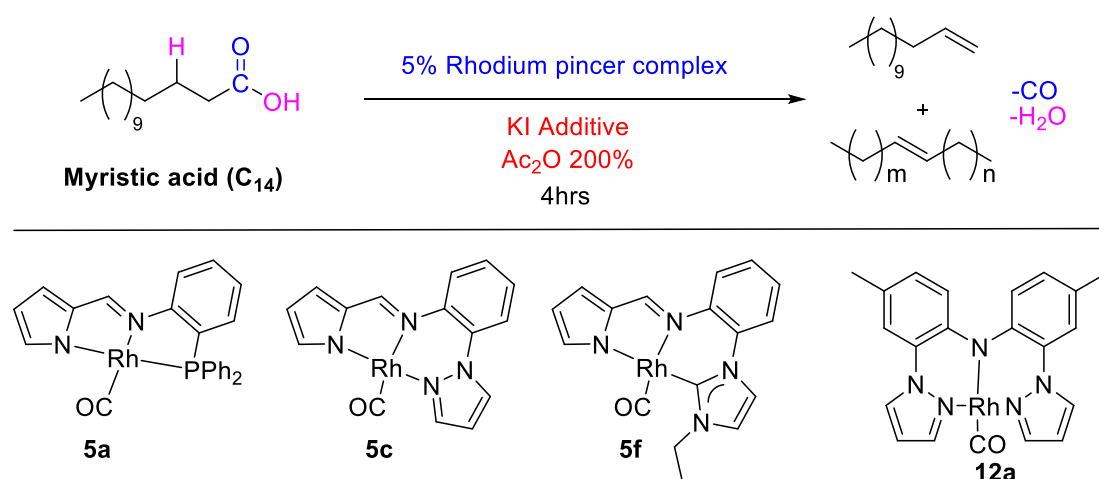
Scheme 5.12: Decarbonylative dehydration of palmitic acid using $[\text{Rh}(\text{CO})(\text{R-PNP})]$ pincer complexes.

R	Yield	Terminal %	Internal %	$^{31}\text{P}\{^1\text{H}\}$ NMR	$\nu(\text{CO})/\text{cm}^{-1}$
<i>i</i> Pr	74	65	35	Doublets	2065, 1935
<i>o</i> -Tol	-	-	-	SM	SM
2- <i>i</i> PrOPh	41	74	26	Doublets	2059
<i>t</i> BuPh	59	68	32	Doublets	2060
Ph	75	82	18	Doublets	2065

Table 5.7: Yield and selectivity of alkenes and selected spectroscopic data obtained when using $[\text{Rh}(\text{CO})(\text{R-PNP})]$ pincer complexes.

Pleasingly the reaction was catalysed by the $[\text{Rh}(\text{R-PNP})(\text{CO})]$ complexes yielding alkenes albeit in modest yield. The only complex that did not catalyse the reaction was the $[\text{Rh}(\textit{o}\text{-Tol-PNP})(\text{CO})]$ which could be due to a steric effect. In all cases doublets due to ^{103}Rh - ^{31}P coupling were observed in the $^{31}\text{P}\{^1\text{H}\}$ NMR spectra, indicating no thermal degradation of the complexes. Infrared spectroscopy confirmed that carbonyl containing species were present in the crude reaction mixture, with all cases except the unreactive $[\text{Rh}(\textit{o}\text{-Tol-PNP})(\text{CO})]$ possessing a $\nu(\text{CO})$ band at 2060-2065 cm^{-1} indicative of Rh(III) oxidation state. In the case of $[\text{Rh}(\textit{i}\text{Pr-PNP})(\text{CO})]$ a $\nu(\text{CO})$ band was also observed at 1935 cm^{-1} indicating the presence of a Rh(I) carbonyl containing species that appears at a lower $\nu(\text{CO})$ than the starting complex.

Rhodium pincer complexes containing NNP, NNN and NNC donors were used both with and without the KI additive (Scheme 5.13) the results are displayed in Table 5.8.



Scheme 5.13: Reaction conditions when using Rh(I) pincer complexes as catalysts.

Catalyst	Additive	Yield	Terminal %	Internal %	$\nu(\text{CO})/\text{cm}^{-1}$
5a	KI 50%	70	75	25	2092
5c	KI 50%	78	67	33	2070
5f	KI 50%	98	61	39	2070, 2039
12a	KI 50%	28	81	19	2092, 2074

Table 5.8: Yield and selectivity of alkenes and selected spectroscopic data obtained when using Rh(I) pincer complexes.

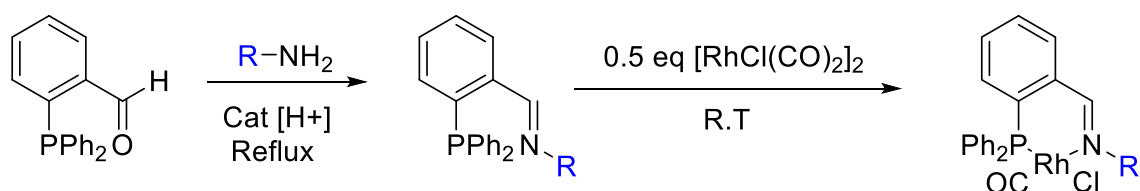
The Rh(I) pincer complexes successfully catalyse the decarbonylative dehydration of myristic acid when combined with KI and acetic anhydride in greater than 70% yield for complexes **5a**, **5c** and **5f**. A substantially lower yield of alkenes was obtained for complex **12a**. ³¹P{¹H} NMR analysis of the crude reaction mixture for complex **5a** revealed the presence of two doublets at δ 40.6 and δ 39.6 with $J_{\text{Rh-P}}$ coupling constants of 90.4 and 90.7 Hz respectively indicating that the phosphine ligand remains coordinated to rhodium. A $\nu(\text{CO})$ band in the Rh(III) region was also observed in the IR spectrum. In all cases without the KI additive no alkene product was observed.

Interestingly, even the highly reactive Rh(I) pincer complexes still require the KI additive for the decarbonylation reaction to occur at this temperature. The mechanism proposed by Maetani et al.⁶ suggests an oxidative addition of a C-O bond of an anhydride formed during the reaction to be the first metal containing step, however the omission of KI results in no alkene product when using pincer complexes. This suggests that the catalytic reaction requires the oxidative addition of a long chain acyl iodide species formed from

reaction of acid or anhydride with KI, supporting the mechanism proposed previously in Figure 5.4.

5.2 Synthesis and catalytic activity of Rh(I) iminophosphine complexes – isolation of Rh(III) products.

This section will discuss the synthesis, catalytic activity and products isolated when using Rh(I) iminophosphine complexes as catalysts. The complexes $[\text{RhCl}(\text{CO})(\text{PN-R})]$ **14a-g** were synthesised using a modified method developed by Best et al.¹⁷ for analogous iodo complexes (Scheme 5.14). The complexes were isolated as strongly coloured powders and were characterized by ^1H , ^{31}P and ^{13}C NMR spectroscopy, IR spectroscopy and mass spectrometry. Selected spectroscopic data for **14a-g** are shown in Table 5.9.

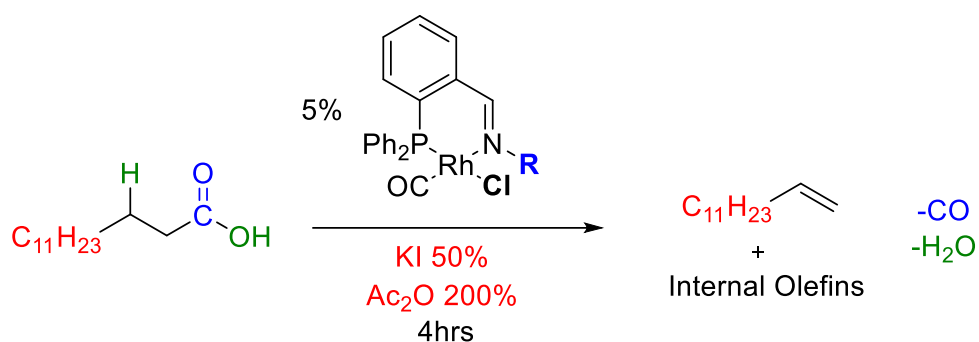


Scheme 5.14: Synthesis of $[\text{RhCl}(\text{CO})(\text{PN-R})]$ complexes **14a-g**.

Complex	R	Yield	$\nu(\text{CO})/\text{cm}^{-1}$	$\delta^{31}\text{P}$	$J_{\text{Rh-P}}/\text{Hz}$
14a	^t Bu	82	2005	52.3	172
14b	2-MeOC ₆ H ₄	81	2008	44.5	171
14c	3,5-(CF ₃) ₂ C ₆ H ₃	72	2011	46.1	165
14d	2,6-Me ₂ C ₆ H ₃	79	2009	47.6	171
14e	2,6-Et ₂ C ₆ H ₃	85	2009	43.4	165
14f	2,6- ⁱ Pr ₂ C ₆ H ₃	75	2009	40.4	172
14g	2,4,6-Me ₃ C ₆ H ₂	81	2008	44.1	167

Table 5.9: Selected spectroscopic data for complexes **14a-g**

The catalytic activity of **14a-g** was investigated (Scheme 5.15). The yields obtained for the decarbonylative dehydration of myristic acid (C₁₄) are displayed in Table 5.10 and comparable results for other long chain acids can be found in the Appendix.



Scheme 5.15: Decarbonylation of myristic acid using [Rh(CO)Cl(PN-R)] complexes **14a-g**.

Catalyst	R	Yield %	Terminal %	Internal %
14a	^t Bu	99	61	39
14b	2-MeOC ₆ H ₄	92	66	34
14c	3,5-(CF ₃) ₂ C ₆ H ₃	93	52	58
14d	2,6-Me ₂ C ₆ H ₃	95	68	32
14e	2,6-Et ₂ C ₆ H ₃	93	64	36
14f	2,6- ⁱ Pr ₂ C ₆ H ₃	81	60	40
14g	2,4,6-Me ₃ C ₆ H ₂	69	63	37

Table 5.10: Yield and selectivity of C₁₃H₂₆ alkene products obtained using complexes **14a-g**.

Pleasingly, the results in Table 5.10 show that the Rh(I) iminophosphine carbonyl complexes **14a-g** effectively catalyse the decarbonylative dehydration of myristic acid with yields >69%. The selectivity slightly favours 1-alkene product.

Analysis of the crude reaction mixtures obtained after catalysis by ¹H, ³¹P and IR spectroscopy revealed some interesting observations. A summary of the spectroscopic data obtained is displayed in Table 5.11 and a sample ³¹P{¹H} NMR spectrum obtained after a catalytic reaction using **14f** is displayed in Figure 5.6.

Catalysts **14a** and **14c** both degrade under catalytic conditions, evidenced by the lack of *J*_{Rh-P} coupling in the ³¹P{¹H} NMR spectra. Analysis of the catalytic residue using **14e** reveals the presence of **14e** and a new doublet at δ 53.5 with a *J*_{Rh-P} coupling constant of 110 Hz. The resulting reaction mixtures after catalysis using complexes **14b** and **14d-g** each display a single doublet at ca. δ 55 with a coupling constant of ca. 110 Hz. IR spectroscopy reveals the presence of a Rh(III) carbonyl containing complex.

Catalyst	$\nu(\text{CO})/\text{cm}^{-1}$	$\delta^{31}\text{P}$ ($J_{\text{Rh-P}}/\text{Hz}$)
14a	multiple	multiple signals
14b	2075	55.6 (108)
14c	multiple	multiple signals
14d	2072	53.4 (110)
14e	2072, 2009	53.5(110), 43.4(165)
14f	2072	53.0 (110)
14g	2071	55.5(109)

Table 5.11: Resulting $\nu(\text{CO})$ and $^{31}\text{P}\{^1\text{H}\}$ NMR data observed after catalysis using **14a-g** as catalysts.

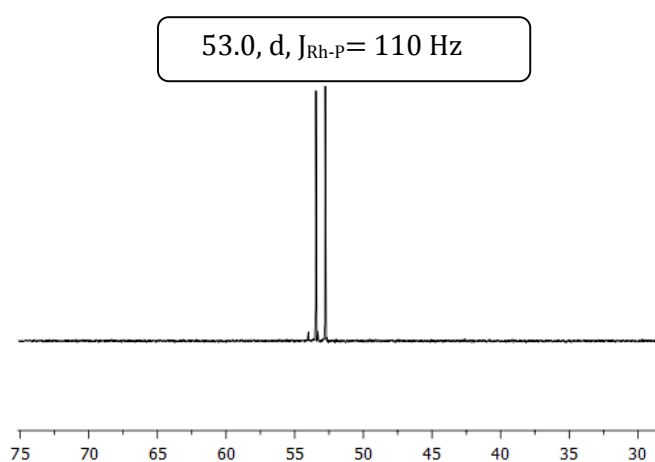


Figure 5.6: $^{31}\text{P}\{^1\text{H}\}$ NMR spectrum obtained using **14f** as a catalyst.

Repeating the catalytic reactions on a larger scale for **14d**, **14f** and **14g** enabled isolation of the Rh species, **15d**, **15f** and **15g** respectively. Mass spectrometry is consistent with species $[\text{Rh}(\text{PN-R})(\text{CO})\text{I}_2(\text{COCH}_3)]$ (associated with a sodium cation) resulting from formal addition of acetyl iodide to $[\text{Rh}(\text{PN-R})(\text{CO})\text{I}]$. IR spectroscopy showed a band at $\sim 1560\text{ cm}^{-1}$, which is significantly lower in frequency than that expected for a rhodium acetyl species such as $[\text{Rh}(\text{PN-R})\text{I}_2(\text{COCH}_3)]$ obtained from oxidative addition of MeI to $[\text{Rh}(\text{PN-R})(\text{CO})\text{I}]$ ($\sim 1720\text{ cm}^{-1}$).¹⁷ A very weak additional doublet is also noted with similar chemical shift and coupling constant (the proposed identity of this species will be discussed later).

Crystals of **15f**, and **15g** suitable for X-ray crystallography were obtained by slow diffusion of hexanes into concentrated CH_2Cl_2 solutions of the complexes. The structures of both **15f** and **15g** are displayed in Figure 5.7 along with selected bond lengths and angles in Table

5.12. The structures revealed that the imino nitrogen of the P,N-R ligand had been acetylated to generate a new tridentate ligand co-ordinated to Rh through phosphorus and carbon as well as the acetyl carbonyl oxygen.

Complexes **15f** and **15g** both display a distorted octahedral geometry with the tridentate ligand bonding in a *fac* coordination geometry. The ligand forms two five-membered rings with the rhodium centre with a P-Rh-O bond angle of ca. 94.4° . The nitrogen now forms part of a 5-membered metallocycle with the large aromatic group being orientated in such a way to minimise steric interaction. The carbon (C(2)) now bound to rhodium is a tetrahedral sp^3 carbon with bond angles of ca. 110° . The C(2)-N bond distances are ca. 1.49 Å, typical for a single bond.

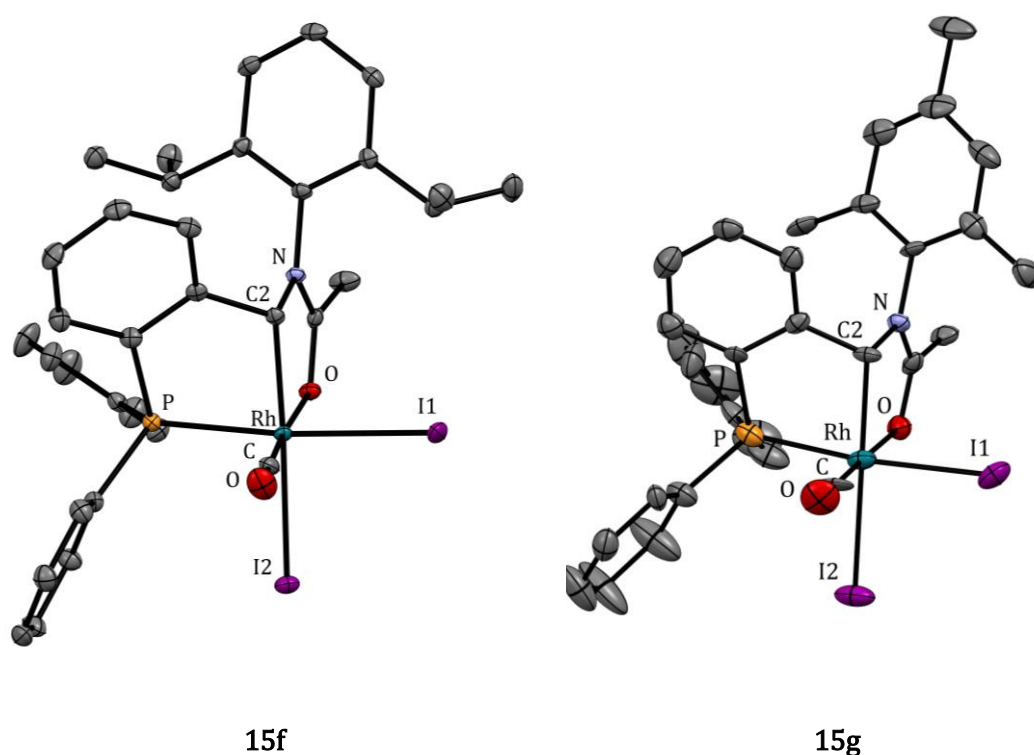
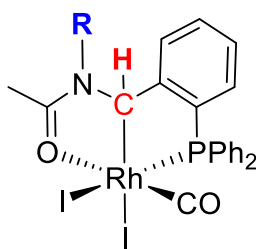


Figure 5.7: X-ray crystal structures of complexes **15f** and **15g** with thermal ellipsoids shown at 50% probability level. Hydrogen atoms and disordered H₂O molecules (for **15g**) are omitted for clarity.

	15f	15g
Rh-C2	2.0800(19)	2.070(9)
Rh-CO	1.845(2)	1.835(11)
Rh-O	2.0479(13)	2.063(6)
Rh-P	2.2880(5)	2.290(3)
Rh-I1	2.7215(2)	2.7101(12)
Rh-I2	2.7569(2)	2.7524(11)
N1-C2	1.495(2)	1.490(11)
P-Rh-I1	172.451(15)	173.13(8)
C2-Rh-I2	172.72(5)	173.3(3)
O2-Rh-CO	173.04(7)	174.4(4)

Table 5.12: Selected bond length (Å) and angles (deg) for complexes **15f** and **15g**

The crystal structures are consistent with the spectroscopic data. A low frequency C=O arises from interaction of N-acetyl group with Rh centre. The acetyl CH₃ gives a singlet at ca. δ 1.3. The backbone methine unit now coordinated to Rh was more difficult to locate by NMR spectroscopy but assignment was aided by HSQC C-H correlation NMR spectra of complex **15f**. The Rh-bound carbons of related complexes (shown in Fig 5.9) give ¹³C resonances near 70 ppm. For **15d,f,g** a doublet is observed near 80 ppm with J_{Rh-C} coupling of approximately 22 Hz. In the HSQC spectrum, this signal correlates with a ¹H doublet at δ 6.8, quite close to the aromatic region with a J_{H-C} coupling constant of approximately 3 Hz (shown in Figure 5.8). The aryl substituents at the 2 and 6 positions are not magnetically equivalent in the ¹H NMR spectra indicating rotation is restricted around the N-aryl bond. The ¹H and ¹³C resonances for the sp³ carbon ligand of **15d**, **15f** and **15g** are displayed in Table 5.13.



Complex	R	$\delta^1\text{H C-H (J/Hz)}$	$\delta^{13}\text{C C-H (J}_{\text{Rh-C}}/\text{Hz})$
15d	2,6-Me ₂ C ₆ H ₃	6.8, d (2.6)	79.42, d (23.2)
15f	2,6- <i>i</i> -Pr ₂ C ₆ H ₃	6.8, d (2.9)	80.75, d (22.8)
15g	2,4,6-Me ₃ C ₆ H ₂	6.7, d (2.7)	79.45, d (23.0)

Table 5.13: Selected ¹H and ¹³C{¹H} NMR data for **15d**, **15f** and **15g**.

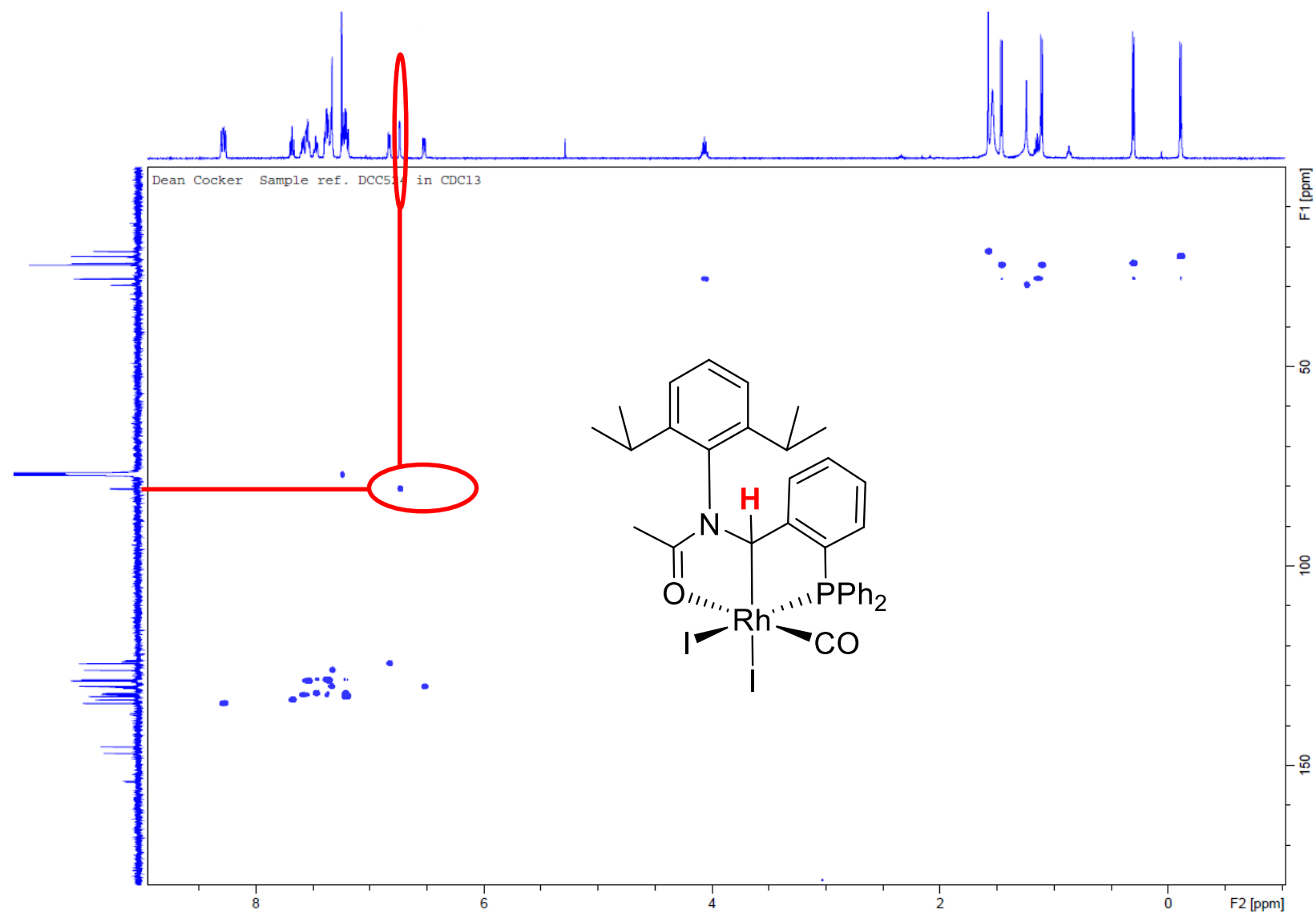


Figure 5.8: HSQC C-H NMR correlation spectrum of **15f** (CDCl₃).

Some related structures are known in the literature but these arise from C-H activation of an N-acylated precursor, these structures are shown in Figure 5.9 along with their ^1H and $^{13}\text{C}\{^1\text{H}\}$ NMR chemical shifts. ^{18,19}

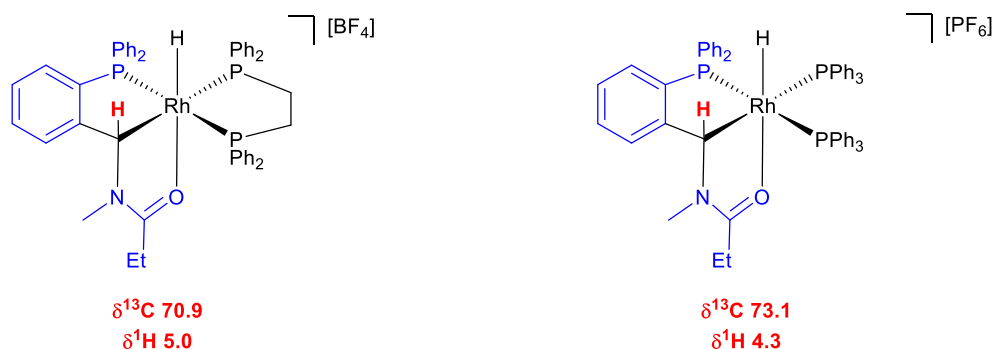
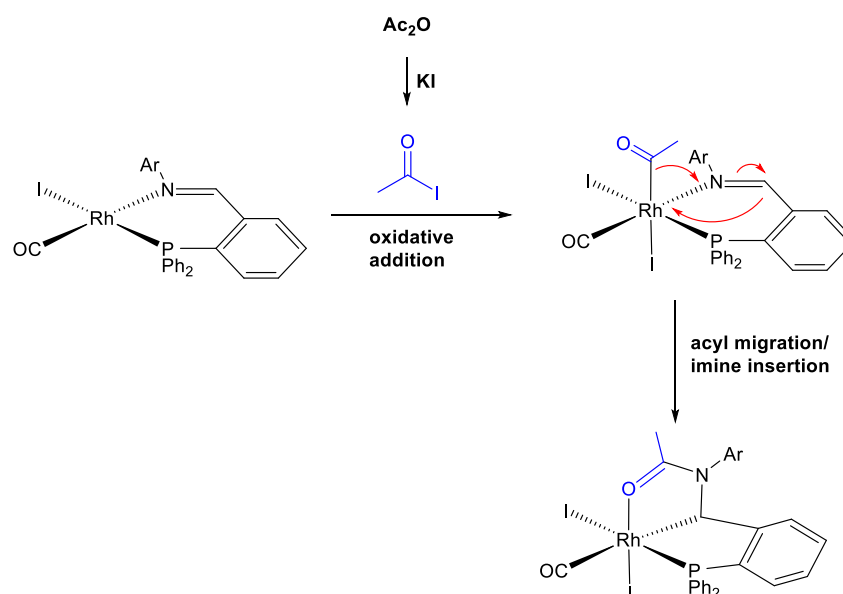


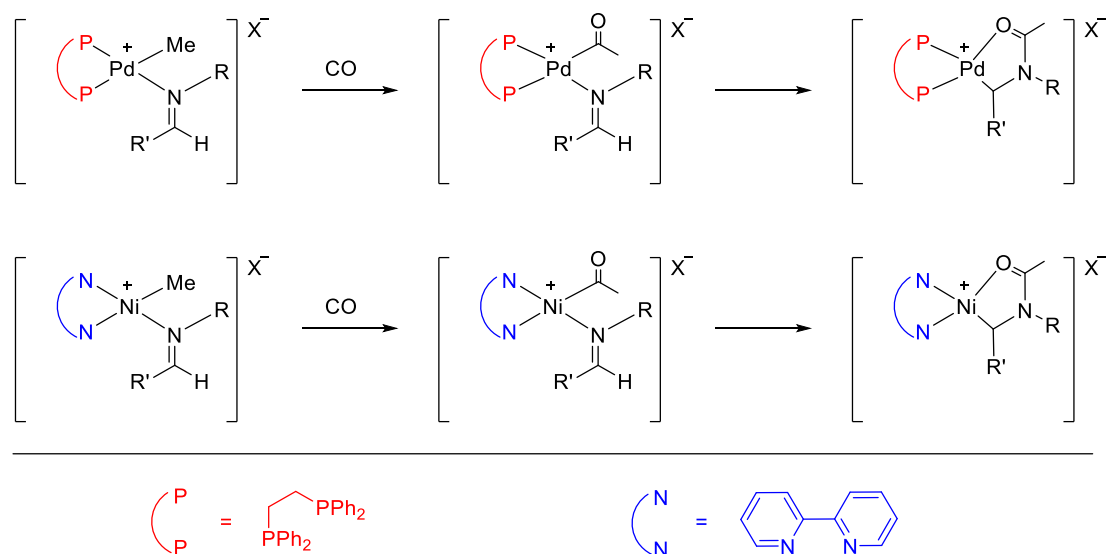
Figure 5.9: Related Rh(III) hydride complexes reported by Sjövall et al.^{18,19}

In complexes **15d**, **15f** and **15g** the acetyl group must originate from acetic anhydride. The proposed mechanism of formation of the Rh(III) species **15b** and **15d-f** is shown in Scheme 5.16 in which the starting Rh(I) complex firstly undergoes halide exchange with iodide, this is followed by oxidative addition of acetyl iodide formed from acetic anhydride and excess KI to form a Rh(III) acetyl complex. Acyl migration (or imine insertion) and coordination of the acyl oxygen affords the observed P,C,O chelate product.



Scheme 5.16: Proposed mechanism of formation of complex **15b** and **15d-g**.

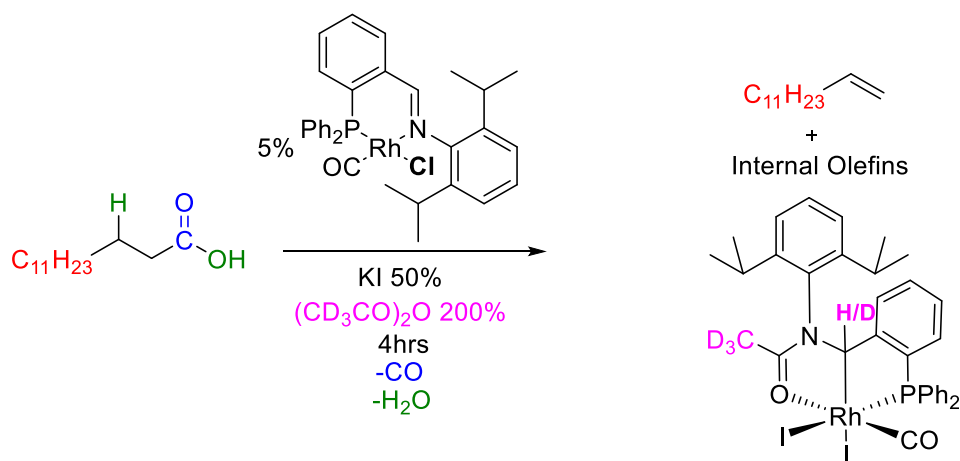
Cationic palladium and nickel complexes as well as neutral manganese complexes are known to undergo this type of insertion reaction.²⁰⁻²² Scheme 5.17 shows imine insertion into M-acetyl bonds of cationic nickel and palladium complexes.



Scheme 5.17: Imine insertion reactions of cationic palladium and nickel complexes.^{20,21}

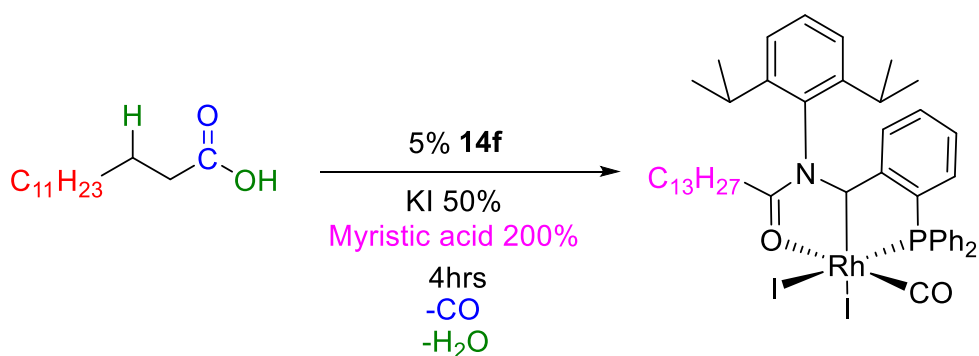
With the identity of these compounds confirmed both spectroscopically and crystallographically, the formation of these complexes was investigated using complex **14f** as a model substrate. Interestingly, in the absence of KI, **15f** was not detected spectroscopically in the crude reaction mixture and no alkene product was produced, highlighting the importance of the KI additive.

Performing the decarbonylation reaction using a deuterated acetic anhydride additive $(\text{CD}_3\text{CO})_2\text{O}$ resulted in the formation of deuterium labelled **15f** (Scheme 5.18) this was isolated and characterised by ^{31}P and ^1H NMR. The ^1H NMR spectrum obtained after the reaction was identical to unlabelled **15f** but lacked the ^1H NMR signal for the acetyl group. Interestingly the signal for the sp^3 C-H proton appears at 50% expected integration intensity indicating 50% deuterium incorporation at this position. This will be discussed later in the next chapter.



Scheme 5.18: Conditions used in the synthesis of deuterium labelled **15f**.

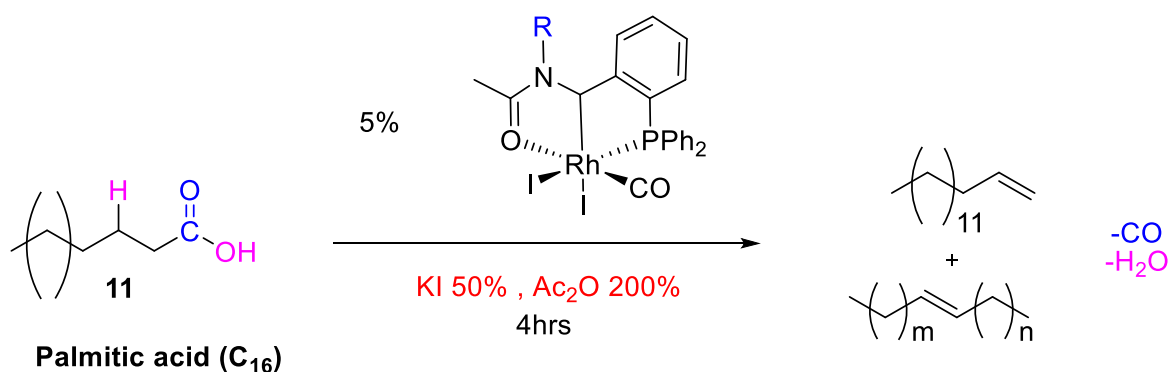
Since the reaction mixture contains long chain carboxylic acid, scrambling between Ac₂O and RCO₂H could give mixed anhydride MeCO₂COR, and hence long chain acyl iodide, RCOI. Addition of RCOI via an analogous mechanism to that proposed in Figure 5.11 would give a complex corresponding to **15f** but with long chain R. This was tested in an experiment with **14f** and myristic acid/myristic anhydride (Scheme 5.19). Analysis of this reaction give a species with ³¹P doublet very close to **15f** and a peak in the mass spectrum (m/z 1068.13) consistent with the long chain analogue. The ³¹P signal also matches the weak additional doublet formed in the experiment using **14f** and myristic acid/acetic anhydride (see Figure 5.7), suggesting that a small amount of the long chain analogue of **15f** is formed in that experiment.



Scheme 5.19: Formation of long chain Rh(III) tridentate complex.

5.2.1 Decarbonylative dehydration of long chain acids using complexes **15d**, **15f** and **15g**

The decarbonylative dehydration of palmitic acid (C₁₆) using **15d**, **15f** and **15g** as catalysts was investigated (Scheme 5.20) to identify if the Rh(III) complexes obtained after catalysis remained catalytically active. The results are displayed in Table 5.14.



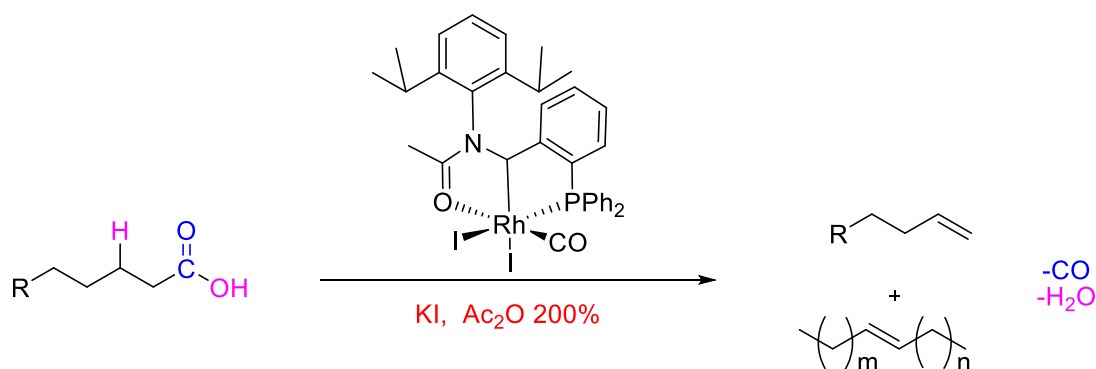
Scheme 5.20: Decarbonylative dehydration of palmitic acid using **15d** **15f** and **15g** as catalysts.

Catalyst	R	Yield %	Terminal %	Internal %
15d	2,6-Me ₂ C ₆ H ₃	0	0	0
15f	2,6- ⁱ Pr ₂ C ₆ H ₃	84	70	30
15g	2,4,6-Me ₃ C ₆ H ₂	73	60	40

Table 5.14: Yields and selectivity of C₁₅H₃₀ alkene obtained after catalysis using **15d**, **15f** and **15g**.

Interestingly, complexes **15f** and **15g** remain catalytically active yielding alkenes in over a 70% yield, however complex **15d** does not catalyse the reaction. In all three cases analysis of the crude reaction mixture reveals **15d**, **15f** and **15g** remain as the only detectable Rh species after catalysis.

The catalytic activity of **15f** was investigated further by changing the carboxylic acid chain length, KI loading and catalyst loading (Scheme 5.21). Complex **15f** decarbonylates C₁₂, C₁₄ and C₁₆ chain length carboxylic acids when combined with 50% loading of KI. The yields are over 80% in each case with moderate selectivity toward the 1-alkene product. Lowering the catalyst loading to 1% results in a decreased yield to 65% which increases to 75% if the reaction is left for 8 hours. Notably, without KI no alkenes are formed. In all cases complex **15f** is the only rhodium species observed in solution, remaining spectroscopically identical before and after the reaction. Table 5.15 displays the results from this study.



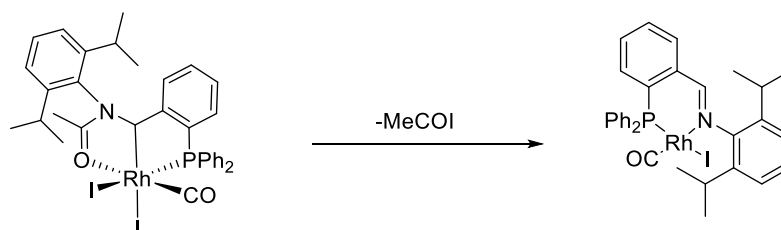
Scheme 5.21: Decarbonylative dehydration of different chain length acids using complex **15f**.

Acid	Catalyst loading %	Time / hrs	KI loading %	Yield %	Terminal %	Internal %
C ₁₂	5	4	50	94	76	24
C ₁₄	5	4	50	85	69	31
C ₁₆	5	4	50	84	70	30
C ₁₆	5	4	0	0	0	0
C ₁₄	1	4	50	65	70	30
C ₁₄	1	8	50	75	72	28

Table 5.15: Results from catalytic studies using **15f**.

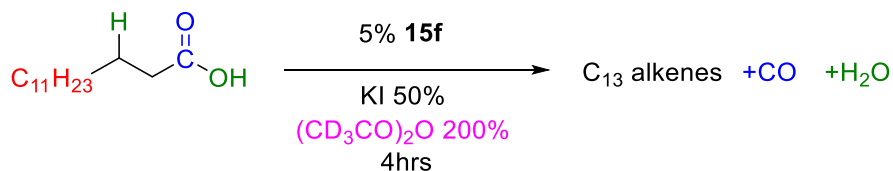
5.2.2 Mechanistic studies

Since **15f** is a coordinatively saturated Rh(III) complex, a reductive elimination would need to occur to generate a Rh(I) species that can participate in the proposed catalytic mechanism (Scheme 5.5) involving oxidative addition of long chain acyl iodide. One possibility is elimination of acetyl iodide (Scheme 5.22) by a reverse of the mechanism shown in Figure 5.11.



Scheme 5.22: Possible elimination route for complex **15f**.

Evidence for such a process was sought in a catalytic experiment using complex **15f** and deuterated acetic anhydride $(\text{CD}_3\text{CO})_2\text{O}$ (Scheme 5.23). However, the ^1H NMR spectrum of recovered **15f** showed no evidence for deuterium incorporation in the acetyl moiety (i.e. the acetyl ^1H NMR signal retained the expected relative intensity for a COCH_3 group). The lack of scrambling of acetyl groups between **15f** and $(\text{CD}_3\text{CO})_2\text{O}$ under catalytic conditions shows that the elimination proposed in Figure 5,12 does not occur. The mechanism by which **15f** acts as a catalyst remains uncertain.



Scheme 5.23: Deuterium labelling experiment using complex **15f**

Interestingly, however, evidence was found for deuterium incorporation in the C_{13} alkene products in this experiment. Figure 5.10 compares ^1H NMR spectra for the alkene products in experiments using $(\text{CH}_3\text{CO})_2\text{O}$ or $(\text{CD}_3\text{CO})_2\text{O}$ additives. The bottom (red) spectrum clearly shows added complexity in the splitting patterns of the olefinic ^1H signals due to coupling to ^2H nuclei. The set of resonances at ca. δ 4.9-5.0, arising from the hydrogens at C-1 of the terminal alkene product also has depleted relative intensity, suggesting preferential replacement by deuterium at this position.

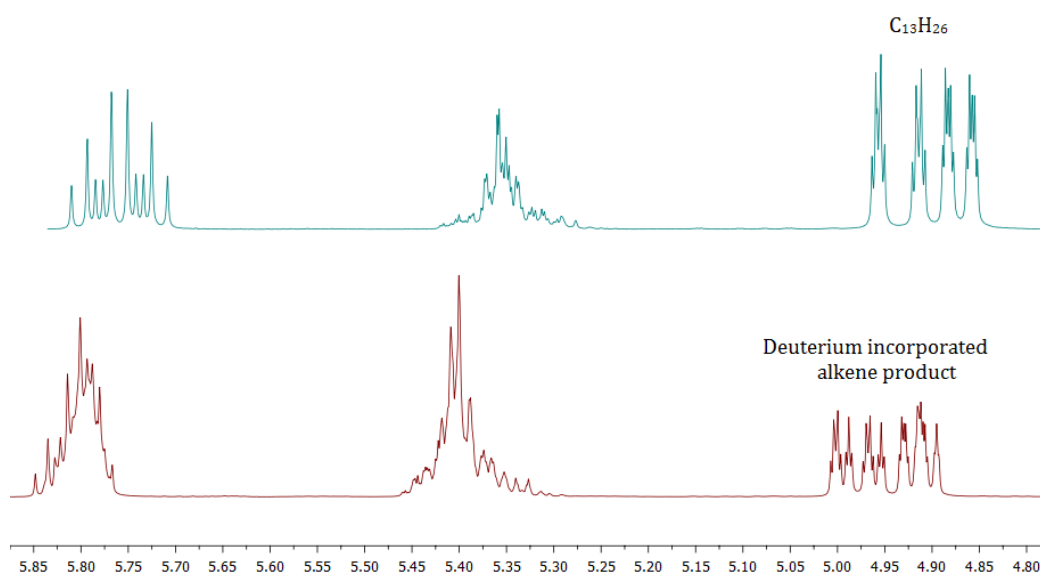


Figure 5.10: Partial ^1H NMR spectra of alkene products from catalytic experiments using $(\text{CH}_3\text{CO})_2\text{O}$ (top) and $(\text{CD}_3\text{CO})_2\text{O}$ (bottom).

A ^2H NMR spectrum (Figure 5.11) shows resonances in the regions δ 4.9-5 and δ 1.6-1.5 confirming the incorporation of deuterium in the alkene products. Assignment was aided by comparison with data from Lazzaroni et al. for deuterated alkenes observed in alkene hydroformylation experiments using CO/D_2 .²³ The signals at δ 5.03-4.94 are attributed to the incorporation of deuterium at the C-1 position of the 1-alkene product, consistent with the ^1H NMR data. The absence of ^2H NMR signals at δ 5.8 and 5.4 indicates that there is no deuterium incorporation at the C-2 position of the terminal alkene product, or at the olefinic positions of internal alkene products. The signals occurring between δ 1.6 to δ 1.56 can be attributed to deuteration at C-1 of internal alkene products. Hence, the data obtained from ^1H and ^2H NMR analysis gives evidence for specific D-incorporation on the terminal carbon of the alkene products.

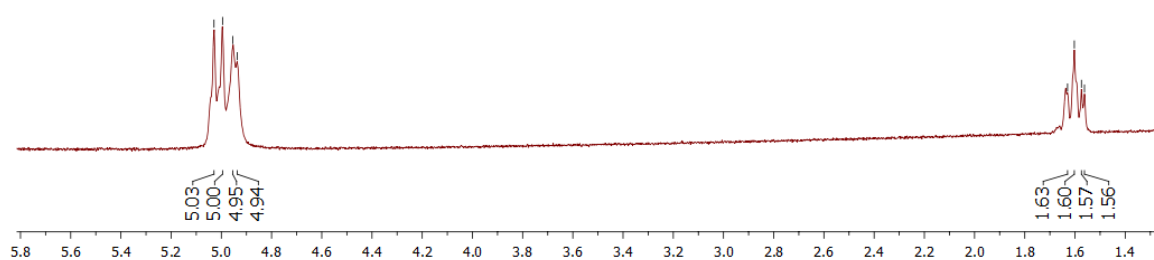
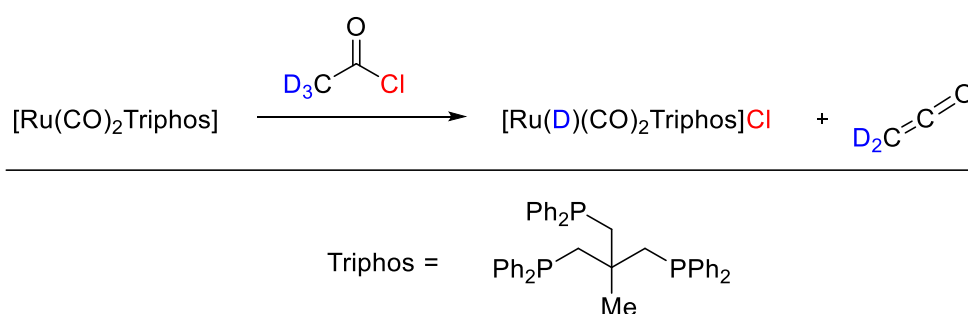


Figure 5.11: Partial ^2H NMR spectrum of deuterated alkene product (CDCl_3 298K).

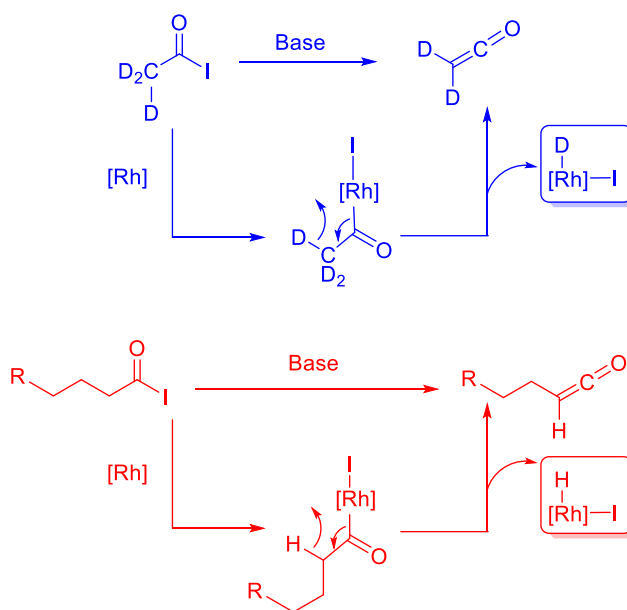
Analysis of alkene product by GCMS reveals the most abundant molecular ion peak at m/z 184.2 which can be assigned to $\text{C}_{13}\text{H}_{24}\text{D}_2$. Weaker peaks at m/z 183.2 and 182.2 can be assigned to $\text{C}_{13}\text{H}_{25}\text{D}_1$ and $\text{C}_{13}\text{H}_{26}$ respectively.

Deuterium incorporation in the alkene product gives insight into an unexpected mechanism occurring during the reaction. The only source of deuterium is from the $(\text{CD}_3\text{CO})_2\text{O}$ additive, therefore a C-D bond must be broken and transferred to the rhodium centre. A search of the literature revealed that deuterated acetyl chloride can be converted to ketene in the presence of a $\text{Ru}(\text{O})$ complex (Scheme 5.24) forming a $\text{Ru}(\text{II})$ deuteride complex and ketene.²⁴



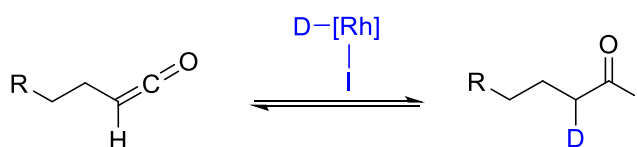
Scheme 5.24: Elimination of ketene from a ruthenium phosphine complex.²⁴

The large amount of KI in the decarbonylation reaction means that CD_3COI will likely be formed by reaction of iodide with $(\text{CD}_3\text{CO})_2\text{O}$. Ketene can then be formed by dehydrohalogenation of acetyl iodide by base (perhaps unlikely under acidic conditions) or by addition to Rh and β -elimination of the resulting rhodium acetyl complex. A long chain acyl iodide formed by reaction of KI with a long chain anhydride could undergo the same transformation to form a long chain ketene as shown in Scheme 5.25. Ketene formation from a Rh(III) phosphine complex has been proposed by Cole-Hamilton for the acyl complex $[\text{Rh}(\text{CO})(\text{COCH}_2\text{I})(\text{PET}_3)_2\text{I}]$ which undergoes loss of iodide and forms a ketene complex.²⁵



Scheme 5.25: proposed mechanism for ketene formation

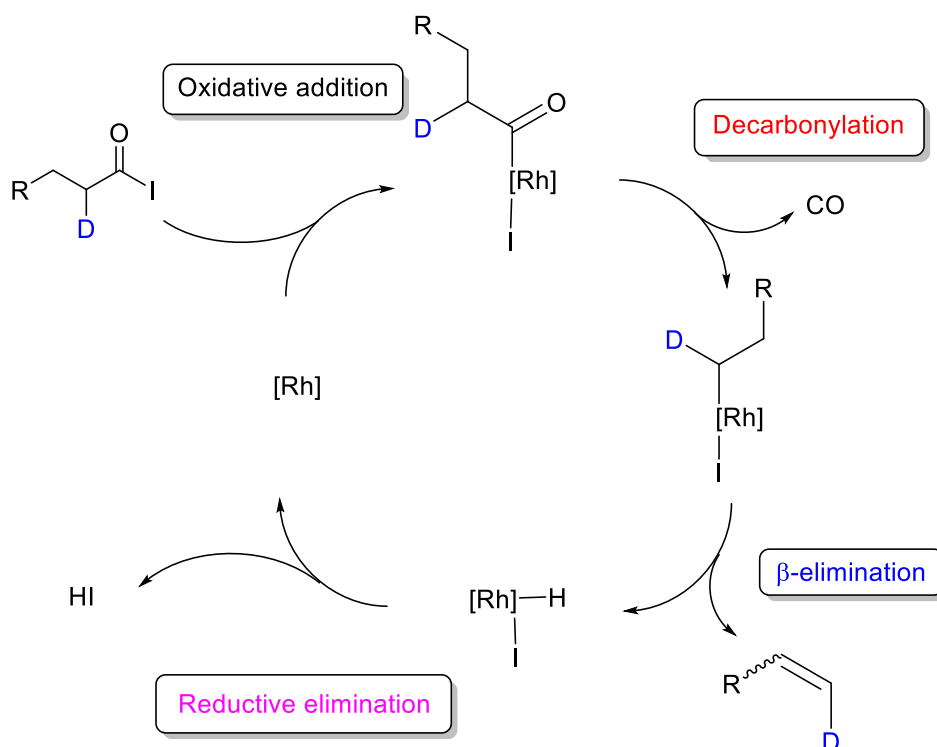
If the formation of the long chain ketene is reversible, deuterium can be incorporated into an acyl moiety by reaction with a Rh-D species as shown in Scheme 5.26. The reversible insertion of ketenes into $[\text{HCo}(\text{CO})_4]$ and $[\text{HMn}(\text{CO})_5]$ has been previously reported by Lindner et al. and Ungváry et al.^{26,27}



Scheme 5.26: Deuterium incorporation into a long chain ketene complex

This reversibility can account for the selective deuteration at the C-1 position of the terminal alkene product. If the formation of the long chain ketene and deuterated long

chain acyl iodide occurs before the decarbonylation reaction, deuterium will be incorporated into the C-1 position as shown in Scheme 5.27. Further deuterium incorporation might be facilitated by a rhodium deuteride complex during alkene isomerisation.



Scheme 5.27: Proposed mechanism for deuterium incorporation at the C-1 position of the 1-alkene product.

It is of interest whether incorporation of deuterium from $(CD_3CO)_2O$ into the alkene products is particular to reactions catalysed by complex **15f** (and relatives) or more general for other complexes that catalyse the decarbonylative dehydration reactions. A control experiment was performed using Vaska's complex with the conditions developed by Maetani et al.⁶ but replacing the $(CH_3CO)_2O$ additive with $(CD_3CO)_2O$. The product 1H NMR spectrum (shown in Figure 5.12) shows additional complexity in the splitting patterns of the olefinic signals and depletion of the integrated intensity for 1H at the C-1 position relative to C-2 of the terminal alkene product. The 2H NMR spectrum again shows peaks at ca. δ 5.0, attributed to the incorporation of deuterium at the C-1 position of the 1-alkene product. The signals between δ 1.6 to δ 1.56 can be attributed to deuterated internal alkene products. These are weak due to the greater selectivity toward terminal alkene of the $[IrCl(CO)(PPh_3)_2]$ catalyst compared to **15f**. The weak peak at δ 5.8 can be assigned to a small amount of deuterium incorporation at the C-2 position of the terminal alkene product. GCMS indicates that the major molecular ion peak is at m/z 184.2 assigned

to $C_{13}H_{24}D_2$. The intensity of the peak at m/z 183.2 for $C_{13}H_{25}D_1$ is substantially smaller and there is no evidence of $C_{13}H_{26}$.

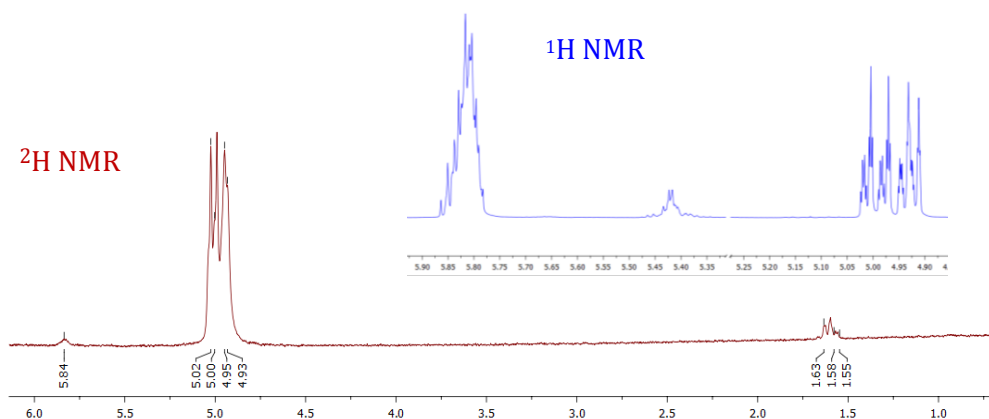


Figure 5.12: 1H and 2H NMR spectra of the alkenes obtained after the control experiment using $[IrCl(CO)(PPh_3)_2]$ catalyst with $(CD_3CO)_2O$ additive.

These results show that deuteration of the alkene products does indeed occur using $[IrCl(CO)(PPh_3)_2]$ as catalyst when and is not unique to the Rh systems described above. The detection of deuterium in the reaction products is indicative of ketene formation and indirect evidence of acyl iodide formation. The evidence collected during this study indicates that oxidative addition of a long chain acyl iodide is a plausible catalytic reaction step when KI and acetic anhydride additives are used. It is also apparent that acetic anhydride does not simply act as a dehydration agent but participates directly in the alkene formation mechanism.

5.3 Summary

The decarbonylative dehydration of a number of fatty acids using KI and acetic anhydride as additives has been investigated using both microwave and standard heating. High yields of alkenes were obtained for Ir(I) monodentate phosphine complexes $[IrCl(CO)(PR_3)_2]$. The complex $[IrCl(CO)(PCy_3)_2]$ has been identified as a highly active catalyst that is selective for internal alkenes. Bidentate and tridentate Ir(I) chelate complexes screened in this study were not catalytically active.

Monodentate and bidentate Rh(I) phosphine catalysts produced high yields of alkene product, however catalyst degradation was observed in the $^{31}P\{^1H\}$ NMR spectra of the reaction mixtures. A series of Rh(I) pincer complexes were tested in the catalytic reaction and all but the PXCXP pincer complexes were active. The crude reaction mixtures of the

pincer complexes incorporating a phosphine ligand were found to show $J_{\text{Rh-P}}$ coupling indicating that the phosphine ligand is still co-ordinated to the rhodium centre.

Interestingly [Rh(R-PN)(CO)Cl] catalysts **14a-g** all yield alkene product, but in some cases also form a tridentate Rh(III) complex which in three cases were isolated as stable solids **15d**, **15f** and **15g**. These complexes were tested under catalytic conditions and in two cases (**15f** and **15g**) were found to remain catalytically active and recyclable.

A mechanistic study using a $(\text{CD}_3\text{CO})_2\text{O}$ additive reveals deuterium incorporation in the final alkene product, indicative of C-D bond breaking and formation of a ketene under the reaction conditions. Ketene formation from acyl halide complexes is known within the literature and supports the mechanistic proposal of formation of long chain acyl iodide and acetyl iodide, however further investigation is needed to probe this mechanism.

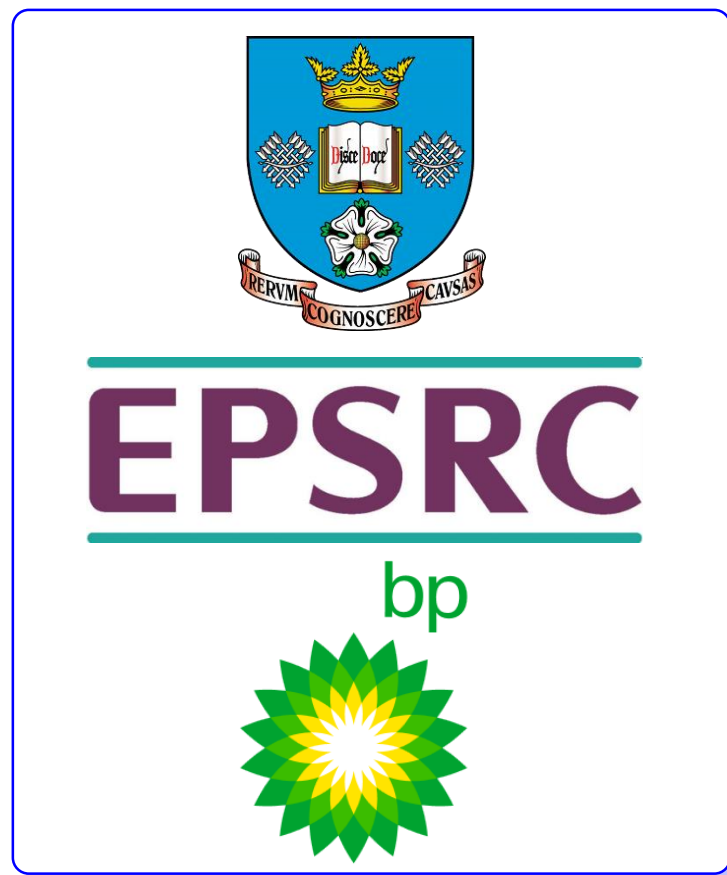
5.4 References

- (1) Foglia, T. Barr, P. *J. Am. Oil Chem. Soc.* **1976**, *53*, 737.
- (2) Gooßen, L.; Rodriguez, N. *Chem. Commun.*, **2004**, 724.
- (3) John, A.; Hogan, L. T.; Hillmyer, M. A.; Tolman, W. B. *Chem. Commun.*, **2015**, *51*, 2731.
- (4) Le Nôtre, J.; Scott, E. L.; Franssen, M. C. R.; Sanders, J. P. M. *Tetrahedron Lett.* **2010**, *51*, 3712.
- (5) Liu, Y.; Kim, K. E.; Herbert, M. B.; Fedorov, A.; Grubbs, R. H.; Stoltz, B. M. *Adv. Synth. Catal.* **2014**, *356*, 130.
- (6) Maetani, S.; Fukuyama, T.; Suzuki, N.; Ishihara, D.; Ryu, I. *Organometallics*. **2011**, *30*, 1389.
- (7) Maetani, S.; Fukuyama, T.; Suzuki, N.; Ishihara, D.; Ryu, I. *Chem. Commun.*, **2012**, *48*, 2552.
- (8) Miller, J. A.; Nelson, J. A.; Byrne, M. P. *J. Org. Chem.*, **1993**, *58*, 20.
- (9) Miranda, M. O.; Pietrangelo, A.; Hillmyer, M. A.; Tolman, W. B. *Green Chem.* **2012**, *14*, 490.
- (10) de la Hoz, A.; Diaz-Ortiz, A.; Moreno, A. *Chem. Soc. Rev.* **2005**, *34*, 164.
- (11) Burk, M. J.; Crabtree, R. H. *Inorg. Chem.* **1986**, *25*, 931.
- (12) Strohmeier, W.; Fleischmann, R. *J. Organometal. Chem.* **1972**, *42*, 163.
- (13) John, C. MChem Thesis, University Of Sheffield. **2011**.
- (14) Basson, S. S.; Leipoldt, J. G.; Roodt, A.; Venter, J. A.; van der Walt, T. J. *Inorg. Chim. Acta.* **1986**, *119*, 35.
- (15) Conradie, M. M.; Conradie, J. *Dalton. Trans.* **2011**, *40*, 8226.

- (16) Brink, A.; Roodt, A.; Steyl, G.; Visser, H. G. *Dalton. Trans.* **2010**, *39*, 5572.
- (17) Best, J.; Wilson, J. M.; Adams, H.; Gonsalvi, L.; Peruzzini, M.; Haynes, A. *Organometallics*. **2007**, *26*, 1960.
- (18) Sjövall, S.; Andersson, C.; Wendt, O. F. *Organometallics*. **2001**, *20*, 4919.
- (19) Sjövall, S.; Svensson, P. H.; Andersson, C. *Organometallics*. **1999**, *18*, 5412.
- (20) Dghaym, R. D.; Yaccato, K. J.; Arndtsen, B. A. *Organometallics*. **1998**, *17*, 4.
- (21) Davis, J. L.; Arndtsen, B. A. *Organometallics*. **2000**, *19*, 4657.
- (22) Lafrance, D.; Davis, J. L.; Dhawan, R.; Arndtsen, B. A. *Organometallics*. **2001**, *20*, 1128.
- (23) Lazzaroni, R.; Uccello-Barretta, G.; Benetti, M. *Organometallics*. **1989**, *8*, 2323.
- (24) Singh, S.; Baird, M. C. *J. Organomet. Chem.* **1988**, *338*, 255.
- (25) Weston, W. S.; Cole-Hamilton, D. J. *Inorg. Chim. Acta*. **1998**, *280*, 99.
- (26) Lindner, E.; Berke, H. *Naturforsch., A*. **1974**, *29A*, 275.
- (27) Ungvary, F. *J. Chem. Soc., Chem. Commun.* **1984**, 824.

Chapter 6

Conclusions and future work



6.1 Conclusions

This project has investigated the effect of systematic variation of both ligand and metal on the catalytic decarbonylative dehydration of long chain acids and anhydrides. Firstly the project investigated ligand and metal effects on oxidative addition (a proposed mechanistic step in this reaction) of a simple substrate in order to identify highly nucleophilic complexes. These complexes were then used in the decarbonylative dehydration of long chain acids in order to identify if nucleophilicity plays a major part in catalytic activity.

Although the complexes synthesised in this study are all relatively electron rich, their reactivity towards MeI is strongly dependent upon the ligand donor set and substituents. For example in chapter 2 it was found that for iridium iminopyrrolyl phosphine carbonyl complexes [Ir(CO)(Ph-NN)(PPh₃)] (**3a**) is 17 times more reactive than [Ir(CO)(2,6-*i*Pr₂C₆H₃-NN)(PPh₃)] (**3k**) due to the bulky aryl substituent in the latter complex.

The Rh(I) NNX complexes synthesised in chapter 3 provide an excellent demonstration of how ligand donor strength can affect the rate of oxidative addition. For the pincer complexes [Rh(CO)(PPh₂NN)] (**5a**), [Rh(CO)(H-NNN)] (**5c**), and [Rh(CO)(Me-CNN)] (**5e**) a systematic change in donor atom from P to N to C results in both an increase in reactivity toward MeI and a lowering of the carbonyl stretching frequency as shown in Figure 6.1.

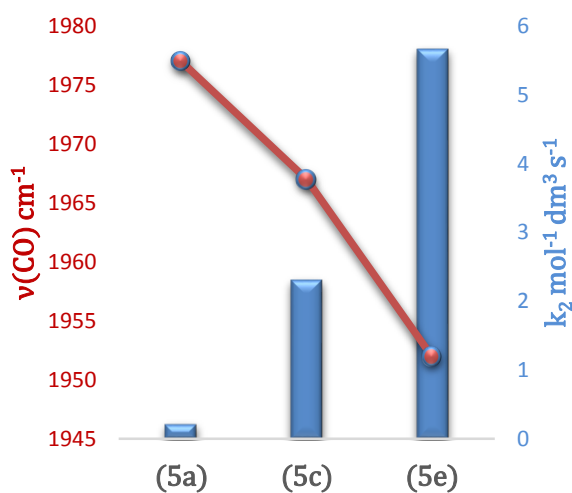


Figure 6.1: Plot showing effect on $\nu(\text{CO})$ and k_2 values on systematic variation of donor ligand.

In general, Ir(I) complexes are at least an order of magnitude more reactive toward MeI than the corresponding Rh(I) congeners. For example complex **8b** [Ir(CO)(*o*-Tol₂PNN)] is

approximately 20 times more reactive toward MeI than the rhodium analogue **5b**. As well as being more reactive, the iridium congeners form stable Ir(III)-methyl complexes and do not undergo migratory insertion. The same can be said for the Ir(PNP) pincer complexes **10a-e** which are an order of magnitude more reactive than the rhodium systems reported by Wells⁴ and form stable Ir(III)-methyl species.

Complexes containing *o*-anisyl substituted phosphine ligands were found to have the highest rates of MeI oxidative addition. It is proposed that a metal-O interaction stabilises the S_N2 transition state for oxidative addition which lowers the barrier of activation.¹⁻³ Complex **10c** [Ir(CO)(*o*-An-PNP)] has a k_2 for MeI oxidative addition of 400 mol⁻¹ dm³ s⁻¹, the highest reported for any Ir(I) complex, and is nucleophilic enough to activate a C-Cl bond of CH₂Cl₂ at ambient temperature.

The decarbonylative dehydration of long chain carboxylic acids has been investigated using rhodium and iridium complexes with monodentate and multidentate ligands. An initial investigation showed that Vaska-type [IrCl(CO)(PR₃)₂] complexes are efficient catalysts for the decarbonylative dehydration reaction. In particular, [IrCl(CO)(PCy₃)₂] showed high activity and was selective for internal alkene products. The multidentate Ir(I) complexes [Ir(CO)(Ar-NN)(PR₃)] and [Ir(CO)(R-PNP)] complexes were not active catalysts for this reaction with or without a KI additive.

A selection of [Rh(acac)(CO)L] and [RhCl(P-P)(CO)] (P-P = dppe, dppms and xanthphos) complexes were tested and were identified as efficient catalysts but ³¹P{¹H} analysis of the crude reaction mixtures indicated loss of phosphine ligand from the rhodium centre. All of the rhodium pincer complexes catalysed the decarbonylative dehydration reaction, except those with the P^tBu₂ groups, presumably due to steric bulk, although ³¹P{¹H} NMR analysis indicated that the ligand remains bound to the metal centre, demonstrating the greater thermal stability of pincer complexes.

Interesting results were obtained when using Rh(I) iminophosphine complexes as catalysts. NMR and IR spectroscopic analysis of the catalytic residues revealed that in some cases a stable Rh(III) carbonyl complex with the Rh-P bond intact was formed cleanly. Crystallographic characterisation showed the structure to contain a PCO chelate ligand and a mechanism involving oxidative addition of acetyl iodide (derived from acetic anhydride) and imine insertion into the Rh-acetyl bond is proposed. Notably these chelate complexes retain catalytic activity. Omission of KI caused activity to cease and prohibit formation of the Rh(III) PCO complexes. Deuterium labelling experiments showed that the formation of the PCO chelate ligand is not reversible. Deuterium incorporation in the

alkene products suggested the possible participation of ketenes in the reaction mechanism.

6.2 Future work

6.2.1 New complexes

Wells⁴ and Reynolds⁵ demonstrated that [Rh(CO)(R-anthraphos)] complexes are highly reactive toward MeI and are approximately an order of magnitude more reactive than corresponding [Rh(CO)(R-PNP)] complexes. To our knowledge, [Ir(CO)(R-anthraphos)] complexes have not been investigated in reactions with MeI. As [Ir(CO)(*o*-An-PNP)] has a k_2 value of $400 \text{ mol}^{-1} \text{ dm}^3 \text{ s}^{-1}$ [Ir(CO)(*o*-An-anthraphos)] (Figure 6.2) could potentially have a k_2 value an order of magnitude higher than this. Quantification of the reactivity of this complex would not be possible using IR or normal UV-Vis spectroscopy, however, stopped flow UV-vis spectroscopy could potentially be utilised to quantify the reactivity of this complex.

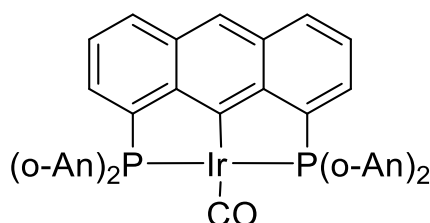
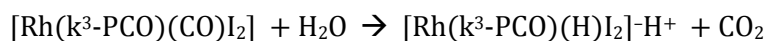


Figure 6.2: Structure of [Ir(CO)(*o*-An-anthaphos)]

6.2.2: Decarbonylative dehydration reactions

Two questions remained to be answered from this project. Firstly, how does the Rh(III) complex **15f** become 50% deuterated at the C-H position of the PCO upon transformation from complex **14f**? Secondly, how do complexes **15f** and **15g** remain catalytically active if they do not eliminate acetyl iodide (indicated by lack of exchange with d_6 -Ac₂O)?

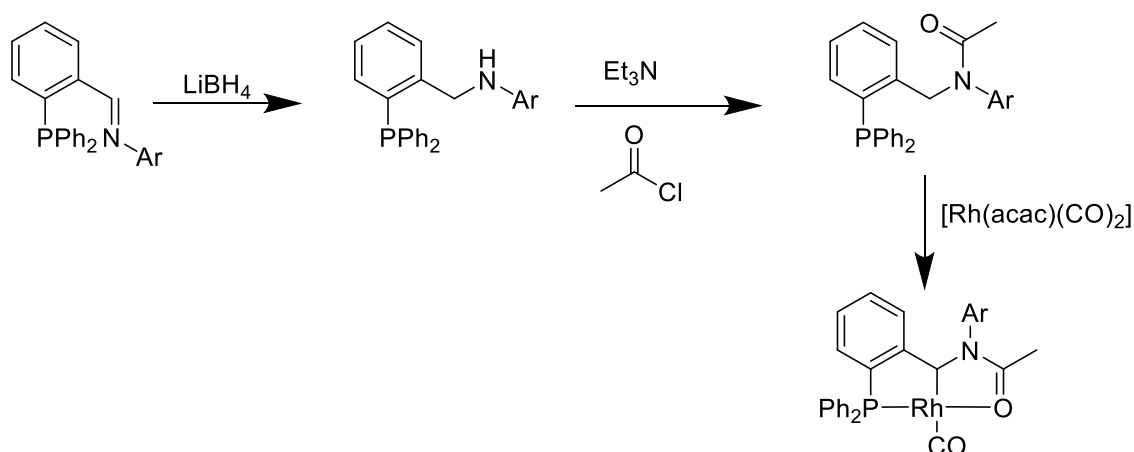
One speculative suggestion is that the Rh(III) PCO complex could be potentially susceptible to nucleophilic attack by water on the CO ligand to release CO₂ (as in the water gas shift reaction reaction) Scheme 6.1 .



Scheme 6.1: Potential WGS reaction.

This would generate a Rh(III)-hydride which could insert ketene to give Rh(III) acyl. This could provide another entry route into catalytic decarbonylation mechanism, not requiring oxidative addition to a Rh(I) complex.

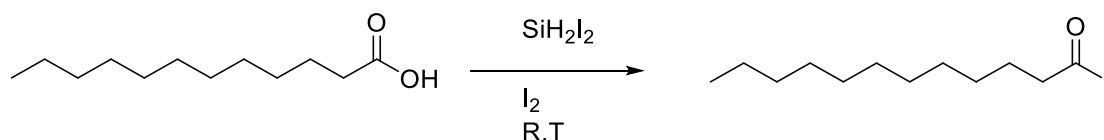
If a hydride ligand is present on Rh(k^3 -PCO) complex then a C-H reductive elimination could occur, this could provide the mechanism for H/D exchange at this position. The synthesis of a Rh(I) PCO complex would enable further investigation into the formation of the Rh(III) complexes a proposed reaction scheme for the synthesis of a Rh(I) PCO complex is displayed in Scheme 6.2.



Scheme 6.2: Proposed scheme for formation of Rh(I) PCO complex

6.2.3 In-Situ reaction monitoring

Keinen et al.⁶ have shown that long chain acyl iodides can be readily synthesised from reacting long chain acid, diiodosilane and iodine at room temperature (Scheme 6.3), these long chain acyl iodides can be isolated as solids and used in reactivity studies. *In-situ* reaction monitoring using both IR and NMR spectroscopy could provide mechanistic insight into reaction between long chain acyl iodides and transition metal complexes, supporting our postulated mechanism.



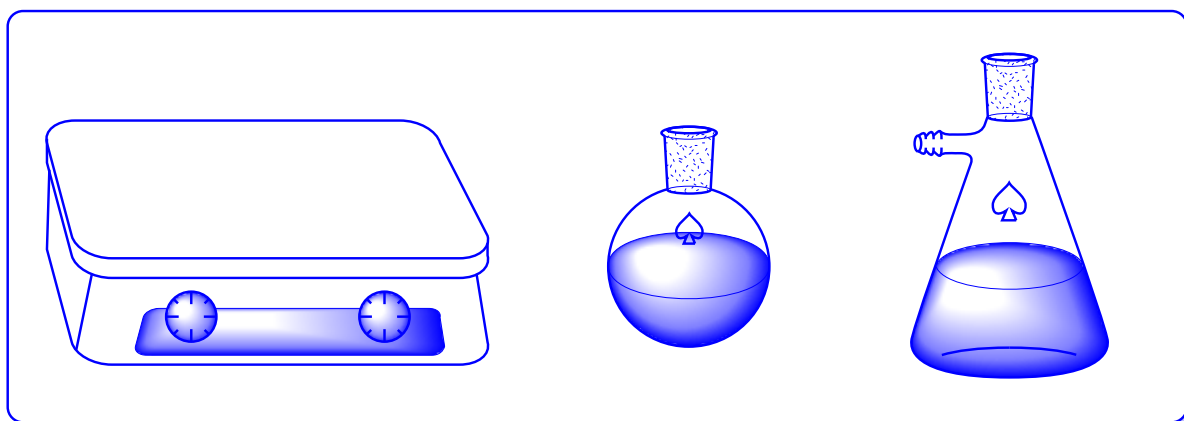
Scheme 6.3: Synthesis of long chain acyl iodides.

6.3 References

- (1) Best, J.; Wilson, J. M.; Adams, H.; Gonsalvi, L.; Peruzzini, M.; Haynes, A. *Organometallics*. **2007**, *26*, 1960.
- (2) Miller, E. M.; Shaw, B. L. *J. Chem. Soc., Dalton Trans.* **1974**, 480.
- (3) Empsall, H. D.; Hyde, E. M.; Jones, C. E.; Shaw, B. L. *J. Chem. Soc., Dalton Trans.* **1974**, 1980.
- (4) Wells, J. PhD Thesis, University Of Sheffield, **2010**.
- (5) Reynolds, T. J. PhD Thesis, Bristol University, **2011**.
- (6) Keinen, E.; Sahai, M. *J. Org. Chem.* **1990**, *55*, 3922.

Chapter 7

Experimental



7.0 Experimental

7.1 Solvents and reagents

The solvents dichloromethane, acetonitrile and hexane were obtained from a Grubbs solvent purification system,¹ in which solvents are vigorously degassed before being passed through two sequential purification columns. Firstly, an activated alumina column removes protic contaminants, followed by a supported copper catalyst that removes trace oxygen from hydrocarbons. The system is fitted with a Schlenk manifold that allows solvents to be collected and stored under a nitrogen atmosphere.

Diethyl ether was distilled after reflux over calcium hydride under a nitrogen atmosphere. Tetrahydrofuran was purified by distillation after reflux over sodium benzophenone ketyl under an argon atmosphere. Solvents were degassed by a minimum of three successive freeze-pump-thaw operations. Methyl iodide was distilled from calcium hydride and stored over mercury in a foil wrapped flask in the refrigerator at ca. 5 °C. All standard reagents were supplied by Sigma-Aldrich Chemicals Ltd and used as supplied, unless otherwise stated. Rhodium trichloride hydrate [$\text{RhCl}_3 \cdot x\text{H}_2\text{O}$] and iridium trichloride hydrate [$\text{IrCl}_3 \cdot x\text{H}_2\text{O}$] were purchased from Precious Metals Online, Monash University LPO, Melbourne, Australia.

Chlorodi-alkyl phosphines, chlorodi-aryl phosphines and bidentate phosphines diphenylphosphinoethane(dppe), 4,5-Bis(diphenylphosphino)-9,9-dimethylxanthene (xantphos), and oxydi-2,1-phenylene bis(diphenylphosphine) (Dpe-Phos) were supplied by Sigma-Aldrich or Alfa-Aesar and used without further purification. Tri-aryl phosphines were supplied by Sigma Aldrich and were used without further purification. Dodecanoic acid, myristic acid, palmitic acid and stearic acid were all supplied by Sigma Aldrich and used without further purification. All other reagents were used as supplied without any further purification. Argon and carbon monoxide (99.9 % CP grade) gases were supplied by BOC.

7.2 Schlenk techniques

Due to the air sensitive nature of many phosphines and their rhodium/iridium complexes, all syntheses and manipulations reported herein were conducted under inert conditions, in flame dried glassware, using standard Schlenk techniques, unless otherwise stated. Solid reagents were typically placed in stoppered flasks equipped with side arms and placed under vacuum before refilling with an argon atmosphere. This process was conducted a minimum of three times. Syringes were degassed by filling with argon from a

previously degassed reaction vessel and expelling outside the flask. This process was repeated a minimum of three times. Steel cannula needles were degassed by purging with a stream of argon for at least 1 minute.

7.3 Instrumentation

Infrared spectra were measured on a Nicolet 560 FTIR spectrometer controlled by Omnic software. Solution spectra were recorded using a solution cell fitted with CaF₂ windows (0.5 mm path length). ¹H, ³¹P and ¹³C NMR spectra were recorded either on a Bruker AC-250 Bruker AV1400 or Bruker AV3-400 spectrometer using the solvent as the internal standard. UV/Visible spectra were recorded on a Varian Cary 50 Probe spectrometer controlled by Cary WinUV© software. A stoppered quartz split cell cuvette, with a 10 mm path length was used for all UV/Visible measurements.

7.4 X-ray Crystallography

Data were collected on a Bruker Smart CCD area detector with Oxford Cryosystems low temperature system using Mo K α radiation ($\lambda = 0.71073$ Å). The structures were solved by direct methods (SHELXS97 or XS from the Shelxtl Bruker Package)² and refined by full-matrix least squares methods on F₂. Hydrogen atoms were placed geometrically and refined using a riding model (including torsional freedom for methyl groups). Complex scattering factors were taken from the SHELXL-97 or XL from the Shelxtl Bruker program package as implemented on the Pentium computer. Full listings of crystallographic data are given in the Appendix.1.

7.5 General Procedure for Ultra-Violet Kinetic studies

A general procedure for UV kinetic studies is set out below. All kinetic experiments were conducted according to this procedure unless otherwise stated. The Varian Cary 50 spectrometer was controlled by a PC running the 'Varian – Cary Win UV' software. Before mixing of reagents, the Cary Win UV software was set up to monitor a single wavelength at 0.1 second intervals over a period 20 minutes.

A stock solution was made up by adding methyl iodide to a volumetric flask, which was then filled to the mark with solvent. A 5 mg sample of metal complex was dissolved in a 25 ml volumetric flask, which was then filled to the mark with solvent. Methyl iodide solutions for each kinetic experiment were created by taking a portion (200-1000 μ l) of the stock solution and adding them to a 5 ml volumetric flask, before making them up to the mark with solvent, concentrations for these experiments are given in the Appendix.2.

Prior to starting kinetic experiments for a given complex a trial experiment was conducted to identify absorption bands associated with reactant and product complexes. The cuvette was filled as above and a background taken of the unmixed solutions. The solutions were then mixed and a series of difference spectra in the region 300-700 nm, over a period of 5 minutes, was recorded. Bands with negative absorbance were attributed to reactant complex. The most intense absorbance of the reactant complex was selected as the band to monitor in subsequent kinetic experiments.

Kinetic experiments were conducted in a stoppered quartz cuvette (path length 10 mm), with two separated compartments, allowing for mixing of reagents inside the cell. Equal volumes of rhodium complex and methyl iodide solutions were added to the two individual compartments and the cuvette inserted into a thermostatically controlled jacket. The cuvette was left in the heating jacket for 10 minutes to allow time to reach the desired temperature. Inverting the stoppered cuvette allowed the solutions from the two compartments to mix, thus starting the reaction.

A range of four different methyl iodide concentrations was used for variable concentration experiments whilst the temperature was kept constant. Temperatures were obtained by the use of an external thermocouple which read the temperature of the solution directly at the end of each kinetic experiment.

The Cary WinUV software exported absorbance versus time data in the Microsoft Excel CSV format. This data was then imported for analysis into the KaleidaGraph software package, which is able to iteratively fit exponential curves to plots of absorbance versus time, allowing a pseudo first order rate constant (k_{obs}) for the reaction to be obtained.

7.6 General Procedure for IR Kinetic studies

A general procedure for IR kinetic studies is detailed below. All kinetic experiments were conducted according to this procedure unless otherwise stated.

Before mixing of reagents, collection parameters were set up on the computer. The Omnic© software is able to control different aspects of the experiment, including the number of scans to record per spectra, the interval at which scans were taken, the total duration of the experiment and the frequency limits for the spectra.

Typically spectra were recorded in the range 2500-1100 cm^{-1} . The number and interval between spectra varied depending on the rate of the reaction being monitored. Stock solutions were prepared in either 5 or 10 ml volumetric flasks. Freshly distilled methyl iodide was added via accurate microlitre syringes and the flask made up to the mark with

solvent (CH₂Cl₂). Samples of between 1-3 mg of complex were pre-weighed in sample vials.

Prior to starting each kinetic experiment, a background spectrum of the methyl iodide solution was taken at the preset temperature. This background was then automatically subtracted from subsequent spectra during the kinetic experiment. A 1000 µl measure of the methyl iodide stock solution was added to the sample of complex, giving a 5-10 mM solution. The solution was thoroughly mixed by pipette and rapidly transferred to an IR transmission cell with a 0.5 mm path length (CaF₂ windows).

The pre-programmed kinetic experiment was started at this point. The temperature during the experiment was kept constant by a thermostatically controlled jacket, which fits securely around the solution cell. The temperature was accurately recorded by an external thermocouple, which fits inside the cell.

Typically four different methyl iodide concentrations were used for variable concentration experiments whilst the temperature was kept constant. Upon completion of an experiment, absorbance vs. time profiles of IR bands corresponding to reactant and products were generated using Omnic®. These were exported in the Microsoft Excel CSV format and imported for analysis in the KaleidaGraph software package. This software is able to iteratively fit exponential curves to plots of absorbance versus time data, allowing a pseudo first order rate constant (k_{obs}) for the reaction to be obtained.

7.7 Synthesis of Rh/Ir precursors

The complexes [Rh(CO)₂Cl]₂,³ [Rh(acac)(CO)₂]⁴ [Ir(COD)(Cl)]₂,^{5,6} [Ir(acac)(CO)₂]^{7,8} and [Ir(CO)₂L₂]₂Ph₄As^{9,10} were all synthesised reported literature methods. Characterisation was in accordance with the reported literature data.

7.8 Synthesis of literature reported ligands

Iminophosphine ligands ^tBu-PN, 2-MeOC₆H₄-PN, 2,6-(CF₃)₂C₆H₃-PN, 2,6-Me₂C₆H₃-PN, 2,6-ⁱPr₂C₆H₃-PN,¹¹⁻¹⁴ bis(2-bromo-4-methyl phenyl)amine,¹⁵ diarylamido NNN pro-ligands,¹⁶⁻¹⁹ and R-PNP(H) pro-ligands (R=Ph and ⁱPr)^{20,21} were all synthesised using reported literature methods. Characterisation was in accordance with the reported literature data.

7.9 Synthesis of literature reported Rh and Ir complexes.

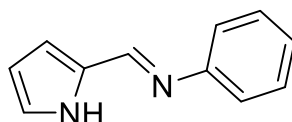
The complexes [Ir(CO)(Cl)L₂] (L=PPh₃, PPhEt₂, PCy₃, P(*o*-Tol)₃, P(*o*-An)₃),²² and [Rh(P-P)(CO)Cl] (P-P = dppe,²³ xanthphos,²⁴ dpe-phos²⁵) were all synthesised using reported methods with spectroscopic data matching that reported within the literature. The

complexes $[\text{Rh}(\text{acac})(\text{CO})\text{L}]$ ($\text{L}=\text{P}(\textit{p}\text{-An})_3$, PCy_3 , $\text{P}(\textit{o}\text{-An})_3$, $\text{P}(4\text{-Cl-C}_6\text{H}_4)_3$, $\text{P}(\textit{o}\text{-Tol})_3$, PPh_3) were synthesised using literature methods or provided by another member of the Haynes group.^{26,27} The complexes $[\text{Rh}(\text{CO})(\text{H-NNN})]$ **12a**, $[\text{Rh}(\text{CO})(\text{Me-NNN})]$ **12b**, $[\text{Rh}(\text{CO})(\text{H-NNN})(\text{Me})\text{I}]$ **13a** and $[\text{Rh}(\text{CO})(\text{Me-NNN})(\text{Me})\text{I}]$ **13b** were all synthesised using literature reported methods with spectroscopic data matching that reported within the literature.¹⁹

7.10 Ligand synthesis

7.10.1 Synthesis of Ph-NN(H)²⁸

The synthetic procedure for the synthesis of Ph-NN(H) is described below. This procedure is representative of the general synthetic procedure for all ligands of this type Ar-NN(H).

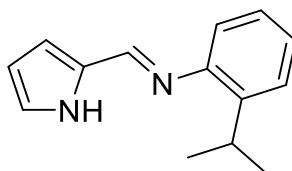


2-pyrrole carboxaldehyde (0.25 g, 2.6 mmol) and aniline (0.24 g, 2.6 mmol) were dissolved in Et_2O (10 ml). To this acetic acid was added (few drops) and the resulting solution was allowed to reflux for 24 hours. The solution was allowed to cool and volatiles were removed to yield Ph-NN(H) as a white powder.

$^1\text{H NMR}$ (250 MHz, CDCl_3) δ 10.13 (s, 1H, N-H), 8.30 (d, $J = 0.7$ Hz, 1H, $\text{HC}=\text{NAr}$), 7.47 – 7.33 (m, 2H, Ar), 7.30 – 7.13 (m, 3H, Ar), 6.91 – 6.80 (m, 1H, pyrrole), 6.72 (dd, $J = 3.6, 1.4$ Hz, 1H, pyrrole), 6.30 (dd, $J = 3.6, 2.6$ Hz, 1H, pyrrole).

Yield 0.38 g, 86%

7.10.2 Synthesis of 2- $^i\text{PrC}_6\text{H}_4\text{NN}(\text{H})$



The 2- $^i\text{PrC}_6\text{H}_4\text{NN}(\text{H})$ pro-ligand was synthesised using the standard method with 2-pyrrole carboxaldehyde (0.22 g, 2.3 mmol) and 2-isopropylaniline (0.312 g, 2.3 mmol) in Et_2O (10 ml) to yield 2- $^i\text{PrC}_6\text{H}_4\text{NN}(\text{H})$ as a pale yellow powder.

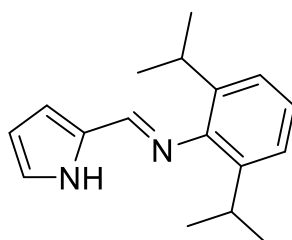
$^1\text{H NMR}$ (400 MHz, CDCl_3) δ 10.06 (s, 1H, N-H), 8.20 (s, 1H, HC=NAr), 7.38 – 7.20 (m, 3H, Ar), 7.02 – 6.91 (m, 1H, Ar), 6.77 (br, 1H, pyrrole), 6.68 (dd, $J = 3.5, 1.3$ Hz, 1H, pyrrole), 6.45 – 6.04 (m, 1H, pyrrole), 3.58 (septet, $J = 6.9$ Hz, 1H, $\text{H}(\text{CH}_3)_2$), 1.22 (d, $J = 6.9$ Hz, 6H, CH_3).

$^{13}\text{C}\{^1\text{H}\}$ NMR (101 MHz, CDCl_3) δ 149.98 (s), 149.86 (s), 142.26 (s), 130.94 (s), 126.72 (s), 125.71 (s), 125.63 (s), 123.40 (s), 118.56 (s), 116.24 (s), 110.17 (s), 27.88 (s), 23.32 (s).

High resolution MS (TOF MS ES+ m/z) 213.1392

Yield 0.35 g, 73 %

7.10.3 Synthesis of 2,6- $i\text{Pr}_2\text{C}_6\text{H}_3\text{NN}(\text{H})$ ²⁹



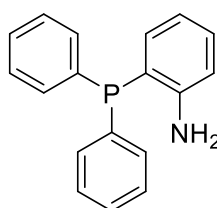
The 2,6- $i\text{Pr}_2\text{C}_6\text{H}_4\text{NN}(\text{H})$ pro-ligand was synthesised using the standard method with 2-pyrrole carboxaldehyde (0.5g, 5.2 mmol) and 2,6-di(isopropyl)aniline (0.9 g, 5.2 mmol) in Et_2O (15 ml) to yield 2,6- $i\text{Pr}_2\text{C}_6\text{H}_3\text{NN}(\text{H})$ as a salmon powder.

$^1\text{H NMR}$ (400 MHz, CDCl_3) δ 10.46 (br, 1H, N-H), 7.99 (d, $J = 0.6$ Hz, 1H, HC=NAr), 7.24 – 7.14 (m, 3H, Ar), 6.65 (dd, $J = 3.6, 1.4$ Hz, 1H, pyrrole), 6.55 – 6.50 (m, 1H, pyrrole), 6.25 (dd, $J = 3.6, 2.7$ Hz, 1H, pyrrole), 3.10 (septet, $J = 6.9$ Hz, 2H, $\text{HC}(\text{CH}_3)_2$), 1.17 (d, $J = 6.9$ Hz, 12H, CH_3).

$^{13}\text{C}\{^1\text{H}\}$ NMR (101 MHz, CDCl_3) δ 152.35 (s), 148.62 (s), 138.73 (s), 130.13 (s), 124.33 (s), 123.52 (s), 123.15 (s), 116.24 (s), 110.04 (s), 27.88 (s), 23.60 (s).

Yield 1.15 g, 87 %

7.10.4 Synthesis of 2-diphenylphosphino aniline



Diphenyl phosphine (0.93 g, 5 mmol), CuI (0.04 g, 0.025 mmol) and $\text{N,N}'$ -Dimethylethylenediamine (0.19 ml, 1.7 mmol) were dissolved in toluene (25 ml) and were

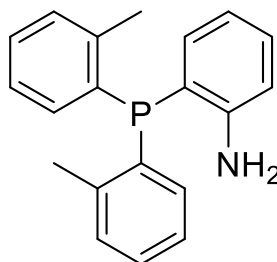
allowed to stir at room temperature. To this 2-iodoaniline (1.0 g, 4.6 mmol) and Cs_2CO_3 (3.0 g, 9.1 mmol) were added and allowed to stir for a further 10 mins. The solution was heated to reflux for 48 hours and allowed to cool to room temperature. Deionised water (50 ml) was added and the organic layer was extracted with CH_2Cl_2 (100 ml). The CH_2Cl_2 was removed under vacuum yielding a brown residue. This residue was then purified by column chromatography using silica eluting with 10:1 hexanes : ethyl acetate (RF 0.4). After the removal of solvent the product was isolated as a white solid.

$^1\text{H NMR}$ (400 MHz, CDCl_3) δ 7.54 – 7.40 (m, 10H, Ar), 7.30 (ddd, $J = 7.9, 7.3, 1.6$ Hz, 1H, Ar), 6.96 – 6.91 (m, 1H, Ar), 6.83 – 6.76 (m, 2H, Ar), 4.25 (s, 2H, NH_2).

$^{31}\text{P}\{^1\text{H}\}$ NMR (162 MHz, CDCl_3) δ -20.28 (s).

Yield 0.66g, 52 %

7.10.5 Synthesis of 2-di(*o*-tolyl)phosphino aniline



Di(*o*-tolyl) phosphine (1.0 g, 4.7 mmol), CuI (0.04 g, 0.023 mmol) and $\text{N,N}'$ -Dimethylethylenediamine (0.185 ml 1.7 mmol) were dissolved in toluene (25 ml) allowed to stir at room temperature. To this 2-iodoaniline (1.0 g, 4.6 mmol) and Cs_2CO_3 (3.0 g, 9.1 mmol) were added and allowed to stir for a further 10 mins. The solution was heated to reflux for 48 hours and allowed to cool to room temperature. Deionised water (50 ml) was added and the organic layer was extracted with CH_2Cl_2 (100 ml). The CH_2Cl_2 was removed under vacuum yielding a brown residue. This residue was then purified by column chromatography using silica eluting with 10:1 hexanes : ethyl acetate (RF 0.5). After the removal of solvent the product was isolated as a white solid.

$^1\text{H NMR}$ (400 MHz, CDCl_3) δ 7.35 – 7.21 (m, 5H, Ar), 7.16 (td, $J = 7.8, 0.8$ Hz, 2H, Ar), 6.92 (ddd, $J = 7.5, 4.8, 1.0$ Hz, 2H, Ar), 6.78 – 6.68 (m, 3H, Ar), 4.19 (s, 2H, NH_2), 2.44 (s, 3H, 2-Me).

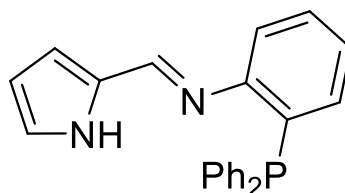
$^{31}\text{P}\{^1\text{H}\}$ NMR (162 MHz, CDCl_3) δ -36.37 (s).

$^{13}\text{C}\{^1\text{H}\}$ NMR (101 MHz, CDCl_3) δ 150.19 (d, $J = 20.5$ Hz), 142.65 (d, $J = 25.6$ Hz), 134.63 (d, $J = 2.1$ Hz), 133.42 (d, $J = 7.5$ Hz), 132.76 (s), 130.36 (s), 130.22 (d, $J = 4.9$ Hz), 128.87 (s), 126.24 (s), 118.94 (d, $J = 1.8$ Hz), 115.32 (d, $J = 2.9$ Hz), 21.21 (d, $J = 20.8$ Hz).

High resolution MS (TOF MS ES+ m/z) 306.1412

Yield 0.49 g, 36 %

7.10.6 Synthesis of $\text{Ph}_2\text{PNN}(\text{H})$



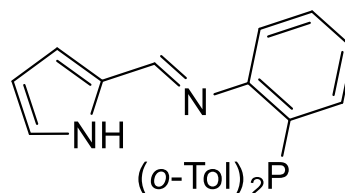
2-diphenylphosphino aniline (0.22 g, 0.79 mmol) and 2-pyrrole carboxaldehyde (0.075 g, 0.79 mmol) were dissolved in Et_2O (15 ml). A few drops of acetic acid was added to the solution which was then refluxed for 48 hours. The solution was allowed to cool and the solvent was removed under vacuum to yield an off brown solid. This solid was recrystallised using MeOH to yield $\text{Ph}_2\text{PNN}(\text{H})$ as a white solid.

^1H NMR (400 MHz, CDCl_3) δ 9.10 (s, 1H, N-H), 8.05 (s, 1H, $\text{HC}=\text{NAr}$), 7.40 – 7.31 (m, 10H, Ar), 7.15 – 7.00 (m, 2H, Ar), 6.87 (s, 1H, Ar), 6.84 – 6.79 (m, 1H, pyrrole), 6.55 – 6.51 (m, 1H, pyrrole), 6.24 – 6.22 (m, 1H, pyrrole).

$^{31}\text{P}\{^1\text{H}\}$ NMR (162 MHz, CDCl_3) δ -13.64 (s).

Yield 0.25 g, 89 %

7.10.7 Synthesis of $o\text{-Tol}_2\text{PNN}(\text{H})$



2-di(*o*-tolyl)phosphino aniline (0.15 g, 0.49 mmol) and 2-pyrrole carboxaldehyde (0.047 g, 0.49 mmol) were dissolved in Et_2O (15 ml). A few drops of acetic acid was added to the solution which was then refluxed for 48 hours. The solution was allowed to cool and the solvent was removed under vacuum to yield a brown solid. This solid was recrystallised using MeOH to yield *o*- $\text{Tol}_2\text{PNN}(\text{H})$ as a white solid.

$^1\text{H NMR}$ (400 MHz, CDCl_3) δ 9.18 (br, 1H, NH), 8.02 (s, 1H, HC=NAr), 7.40 (td, $J = 7.6, 1.1$ Hz, 1H, Ar), 7.28 – 7.19 (m, 5H, Ar), 7.17 – 7.03 (m, 4H, Ar), 6.93 – 6.77 (m, 4H, Ar), 6.53 (dd, $J = 3.6, 1.2$ Hz, 1H, Pyrolle), 6.24 (dd, $J = 3.5, 2.7$ Hz, 1H, Pyrolle), 2.46 (s, 6H, 2-Me).

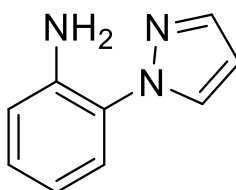
$^{31}\text{P}\{^1\text{H}\}$ NMR (162 MHz, CDCl_3) δ -30.01 (s).

$^{13}\text{C}\{^1\text{H}\}$ NMR (101 MHz, CDCl_3) δ 154.38 (d, $J = 18.2$ Hz), 148.36 (s), 142.51 (d, $J = 26.7$ Hz), 135.23 (d, $J = 11.3$ Hz), 133.74 (s), 132.99 (s), 131.00 (d, $J = 13.9$ Hz), 129.87 (d, $J = 4.8$ Hz), 129.78 (s), 128.48 (s), 125.96 (s), 125.55 (s), 122.53 (s), 117.31 (s), 115.64 (s), 110.21 (s), 21.30 (d, $J = 22.1$ Hz).

High resolution MS (TOF MS ES+ m/z) 383.1677

Yield 0.1 g, 53 %

7.10.8 Synthesis of 2-Pyrazolyl aniline³⁰

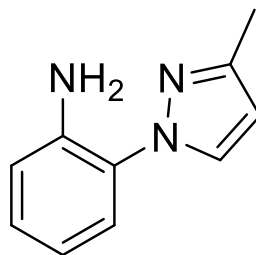


Pyrazole (0.62 g, 9.1 mmol) was dissolved in DMF (10 ml). To this NaH (0.18 g, 7.6 mmol) was added slowly (**caution H₂ gas evolved rapidly**) and allowed to stir at room temperature for 10 mins. To this 2-iodo aniline (1.65 g, 7.6 mmol) and CuI (0.146 g, 0.76 mmol) was added and refluxed for 48 hours and then allowed to cool to room temperature. Deionised water (250 ml) was added and the organic layer was extracted with CH_2Cl_2 (100 ml). The CH_2Cl_2 was removed under vacuum yielding a brown oil. This oil was then purified by column chromatography using silica eluting with 8:1 hexanes :ethyl acetate (RF 0.4). After the removal of solvent the product was isolated as a white solid.

$^1\text{H NMR}$ (400 MHz, CDCl_3) δ 7.72 (d, $J = 1.5$ Hz, 1H, pyrazole), 7.68 (d, $J = 2.3$ Hz, 1H, pyrazole), 7.18 – 7.05 (m, 2H, Ar), 6.79 – 6.70 (m, 2H, Ar), 6.40 (t, $J = 2.1$ Hz, 1H, pyrazole), 4.74 (s, 2H, NH_2).

Yield 0.7g, 55 %

7.10.9 Synthesis of 2-(3-methylpyrazolyl) aniline



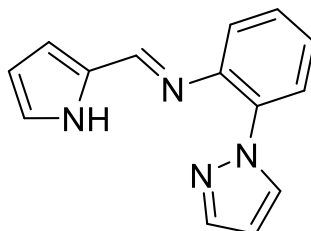
3-methyl pyrazole (0.84 ml, 10 mmol) was dissolved in DMF (10ml). To this NaH (0.2 g, 8.7 mmol) was added slowly (**caution H₂ gas evolved rapidly**) and allowed to stir at room temperature for 10 mins. To this 2-iodo aniline (1.75 g, 8.7 mmol) and CuI (0.16 g, 0.87 mmol) was added and refluxed for 48 hours and then allowed to cool to room temperature. Deionised water (250 ml) was added and the organic layer was extracted with CH₂Cl₂ (100 ml). The CH₂Cl₂ was removed under vacuum yielding a black oil. This oil was then purified by column chromatography using silica eluting with 8:1 hexanes :ethyl acetate (RF 0.6). After the removal of solvent the product was isolated as a white solid.

¹H NMR (250 MHz, CDCl₃) δ 7.59 (d, *J* = 2.3 Hz, 1H, pyrazole), 7.19 – 7.06 (m, 2H, Ar), 6.79 (s, 1H, Ar), 6.76 (br, 1H, Ar), 6.22 (d, *J* = 2.3 Hz, 1H, pyrazole), 4.74 (s, 2H, NH₂), 2.40 (s, 3H, CH₃).

¹³C{¹H} NMR (63 MHz, CDCl₃) δ 132.54 (s), 130.66 (s), 128.23 (s), 124.03 (s), 119.17 (s), 117.93 (s), 117.22 (s), 115.82 (s), 106.23 (s), 13.82 (s).

Yield 0.62 g, 41 %

7.10.10 Synthesis of H-NNN(H)



2-pyrrole carboxaldehyde (0.19 g, 2.0 mmol) and 2-pyrazolyl aniline (0.32 g, 2.0 mmol) were dissolved in Et₂O (15 ml) and a catalytic amount acetic acid was added. The resulting solution was refluxed for 24 hours and allowed to cool to room temperature. Solvent was

removed under vacuum to yield a brown wax, this was recrystallised using CH_2Cl_2 and hexanes to yield a light brown solid.

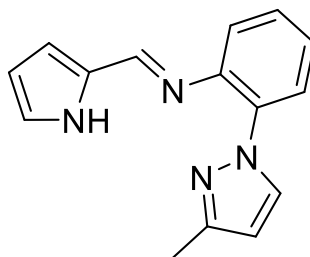
$^1\text{H NMR}$ (400 MHz, CDCl_3) δ 9.41 (s, 1H, N-H), 8.33 (s, 1H, $\text{CH}=\text{NAr}$), 7.93 (d, $J = 2.3$ Hz, 1H, pyrazole), 7.83 (dd, $J = 7.6, 1.7$ Hz, 1H, Ar), 7.74 (d, $J = 1.4$ Hz, 1H, pyrazole), 7.40 – 7.31 (m, 2H, Ar), 7.15 (dd, $J = 7.5, 1.7$ Hz, 1H, Ar), 7.01 (br, 1H, pyrrole), 6.75 (d, $J = 2.6$ Hz, 1H, pyrrole), 6.42 (t, $J = 2.0$ Hz, 1H, pyrrole), 6.38 – 6.33 (m, 1H, pyrazole).

$^{13}\text{C}\{^1\text{H}\}$ NMR (101 MHz, CDCl_3) δ 150.29 (s), 143.80 (s), 140.25 (s), 134.21 (s), 132.36 (s), 130.92 (s), 127.93 (s), 126.08 (s), 124.91 (s), 123.43 (s), 119.61 (s), 116.87 (s), 110.77 (s), 106.17 (s).

High resolution MS (TOF MS ES+ m/z) 237.1140

Yield 0.36 g, 77 %

7.10.11 Synthesis of Me-NNN(H)



2-pyrrole carboxaldehyde (0.34 g, 3.58 mmol) and 2-(3-methylpyrazolyl) aniline (0.62 g, 3.58 mmol) were dissolved in Et_2O (20 ml) and a catalytic amount of acetic acid was added. The resulting solution was refluxed for 24 hours and allowed to cool to room temperature. Solvent was removed under vacuum to yield a yellow solid, this was recrystallised using CH_2Cl_2 and hexanes to yield a white solid.

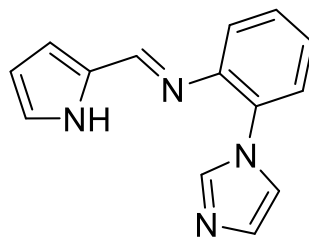
$^1\text{H NMR}$ (400 MHz, CDCl_3) δ 9.45 (br, 1H, N-H), 8.32 (s, 1H, $\text{CH}=\text{NAr}$), 7.84 – 7.70 (m, 2H, pyrazole), 7.39 – 7.22 (m, 2H, Ar), 7.16 – 7.05 (m, 1H, Ar), 7.01 (br, 1H, Ar), 6.77 – 6.69 (m, 1H, pyrrole), 6.39 – 6.29 (m, 1H, pyrrole), 6.19 (d, $J = 2.2$ Hz, 1H, pyrrole), 2.40 (s, 3H, Me).

$^{13}\text{C}\{^1\text{H}\}$ NMR (101 MHz, CDCl_3) δ 150.42 – 150.08 (m), 149.57 (s), 143.41 (s), 134.25 (s), 133.19 (s), 131.01 (s), 127.40 (s), 126.10 (s), 124.63 (s), 123.23 (s), 119.46 (s), 116.61 (s), 110.75 (s), 106.18 (s), 13.68 (s).

High resolution MS (TOF MS ES+ m/z) 251.1297

Yield 0.7 g, 86 %

7.10.12 Synthesis of CNN(H)



2-pyrrole carboxaldehyde (0.15 g, 1.57 mmol) and 2-imidazolyl aniline (0.25 g, 1.57 mmol) were dissolved in Et₂O (15 ml) and a catalytic amount of acetic acid was added. The resulting mixture was refluxed for 24 hours and allowed to cool and solvent removed under vacuum to yield an oily residue. The oily residue was washed several times with hexanes and dried under high vacuum to yield a salmon coloured solid.

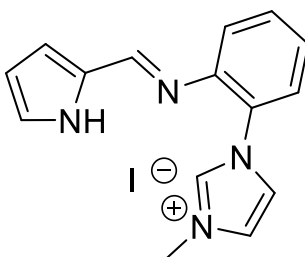
¹H NMR (400 MHz, CDCl₃) δ 9.57 (br, 1H, N-H), 8.33 (s, 1H, HC=NAr), 7.83 (s, 1H, imidazole), 7.45 – 7.30 (m, 3H, Ar), 7.23 (d, *J* = 7.8 Hz, 2H, Ar), 7.01 (br, 1H, pyrrole), 6.74 (d, *J* = 3.3 Hz, 1H, pyrrole), 6.34 – 6.32 (m, 1H, pyrrole).

¹³C{¹H} NMR (101 MHz, CDCl₃) δ 150.36 (s), 145.25 (s), 131.77 – 131.62 (m), 130.75 (s), 128.79 (s), 126.11 (s), 125.13 (s), 123.85 (s), 120.86 (s), 119.44 (s), 117.21 (s), 110.75 (s).

High resolution MS (TOF MS ES+ *m/z*) 237.1140

Yield 0.27 g, 73 %

7.10.13 Synthesis of Me-CNN(H)



To a solution of CNN(H) (0.2 g 0.85 mmol) in MeCN (10 ml), MeI (excess) was added and left to stir for 48 hours. The volatiles were removed under vacuum to yield a red hygroscopic solid.

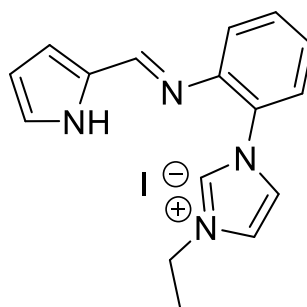
¹H NMR (400 MHz, CDCl₃) δ 10.30 (s, 1H, imidazolium), 8.20 (s, 1H, HC=NAr), 7.52 – 7.47 (m, 4H, Ar), 7.32 (m, 1H, Ar), 7.22 (m, 2H, Ar), 6.78 – 6.74 (m, 1H, pyrrole), 6.27 (dt, *J* = 3.7, 2.3 Hz, 1H, pyrrole), 4.32 (s, 3H, N-Me).

$^{13}\text{C}\{^1\text{H}\}$ NMR (101 MHz, CDCl_3) δ 151.75 (s), 145.43 (s), 137.42 (s), 131.56 (s), 130.19 (s), 128.30 (s), 126.08 (d, $J = 12.4$ Hz), 124.37 (s), 123.39 (s), 122.75 (s), 120.28 (s), 119.30 (s), 110.39 (s), 37.95 (s).

High resolution MS (TOF MS ES+ m/z) 251.1297

Yield 0.27 g, 85%

7.10.14 Synthesis of Et-CNN(H)



To a solution of CNN(H) (0.2 g 0.85 mmol) in MeCN (10ml), EtI (excess) was added and left to stir for 48 hours. The volatiles were removed under vacuum to yield a red hygroscopic solid.

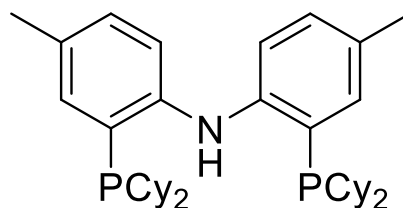
^1H NMR (400 MHz, CDCl_3) δ 11.17 (s, 1H, N-H), 10.47 (s, 1H, imidazolium), 8.20 (s, 1H, HC=NAr), 7.53 – 7.47 (m, 2H, imidazolium), 7.35 – 7.30 (m, 1H, Ar), 7.24 – 7.20 (m, 2H, Ar), 6.77 (br, 1H, pyrrole), 6.28 (dt, $J = 3.4, 2.3$ Hz, 1H, pyrrole), 4.80 (q, $J = 7.3$ Hz, 2H), 1.61 (t, $J = 7.3$ Hz, 3H).

$^{13}\text{C}\{^1\text{H}\}$ NMR (101 MHz, CDCl_3) δ 151.75 (s), 145.55 (s), 136.97 (s), 131.55 (s), 130.26 (s), 128.34 (s), 126.07 (d, $J = 2.5$ Hz), 124.22 (s), 122.71 (s), 121.41 (s), 120.36 (s), 119.20 (s), 110.36 (s), 46.04 (s), 15.98 (s).

High resolution MS (TOF MS ES+ m/z) 265.1453

Yield 0.26 g, 78%

7.10.15 Synthesis of Cy-PNP(H)



Bis(2-bromo-4-methyl phenyl)amine (0.76 g, 2.15 mmol) was dissolved in Et₂O (25 ml). The solution was cooled to -78 °C and n-BuLi (2.6 ml, 2.5 M in hexanes, 6.5 mmol) was added dropwise. The mixture was allowed to warm to room temperature and further stirred for 2 hours, before again being cooled to -78 °C and ClPCy₂ (1.0 g 4.3 mmol) in Et₂O (2 ml) added dropwise. The reaction mixture was stirred overnight yielding a brown solution. The solution was quenched using degassed water (50 ml) and stirred for 45 minutes. The organic layer was separated, dried using magnesium sulphate and solvent removed under vacuum. The yellow brown oil was recrystallized using degassed methanol isolating Cy-PNP(H) as a yellow powder.

¹H NMR (400 MHz, CDCl₃) δ 7.46 (t, *J* = 7.3 Hz, 1H), 7.19 – 7.16 (m, 2H), 7.12 (dd, *J* = 8.2, 4.0 Hz, 2H), 7.01 (dd, *J* = 8.3, 1.7 Hz, 2H), 2.32 (s, 6H), 2.08 – 0.98 (m, 44H).

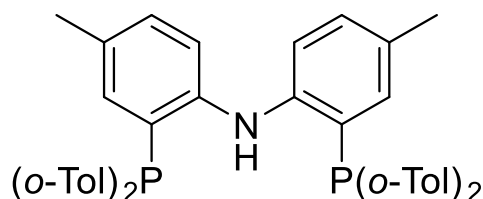
³¹P{¹H} NMR (162 MHz, CDCl₃) δ -17.21 to -21.15, (br).

¹³C{¹H} NMR (101 MHz, CDCl₃) δ 146.60 (d, *J* = 16.2 Hz), 134.61 (s), 129.95 (s), 128.62 (s), 123.01 (d, *J* = 17.7 Hz), 117.09 (s), 33.25 (d, *J* = 11.4 Hz), 30.71 (d, *J* = 16.9 Hz), 29.25 (d, *J* = 8.3 Hz), 27.22 (d, *J* = 12.4 Hz), 27.04 (d, *J* = 8.1 Hz), 26.45 (s), 20.85 (s).

High resolution MS (TOF MS ES+ *m/z*) 590.4162

Yield: 1.25 g, 97 %

7.10.16 Synthesis of *o*-Tol-PNP(H)



Bis(2-bromo-4-methyl phenyl)amine (0.71 g, 2.01 mmol) was dissolved in Et₂O (50 ml). The solution was cooled to -78 °C and n-BuLi (2.66 ml, 2.5 M in hexanes, 6.65 mmol) was added dropwise. The mixture was allowed to warm to room temperature and further stirred for 2 hours, before again being cooled to -78 °C and PCl(*o*-Tol)₂ (1.0g, 4.03 mmol) in THF (10 ml) was added dropwise. The reaction mixture was stirred overnight yielding a brown solution with a large amount of cream precipitate. The suspension was reduced to 50% under vacuum and quenched with degassed water (50 ml) with further stirring for 45 minutes. The cream precipitate was then collected using a Buchner funnel air dried and then dried under vacuum yielding a cream powder.

$^1\text{H NMR}$ (400 MHz, CDCl_3) δ 7.26 - 7.06 (m, 10 H, Ar) δ 6.81 (d, $J = 3.1$ Hz, 2H, Ar), 6.79 (d, $J = 3.1$ Hz, 2H, Ar). 6.61 (t, $J = 5.5$ Hz, 1H, N-H) 6.51 (br, 2H, Ar), 2.27 (s, 12H, *o*-Tol), 2.14 (s, 6H, 4-Me).

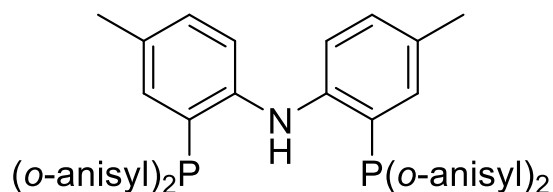
$^{31}\text{P}\{^1\text{H}\}$ NMR (162 MHz, CDCl_3) δ -36.43 (s).

$^{13}\text{C}\{^1\text{H}\}$ NMR (101 MHz, CDCl_3) δ 145.12 (d, $J = 22.5$ Hz), 142.57 (d, $J = 26.7$ Hz), 134.71 (s), 134.19 (d, $J = 8.9$ Hz), 132.74 (s), 130.51 (s), 130.45 (s), 130.02 (s), 128.58 (s), 126.05 (s), 118.24 (s), 21.20 (d, $J = 22.2$ Hz), 20.79 (s).

High resolution MS (TOF MS ES+ m/z) 622.27

Yield 0.73g, 55%

7.10.17 Synthesis of *o*-An-PNP(H)



Bis(2-bromo-4-methyl phenyl)amine (0.62 g, 1.78 mmol) was dissolved in Et_2O (25 ml). The solution was cooled to -78 °C and $n\text{-BuLi}$ (2.1 ml, 2.5 M in hexanes, 5.37 mmol) was added dropwise. The mixture was allowed to warm to room temperature and further stirred for 2 hours, before again being cooled to -78 °C and $\text{ClP}(\textit{o}\text{-anisyl})_2$ (1.0 g, 3.57 mmol) in THF (5 ml) was added dropwise. The reaction mixture was stirred overnight yielding a brown solution with an off white precipitate. The solution was quenched using degassed water (50 ml) and stirred for 60 minutes. The suspension was reduced to 50% under vacuum until a white precipitate was formed. The white precipitate was then collected using a Buchner funnel and recrystallized using methanol.

$^1\text{H NMR}$ (400 MHz, CDCl_3) δ 7.33 - 7.25 (m, 4H, Ar), 7.05 - 6.96 (m, 4H, Ar), 6.82 (m, 12H, Ar), 6.62 (d, $J = 3.5$ Hz, 2H, Ar), 6.58 (br, 1H, N-H), 3.70 (s, 12H, O- CH_3), 2.14 (s, 6H, 4-Me).

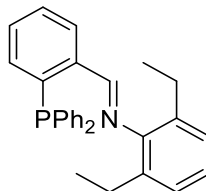
$^{31}\text{P}\{^1\text{H}\}$ NMR (162 MHz, CDCl_3) δ -40.02 (s).

$^{13}\text{C}\{^1\text{H}\}$ NMR (101 MHz, CDCl_3) δ 161.29 (d, $J = 16.5$ Hz), 146.23 (d, $J = 22.3$ Hz), 134.84 (s), 133.53 (s), 130.21 (s), 129.63 (s), 125.81 (d, $J = 9.2$ Hz), 124.76 (d, $J = 12.0$ Hz), 120.84 (s), 119.26 (s), 110.18 (s), 55.58 (s), 20.78 (s).

High resolution MS (TOF MS ES+ m/z) 686.25

Yield 0.83g, 68%

7.10.18 Synthesis of 2,6-Et₂C₆H₃PN



Diphenylphosphino benzaldehyde (0.25 g, 0.86 mmol) was dissolved in methanol (10 ml), to this 2,6-diethyl aniline (0.13 g, 0.86 mmol) was added with a catalytic amount of formic acid. This was heated to reflux for 2 days and then allowed to cool, The solvent was reduced to ca. 30% until a yellow precipitate was formed. This was then placed in the freezer overnight and the resulting precipitate was filtered to yield the 2,6-Et₂C₆H₃PN iminophosphine ligand as a yellow solid.

¹H NMR (400 MHz, CDCl₃) δ 8.84 (d, *J* = 5.6 Hz, 1H, HC=NAr), 8.21 (ddd, *J* = 7.7, 3.9, 1.3 Hz, 1H, Ar), 7.47 – 6.80 (m, 16H, Ar), 2.15 (q, *J* = 7.5 Hz, 4H, CH₂), 0.87 (t, *J* = 7.5 Hz, 6H, CH₃).

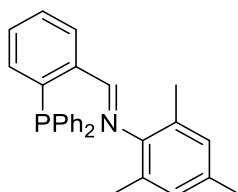
³¹P{¹H} NMR (162 MHz, CDCl₃) δ -15.20 (s).

¹³C NMR (101 MHz, CDCl₃) δ 160.71 (d, *J* = 24.4 Hz), 150.24 (s), 139.48 (d, *J* = 17.8 Hz), 138.55 (d, *J* = 20.2 Hz), 136.31 (d, *J* = 10.1 Hz), 134.12 (d, *J* = 20.0 Hz), 133.53 (s), 133.07 (s), 131.05 (s), 129.12 (s), 128.98 (s), 128.71 (d, *J* = 7.1 Hz), 127.62 (d, *J* = 4.4 Hz), 125.98 (s), 123.82 (s), 24.43 (s), 14.46 (s).

High resolution MS (TOF MS ES+ m/z) 422.2038

Yield 0.24 g, 66 %

7.10.19 Synthesis of 2,4,6-Me₃C₆H₂PN



Diphenylphosphino benzaldehyde (0.25 g, 0.86 mmol) was dissolved in methanol (10 ml), to this 2,4,6-trimethyl aniline (0.125 g, 0.86 mmol) was added with a catalytic amount of formic acid. This was heated to reflux for 2 days and then allowed to cool, the solvent was reduced to ca. 30% until a yellow precipitate was formed. This was then placed in the

freezer overnight and the resulting precipitate was filtered to yield the 2,4,6-Me₃C₆H₂ PN iminophosphine ligand as a yellow solid.

¹H NMR (250 MHz, CDCl₃) δ 8.90 (d, *J* = 5.5 Hz, 1H, HC=NAr), 8.29 (ddd, *J* = 7.6, 3.9, 1.3 Hz, 1H, Ar), 7.50 (t, *J* = 7.1 Hz, 1H, Ar), 7.44 – 7.16 (m, 11H), 6.94 (dd, *J* = 7.5, 4.6 Hz, 1H, Ar), 6.82 (s, 2H, Ar), 2.26 (s, 3H), 1.85 (s, 6H).

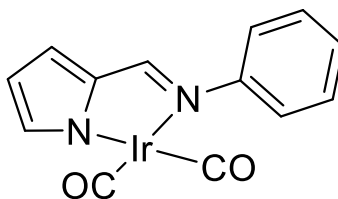
³¹P{¹H} NMR (101 MHz, CDCl₃) δ -14.54 (s).

¹³C{¹H} NMR (101 MHz, CDCl₃) δ 161.23 (d, *J* = 23.6 Hz), 148.60 (s), 139.49 (d, *J* = 17.6 Hz), 138.49 (d, *J* = 20.2 Hz), 136.35 (d, *J* = 10.1 Hz), 134.11 (d, *J* = 20.0 Hz), 133.37 (s), 132.80 (s), 130.88 (s), 128.98 (s), 128.93 (s), 128.67 (d, *J* = 7.1 Hz), 128.52 (s), 127.58 (d, *J* = 4.3 Hz), 127.07 (s), 20.70 (s), 17.87 (s).

Yield 0.2 g, 57 %

7.11 Synthesis of Rh and Ir complexes

7.11.1 Synthesis of [Ir(Ph-NN)(CO)₂] 1a



A solution of [Ir(acac)(CO)₂] (0.1g 0.28mmol) and Ph-NN(H) (0.047g, 0.028mmol) in MeCN (10 ml) was heated to reflux and was monitored by IR. Once complete the reaction was cooled resulting in a dark red precipitate which was filtered to yield analytically pure **1a**.

¹H NMR (250 MHz, CDCl₃) δ 7.89 (d, *J* = 0.7 Hz, 1H), 7.52 – 7.36 (m, 2H), 7.36 – 7.27 (m, 3H), 7.19 (s, 1H), 6.86 (dd, *J* = 3.9, 0.8 Hz, 1H), 6.31 (dd, *J* = 3.9, 1.8 Hz, 1H).

¹³C{¹H} NMR (101 MHz, CDCl₃) δ 176.94(s), 173.69(s), 162.65(s), 151.34(s), 143.99(s), 142.59(s), 129.40(s), 127.18(s), 123.16(s), 122.25(s), 115.59(s).

IR ν(CO) 2064, 1993 cm⁻¹ (MeCN)

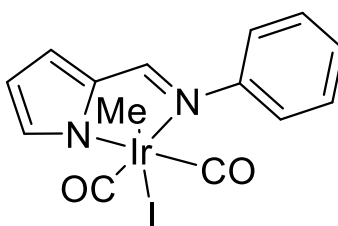
High resolution MS(TOF MS EI+ *m/z*) 418.02 .

Elemental analysis

Calculated for $C_{13}H_9IrN_2O_2$. C: 37.4%, H: 2.17%, N:6.71%. Found: C:37.50% ,H: 1.97%, N:6.66%.

Yield 0.09 g, 77 %

Complexes **1b,c** were synthesised in the same way but were not isolated and were used in reactions with phosphines (vide infra).

7.11.2 Synthesis of [Ir(Ph-NN)(CO)₂(Me)I] 2a

1a (0.03 g, 0.05mmol) was dissolved in CH_2Cl_2 (5 ml) and to this solution MeI (excess) was added and allowed to stir overnight. Volatiles were removed under vacuum to yield a brown solid.

1H NMR (400 MHz, $CDCl_3$) δ 7.70 (s, J = 7.9 Hz, 1H, HC=NAr), 7.55 – 7.33 (m, 6H, Ar), 7.03 (d, J = 4.1 Hz, 1H, pyrrole), 6.40 (dd, J = 4.1, 1.8 Hz, 1H, pyrrole), 1.19 (s, 3H, CH_3).

$^{13}C\{^1H\}$ NMR (63 MHz, $CDCl_3$) δ 160.55 (s), 158.80 (s), 150.74 (s), 140.63 (s), 138.91 (s), 129.64 (s), 128.09 (s), 123.49 (s), 121.72 (s), 115.71 (s), -8.43 (s).

High resolution MS (TOF MS EI+ m/z) 559.957

IR ν (CO) 2118, 2072 cm^{-1} (CH_2Cl_2)

Yield 0.018 g 65%

Note, other minor species were formed during this reaction giving weak signals in the 1H and ^{13}C NMR spectra.

7.11.3 Synthesis of [Ir(Ar-NN)(CO)L] complexes**Method A**

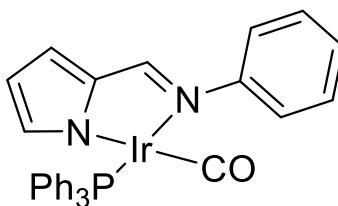
[Ir(acac)(CO)₂] and the Ar-NN(H) ligand were dissolved in MeCN, heated to reflux and monitored by IR to check for complete conversion of [Ir(acac)(CO)₂]. The reaction mixture was cooled to room temperature and after addition of the phosphine as a solid under a blanket of N_2 the solution was heated to reflux once more. The displacement of CO was

monitored by IR, once complete the reaction mixture was cooled and solvent was removed under vacuum yielding the $[\text{Ir}(\text{Ar-NN})(\text{CO})\text{PR}_3]$ complex as a red powder with no further purification required.

Method B

$[\text{Ir}(\text{acac})(\text{CO})_2]$ and Ar-NN(H) ligand were dissolved in MeCN, heated to reflux and monitored by IR to check for complete conversion of $[\text{Ir}(\text{acac})(\text{CO})_2]$. The reaction mixture was cooled to room temperature and after addition of the phosphine as a solid under a blanket of N_2 the solution was heated to reflux once more. The displacement of CO was monitored by IR and once complete, the reaction mixture was cooled to room temperature forming a red precipitate. The red precipitate was filtered, washed with MeCN and dried under high vacuum to yield the $[\text{Ir}(\text{Ar-NN})(\text{CO})(\text{PR}_3)]$ complex with no further purification required.

7.11.4 Synthesis of $[\text{Ir}(\text{Ph-NN})(\text{CO})(\text{PPh}_3)]$ **3a**



Using method A and the following quantities: $[\text{Ir}(\text{acac})(\text{CO})_2]$ (0.1 g, 0.28 mmol), Ph-NN(H) (0.048 g, 0.28 mmol), PPh_3 (0.073 g, 0.28 mmol) and MeCN (10 ml). Complex **3a** was isolated as a red/brown powder.

$^1\text{H NMR}$ (400 MHz, CDCl_3) δ 8.14 (d, $J=6.6\text{Hz}$, 1H, $\text{HC}=\text{NAr}$), 7.81 – 7.66 (m, 5H, Ar), 7.55 – 7.34 (m, 15H, Ar), 6.74 (t, $J=8.9\text{ Hz}$, 1H, pyrrole), 6.02 (s, 1H, pyrrole), 5.91 (dd, $J=3.6, 1.9\text{ Hz}$, 1H, pyrrole).

$^{31}\text{P}\{^1\text{H}\}$ NMR (162 MHz, CDCl_3) δ 17.40 (s).

$^{13}\text{C}\{^1\text{H}\}$ NMR (101 MHz, CDCl_3) δ 159.81 (s), 152.63 (s), 145.61 (s), 141.83 (s), 134.77 (d, $J=11.5\text{ Hz}$), 132.12 (d, $J=9.9\text{ Hz}$), 130.39 (s), 128.76 (s), 128.51 (d, $J=12.3\text{ Hz}$), 128.14 (d, $J=10.3\text{ Hz}$), 126.37 (s), 122.87 (s), 119.83 (s), 112.85 (s).

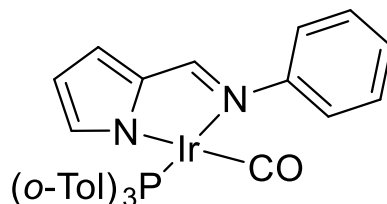
High resolution MS (TOF MS AP+ m/z) 653.1334

Elemental analysis: satisfactory elemental analysis for this compound could not be achieved presumably due to air sensitivity.

IR $\nu(\text{CO})$ 1965 cm^{-1} (MeCN)

Yield 0.13 g, 73 %

7.11.5 Synthesis of $[\text{Ir}(\text{Ph-NN})(\text{CO})(\text{P-}o\text{-Tol}_3)]$ **3b**



Using method B and the following quantities: $[\text{Ir}(\text{acac})(\text{CO})_2]$ (0.1 g, 0.28 mmol), Ph-NN(H) (0.048 g, 0.28 mmol), $\text{P}(o\text{-Tol})_3$ (0.085 g, 0.28 mmol) and MeCN (10 ml). Complex **3b** was isolated as a red powder.

^1H NMR (400 MHz, CDCl_3) δ 9.04 (br, 1H, Ar), 8.08 (d, $J = 6.6$ Hz, 1H, $\text{HC}=\text{NAr}$), 7.63 – 6.96 (m, 16H, Ar), 6.71 (d, $J = 3.5$ Hz, 1H, pyrrole), 6.18 (br, 1H, pyrrole), 5.87 (dd, $J = 3.6, 1.9$ Hz, 1H, pyrrole), 3.37 (br, 3H, 2-Me), 2.26 (br, 3H, 2-Me), 1.70 (br, 3H, 2-Me).

$^{31}\text{P}\{^1\text{H}\}$ NMR (101 MHz, CDCl_3) δ 11.18 (s).

$^{13}\text{C}\{^1\text{H}\}$ NMR (101 MHz, CDCl_3) δ 159.18 (s), 152.87 (s), 145.34 (s), 144.43 – 140.17 (br), 133.50 – 129.51 (br), 128.74 (s), 126.27 (s), 125.98 (d, $J = 59.6$ Hz), 122.83 (s), 119.35 (s), 112.45 (s), 27.04 – 26.00 (br), 23.34 – 22.66 (br), 22.66 – 21.72 (br).

High resolution MS (TOF MS AP+ m/z) 695.1803

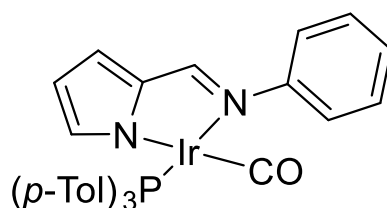
Elemental analysis

Calculated for $\text{C}_{33}\text{H}_{30}\text{IrN}_2\text{OP}$: C, 57.13 H, 4.36 N, 4.04. Found: C, 57.07 H, 4.26 N, 3.98.

IR $\nu(\text{CO})$ 1962 cm^{-1} (MeCN)

Yield 0.16 g, 82%

7.11.6 Synthesis of $[\text{Ir}(\text{Ph-NN})(\text{CO})(\text{P-}p\text{-Tol}_3)]$ **3c**



Using method A and the following quantities: [Ir(acac)(CO)₂] (0.1 g, 0.28 mmol), Ph-NN(H) (0.048 g, 0.28 mmol), P(*p*-Tol)₃ (0.085 g, 0.28 mmol) and MeCN (10 ml). Complex **3c** was isolated as a red/brown powder.

¹H NMR (400 MHz, CDCl₃) δ 8.15 (d, *J* = 6.6 Hz, 1H, HC=NAr), 7.63 (dd, *J* = 11.2, 8.1 Hz, 6H, Ar), 7.53 – 7.11 (m, 11H, Ar), 6.75 (d, *J* = 3.4 Hz, 1H, pyrrole), 6.07 (s, 1H, pyrrole), 5.92 (d, *J* = 1.5 Hz, 1H, pyrrole), 2.41 (s, 9H, 4-Me).

³¹P{¹H} NMR (162 MHz, CDCl₃) δ 14.74 (s).

¹³C{¹H} NMR (101 MHz, CDCl₃) δ 179.84 (s), 159.65 (s), 152.67 (s), 145.62 (s), 141.85 (s), 140.50 (s), 134.68 (d, *J* = 11.7 Hz), 128.82 (d, *J* = 10.9 Hz), 128.72 (s), 126.28 (s), 122.89 (s), 119.68 (s), 112.71 (s), 21.39 (s).

High resolution MS (TOF MS AP+ *m/z*) 695.1803

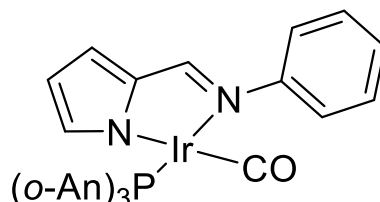
Elemental analysis

Calculated for C₃₃H₃₀IrN₂OP: C, 57.13 H, 4.36 N, 4.04. Found: C, 57.19 H, 4.24 N, 3.96.

IR ν(CO) 1962 cm⁻¹ (MeCN)

Yield 0.126 g, 65 %

7.11.7 Synthesis of [Ir(Ph-NN)(CO)(P-*o*-An₃)] **3d**



Using method B and the following quantities: [Ir(acac)(CO)₂] (0.1 g, 0.28 mmol), Ph-NN(H) (0.048 g, 0.28 mmol), P(*o*-An)₃ (0.1 g, 0.28 mmol) and MeCN (10 ml). Complex **3d** was isolated as a red/orange powder.

¹H NMR (400 MHz, CDCl₃) δ 7.99 (dd, *J* = 6.9, 0.6 Hz, 1H, HC=NAr), 7.66 (br, 2H, Ar), 7.40 – 7.21 (m, 7H, Ar), 7.12 – 7.06 (m, 1H, Ar), 6.88 (t, *J* = 7.5 Hz, 3H, Ar), 6.73 (dd, *J* = 8.1, 4.5 Hz, 3H, Ar), 6.57 (dd, *J* = 3.7, 0.9 Hz, 1H, pyrrole), 6.06 (s, *J* = 15.7 Hz, 1H, pyrrole), 5.77 (dd, *J* = 3.7, 1.9 Hz, 1H, pyrrole), 3.40 (s, 9H, 2-OMe).

³¹P{¹H} NMR (162 MHz, CDCl₃) δ 0.26 (s).

$^{13}\text{C}\{^1\text{H}\}$ NMR (101 MHz, CDCl_3) δ 160.83 (s), 158.75 (s), 153.63 – 152.47 (s), 145.56 (s), 140.71 (s), 131.71 (s), 128.57 (s), 125.97 (s), 122.99 (s), 121.17 (s), 120.55 (s), 120.04 (d, $J = 10.7$ Hz), 118.79 (s), 111.93 (s), 111.60 – 111.49 (m), 55.24 (s).

High resolution MS (TOF MS ES+ m/z) 743.1651

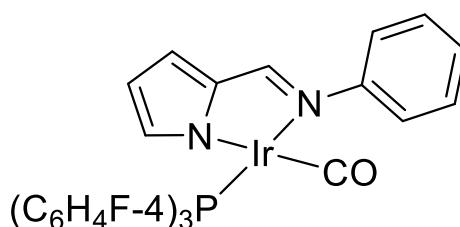
Elemental analysis

Calculated for $\text{C}_{33}\text{H}_{31}\text{IrN}_2\text{O}_4\text{P}$: C, 53.36 H, 4.21 N, 3.77. Found: C, 53.12 H, 4.07 N, 3.97.

IR $\nu(\text{CO})$ 1957 cm^{-1} (MeCN)

Yield 0.176 g, 85 %

7.11.8 Synthesis of $[\text{Ir}(\text{Ph-NN})(\text{CO})(\text{P}(\text{4-FC}_6\text{H}_4)_3)]$ **3e**



Using method A and the following quantities: $[\text{Ir}(\text{acac})(\text{CO})_2]$ (0.1 g, 0.28 mmol), Ph-NN(H) (0.048 g, 0.28 mmol), $\text{P}(\text{4-FC}_6\text{H}_4)_3$ (0.088 g, 0.28 mmol) and MeCN (10 ml). Complex **3e** was isolated as a red/brown powder.

^1H NMR (400 MHz, CDCl_3) δ 8.13 (dd, $J = 6.9, 0.6$ Hz, 1H, $\text{HC}=\text{NAr}$), 7.79 – 7.64 (m, 6H, Ar), 7.48 – 7.35 (m, 5H, Ar), 7.18 – 7.08 (m, 6H, Ar), 6.76 (dd, $J = 3.7, 0.9$ Hz, 1H, pyrrole), 5.98 (dd, $J = 1.7, 0.8$ Hz, 1H, pyrrole), 5.94 (dd, $J = 3.7, 2.0$ Hz, 1H, pyrrole).

$^{31}\text{P}\{^1\text{H}\}$ NMR (162 MHz, CDCl_3) δ 15.57 (s).

^{19}F NMR (377 MHz, CDCl_3) δ -108.77 (d, $J = 2.3$ Hz).

$^{13}\text{C}\{^1\text{H}\}$ NMR (101 MHz, CDCl_3) δ 179.43 (s), 165.47 (s), 162.96 (s), 160.07 (s), 152.51 (s), 145.64 (d, $J = 3.6$ Hz), 141.45 (d, $J = 0.8$ Hz), 136.79 (d, $J = 8.4$ Hz), 136.66 (d, $J = 8.4$ Hz), 129.61 (d, $J = 3.5$ Hz), 129.02 (d, $J = 3.7$ Hz), 128.87 (s), 126.58 (s), 122.77 (d, $J = 0.9$ Hz), 120.13 (s), 115.69 (d, $J = 11.9$ Hz), 115.48 (d, $J = 11.9$ Hz), 113.17 (s).

High resolution MS (TOF MS EI+ m/z) 706.0941

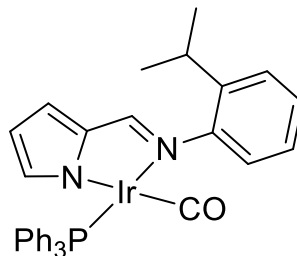
Elemental analysis

Calculated for $\text{C}_{30}\text{H}_{21}\text{F}_3\text{IrN}_2\text{OP}$: C, 51.06 H, 3.0 N, 3.97. Found: C, 50.45 H, 3.0 N, 3.73.

IR $\nu(\text{CO})$ 1968 cm^{-1} (MeCN)

Yield 0.142 g, 72 %

7.11.9 Synthesis of $[\text{Ir}(2\text{-}i\text{PrC}_6\text{H}_4\text{-NN})(\text{CO})(\text{PPh}_3)]$ **3f**



Using method B and the following quantities: $[\text{Ir}(\text{acac})(\text{CO})_2]$ (0.1 g, 0.28 mmol), 2-*i*-Pr- $\text{C}_6\text{H}_4\text{-NN}(\text{H})$ (0.059 g, 0.28 mmol), PPh_3 (0.073 g, 0.28 mmol) and MeCN (10 ml). Complex **3f** was isolated as a red/brown powder.

^1H NMR (400 MHz, CDCl_3) δ 7.91 (d, $J = 7.0$ Hz, 1H, HC=NAr), 7.68 – 7.55 (m, 6H, Ar), 7.40 – 7.21 (m, 10H, Ar), 7.11 (d, $J = 1.7$ Hz, 3H), 6.63 (d, $J = 3.0$ Hz, 1H, pyrrole), 5.87 (br, 1H, pyrrole), 5.81 (br, 1H, pyrrole), 3.91 – 3.78 (m, 1H, HC(CH₃)₂), 1.27 (d, $J = 6.7$ Hz, 3H, CH₃), 1.11 (d, $J = 6.7$ Hz, 3H, CH₃).

$^{31}\text{P}\{^1\text{H}\}$ NMR (162 MHz, CDCl_3) δ 17.91 (s).

$^{13}\text{C}\{^1\text{H}\}$ NMR (101 MHz, CDCl_3) δ 178.97 (d, $J = 12.7$ Hz), 160.44 (s), 150.94 (s), 144.90 (d, $J = 3.8$ Hz), 141.91 (s), 141.17 (s), 134.79 (d, $J = 11.4$ Hz), 134.30 (s), 133.74 (s), 130.39 (d, $J = 2.2$ Hz), 128.09 (d, $J = 10.6$ Hz), 126.78 (s), 125.93 (d, $J = 25.1$ Hz), 123.74 (s), 118.69 (s), 112.34 (s), 27.52 (s), 25.18 (s), 22.20 (s).

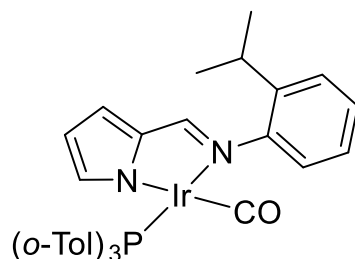
High resolution MS (TOF MS EI+ m/z) 694.1717

Elemental analysis

Calculated for $\text{C}_{33}\text{H}_{30}\text{IrN}_2\text{OP}$: C, 57.13 H, 4.36 N, 4.04. Found: C, 56.8 H, 4.33 N, 4.07.

IR $\nu(\text{CO})$ 1965 cm^{-1} (MeCN)

Yield 0.143 g, 74%

7.11.10 Synthesis of $[\text{Ir}(2\text{-}^i\text{PrC}_6\text{H}_4\text{-NN})(\text{CO})(\text{P}\text{-}o\text{-Tol}_3)]$ **3g**

Using method B and the following quantities: $[\text{Ir}(\text{acac})(\text{CO})_2]$ (0.1 g, 0.28 mmol), 2- $^i\text{PrC}_6\text{H}_4\text{-NN}(\text{H})$ (0.059 g, 0.28 mmol), $P\text{-}o\text{-Tol}_3$ (0.085 g, 0.28 mmol) and MeCN (10 ml). Complex **3g** was isolated as a red/brown powder.

$^1\text{H NMR}$ (400 MHz, Tol, 373K) δ 7.57 (dd, $J = 7.0, 0.6$ Hz, 1H, $\text{HC}=\text{NAr}$), 7.30 – 7.14 (m, 1H), 7.13 – 6.83 (m, 15H), 6.68 (dd, $J = 3.7, 0.8$, 1H, pyrrole), 6.36 (br, 1H, pyrrole), 5.98 (dd, $J = 3.7, 1.9$ Hz, 1H, pyrrole), 4.17 (m, 1H, $\text{HC}(\text{CH}_3)_2$), 2.13 (s, 9H, 2-Me), 1.41 (br, 3H, CH_3), 1.14 (br, 3H, CH_3).

$^{31}\text{P}\{^1\text{H}\}$ NMR (162 MHz, Tol, 373K) δ 11.91 (s).

$^{31}\text{P}\{^1\text{H}\}$ NMR (162 MHz, CDCl_3) δ 11.56 (br), 11.06 (br).

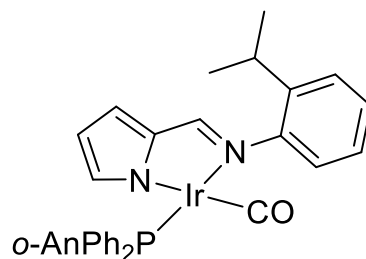
Elemental analysis

Calculated for $\text{C}_{36}\text{H}_{36}\text{IrN}_2\text{OP}$: C, 58.76 H, 4.93 N, 3.81. Found: C, 58.42 H, 4.77 N, 3.68.

IR $\nu(\text{CO})$ 1963 cm^{-1} (MeCN)

Yield 0.144 g, 70%

A single crystal of **3g** suitable for X-ray crystallography was obtained by slow evaporation of MeCN from a concentrated solution of the complex.

7.11.11 Synthesis of $[\text{Ir}(2\text{-}^i\text{PrC}_6\text{H}_4\text{-NN})(\text{CO})(\text{PPh}_2\text{-}o\text{-An})]$ **3h**

Using method B and the following quantities: $[\text{Ir}(\text{acac})(\text{CO})_2]$ (0.1 g, 0.28 mmol), 2- $^i\text{PrC}_6\text{H}_4\text{-NN}(\text{H})$ (0.059 g, 0.28 mmol), $\text{PPh}_2\text{-}o\text{-An}$ (0.081 g, 0.28 mmol) and MeCN (10 ml). Complex **3h** was isolated as a red powder.

$^1\text{H NMR}$ (400 MHz, CDCl_3) δ 8.02 (d, $J = 7.1$ Hz, 1H, HC=NAr), 7.94 – 7.75 (m, 4H, Ar), 7.47 – 7.33 (m, 8H, Ar), 7.22 (d, $J = 3.0$ Hz, 3H, Ar), 7.12 (ddd, $J = 12.5, 7.6, 1.6$ Hz, 1H, Ar), 6.96 – 6.90 (m, 1H, Ar), 6.85 (dd, $J = 8.2, 4.6$ Hz, 1H, Ar), 6.72 (d, $J = 3.6$ Hz, 1H, pyrrole), 6.05 (br, 1H, pyrrole), 5.92 (dd, $J = 3.7, 1.9$ Hz, 1H, pyrrole), 4.11 – 4.00 (m, 1H, HC(CH₃)₂), 3.50 (s, 3H, 2-OMe), 1.39 (d, $J = 6.8$ Hz, 3H, CH₃), 1.21 (d, $J = 6.9$ Hz, 3H, CH₃).

$^{31}\text{P}\{^1\text{H}\}$ NMR (162 MHz, CDCl_3) δ 11.31 (s)

$^{13}\text{C}\{^1\text{H}\}$ NMR (101 MHz, CDCl_3) δ 160.33 (d, $J = 3.3$ Hz), 160.17 (s), 151.04 (s), 144.82 (d, $J = 3.9$ Hz), 142.05 (s), 141.12 (s), 134.98 (d, $J = 11.9$ Hz), 134.75 (d, $J = 11.5$ Hz), 133.92 (d, $J = 30.9$ Hz), 133.35 (d, $J = 31.1$ Hz), 132.38 (s), 130.03 (s), 127.90 (d, $J = 10.7$ Hz), 126.65 (s), 125.98 (s), 125.71 (s), 123.73 (s), 122.35 (s), 121.76 (s), 120.34 (d, $J = 10.0$ Hz), 118.30 (s), 112.05 (s), 111.10 (d, $J = 4.8$ Hz), 54.91 (s), 27.49 (s), 25.16 (s), 22.10 (s).

MS (TOF MS EI+ m/z) 725.2

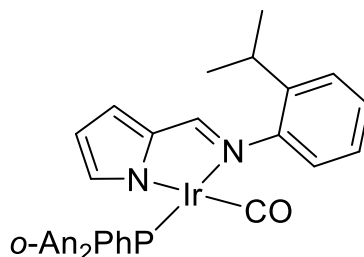
Elemental analysis

Calculated for $\text{C}_{34}\text{H}_{32}\text{IrN}_2\text{O}_2\text{P}$: C, 56.42 H, 4.46 N, 3.87. Found: C, 55.73 H, 4.24 N, 3.69.

IR $\nu(\text{CO})$ 1964 cm^{-1} (MeCN)

Yield 0.150g, 72%

7.11.12 Synthesis of $[\text{Ir}(2\text{-}i\text{PrC}_6\text{H}_4\text{-NN})(\text{CO})(\text{PPh-}o\text{-An}_2)]$ **3i**



Using method B and the following quantities: $[\text{Ir}(\text{acac})(\text{CO})_2]$ (0.1 g, 0.28 mmol), 2-*i*-Pr- $\text{C}_6\text{H}_4\text{-NN}(\text{H})$ (0.059 g, 0.28 mmol), $\text{PPh-}o\text{-An}_2$ (0.09 g, 0.28 mmol) and MeCN(10ml). Complex **3i** was isolated as a red powder.

$^1\text{H NMR}$ (250 MHz, CDCl_3) δ 7.98 (d, $J = 7.1$ Hz, 1H, HC=NAr), 7.91 – 7.77 (m, 2H, Ar), 7.77 – 7.64 (m, 1H, Ar), 7.56 (dd, $J = 13.2, 7.6$ Hz, 1H, Ar), 7.45 – 7.29 (m, 6H, Ar), 7.23 – 7.15 (m, 3H, Ar), 7.02 – 6.90 (m, 2H, Ar), 6.83 (dd, $J = 8.1, 4.4$ Hz, 2H, Ar), 6.67 (dd, $J = 3.7, 1.0$ Hz, 1H, pyrrole), 6.09 (dd, $J = 1.7, 0.8$ Hz, 1H, pyrrole), 5.88 (dd, $J = 3.7, 1.9$ Hz, 1H, pyrrole), 4.18 – 3.98 (m, 1H, CH(CH₃)), 3.47 (d, $J = 5.5$ Hz, 6H, 2-OMe), 1.36 (d, $J = 6.8$ Hz, 3H, CH₃), 1.17 (d, $J = 6.9$ Hz, 3H, CH₃).

$^{31}\text{P}\{^1\text{H}\}$ NMR (101 MHz, CDCl_3) δ 6.61 (s).

$^{13}\text{C}\{^1\text{H}\}$ NMR (101 MHz, CDCl_3) δ 160.56 (d, $J = 4.1$ Hz), 159.75 (s), 151.18 (s), 144.66 (d, $J = 4.0$ Hz), 142.04 (s), 140.56 (s), 136.58 (d, $J = 12.8$ Hz), 135.45 (d, $J = 10.4$ Hz), 134.86 (d, $J = 11.9$ Hz), 133.69 (s), 133.10 (s), 131.98 (d, $J = 19.5$ Hz), 129.52 (s), 127.37 (d, $J = 11.0$ Hz), 126.52 (s), 125.94 (s), 125.62 (s), 123.73 (s), 122.23 (s), 120.30 (dd, $J = 10.9$, 6.2 Hz), 117.91 (s), 111.72 (s), 111.23 (dd, $J = 11.0$, 4.5 Hz), 55.00 (s), 27.43 (s), 25.14 (s), 22.05 (s).

High resolution MS (TOF MS ES+ m/z) 755.2015

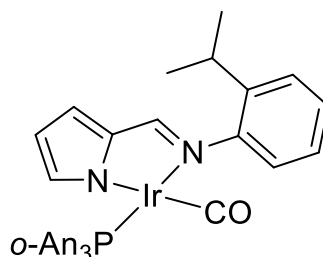
Elemental analysis

Calculated for $\text{C}_{35}\text{H}_{34}\text{IrN}_2\text{O}_3\text{P}$: C, 55.76 H, 4.55 N, 3.72. Found: C, 55.60 H, 4.37 N, 3.61.

IR $\nu(\text{CO})$ 1963 cm^{-1} (MeCN)

Yield 0.145 g, 69%

7.11.13 Synthesis of $[\text{Ir}(2\text{-}i\text{PrC}_6\text{H}_4\text{-NN})(\text{CO})(\text{P-}o\text{-An}_3)]$ 3j



Using method B and the following quantities of $[\text{Ir}(\text{acac})(\text{CO})_2]$ (0.1g, 0.28mmol), 2-*i*-Pr- $\text{C}_6\text{H}_4\text{-NN}(\text{H})$ (0.059g, 0.28 mmol), $\text{P}(o\text{-An})_3$ (0.1 g, 0.28 mmol) and MeCN(10ml). Complex 3j was isolated as a red powder.

^1H NMR (250 MHz, CDCl_3) δ 7.96 (d, $J = 7.2$ Hz, 1H, $\text{HC}=\text{NAr}$), 7.82-7.6 (br, 2H, Ar), 7.45 – 7.29 (m, 4H), 7.24 – 7.13 (m, 3H, Ar), 6.95 (t, $J = 7.5$ Hz, 3H, Ar), 6.80 (dd, $J = 8.1$, 4.5 Hz, 2H, Ar), 6.65 (dd, $J = 3.6$, 0.9 Hz, 1H, Ar), 6.13 (br, 1H, Ar), 5.88 (dd, $J = 3.6$, 1.9 Hz, 1H, Ar), 4.23 – 4.02 (m, 1H, $\text{HC}(\text{CH}_3)_2$), 3.46 (s, 9H, 2-OMe), 1.36 (d, $J = 6.8$ Hz, 3H, CH_3), 1.15 (d, $J = 6.9$ Hz, 3H, CH_3).

$^{31}\text{P}\{^1\text{H}\}$ NMR (101 MHz, CDCl_3) δ 0.25 (s).

$^{13}\text{C}\{^1\text{H}\}$ NMR (101 MHz, CDCl_3) δ 179.11 (d, $J = 14.3$ Hz), 160.71 (s), 159.29 (s), 151.45 (s), 144.54 (d, $J = 4.0$ Hz), 142.02 (s), 139.98 (s), 131.59 (s), 127.91 – 127.73 (m), 126.38

(s), 125.72 (d, $J = 35.0$ Hz), 123.79 (s), 121.26 (s), 120.67 (s), 119.91 (d, $J = 10.8$ Hz), 117.50 (s), 112.04 (s), 111.36 (s), 55.07 (s), 27.36 (s), 25.09 (s), 22.11 (s).

High resolution MS (TOF MS ES+ m/z) 784.2057

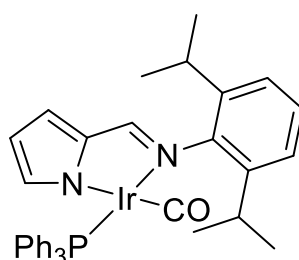
Elemental analysis

Calculated for $C_{36}H_{36}IrN_2O_4P$: C, 55.16 H, 4.63 N, 3.57. Found: C, 54.04 H, 4.56 N, 3.32.

IR $\nu(\text{CO})$ 1957 cm^{-1} (MeCN)

Yield 0.171g, 78%

7.11.14 Synthesis of $[\text{Ir}(2,6\text{-}^i\text{Pr}_2\text{C}_6\text{H}_3\text{-NN})(\text{CO})(\text{PPh}_3)]$ **3k**



Using method B and the following quantities: $[\text{Ir}(\text{acac})(\text{CO})_2]$ (0.1 g, 0.28 mmol), 2,6- $^i\text{Pr}_2\text{-C}_6\text{H}_4\text{-NN}(\text{H})$ (0.071 g, 0.28 mmol), PPh_3 (0.073 g, 0.28 mmol) and MeCN (10 ml). Complex **3k** was isolated as a red powder.

^1H NMR (400 MHz, CDCl_3) δ 7.94 (d, $J = 7.3$ Hz, 1H, $\text{HC}=\text{NAr}$), 7.80 – 7.67 (m, 6H, Ar), 7.48 – 7.34 (m, 9H, Ar), 7.21 (s, 3H, Ar), 6.74 (dd, $J = 3.6, 1.0$ Hz, 1H, pyrrole), 5.98 – 5.89 (m, 2H, Ar), 3.78 (hept, $J = 6.9$ Hz, 2H, $\text{HC}(\text{CH}_3)_2$), 1.38 (d, $J = 6.8$ Hz, 6H, CH_3), 1.25 (d, $J = 6.9$ Hz, 6H, CH_3).

$^{31}\text{P}\{^1\text{H}\}$ NMR (101 MHz, CDCl_3) δ 18.30 (s).

$^{13}\text{C}\{^1\text{H}\}$ NMR (101 MHz, CDCl_3) δ 178.77 (d, $J = 12.6$ Hz), 160.70 (s), 148.26 (s), 144.65 (d, $J = 4.0$ Hz), 141.70 (s), 140.78 (s), 134.77 (d, $J = 11.5$ Hz), 134.46 (s), 133.90 (s), 130.33 (d, $J = 2.3$ Hz), 128.06 (d, $J = 10.5$ Hz), 126.73 (s), 123.17 (s), 118.31 (s), 112.19 (s), 27.65 (s), 24.98 (s), 22.95 (s).

High resolution MS (TOF MS ES+ m/z) 737.2273

Elemental analysis

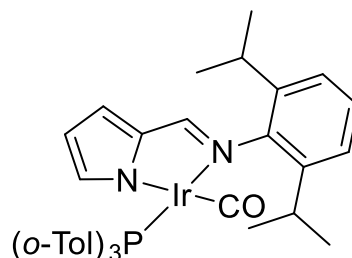
Calculated for $C_{36}H_{36}IrN_2O_4P$: C, 58.76 H, 4.93 N, 3.81. Found: C, 58.49 H, 4.60 N, 4.22.

IR $\nu(\text{CO})$ 1965 cm^{-1} (MeCN)

Yield 0.162 g, 79%

A single crystal of **3k** suitable for X-ray crystallography was obtained by slow evaporation of MeCN from a concentrated solution of the complex.

7.11.15 Synthesis of $[\text{Ir}(\text{2,6-}^i\text{Pr}_2\text{C}_6\text{H}_4\text{-NN})(\text{CO})(\text{P-}o\text{-Tol}_3)]$ **3l**



Using method B and the following quantities: $[\text{Ir}(\text{acac})(\text{CO})_2]$ (0.1 g, 0.28mmol), 2,6- $^i\text{Pr}_2\text{-C}_6\text{H}_4\text{-NN}(\text{H})$ (0.071 g, 0.28 mmol), $\text{P}(o\text{-Tol})_3$ (0.085 g, 0.28 mmol) and MeCN (10 ml). Complex **3l** was isolated as a red powder.

$^1\text{H NMR}$ (400 MHz, CDCl_3) δ 7.88 (d, $J = 7.3$ Hz, 1H, $\text{HC}=\text{NAr}$), 7.60 – 6.96 (m, 16H), 6.70 (d, $J = 3.1$ Hz, 1H, pyrrole), 6.19 (br, 1H, pyrrole), 5.90 (dd, $J = 3.6, 1.9$ Hz, 1H, pyrrole), 3.84 (br, 1H, $\text{CH}(\text{CH}_3)_2$), 3.68 (br, 1H, $\text{CH}(\text{CH}_3)_2$), 3.29 (br, 3H, 2-Me), 2.20 (br, 3H, 2-Me), 1.68 (br, 3H, 2-Me), 1.44 – 1.09 (m, 12H, CH_3).

$^{31}\text{P}\{^1\text{H}\}$ NMR (162 MHz, CDCl_3) δ 11.32 (s).

High resolution MS (TOF MS ES+ m/z) 779.2742

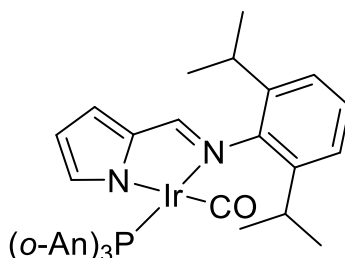
Elemental analysis

Calculated for $\text{C}_{39}\text{H}_{42}\text{N}_2\text{OP}$: C, 60.21 H, 5.44 N, 3.60. Found: C, 60.58 H, 5.20 N, 3.57.

IR $\nu(\text{CO})$ 1962 cm^{-1} (MeCN)

Yield 0.198 g, 91%

7.11.16 Synthesis of $[\text{Ir}(\text{2,6-}^i\text{Pr}_2\text{C}_6\text{H}_4\text{-NN})(\text{CO})(\text{P-}o\text{-An}_3)]$ **3m**



Using method B and the following quantities of [Ir(acac)(CO)₂] (0.1g, 0.28mmol), 2,6-*i*Pr₂-C₆H₄-NN(H) (0.071g, 0.28 mmol), P(*o*-An)₃ (0.1 g, 0.28 mmol) and MeCN (10 ml). Complex **3m** was isolated as a red powder.

¹H NMR (400 MHz, CDCl₃) δ 7.91 (d, *J* = 7.5 Hz, 1H, HC=NAr), 7.87 – 7.57 (m, 2H, Ar), 7.39 (dd, *J* = 16.8, 9.2 Hz, 3H, Ar), 7.20 (s, 3H, Ar), 6.97 (t, *J* = 7.5 Hz, 3H, Ar), 6.81 (dd, *J* = 7.3, 4.3 Hz, 3H, Ar), 6.68 (dd, *J* = 3.6, 0.8 Hz, 1H, pyrrole), 6.24 (br, 1H, pyrrole), 5.92 (dd, *J* = 3.6, 1.9 Hz, 1H, pyrrole), 3.87 – 3.76 (m, 2H, HC(CH₃)₂), 3.47 (s, 9H, 2-OMe), 1.38 (d, *J* = 6.8 Hz, 6H, CH₃), 1.21 (d, *J* = 6.9 Hz, 6H, CH₃).

³¹P{¹H} NMR (101 MHz, CDCl₃) δ 0.13 (s).

¹³C{¹H} NMR (101 MHz, CDCl₃) δ 179.19 (d, *J* = 14.6 Hz), 160.66 (s), 159.50 (s), 148.76 (s), 144.32 (d, *J* = 4.1 Hz), 141.71 (s), 139.82 (s), 131.55 (s), 126.38 (s), 122.97 (s), 119.81 (d, *J* = 10.9 Hz), 117.04 (s), 111.28 (s), 54.97 (s), 27.41 (s), 24.88 (s), 22.99 (s).

High resolution MS (TOF MS ES+ *m/z*) 827.2590

Elemental analysis

Calculated for C₃₉H₄₂IrN₂O₄P: C, 56.71 H, 5.13 N, 3.39. Found: C, 55.65 H, 4.96 N, 3.68.

Note despite multiple attempts satisfactory elemental analysis was not obtained for **3m**

IR ν(CO) 1957 cm⁻¹ (MeCN)

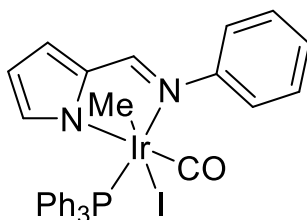
Yield 0.157 g, 68%

A single crystal of **3m** suitable for X-ray crystallography was obtained by slow evaporation of MeCN from a concentrated solution of the complex.

7.11.17 Synthesis of [Ir(Ar-NN)(CO)L(Me)I] complexes 4a-k

7.11.18 Synthesis of [Ir(Ph-NN)(CO)(PPh₃)(Me)I] 4a

The synthetic procedure for the synthesis of [Ir(Ph-NN)(CO)(PPh₃)(Me)I] is described below. This procedure is representative of the general synthetic procedure for all complexes of this type [Ir(Ar-NN)(CO)L(Me)I] **4a-k**



[Ir(Ph-NN)(CO)(PPh₃)] **3a** (0.04g, 0.06 mmol) was dissolved in CH₂Cl₂ (5 ml). To this solution MeI (excess) was added and allowed to stir overnight. The volatiles were removed under vacuum to yield **4a** as a yellow solid.

¹H NMR (250 MHz, CDCl₃) δ 8.04 – 7.85 (m, 6H, Ar), 7.74 (d, *J* = 9.2 Hz, 1H, HC=NAr), 7.67 – 7.57 (m, 2H, Ar), 7.52 – 7.30 (m, 12H, Ar), 6.96 (dd, *J* = 4.0, 1.0 Hz, 1H, pyrrole), 6.76 (d, *J* = 0.8 Hz, 1H, pyrrole), 6.15 (dd, *J* = 4.0, 1.9 Hz, 1H, pyrrole), 0.54 (d, *J* = 2.8 Hz, 3H, Ir-CH₃).

³¹P{¹H} NMR (101 MHz, CDCl₃) δ -8.41 (s).

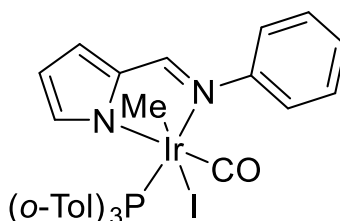
¹³C{¹H} NMR (101 MHz, CDCl₃) δ 167.45 (d, *J* = 10.4 Hz), 157.83 (s), 151.45 (s), 143.31 – 142.81 (m), 139.79 (s), 134.97 (d, *J* = 9.6 Hz), 131.29 (d, *J* = 2.6 Hz), 130.46 (d, *J* = 13.0 Hz), 129.68 (s), 129.09 (s), 129.02 (s), 128.27 (d, *J* = 10.9 Hz), 127.16 (s), 124.10 (s), 120.40 (s), 112.85 (s), -3.02 (d, *J* = 3.1 Hz).

MS (TOF MS ES+ *m/z*) 667 [M+][I-]

IR ν(CO) 2046 cm⁻¹ (CH₂Cl₂)

Yield 0.039 g 82 %

7.11.19 Synthesis of [Ir(Ph-NN)(CO)(P-*o*-Tol₃)(Me)I] **4b**



Complex **4b** was synthesised using the general method from **3b** (0.25g, 0.36 mmol) in CH₂Cl₂ (10 ml) and MeI (excess) to yield **4b** as a pale yellow solid.

¹H NMR (400 MHz, CDCl₃) δ 8.33 (br, 3H, Ar), 7.66-7.62 (m, 3H, Ar), 7.49 – 7.17 (m, 13H, Ar), 7.00 (dd, *J* = 3.9, 1.0 Hz, 1H, pyrrole), 6.91 (br, 1H, pyrrole), 6.18 (dd, *J* = 3.9, 1.9 Hz, 1H, pyrrole), 2.21 (s, 9H, 2-Me), 0.91 (d, *J* = 3.0 Hz, 3H, Ir-CH₃).

³¹P{¹H} NMR (101MHz, CDCl₃) δ -10.76 (s)

¹³C{¹H} NMR (101 MHz, CDCl₃) δ 166.59 (d, *J* = 10.9 Hz), 157.73 (s), 151.22 (s), 143.13 (d, *J* = 3.5 Hz), 142.81 (d, *J* = 6.4 Hz), 140.31 (s), 138.49 (s), 132.37 (d, *J* = 8.5 Hz), 131.64 (d, *J* = 2.5 Hz), 128.88 (s), 127.21 (s), 125.89 (s), 125.35 (d, *J* = 11.8 Hz), 124.69 (s), 120.71 (s), 112.56 (s), 25.59 (d, *J* = 3.3 Hz), -3.63 (br).

High resolution MS (TOF MS ES+ m/z) 837.1083

IR $\nu(\text{CO})$ 2042 cm^{-1} (CH_2Cl_2)

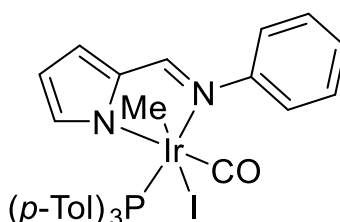
Elemental Analysis

Calculated for $\text{C}_{34}\text{H}_{33}\text{IrN}_2\text{OP}$: C, 48.86 H, 3.98 N, 3.35. Found: C, 48.44 H, 4.02 N, 2.96.

Yield 0.249 g 83 %

Note, elemental analysis was performed on this Ir(III) sample only as it was synthesised in a large scale.

7.11.20 Synthesis of $[\text{Ir}(\text{Ph-NN})(\text{CO})(\text{P}p\text{-Tol}_3)(\text{Me})\text{I}]$ **4c**



Complex **4c** was synthesised using the general method from **3c** (0.044 g, 0.063 mmol) in CH_2Cl_2 (5 ml) and excess MeI to yield **4c** as a pale brown solid.

^1H NMR (400 MHz, CDCl_3) δ 7.80 (dd, $J = 11.2, 8.2$ Hz, 6H, Ar), 7.75 (d, $J = 9.1$ Hz, 1H, $\text{HC}=\text{NAr}$), 7.68 – 7.58 (m, 3H, Ar), 7.54 – 7.35 (m, 3H, Ar), 7.27 – 7.19 (m, 5H), 6.97 (d, $J = 3.3$ Hz, 1H, pyrrole), 6.81 (s, 1H, pyrrole), 6.16 (dd, $J = 3.9, 1.8$ Hz, 1H, pyrrole), 2.41 (s, 9H, 2-Me), 0.56 (d, $J = 2.8$ Hz, 3H, Ir- CH_3).

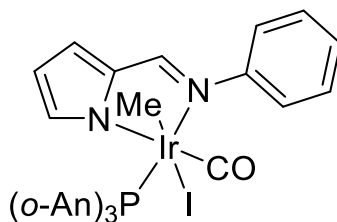
$^{31}\text{P}\{^1\text{H}\}$ NMR (162MHz, CDCl_3) δ -10.4(s)

$^{13}\text{C}\{^1\text{H}\}$ NMR (101 MHz, CDCl_3) δ 167.60 (d, $J = 10.5$ Hz), 157.72 (s), 151.50 (s), 143.10 (d, $J = 3.4$ Hz), 141.51 (d, $J = 2.6$ Hz), 139.82 (s), 134.87 (d, $J = 9.9$ Hz), 133.20 (d, $J = 11.1$ Hz), 131.14 (d, $J = 13.4$ Hz), 128.96 (s), 128.84 (s), 127.03 (s), 126.66 (s), 126.05 (s), 124.07 (d, $J = 1.0$ Hz), 120.25 (s), 112.68 (s), 21.39 (d, $J = 1.3$ Hz), -3.20 (d, $J = 3.0$ Hz).

High resolution MS (TOF MS AP+ m/z) 837.1083

IR $\nu(\text{CO})$ 2044 cm^{-1} (CH_2Cl_2)

Yield 0.039 g, 74 %

7.11.21 Synthesis of $[\text{Ir}(\text{Ph-NN})(\text{CO})(\text{P}(o\text{-An})_3)(\text{Me})\text{I}]$ **4d**

Complex **4d** was synthesised using the general method from **3d** (0.05 g, 0.067 mmol) in CH_2Cl_2 (10 ml) and excess MeI to yield **4d** as a white powder.

^1H NMR (400 MHz, CDCl_3) δ 8.08 (s, $J = 26.4$ Hz, 1H), 7.69 (d, $J = 9.6$ Hz, 1H), 7.64 (d, $J = 7.8$ Hz, 1H), 7.48 – 7.24 (m, 2H), 7.07 – 6.93 (m, 2H), 6.82 (dd, $J = 8.0, 4.8$ Hz, 1H), 6.20 (dd, $J = 3.9, 1.9$ Hz, 1H), 3.46 (s, $J = 17.5$ Hz, 3H), 0.85 (d, $J = 3.5$ Hz, 3H Ir- CH_3).

$^{31}\text{P}\{^1\text{H}\}$ NMR (162 MHz, CDCl_3) δ -21.48 (s).

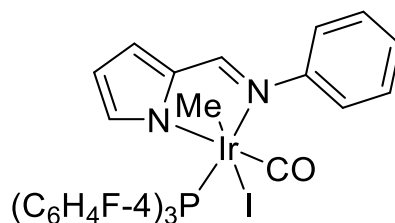
$^{13}\text{C}\{^1\text{H}\}$ NMR (101 MHz, CDCl_3) δ 167.03 (d, $J = 10.6$ Hz), 160.35 (s), 157.83 (s), 151.52 (s), 142.72 (d, $J = 3.3$ Hz), 142.10 (s), 132.72 (s), 128.72 (s), 126.82 (s), 124.64 (s), 119.97 (s), 119.62 (d, $J = 12.0$ Hz), 111.71 (s), 110.36 (d, $J = 4.9$ Hz), 54.50 (s), -6.55 (d, $J = 3.8$ Hz).

High resolution MS (TOF MS ES+ m/z) 885.0930

IR $\nu(\text{CO})$ 2044 cm^{-1} (CH_2Cl_2)

Yield 0.042 g, 72%

A single crystal of **4d** suitable for X-ray crystallography was obtained from a concentrated solution of CH_2Cl_2 by slow evaporation

7.11.22 Synthesis of $[\text{Ir}(\text{Ph-NN})(\text{CO})(\text{P}(\text{4-FC}_6\text{H}_4)_3)(\text{Me})\text{I}]$ **4e**

Complex **4e** was synthesised using the general method from **3e** (0.032 g, 0.045 mmol) in CH_2Cl_2 (10 ml) and excess MeI to yield **4e** as a yellow solid.

^1H NMR (400 MHz, CDCl_3) δ 7.79 – 7.66 (m, 6H, Ar), 7.64 (d, $J = 9.5$ Hz, 1H, HC=NAr), 7.54 – 7.47 (m, 2H, Ar), 7.37 – 7.20 (m, 8H), 6.89 (dd, $J = 4.0, 0.9$ Hz, 1H, Pyrrole), 6.64 – 6.61

(m, $J = 0.8$ Hz, 1H, pyrrole), 6.09 (dd, $J = 4.0, 1.9$ Hz, 1H, pyrrole), 0.45 (d, $J = 3.0$ Hz, 3H, Ir-CH₃).

³¹P{¹H} NMR (162 MHz, CDCl₃) δ -9.44 (s).

¹³C{¹H} NMR (101 MHz, CDCl₃) δ 167.07 (d, $J = 10.5$ Hz), 158.09 (s), 151.32 (s), 143.11 (d, $J = 3.5$ Hz), 139.46 (s), 138.44 (d, $J = 2.9$ Hz), 136.04 (d, $J = 10.7$ Hz), 129.12 (s), 128.88 (d, $J = 11.5$ Hz), 127.44 (d, $J = 3.1$ Hz), 126.86 (s), 124.01 (s), 120.73 (s), 113.22 (s), -2.77 (d, $J = 3.0$ Hz).

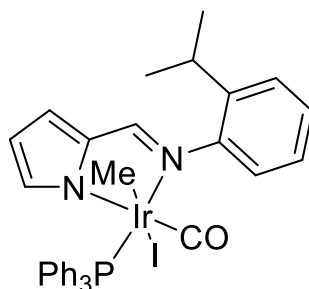
¹⁹F NMR (377 MHz, CDCl₃) δ -106.85 (s).

High resolution MS (TOF MS ES+ m/z) 849.0331.

IR ν (CO) 2046 cm⁻¹ (CH₂Cl₂)

Yield 0.031 g, 81 %

7.11.23 Synthesis of [Ir(2-ⁱPrC₆H₄-NN)(CO)(PPh₃)(Me)I] 4f



Complex **4f** was synthesised using the general method from **3f** (0.029g, 0.041 mmol) in CH₂Cl₂ (10 ml) and excess MeI to yield **4f** as a yellow solid.

Major isomer

¹H NMR (400 MHz, CDCl₃) δ 7.99 – 7.86 (m, 6H, Ar), 7.56 (d, $J = 9.5$ Hz, 1H, HC=NAr), 7.47 – 7.40 (m, 10H, Ar), 7.30 – 7.18 (m, 3H, Ar), 7.01 (dd, $J = 3.9, 0.8$ Hz, 1H, pyrrole), 6.85 (s, 1H, pyrrole), 6.20 (dd, $J = 3.9, 1.9$ Hz, 1H, pyrrole), 3.13 (septet, $J = 6.8$ Hz, 1H, H(CH₃)₂), 1.26 (d, $J = 6.7$ Hz, 3H, CH₃), 1.15 (d, $J = 6.8$ Hz, 3H, CH₃), 0.64 (d, $J = 2.9$ Hz, 3H, Ir-CH₃).

³¹P{¹H} NMR (162 MHz, CDCl₃) δ -9.32 (s).

Minor isomer

¹H NMR (400 MHz, CDCl₃) δ 8.59 – 8.48 (m, 2H, Ar), 8.02 – 7.87 (m, 5H, Ar), 7.52 (d, $J = 9.5$ Hz, 1H, HC=NAr), 7.51 – 7.38 (m, 8H), 7.37 – 7.32 (m, 2H, Ar), 7.18 – 7.09 (m, 1H, Ar), 6.94 (d, $J = 3.2$ Hz, 1H, pyrrole), 6.78 (br, 1H, pyrrole), 6.16 (dd, $J = 3.9, 1.9$ Hz, 1H, pyrrole),

3.75 (septet, $J = 6.8$ Hz, 1H), 1.42 (d, $J = 6.6$ Hz, 1H, CH₃), 1.36 (d, $J = 6.9$ Hz, 3H, CH₃), 0.62 (d, $J = 3.2$ Hz, 3H, Ir-CH₃).

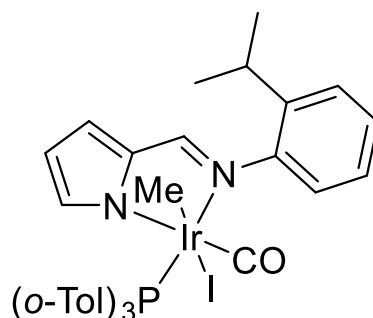
³¹P{¹H} NMR (162 MHz, CDCl₃) δ -7.92 (s).

High resolution MS (TOF MS EI+ m/z) 836.1004.

IR ν (CO) 2046 cm⁻¹ (CH₂Cl₂)

Yield 0.028 g, 81 %

7.11.24 Synthesis of [Ir(2-*i*PrC₆H₄-NN)(CO)(P-*o*-Tol₃)(Me)I] 4g



Complex **4g** was synthesised using the general method from **3g** (0.045 g, 0.06 mmol) in CH₂Cl₂ (10 ml) and excess MeI to yield **4g** as a yellow solid.

Major Isomer

¹H NMR (400 MHz, CDCl₃) δ 8.45 – 8.45 (m, 2H, Ar), 8.11 (br, 2H, Ar), 7.47 – 6.80 (m, 14H, Ar), 6.16 (dd, $J = 3.9, 1.9$ Hz, 1H, pyrrole), 3.04 (septet, $J = 7.8$ Hz, 1H, H(CH₃)₂), 2.08 (d, $J = 6.0$ Hz, 9H, 2-Me), 1.16 (d, $J = 6.8$ Hz, 3H, CH₃), 1.06 (d, $J = 6.7$ Hz, 3H, CH₃), 0.94 (d, $J = 3.0$ Hz, 3H, Ir-CH₃).

³¹P NMR (162 MHz, CDCl₃) δ -13.28 (s).

Minor isomer

¹H NMR (400 MHz, CDCl₃) δ 8.50 – 8.41 (m, 2H, Ar), 8.27 (br, 2H, Ar), 7.48 – 6.78 (m, 14H), 6.10 (dd, $J = 3.9, 1.9$ Hz, 1H, Pyrrole), 3.74 (septet, $J = 6.5$ Hz, 1H, H(CH₃)₂), 2.31 (d, $J = 3.3$ Hz, 9H), 1.25 (d, $J = 6.6$ Hz, 3H, CH₃), 1.20 (d, $J = 7.0$ Hz, 1H), 0.97 (d, $J = 3.6$ Hz, 1H).

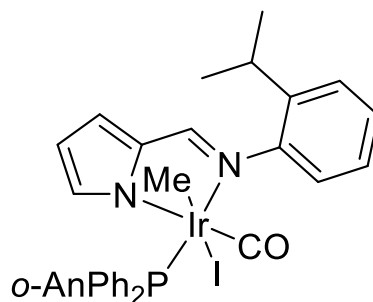
³¹P{¹H} NMR (162 MHz, CDCl₃) δ -10.83 (s).

MS (TOF MS EI+ m/z) 751.24[M+][I-]

IR ν (CO) 2046 cm⁻¹ (CH₂Cl₂)

Yield 0.044 g, 82 %

7.11.25 Synthesis of $[\text{Ir}(\text{2-}^i\text{PrC}_6\text{H}_4\text{-NN})(\text{CO})(\text{PPh}_2\text{-}o\text{-An})(\text{Me})\text{I}]$ **4h**



Complex **4h** was synthesised using the general method from **3h** (0.048g, 0.063 mmol) in CH_2Cl_2 (10 ml) and excess MeI to yield **4h** as an off yellow solid.

Major isomer

$^1\text{H NMR}$ (400 MHz, CDCl_3) δ 8.59 – 8.58 (m, 2H, Ar), 8.27 – 8.12 (m, 4H, Ar), 7.59 (d, $J = 9.6$ Hz, 1H, $\text{HC}=\text{NAr}$), 7.55 – 6.82 (m, 14H), 6.19 (dd, $J = 3.8, 1.8$ Hz, 1H, Pyrrole), 3.59 (s, 3H, 2-OMe), 3.17 (septet, $J = 6.7$ Hz, 1H, $\text{HC}(\text{CH}_3)_2$), 1.27 (d, $J = 6.8$ Hz, 3H, CH_3), 1.16 (d, $J = 6.7$ Hz, 3H, CH_3), 0.64 (d, $J = 3.0$ Hz, 3H, Ir- CH_3).

$^{31}\text{P}\{^1\text{H}\}$ NMR (162 MHz, CDCl_3) δ -12.03 (s).

Minor isomer

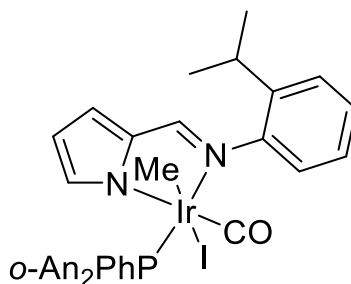
$^1\text{H NMR}$ (400 MHz, CDCl_3) δ 8.58 (m, 1H, Ar), 8.11 – 7.97 (m, 4H), 7.62 – 6.84 (m, 15H), 6.16 (dd, $J = 3.8, 1.8$ Hz, 1H, pyrrole), 3.79 (septet, $J = 6.4$ Hz, 1H, $\text{HC}(\text{CH}_3)_2$), 3.69 (s, 3H, 2-OMe), 1.44 (d, $J = 6.5$ Hz, 3H, CH_3), 1.38 (d, $J = 6.9$ Hz, 3H, CH_3), 0.62 (d, $J = 3.2$ Hz, 3Hm Ir- CH_3).

$^{31}\text{P}\{^1\text{H}\}$ NMR (162 MHz, CDCl_3) δ -14.83 (s).

MS (TOF MS EI+ m/z) 739.21[M+][I-]

IR $\nu(\text{CO})$ 2045 cm^{-1} (CH_2Cl_2)

Yield 0.045 g, 79 %

7.11.26 Synthesis of $[\text{Ir}(\text{2-}^i\text{PrC}_6\text{H}_4\text{-NN})(\text{CO})(\text{PPh-}o\text{-An}_2)(\text{Me})\text{I}]$ **4i**

Complex **4i** was synthesised using the general method from **3i** (0.032g, 0.042 mmol) in CH_2Cl_2 (10 ml) and excess MeI to yield **4i** as a white powder.

Major isomer

$^1\text{H NMR}$ (400 MHz, CDCl_3) δ 8.57 (dd, $J = 5.8, 3.6$ Hz, 1H, Ar), 8.27 (br, 3H, Ar), 7.56 (d, $J = 9.7$ Hz, 1H, $\text{HC}=\text{NAr}$), 7.52 – 6.75 (m, 15H), 6.18 (dd, $J = 3.8, 1.8$ Hz, 1H, pyrrole), 3.44 (s, 3H, 2-OMe), 3.39 (s, 3H, 2-OMe), 3.18 (septet, $J = 6.7$ Hz, 1H, $\text{HC}(\text{CH}_3)_2$), 1.26 (d, $J = 6.8$ Hz, 3H, CH_3), 1.16 (d, $J = 6.8$ Hz, 3H, CH_3), 0.61 (br, 3H, Ir- CH_3).

$^{31}\text{P}\{^1\text{H}\}$ NMR (162 MHz, CDCl_3) δ -14.96 (br).

Minor isomer

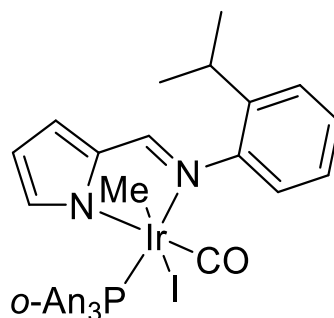
$^1\text{H NMR}$ (400 MHz, CDCl_3) δ 8.57 (dd, $J = 5.8, 3.6$ Hz, 1H), 8.27 (br, 3H), 7.61 – 6.74 (m, 16H, Ar), 6.16 (dd, $J = 3.8, 1.7$ Hz, 1H, pyrrole), 3.80 (dt, $J =$ septet, 6.6 Hz, 1H, $\text{HC}(\text{CH}_3)_2$), 3.65 (s, 3H, 2-OMe), 3.53 (s, 3H, 2-OMe), 1.45 (d, $J = 6.5$ Hz, 3H, CH_3), 1.38 (d, $J = 6.9$ Hz, 3H, CH_3), 0.61 (br, 3H, Ir- CH_3).

$^{31}\text{P}\{^1\text{H}\}$ NMR (162 MHz, CDCl_3) δ -12.48 (br)

MS (TOF MS EI+ m/z) 769.31[M+][I-]

IR $\nu(\text{CO})$ 2044 cm^{-1} (CH_2Cl_2)

Yield 0.029 g, 76 %

7.11.27 Synthesis of $[\text{Ir}(\text{2-}^i\text{PrC}_6\text{H}_4\text{-NN})(\text{CO})(\text{P-}o\text{-An}_3)(\text{Me})\text{I}]$ **4j**

Complex **4j** was synthesised using the general method from **3j** (0.051 g, 0.065 mmol) in CH_2Cl_2 (10 ml) and excess MeI to yield **4j** as a white powder.

Major isomer

$^1\text{H NMR}$ (400 MHz, CDCl_3) δ 8.47 (d, $J = 7.9$ Hz, 1H, Ar), 7.98 (br, 2H, Ar), 7.53 (d, $J = 10.1$ Hz, 1H, $\text{HC}=\text{NAr}$), 7.47 – 7.10 (m, 8H), 7.04 – 6.98 (m, 3H, Ar), 6.82 (m, 4H, Ar), 6.25 (dd, $J = 3.9, 1.8$ Hz, 1H, pyrrole), 3.45 (s, 9H, 2-OMe), 3.24 (septet, $J = 6.7$ Hz, 1H, $\text{HC}(\text{CH}_3)_2$), 1.29 (d, $J = 6.9$ Hz, 3H, CH_3), 1.20 (d, $J = 6.7$ Hz, 3H, CH_3), 0.97 (d, $J = 3.8$ Hz, 3H, Ir- CH_3).

$^{31}\text{P}\{^1\text{H}\}$ NMR (162 MHz, CDCl_3) δ -22.67 (s).

Minor isomer

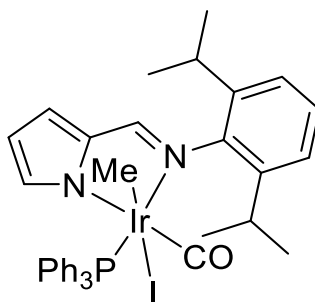
$^1\text{H NMR}$ (400 MHz, CDCl_3) δ 8.47 (d, $J = 7.9$ Hz, 1H, Ar), 7.98 (br, 2H, Ar), 7.47 – 6.90 (m, 12H, Ar), 6.82 (dd, $J = 7.9, 4.9$ Hz, 3H, Ar), 6.20 (dd, $J = 3.8, 1.9$ Hz, 1H, pyrrole), 3.84 (septet, $J = 6.8$ Hz, 1H, $\text{HC}(\text{CH}_3)_2$), 3.48 (s, 9H, 2-OMe), 1.36 (d, $J = 6.6$ Hz, 3H, CH_3), 1.31 (d, $J = 8.5$ Hz, 3H, CH_3), 0.98 (br, 3H, Ir- CH_3).

$^{31}\text{P}\{^1\text{H}\}$ NMR (162 MHz, CDCl_3) δ -20.69 (s).

High resolution MS (TOF MS EI+ m/z) 799.2277[M+] $[\text{I}^-]$

IR $\nu(\text{CO})$ 2043 cm^{-1} (CH_2Cl_2)

Yield 0.042 g, 71 %

7.11.28 Synthesis of $[\text{Ir}(\text{2,6}^i\text{Pr}_2\text{C}_6\text{H}_4\text{-NN})(\text{CO})(\text{PPh}_3)(\text{Me})\text{I}]$ **4k**

Complex **4k** was synthesised using the general method from **3k** (0.07g, 0.09 mmol) in CH_2Cl_2 (10 ml) and excess MeI to yield **4k** as a light yellow powder.

^1H NMR (400 MHz, CDCl_3) δ 8.00 – 7.87 (m, 6H, Ar), 7.65 (d, $J = 9.2$ Hz, 1H, HC=NAr), 7.53 – 7.38 (m, 8H, Ar), 7.33 (dd, $J = 7.7, 1.6$ Hz, 1H, Ar), 7.27 (d, $J = 7.7$ Hz, 1H, Ar), 7.20 (dd, $J = 7.6, 1.7$ Hz, 1H, Ar), 6.99 (dd, $J = 3.9, 1.0$ Hz, 1H, pyrrole), 6.93 (br, 1H, pyrrole), 6.23 (dd, $J = 3.9, 1.9$ Hz, 1H, pyrrole), 4.08 – 3.95 (septet, $J = 6.7$ Hz, 1H, $\text{H}(\text{CH}_3)_2$), 3.34 (septet, $J = 6.7$ Hz, 1H, HC=NAr), 1.45 (d, $J = 6.5$ Hz, 3H, CH_3), 1.28 (d, $J = 6.7$ Hz, 1H, CH_3), 1.22 (d, $J = 6.7$ Hz, 3H, CH_3), 1.04 (d, $J = 6.7$ Hz, 3H, CH_3), 0.65 (d, $J = 3.1$ Hz, 3H, Ir- CH_3).

$^{31}\text{P}\{^1\text{H}\}$ NMR (162 MHz, CDCl_3) δ -9.00 (s).

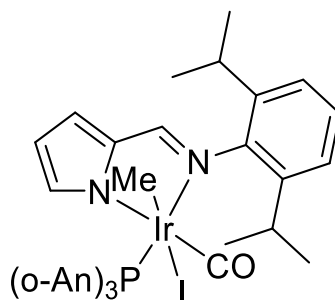
$^{13}\text{C}\{^1\text{H}\}$ NMR (101 MHz, CDCl_3) δ 167.55 (d, $J = 10.2$ Hz), 161.33 (s), 146.50 (s), 144.95 (s), 143.20 (s), 142.37 (d, $J = 3.2$ Hz), 139.86 (s), 135.22 (d, $J = 9.3$ Hz), 131.25 (d, $J = 2.6$ Hz), 129.58 (s), 128.99 (s), 128.07 (d, $J = 10.9$ Hz), 127.56 (s), 124.93 (s), 123.13 (s), 120.25 (s), 113.07 (s), 29.03 (s), 28.27 (s), 27.29 (s), 26.50 (s), 24.45 (s), 21.55 (s), 0.68 (d, $J = 3.3$ Hz).

MS (TOF MS ES+ m/z) 751 $[\text{M}^+][\text{I}^-]$

IR $\nu(\text{CO})$ 2045 cm^{-1} (CH_2Cl_2)

Yield 0.074 g, 89 %

A single crystal of **4k** suitable for X-ray crystallography was obtained by slow diffusion of hexanes into a concentrated solution in CH_2Cl_2 .

7.11.29 Synthesis of $[\text{Ir}(\text{2,6}^i\text{Pr}_2\text{C}_6\text{H}_4\text{-NN})(\text{CO})(\text{P}^o\text{-An}_3)(\text{Me})\text{I}]$ **4m**

Complex **4m** was synthesised using the general method from **3m** (0.037 g, 0.047 mmol) in CH_2Cl_2 (10 ml) and excess MeI to yield **4m** as a white powder.

Major isomer

^1H NMR (400 MHz, CDCl_3) δ 8.13 (dd, $J = 15.8, 6.7$ Hz, 1H, Ar), 7.84 (dd, $J = 8.6, 0.6$ Hz, 1H, HC=NAr), 7.76 (dd, $J = 7.9, 1.6$ Hz, 1H, Ar), 7.73 (dd, $J = 7.9, 1.5$ Hz, 1H, Ar), 7.5-6.5(m, 11H), 6.47 (dddd, $J = 9.4, 8.3, 7.5, 5.9$ Hz, 2H, Ar), 6.18 (br, 1H, pyrrole), 6.01 (dd, $J = 3.8, 1.7$ Hz, 1H, pyrrole), 3.93 (septet, $J = 6.8$ Hz, 1H), 3.35- 3.30 (d, 9H, 19Hz), 3.31 - 3.22 (m, 1H HC=NAr), 1.13 (d, $J = 7.0$ Hz, 3H, CH_3), 1.12 (d, $J = 6.9$ Hz, 3H, CH_3), 1.03 (d, $J = 6.9$ Hz, 3H, CH_3), 0.00 (d, $J = 3.3$ Hz, 3H, Ir- CH_3).

$^{31}\text{P}\{^1\text{H}\}$ NMR (162 MHz, CDCl_3) δ 14.3 (s),

IR $\nu(\text{CO})$ 2039 (CH_2Cl_2)

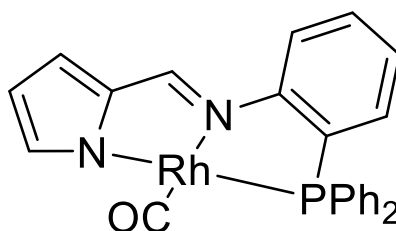
Minor isomer

Due to the low intensity of the minor isomer in the ^1H NMR spectrum an accurate description of the proton spectrum cannot be performed.

$^{31}\text{P}\{^1\text{H}\}$ NMR (162 MHz, CDCl_3) δ -6.1 (s)

$\nu(\text{CO})$ 2020 cm^{-1} (CH_2Cl_2)

Yield 0.03 g 71 %

7.11.30 Synthesis of $[\text{Rh}(\text{Ph}_2\text{PNN})(\text{CO})]$ **5a**

[Rh(acac)(CO)₂] (0.065g, 0.25mmol) and Ph₂PNN(H) (0.09 g, 0.25 mmol) were dissolved in MeCN (10 ml). The solution was refluxed and monitored by IR spectroscopy, once the reaction was complete the solution was allowed to cool and solvent removed under vacuum yielding an orange solid.

¹H NMR (400 MHz, CDCl₃) δ 8.41 (s, 1H, HC=NAr), 7.74 – 7.67 (m, 4H, Ar), 7.61 – 7.57 (m, 1H, Ar), 7.52 – 7.37 (m, 9H, Ar), 7.22 – 7.15 (m, 1H, pyrrole), 7.01 (dt, *J* = 4.0, 1.0 Hz, 1H, pyrrole), 6.43 – 6.39 (m, 1H, pyrrole).

³¹P{¹H} NMR (162 MHz, CDCl₃) δ 56.47 (d, *J* = 149.0 Hz).

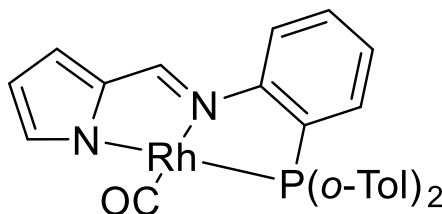
¹³C{¹H} NMR (101 MHz, CDCl₃) δ 192.03 (dd, *J* = 72.2, 16.9 Hz), 152.90 (d, *J* = 17.5 Hz), 150.33 (s), 143.82 (d, *J* = 24.0 Hz), 133.94 (d, *J* = 21.2 Hz), 133.84 (s), 133.54 (s), 133.12 (d, *J* = 12.8 Hz), 132.13 (s), 130.46 (d, *J* = 2.1 Hz), 129.93 (s), 128.69 (d, *J* = 10.9 Hz), 125.57 (d, *J* = 6.5 Hz), 122.66 (s), 115.43 (d, *J* = 3.3 Hz), 114.36 (d, *J* = 11.3 Hz).

High resolution MS (TOF MS AP+ *m/z*) 485.0285

IR ν(CO) 1977 cm⁻¹ (MeCN)

Yield 0.087g, 72%

7.11.31 Synthesis of [Rh(*o*-Tol₂PNN)(CO)] 5b



[Rh(acac)(CO)₂] (0.13g, 0.5mmol) and *o*-Tol₂PNN(H) (0.19 g, 0.5 mmol) were dissolved in MeCN (10 ml). The solution was refluxed and monitored by IR spectroscopy, once the reaction was complete the solution was allowed to cool and solvent removed under vacuum yielding an orange solid.

¹H NMR (400 MHz, CDCl₃) δ 8.42 (s, 1H, HC=NAr), 7.63 (dd, *J* = 8.3, 4.2 Hz, 1H, Ar), 7.54 – 7.46 (m, 1H, Ar), 7.43 – 7.36 (m, 3H, Ar), 7.33 – 7.26 (m, 2H, Ar), 7.15 (m, 3H, Ar), 7.08 – 6.97 (m, 2H, pyrrole), 6.42 – 6.38 (m, 1H, pyrrole), 2.67 (Br, 6H, 2-Me).

³¹P{¹H} NMR (162 MHz, CDCl₃) δ 40.68 (d, *J* = 147.5 Hz).

$^{13}\text{C}\{^1\text{H}\}$ NMR (101 MHz, CDCl_3) δ 193.45 (dd, $J = 73.2, 14.9$ Hz), 152.65 (d, $J = 3.2$ Hz), 152.46 (d, $J = 3.1$ Hz), 150.20 (s), 143.94 (s), 143.33 (d, $J = 2.3$ Hz), 134.93 (s), 132.01 (d, $J = 1.9$ Hz), 130.49 (s), 130.06 – 130.04 (m), 125.74 (d, $J = 6.6$ Hz), 122.30 (t, $J = 1.1$ Hz), 115.46 (d, $J = 1.5$ Hz), 115.42 (d, $J = 1.5$ Hz), 114.23 (d, $J = 9.6$ Hz), 23.65 – 23.15 (br).

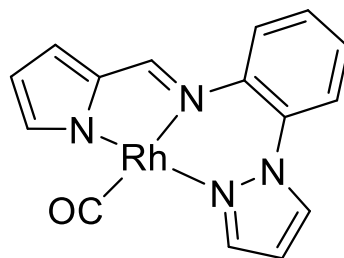
High resolution MS (TOF MS EI+ m/z) 513.0603

IR $\nu(\text{CO})$ 1973 cm^{-1} (MeCN)

Yield 0.2g, 81%

Crystals suitable for X-ray crystallography were obtained by slow evaporation of a concentrated CH_2Cl_2 solution.

7.11.32 Synthesis of $[\text{Rh}(\text{H-NNN})(\text{CO})]$ 5c



$[\text{Rh}(\text{acac})(\text{CO})_2]$ (0.11g, 0.46 mmol) and H-NNN(H) (0.12 g, 0.46 mmol) were dissolved in MeCN (5 ml). The solution was refluxed and monitored by IR spectroscopy, once the reaction was complete the red solution was allowed to cool and solvent removed under vacuum yielding a black solid.

^1H NMR (400 MHz, CDCl_3) δ 8.07 (s, 1H, $\text{HC}=\text{NAr}$), 8.06 (d, $J = 2.8$ Hz, 1H, pyrazole), 7.86 (d, $J = 1.7$ Hz, 1H, pyrazole), 7.42 (dd, $J = 8.2, 0.9$ Hz, 1H), 7.35 – 7.28 (m, 2H, Ar), 7.13 (m, 2H, Ar), 6.94 (d, $J = 3.9$ Hz, 1H, pyrrole), 6.54 – 6.52 (m, 1H, pyrrole), 6.25 (dd, $J = 4.2, 1.4$ Hz, 1H, pyrrole).

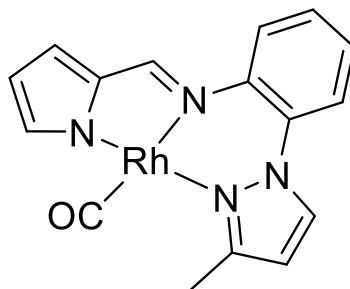
$^{13}\text{C}\{^1\text{H}\}$ NMR (101 MHz, CDCl_3) δ 152.16 (s), 149.33 (s), 144.89 (s), 142.36(s), 138.27(s), 131.53(s), 131.47 (s), 128.91 (s), 124.62 (s), 123.73 (s), 123.29 (s), 118.81 (s), 116.40 (s), 108.56(s).

High resolution MS (TOF MS EI+ m/z) 367.0070

IR $\nu(\text{CO})$ 1967 cm^{-1} (MeCN)

Yield 0.124g, 74 %

7.11.33 Synthesis of [Rh(Me-NNN)(CO)] 5d



[Rh(acac)(CO)₂] (0.155g, 0.6 mmol) and Me-NNN(H) (0.15g, 0.6 mmol) were dissolved in MeCN (5 ml). The solution was refluxed and monitored by IR spectroscopy, once the reaction was complete the red solution was allowed to cool and solvent removed under vacuum yielding a red solid.

¹H NMR (400 MHz, CDCl₃) δ 8.07 (s, 1H, HC=NAr), 7.92 (d, *J* = 2.7 Hz, 1H, pyrazole), 7.42 – 7.15 (m, 6H, Ar), 7.14 – 7.07 (m, 1H, Ar), 6.96 (dd, *J* = 4.2, 0.9 Hz, 1H, pyrrole), 6.39 (d, *J* = 2.7 Hz, 1H, pyrrole), 6.27 (dd, *J* = 4.0, 1.2 Hz, 1H, pyrrole), 2.51 (s, 3H, Me).

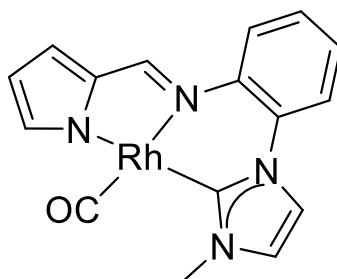
¹³C NMR (101 MHz, CDCl₃) δ 157.62 (s), 151.74 (s), 144.12 (s), 142.94 (s), 139.07 (s), 133.30 (s), 132.54 (s), 128.76 (s), 124.55 (s), 124.37 (s), 122.69 (s), 118.95 (s), 116.45 (s), 109.84 (s), 17.65 (s).

High resolution MS (TOF MS EI+ *m/z*) 381.0217

IR ν(CO) 1961 cm⁻¹ (MeCN)

Yield 0.175 g, 77 %

7.11.34 Synthesis of [Rh(Me-CNN)(CO)] 5e



[Rh(acac)(CO)₂] (0.102 g, 0.4 mmol), Me-CNN(H) (0.15 g, 0.4 mmol) and Cs₂CO₃ (0.13 g, 0.4 mmol) were dissolved in MeCN (10 ml). The solution was refluxed and monitored by IR spectroscopy, the red solution was allowed to cool and was then filtered through a pad

of Celite. The resultant red solution had the solvent removed under vacuum yielding a red solid.

$^1\text{H NMR}$ (400 MHz, CDCl_3) δ 8.11(s, 1H, HC=NAr), δ 7.43 (d, J = 2.2 Hz, 1H, Ar), δ 7.38 (dd, J = 3.8, 1.4 Hz, 1H, imidazolium), 7.36 (dd, J = 3.7, 1.4 Hz, 1H, imidazolium), 7.28 – 7.20 (m, 2H, Ar), 7.18 – 7.09 (m, 1H, Ar), 7.02 (d, J = 2.1 Hz, 1H, pyrrole), 6.92 (d, J = 3.9 Hz, 1H, pyrrole), 6.31 (dd, J = 4.0, 1.4 Hz, 1H, pyrrole), 3.83 (s, 3H, N- CH_3).

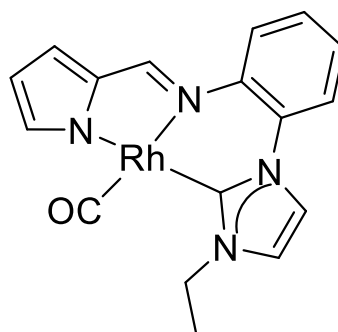
$^{13}\text{C}\{^1\text{H}\}$ NMR (101 MHz, CDCl_3) δ 153.81 (s), 144.32 (s), 143.04 (s), 138.21 (s), 127.29 (s), 124.66 (s), 123.69 (s), 123.45 (s), 122.06 (s), 118.51 (d, J = 20.8 Hz), 116.38 (s), 39.77 (s).

High resolution MS (TOF MS EI+ m/z) 381.022

IR $\nu(\text{CO})$ 1955 cm^{-1} (MeCN)

Yield 0.105 g, 69%

7.11.35 Synthesis of $[\text{Rh}(\text{EtCNN})(\text{CO})]$ 5f



$[\text{Rh}(\text{acac})(\text{CO})_2]$ (0.168 g, 0.65 mmol), Et-CNN(H) (0.265 g, 0.65 mmol) and Cs_2CO_3 (0.24 g, 0.65 mmol) were dissolved in MeCN (10 ml). The solution was refluxed and monitored by IR spectroscopy. Once complete the red solution was allowed to cool and was then filtered through a pad of Celite. The resultant red solution had the solvent removed under vacuum yielding a red solid.

$^1\text{H NMR}$ (400 MHz, CDCl_3) δ 8.02 (s, 1H, HC=NAr), 7.35 (d, J = 2.2 Hz, 1H, Ar), 7.28 (dd, J = 2.5, 1.5 Hz, 1H, imidazole), 7.26 (dd, J = 2.3, 1.5 Hz, 1H, imidazole), 7.18 – 7.11 (m, 2H, Ar), 7.08 – 7.01 (m, 1H), 6.99 (d, J = 2.1 Hz, 1H, pyrrole), 6.84 (dd, J = 4.0, 0.8 Hz, 1H, pyrrole), 6.22 (dd, J = 4.0, 1.4 Hz, 1H, pyrrole), 4.18 (q, J = 7.3 Hz, 2H, CH_2), 1.46 (t, J = 7.3 Hz, 3H, CH_3).

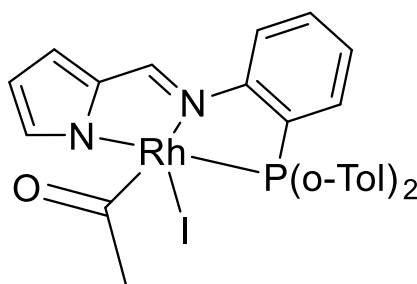
$^{13}\text{C}\{^1\text{H}\}$ NMR (101 MHz, CDCl_3) δ 153.64 (s), 144.10 (d, $J = 3.5$ Hz), 143.08 (s), 138.36 (s), 133.44 (s), 127.26 (s), 126.6(s), 124.63 (s), 123.24 (s), 122.24 (s), 121.77 (s), 119.25 (s), 118.37 (s), 116.29 (s), 46.63 (s), 16.33 (s).

High resolution MS (TOF MS ES+ m/z) 395.0379

IR $\nu(\text{CO})$ 1952 cm^{-1} (MeCN)

Yield 0.18g, 70 %

7.11.36 Synthesis of $[\text{Rh}(\text{o-Tol}_2\text{PNN})\text{I}(\text{COMe})]$ **7b**



In a NMR tube **5b** (0.015 g, 0.029 mmol) was dissolved in CDCl_3 . MeI was added (excess) and the resulting solution was monitored by $^{31}\text{P}\{^1\text{H}\}$ and ^1H NMR spectroscopy at regular intervals. After approximately four days complex **7b** was formed with a yellow to brown colour change observed in solution.

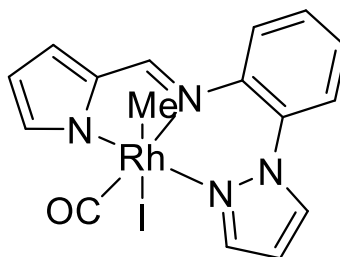
^1H NMR (400 MHz, CDCl_3) δ 8.42 (d, $J = 3.1$ Hz, 1H, Ar), 8.35 (s, 1H, $\text{HC}=\text{NAr}$), 7.60 – 7.07 (m, 16H, Ar), 6.58 – 6.53 (m, 1H, pyrrole), 2.66 (s, 3H, 2-Me), 2.56 (s, 1H, 2-Me), 2.21 (s, 3H, COMe).

$^{31}\text{P}\{^1\text{H}\}$ NMR (162 MHz, CDCl_3) δ 45.92 (d, $J = 138.1$ Hz).

$^{13}\text{C}\{^1\text{H}\}$ NMR (101 MHz, CDCl_3) δ 151.32 (d, $J = 2.2$ Hz), 151.15 (d, $J = 2.1$ Hz), 149.12 (s), 144.11 (s, $J = 1.9$ Hz), 143.46 (s), 143.34 (s), 140.35 (d, $J = 16.1$ Hz), 135.95 (d, $J = 7.8$ Hz), 135.33 (s), 132.14 (s), 132.05 (s), 131.30 (s), 131.19 (d, $J = 2.3$ Hz), 131.07 (s), 130.86 – 130.79 (m), 130.60 (s), 130.40 – 130.32 (m), 126.32 (dd, $J = 11.4, 7.3$ Hz), 125.70 (s), 125.14 (d, $J = 9.4$ Hz), 123.50 (s), 116.53 (d, $J = 5.0$ Hz), 115.46 (d, $J = 10.9$ Hz), 43.34 (s), 27.35 (d, $J = 4.8$ Hz), 23.66 (d, $J = 10.0$ Hz).

High resolution MS (TOF MS ES+ m/z) 527.0771

IR $\nu(\text{C}=\text{O})$ 1720 cm^{-1} (CDCl_3)

7.11.37 Synthesis of $[\text{Rh}(\text{H-NNN})(\text{CO})(\text{Me})\text{I}]$ **6c**

To a solution of **5c** (0.06 g 0.16 mmol) in CH_2Cl_2 (5ml), MeI was added (excess) and allowed to stir for 2-3 hours. The solvent was removed under vacuum to yield **6c** a yellow solid.

Note over time this solution darkened and formed uncharacterised black precipitates.

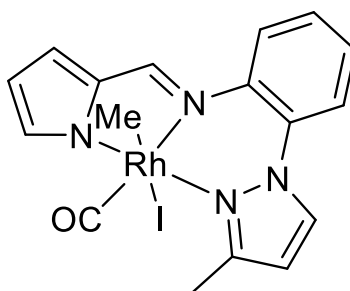
$^1\text{H NMR}$ (400 MHz, CDCl_3) δ 8.34 (s, 1H, $\text{HC}=\text{NAr}$), 8.27 (d, $J = 2.8$ Hz, 1H, pyrazole), 7.90 (d, $J = 2.0$ Hz, 1H, pyrazole), 7.67 (d, $J = 8.3$ Hz, 1H, pyrazole), 7.54 – 7.34 (m, 3H, Ar), 7.31 – 7.25 (m, 1H, Ar), 7.15 (d, $J = 4.3$ Hz, 1H, pyrrole), 6.68 (t, $J = 2.6$ Hz, 1H, pyrrole), 6.37 (dd, $J = 4.2, 1.5$ Hz, 1H, pyrrole), 1.19 (d, $J = 1.9$ Hz, 1H, Rh-CH_3).

$^{13}\text{C}\{^1\text{H}\}$ NMR (101 MHz, CDCl_3) δ 150.33 (s), 150.01 (s), 142.82 (s), 140.82 (s), 136.66 (s), 133.36 (s), 130.41 (s), 129.42 (s), 125.96 (s), 124.10 (s), 123.72 (s), 119.73 (s), 117.25 (s), 109.81 (s), 11.14 (d, $J = 19.1$ Hz).

High resolution MS (TOF MS ES+ m/z) 381.0223 $[\text{M}^+][\text{I}^-]$

IR $\nu(\text{CO})$ 2075 cm^{-1} (CH_2Cl_2)

Yield 0.06 g, 72 %

7.11.38 Synthesis of $[\text{Rh}(\text{Me-NNN})(\text{CO})(\text{Me})\text{I}]$ **6d**

To a solution of **5d** (0.075 g 0.18 mmol) in CH_2Cl_2 (5 ml), MeI (excess) was added and allowed to stir for 2-3 hours. The solvent was removed under vacuum to yield **6d** a yellow solid.

^1H NMR (400 MHz, CDCl_3) δ 8.33 (s, 1H, HC=NAr), 8.17 (d, $J = 2.6$ Hz, 1H, pyrazole), 7.62 (d, $J = 8.1$ Hz, 1H, pyrazole), 7.49 – 7.38 (m, 2H, Ar), 7.33 – 7.24 (m, 2H, Ar), 7.18 (d, $J = 4.2$ Hz, 1H, pyrrole), 6.51 (d, $J = 2.7$ Hz, 1H, pyrrole), 6.40 (dd, $J = 4.2, 1.4$ Hz, 1H, pyrrole), 2.68 (s, 3H, CH_3), 1.14 (d, $J = 1.9$ Hz, 3H, Rh-Me).

$^{13}\text{C}\{^1\text{H}\}$ NMR (101 MHz, CDCl_3) δ 158.34 (s), 150.75 (s), 142.00 (s), 141.13 (s), 137.84 (s), 135.39 (s), 131.32 (s), 129.23 (s), 125.99 (s), 124.94 (s), 123.41 (s), 119.96 (s), 117.12 (s), 111.10 (s), 18.03 (s), 9.70 (d, $J = 19.1$ Hz).

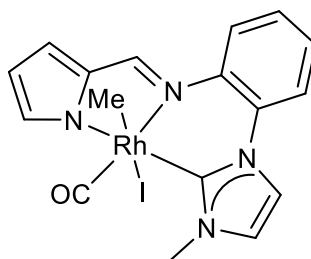
High resolution MS (TOF MS ES+ m/z) 395.0379 [M^+][I^-]

IR $\nu(\text{CO})$ 2073 cm^{-1} (CH_2Cl_2)

Yield 0.074 g, 78 %

Crystals suitable for X-ray crystallography were obtained by slow vapour diffusion of hexanes into concentrated CH_2Cl_2 solution.

7.11.39 Synthesis of $[\text{Rh}(\text{Me-CNN})(\text{CO})(\text{Me})\text{I}]$ **6e**



To a solution of **5e** (0.064 g 0.17 mmol) in CH_2Cl_2 (5 ml), MeI (excess) was added and allowed to stir for 2-3 hours. The solvent was removed under vacuum to yield a yellow solid.

^1H NMR (400 MHz, CDCl_3) δ 8.31 (s, 1H, HC=NAr), 7.65 (d, $J = 2.1$ Hz, 1H, Ar), 7.60 – 7.55 (m, 2H, Ar), 7.48 (dd, $J = 8.2, 1.2$ Hz, 1H, imidazolium), 7.40 – 7.33 (m, 1H, Ar), 7.27 – 7.23 (m, 1H, Ar), 7.22 (dd, $J = 4.0, 0.7$ Hz, 1H, pyrrole), 7.13 (d, $J = 2.1$ Hz, 1H, pyrrole), 6.46 (dd, $J = 4.1, 1.4$ Hz, 1H, pyrrole), 4.07 (s, 3H, N-Me), 0.95 (d, $J = 2.1$ Hz, 3H, Rh-Me).

$^{13}\text{C}\{^1\text{H}\}$ NMR (101 MHz, CDCl_3) δ 151.04 (s), 142.96 (s), 142.09 (s), 136.35 (s), 131.09 (s), 128.40 (s), 125.26 (s), 124.71 (s), 124.00 (s), 122.10 (s), 119.64 (d, $J = 5.4$ Hz), 117.34 (s), 40.66 (s), 4.17 (d, $J = 20.2$ Hz).

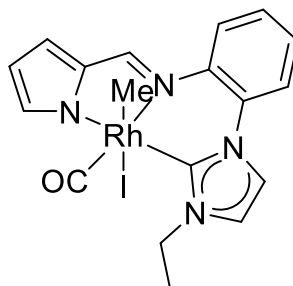
High resolution MS (TOF MS ES+ m/z) 395.0379 [M^+][I^-]

IR $\nu(\text{CO})$ 2057 cm^{-1} (CH_2Cl_2)

Yield 0.067 g, 77%

Crystals suitable for X-ray crystallography were obtained by slow vapour diffusion of hexanes into concentrated CH₂Cl₂ solution.

7.11.40 Synthesis of [Rh(Et-CNN)(CO)(Me)] 6f



To a solution of **5f** (0.056g 0.14 mmol) in CH₂Cl₂ (5 ml), MeI (excess) was added and allowed to stir for 2-3 hours. The solvent was removed under vacuum to yield a yellow solid. Note over time formation of multiple Rh(III) methyl isomers are observed both in NMR and IR.

¹H NMR (400 MHz, CDCl₃) δ 8.30 (s, 1H, HC=NAr), 7.67 (d, *J* = 2.2 Hz, 1H, Ar), 7.59 – 7.55 (m, 2H, Ar), 7.48 (dd, *J* = 8.2, 1.3 Hz, 1H, imidazolium), 7.40 – 7.35 (m, 1H, Ar), 7.27 – 7.21 (m, 2H, Ar), 7.20 (d, *J* = 2.2 Hz, 1H, pyrrole), 6.46 (dd, *J* = 4.1, 1.4 Hz, 1H, pyrrole), 4.52 (dq, *J* = 14.7, 7.3 Hz, 1H, CH₂), 4.35 (dq, *J* = 14.8, 7.5 Hz, 2H, CH₂), 1.65 (t, *J* = 7.4 Hz, 3H, CH₃), 0.93 (d, *J* = 2.1 Hz, 3H, Rh-Me).

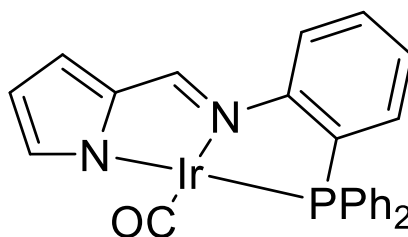
¹³C{¹H} NMR (101 MHz, CDCl₃) δ 150.99 (s), 142.81 (s), 142.23 (s), 136.55 (s), 131.31(s), 128.34 (s), 125.25 (s), 123.93 (s), 122.27 (d, *J* = 14.7 Hz), 120.17 (s), 119.62 (s), 117.30 (s), 47.58 (s), 16.24 (s), 4.74 (d, *J* = 20.4 Hz).

High resolution MS (TOF MS ES+ m/z) 409.0536 [M+][I-]

IR v(CO) 2055 cm⁻¹ (CH₂Cl₂)

Yield 0.062 g, 82 %

7.11.41 Synthesis of [Ir(Ph₂PNN)(CO)] 8a



[Ir(acac)(CO)₂] (0.09 g, 0.26 mmol) and Ph₂PNN(H) (0.092 g, 0.26 mmol) were dissolved in MeCN (10 ml). The solution was refluxed and a red precipitate was formed. After 1 hour the solution was allowed to cool and the precipitate was filtered to yield **8a** as a red solid.

¹H NMR (400 MHz, CDCl₃) δ 8.54 (s, 1H, HC=NAr), 7.80 – 7.66 (m, 4H), 7.63 (dd, *J* = 8.3, 4.2 Hz, 1H, Ar), 7.58 – 7.37 (m, 9H, Ar), 7.28 – 7.19 (m, 1H, pyrrole), 7.04 – 7.00 (m, 1H, pyrrole), 6.43 (dt, *J* = 4.0, 1.6 Hz, 1H, pyrrole).

³¹P{¹H} NMR (162 MHz, CDCl₃) δ 31.24 (s).

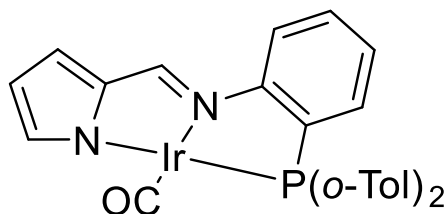
¹³C{¹H} NMR (101 MHz, CDCl₃) δ 181.53 (d, *J* = 10.0 Hz), 153.26 (s), 153.08 (s), 151.37 (d, *J* = 2.1 Hz), 145.51 (s), 144.32 (d, *J* = 1.4 Hz), 134.00 (s), 133.69 (s), 133.13 (s), 133.09 (s), 133.01 (s), 132.07 (d, *J* = 1.9 Hz), 130.98 (s), 130.54 (d, *J* = 2.5 Hz), 130.47 (s), 128.60 (d, *J* = 11.1 Hz), 126.09 (d, *J* = 7.1 Hz), 123.95 (d, *J* = 1.3 Hz), 116.61 (d, *J* = 4.5 Hz), 114.58 (d, *J* = 10.2 Hz).

High resolution MS (TOF MS ES+ *m/z*) 575.0880

IR ν(CO) 1962 cm⁻¹ (MeCN)

Yield 0.107 g, 72 %

7.11.42 Synthesis of [Ir(*o*-Tol₂PNN)(CO)] **8b**



[Ir(acac)(CO)₂] (0.073 g, 0.21 mmol) and *o*-Tol₂PNN(H) (0.08 g, 0.21 mmol) were dissolved in MeCN (5 ml). The solution was refluxed and a red precipitate was formed. After approximately 1 hour the solution was allowed to cool and the precipitate was filtered to yield **8b** as a red solid.

¹H NMR (400 MHz, CDCl₃) δ 8.54 (s, 1H, HC=NAr), 7.65 (dd, *J* = 8.3, 4.2 Hz, 1H, Ar), 7.51 (ddt, *J* = 8.4, 7.2, 1.4 Hz, 1H, Ar), 7.48 (d, *J* = 0.7 Hz, 1H, Ar), 7.37 (m, 5H, Ar), 7.20 – 7.13 (m, 3H, Ar), 7.09 (ddd, *J* = 9.2, 7.8, 1.3 Hz, 1H, pyrrole), 7.05 – 7.02 (m, 1H, pyrrole), 6.41 (dt, *J* = 4.1, 1.6 Hz, 1H, pyrrole), 2.84 (br, 3H, 2-Me), 2.49 (br, 3H, 2-Me).

³¹P{¹H} NMR (162 MHz, CDCl₃) δ 17.43 (s).

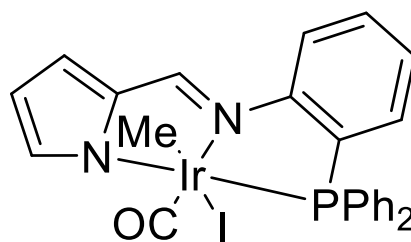
$^{13}\text{C}\{^1\text{H}\}$ NMR (101 MHz, CDCl_3) δ 182.75 (d, $J = 8.4$ Hz), 152.88 (d, $J = 16.2$ Hz), 151.27 (d, $J = 2.2$ Hz), 145.36 (s), 143.87 (d, $J = 1.7$ Hz), 134.98 (s), 132.09 (d, $J = 7.4$ Hz), 131.95 (d, $J = 1.9$ Hz), 131.32 (s), 130.81 (s), 130.52 – 130.28 (m), 126.24 (d, $J = 7.1$ Hz), 126.17 – 125.28 (m), 123.52 (s), 116.64 (d, $J = 4.7$ Hz), 114.40 (d, $J = 9.6$ Hz), 23.81 – 23.07 (m).

High resolution MS (TOF MS ES+ m/z) 603.1201

IR $\nu(\text{CO})$ 1961 cm^{-1} (CH_2Cl_2)

Yield 0.1g, 79%

7.11.43 Synthesis of $[\text{Ir}(\text{Ph}_2\text{PNN})(\text{CO})(\text{Me})\text{I}]$ **9a**



To a solution of **8a** (0.04g 0.07mmol) in CH_2Cl_2 (5 ml) MeI (excess) was added and allowed to stir overnight. Volatiles were removed under vacuum to yield **9a** as a yellow solid.

^1H NMR (400 MHz, CDCl_3) δ 8.47 (s, 1H, HC=NAr), 7.99 – 7.90 (m, 2H, Ar), 7.85 (dd, $J = 8.4$, 4.6 Hz, 1H, Ar), 7.68 – 7.56 (m, 3H, Ar), 7.54 – 7.33 (m, 8H), 7.17 (dt, $J = 4.2$, 1.1 Hz, 1H, pyrrole), 6.49 – 6.41 (m, 1H, pyrrole), 0.26 (d, $J = 4.0$ Hz, 3H, Ir-Me).

$^{31}\text{P}\{^1\text{H}\}$ NMR (162 MHz, CDCl_3) δ 11.44 (s).

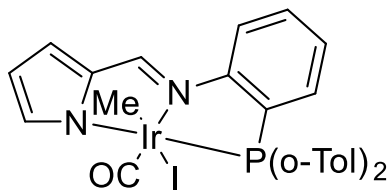
$^{13}\text{C}\{^1\text{H}\}$ NMR (101 MHz, CDCl_3) δ 169.14 (d, $J = 7.9$ Hz), 153.69 (d, $J = 15.3$ Hz), 148.10 (s), 143.07 (s), 142.56 (d, $J = 2.0$ Hz), 135.43 (s), 134.63 (d, $J = 10.0$ Hz), 133.38 (d, $J = 2.0$ Hz), 132.31 (d, $J = 9.5$ Hz), 131.49 (d, $J = 2.8$ Hz), 130.87 (d, $J = 2.7$ Hz), 130.07 (s), 129.43 (s), 128.83 (s), 128.69 (d, $J = 11.1$ Hz), 128.20 (s), 128.17 (d, $J = 11.7$ Hz), 126.00 (d, $J = 7.8$ Hz), 125.63 (s), 125.06 (s), 123.77 (d, $J = 2.0$ Hz), 117.23 (d, $J = 5.5$ Hz), 116.05 (d, $J = 10.6$ Hz), -4.77 (d, $J = 3.3$ Hz).

High resolution MS (TOF MS ES+ m/z) 717.0144

IR $\nu(\text{CO})$ 2038 cm^{-1} (CH_2Cl_2)

Yield 0.04g, 81%

A crystal of **9a** suitable for X-ray crystallography was obtained by slow evaporation of CH_2Cl_2 from a concentrated solution.

7.11.44 Synthesis of $[\text{Ir}(\text{o-Tol}_2\text{PNN})(\text{CO})(\text{Me})\text{I}]$ **9b**

To a solution of **8b** (0.037 g, 0.05 mmol) in CH_2Cl_2 (5 ml) MeI (excess) was added and allowed to stir overnight. Volatiles were removed under vacuum to yield **9b** as a yellow solid.

^1H NMR (400 MHz, CDCl_3) δ 9.14 (br, 1H, Ar), 8.46 (s, 1H, HC=NAr), 7.77 (dd, $J = 8.3, 4.6$ Hz, 1H, Ar), 7.67 (d, $J = 0.7$ Hz, 1H, Ar), 7.64 – 7.43 (m, 4H, Ar), 7.38 – 7.11 (m, 7H, Ar), 6.74 – 6.72 (br, 1H,), 6.52 – 6.39 (m, 1H, pyrrole), 2.06 (s, 3H, 2-Me), 2.00 (s, 3H, 2-Me), 0.15 (s, 3H, Ir-Me).

$^{31}\text{P}\{^1\text{H}\}$ NMR (162 MHz, CDCl_3) δ 13.41 (s).

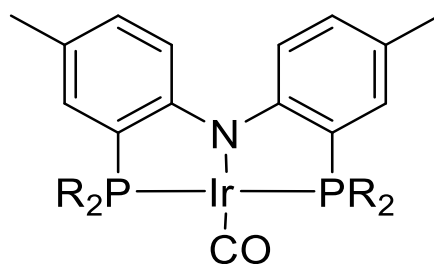
$^{13}\text{C}\{^1\text{H}\}$ NMR (101 MHz, CDCl_3) δ 169.34 (d, $J = 7.5$ Hz), 152.96 (d, $J = 14.0$ Hz), 148.09 (d, $J = 1.6$ Hz), 142.85 (s), 142.34 (s), 140.86 (d, $J = 3.0$ Hz), 140.25 (d, $J = 9.9$ Hz), 133.62 (s), 132.81 (d, $J = 2.0$ Hz), 132.68 (d, $J = 8.8$ Hz), 132.51 (s), 132.09 – 131.81 (m), 131.42 (s), 131.12 (s), 128.64 (s), 128.08 (s), 126.86 (s), 126.44 (dd, $J = 9.2, 6.7$ Hz), 123.64 (d, $J = 2.1$ Hz), 117.01 (d, $J = 5.5$ Hz), 115.81 (d, $J = 9.8$ Hz), 21.37 (d, $J = 6.7$ Hz), -3.76 (d, $J = 2.8$ Hz).

High resolution MS (TOF MS ES+ m/z) 767.0305

IR $\nu(\text{CO})$ 2038 cm^{-1} (CH_2Cl_2)

Yield 0.33 g, 72 %

A crystal of **9b** suitable for X-ray crystallography was obtained by slow evaporation of CH_2Cl_2 from a concentrated solution.

7.11.45 Synthesis of $[\text{Ir}(\text{CO})(\text{R-PNP})]$ complexes

The synthetic procedure for the synthesis of [Ir(CO)(Ph-PNP)] is described below. This procedure is representative of the general synthetic procedure for all complexes of this type [Ir(CO)(R-PNP)] **10a-e**.

7.11.46 Synthesis of [Ir(CO)(Ph-PNP)] **10a**

[Ir(acac)(CO)₂] (0.23 g, 0.64 mmol) and Ph-PNP(H) (0.37g, 0.64mmol) were dissolved in MeCN (10ml) and heated to reflux. After ca. one hour a yellow/orange precipitate was formed, the solution was cooled and filtered using a Buchner funnel yielding an air sensitive yellow/orange microcrystalline solid with no further purification being required.

¹H NMR (400 MHz, CDCl₃) δ 7.86 – 7.70 (m, 8H, Ar), 7.57 – 7.50 (m, 2H, Ar), 7.49 – 7.41 (m, 12H, Ar), 7.01 – 6.89 (m, 4H, Ar), 2.19 (s, 6H, 4-Me).

³¹P{¹H} NMR (162 MHz, CDCl₃) δ 36.42 (s).

¹³C{¹H} NMR (101 MHz, CDCl₃) δ 161.37 (t, *J* = 12.9 Hz), 134.31 (s), 133.65 (t, *J* = 6.9 Hz), 133.45 (s), 133.18 (s), 132.22 (s), 130.39 (s), 128.54 (t, *J* = 5.4 Hz), 126.87 (t, *J* = 4.0 Hz), 122.91 (t, *J* = 26.3 Hz), 116.16 (t, *J* = 5.9 Hz), 20.21 (s).

High resolution MS (TOF MS ES+ *m/z*) 786.20 [M⁺]

Elemental Analysis

Calculated for C₃₉H₃₂IrNOP₂: C, 59.68 H, 4.11 N, 1.78. Found: C, 59.4 H, 4.02 N, 1.90.

IR ν(CO) 1943 cm⁻¹ (CH₂Cl₂)

Yield: 0.4g 80%

7.11.47 Synthesis of [Ir(CO)(*o*-Tol-PNP)] **10b**

Complex **10b** was synthesised according to the general synthetic procedure using [Ir(acac)(CO)₂] (0.056 g, 0.16 mmol) and *o*-tol-PNP(H) (0.1g, 0.16 mmol). [Ir(CO)(*o*-Tol-PNP)] was obtained as a yellow powder.

H NMR (400 MHz, CDCl₃) δ 7.53 – 7.10 (br, 18H, Ar), 6.93 (dd, *J* = 8.5, 1.6 Hz, 2H, Ar), 6.51 (s, 2H, Ar), 2.62 (s, 12H, 2-Me), 2.11 (s, 6H, 4-Me).

³¹P{¹H} NMR (162 MHz, CDCl₃) δ 24.64 (s).

¹³C{¹H} NMR (101 MHz, CDCl₃) δ 160.08 (s), 142.21 (br), 134.07 (s), 133.05 (br), 131.98 (s), 131.51 (s), 130.18 (s), 126.52 (s), 125.46 (br), 123.71 (s), 115.41 (s), 23.17 (br), 20.19 (s).

High resolution MS(TOF MS ES+ m/z) 842.22 [M⁺]

Elemental Analysis

Calculated for C₄₃H₄₀IrNOP₂: C, 61.41 H, 4.79 N, 1.67. Found: C, 59.09 H, 4.65 N, 1.55.

Note: consistently low carbon values were obtained for multiple samples.

IR ν(CO) 1941 cm⁻¹ (CH₂Cl₂)

Yield: 0.12 g, 88%

7.11.48 Synthesis of [Ir(CO)(*o*-An-PNP)] 10c

Complex **10c** was synthesised according to the general synthetic procedure using [Ir(acac)(CO)₂] 0.05g, 0.145 mmol and *o*-An-PNP(H) (0.1 g, 0.145 mmol). [Ir(CO)(*o*-An-PNP)] was obtained as a yellow powder.

¹H NMR (400 MHz, CDCl₃) δ 7.74 (br, 4H, Ar), 7.56 (dt, *J* = 8.6, 2.7 Hz, 2H, Ar), 7.41 – 7.35 (m, 4H, Ar), 7.10 (dd, *J* = 9.1, 3.8 Hz, 2H, Ar), 6.96 (t, *J* = 7.5 Hz, 4H, Ar), 6.92 – 6.82 (m, 6H, Ar), 3.52 (s, 12H, 2-OMe), 2.16 (s, 6H, 4-Me).

³¹P{¹H} NMR (162 MHz, CDCl₃) δ 25.28 (s).

¹³C{¹H} NMR (101 MHz, CDCl₃) δ 161.36 (t, *J* = 13.1 Hz), 160.87 (t, *J* = 2.2 Hz), 134.82 (s), 131.37 (d, *J* = 23.0 Hz), 125.86 (t, *J* = 4.0 Hz), 123.82 – 123.13 (m), 120.44 (t, *J* = 5.5 Hz), 115.74 (t, *J* = 5.9 Hz), 111.01 (s), 55.31 (s), 20.32 (s).

High resolution MS(TOF MS AP+ : m/z) 906.20 [M⁺]

Elemental analysis

Calculated for C₄₃H₄₀IrNO₅P₂: C, 57.07 H, 4.46 N, 1.55. Found C, 56.63 H, 4.34 N, 1.55

IR ν(CO) 1945 cm⁻¹ (CH₂Cl₂)

Yield: 0.1 g, 75%

7.11.49 Synthesis of [Ir(CO)(*i*Pr-PNP)] 10d

Complex **10d** was synthesised according to the general synthetic procedure using [Ir(acac)(CO)₂] (0.083g, 0.24 mmol) and *i*Pr-PNP(H) (0.1g, 0.24 mmol). [Ir(CO)(*i*Pr-PNP)] **10d** was obtained as a yellow powder.

¹H NMR (400 MHz, CDCl₃) δ 7.43 (dt, *J* = 8.5, 2.1 Hz, 2H, Ar), 7.02 – 6.97 (m, 2H, Ar), 6.91 (dd, *J* = 8.5, 1.6 Hz, 2H, Ar), 2.66 – 2.56 (m, 4H, CH(CH₃)₂), 2.27 (s, 6H, 4-Me), 1.34 (dd, *J* = 16.8, 7.1 Hz, 12H, CH₃), 1.19 (dd, *J* = 15.2, 7.0 Hz, 12H, CH₃).

³¹P{¹H} NMR (162 MHz, CDCl₃) δ 56.84 (s).

¹³C{¹H} NMR (101 MHz, CDCl₃) δ 186.80 (t, *J* = 8.2 Hz), 162.79 (t, *J* = 11.4 Hz), 132.44 (s), 131.48 (s), 125.57 (t, *J* = 3.6 Hz), 121.82 (t, *J* = 22.0 Hz), 115.14 (t, *J* = 5.3 Hz), 26.26 (t, *J* = 15.6 Hz), 20.27 (s), 19.24 (t, *J* = 2.4 Hz), 18.45 (s).

High resolution MS(TOF MS AP+; m/z) 650.20 [M⁺]

Elemental analysis

Calculated for C₂₇H₄₀IrNOP₂: C, 50.0 H, 6.21 N, 2.16 Found C, 50.68 H, 6.42 N, 2.20

IR ν(CO) 1924 cm⁻¹ (CH₂Cl₂)

Yield: 0.12 g, 77%

7.11.50 Synthesis of [Ir(CO)(Cy-PNP)] 10e

Complex **10e** was synthesised according to the general synthetic procedure using [Ir(acac)(CO)₂] 0.059g, 0.17 mmol and Cy-PNP(H) (0.1g, 0.17 mmol). [Ir(CO)(ⁱPr-PNP)] **10e** was obtained as a yellow powder.

¹H NMR (400 MHz, CDCl₃) δ 7.41 (dt, *J* = 8.5, 2.0 Hz, 2H, Ar), 7.02 – 6.96 (m, 2H, Ar), 6.90 (dd, *J* = 8.5, 1.5 Hz, 2H, Ar), 2.29 (s, 6H, 4-Me), 2.42 – 1.14 (m, 44H, Cy).

³¹P{¹H} NMR (162 MHz, CDCl₃) δ 47.67 (s).

¹³C{¹H} NMR (101 MHz, CDCl₃) δ 187.31 – 187.16 (m), 162.80 (t, *J* = 11.5 Hz), 132.52 (s), 131.32 (s), 125.36 (t, *J* = 3.5 Hz), 121.91 (t, *J* = 22.0 Hz), 115.04 (t, *J* = 5.3 Hz), 35.63 (t, *J* = 15.6 Hz), 29.12 (s), 28.18 (s), 26.88 (t, *J* = 6.2 Hz), 26.17 (s), 20.33 (s).

High resolution MS(TOF MS ES+; m/z) 810.35 [M⁺]

Elemental Analysis

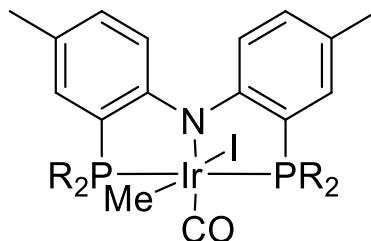
Calculated for C₃₉H₅₆IrNOP₂: C, 57.90 H, 6.98 N, 1.73 Found C, 58.21 H, 6.89 N, 1.75

IR ν(CO) 1923 cm⁻¹ (CH₂Cl₂)

Yield: 0.096 g, 70%

7.11.51 Synthesis of Ir(III) Methyl complexes **11 a-e**

The synthetic procedure for the synthesis of [Ir(CO)(Ph-PNP)(I)Me] **11a** is described below. This procedure is representative of the general synthetic procedure for all complexes of this type [Ir(CO)(R-PNP)(I)Me] **11a-e**



7.11.52 Synthesis of [Ir(CO)(Ph-PNP)I(Me)] complex **11a**

To a solution of **10a** (0.04g 0.05mmol) in CH₂Cl₂ (5 ml) MeI (excess) was added and allowed to stir overnight. Volatiles were removed under vacuum to yield **11a** as a yellow solid.

¹H NMR (400 MHz, CDCl₃) δ 7.99 (dd, *J* = 12.0, 6.0 Hz, 4H, Ar), 7.74 (dt, *J* = 8.6, 2.8 Hz, 2H, Ar), 7.57 – 7.35 (m, 16H, Ar), 7.20 (t, *J* = 4.6 Hz, 2H, Ar), 7.00 (d, *J* = 8.6 Hz, 2H, Ar), 2.27 (s, 6H, 4-Me), 0.09 (t, *J* = 5.6 Hz, 3H, Ir-CH₃).

³¹P{¹H} NMR (162 MHz, CDCl₃) δ 17.52 (s).

¹³C{¹H} NMR (101 MHz, CDCl₃) δ 171.17 (t, *J* = 6.7 Hz), 160.16 (t, *J* = 10.8 Hz), 135.52 (t, *J* = 5.6 Hz), 133.94 (s), 133.23 (t, *J* = 5.2 Hz), 132.67 (s), 131.53 (t, *J* = 31.9 Hz), 130.87 (s), 130.21 (s), 129.81 (t, *J* = 28.8 Hz), 128.30 (t, *J* = 5.2 Hz), 127.98 (t, *J* = 5.7 Hz), 126.86 (t, *J* = 4.4 Hz), 119.07 (t, *J* = 29.5 Hz), 118.57 (t, *J* = 6.0 Hz), 20.39 (s), -5.89 (t, *J* = 3.2 Hz).

High resolution MS(TOF MS ES+: *m/z*) 800.18 [M+][I-]

Elemental Analysis

Calculated for C₄₀H₃₅IIrNOP₂: C, 51.84 H, 3.81 N, 1.51 Found C, 51.30 H, 3.75 N, 1.46

IR ν(CO) 2017 cm⁻¹ (CH₂Cl₂)

Yield: 0.035g, 75%

7.11.53 Synthesis of [Ir(CO)(*o*-Tol-PNP)I(Me)] 11b

Complex **11b** was synthesised according to the general synthetic procedure from **10b** (0.05g, 0.06 mmol) and MeI (excess), yielding **11b** as a yellow solid.

¹H NMR (400 MHz, CDCl₃) δ 9.06 (br, 2H, Ar), 7.94 (br, 2H, Ar), 7.59 – 6.84 (m, 22H), 2.16 (s, 6H, 4-Me), 2.03 (br, 3H, 2-Me), 1.96 (br, 3H, 2-Me), 1.88 (br, 3H, 2-Me), 0.51 (t, *J* = 4.7 Hz, 3H, Ir-CH₃).

¹³C{¹H} NMR (101 MHz, CDCl₃) δ 172.44 (t, *J* = 5.1 Hz), 158.99 (br), 157.79 – 157.29 (m), 142.79 (br), 140.72 – 140.43 (m), 139.64 (br), 133.10 (br), 132.02 (m), 131.08 – 130.07 (m), 127.15 – 125.42 (m), 123.22 – 121.99 (m), 117.82 (br), 116.86 (br), 23.77 (d, *J* = 23.6 Hz), 22.93 (br), 21.57 (br), 20.49 (br), -8.80 (br).

³¹P{¹H} NMR (162 MHz, CDCl₃) δ 21.7, 19.8 (*J*_{p-p} 360 Hz), AB splitting pattern.

High resolution MS(TOF MS ES+: m/z) 856 [M⁺][I⁻]

Elemental analysis: despite numerous attempts values for elemental analysis were consistently inaccurate.

IR ν(CO) 2012 cm⁻¹ (CH₂Cl₂)

Yield: 0.04g, 69%

7.11.54 Synthesis of [Ir(CO)(*o*-An-PNP)I(Me)] 11c

Complex **11c** was synthesised according to the general synthetic procedure from **10c** (0.06 g, 0.068 mmol) and MeI (excess), yielding **11c** as a yellow solid.

¹H NMR (400 MHz, CDCl₃) δ 8.06 (br, 2H, Ar), 7.60 (td, *J* = 5.9, 1.5 Hz, 2H, Ar), 7.53 (dt, *J* = 8.5, 2.8 Hz, 4H, Ar), 7.37 (td, *J* = 9.5, 1.3 Hz, 4H, Ar), 7.06 (dt, *J* = 23.3, 7.2 Hz, 4H, Ar), 6.90 – 6.78 (m, 6H, Ar), 3.47 (s, 6H, 2-OMe), 3.42 (s, 6H, 2-OMe), 2.19 (s, 6H, 4-Me), 0.46 (t, *J* = 5.6 Hz, 3H, Ir-CH₃).

³¹P{¹H} NMR (162 MHz, CDCl₃) δ 15.63 (s).

¹³C{¹H} NMR (101 MHz, CDCl₃) δ 172.88 (t, *J* = 6.9 Hz), 159.86 (s), 159.23 (t, *J* = 10.9 Hz), 136.06 – 135.91 (m), 134.93 (s), 131.96 (s), 131.76 (d, *J* = 7.6 Hz), 125.64 (t, *J* = 4.5 Hz), 120.46 (t, *J* = 5.8 Hz), 120.18 (t, *J* = 6.3 Hz), 111.63 (d, *J* = 36.9 Hz), 55.24 (s), 55.21 (s), 20.61 (s), -9.77 (t, *J* = 3.7 Hz).

High resolution MS(TOF MS ES+: m/z) 922 [M⁺][I⁻]

Elemental Analysis

Calculated for $C_{44}H_{43}IrNO_5P_2$: C, 50.48 H, 4.14 N, 1.34 Found C, 50.30 H, 4.17 N, 1.29

IR $\nu(\text{CO})$ 2016 cm^{-1} (CH_2Cl_2)

Yield: 0.054 g, 76%

7.11.55 Synthesis of $[\text{Ir}(\text{CO})(^i\text{Pr-PNP})\text{I}(\text{Me})]$ **11d**

Complex **11d** was synthesised according to the general synthetic procedure from **10d** (0.071 g, 0.1 mmol) and MeI (excess), yielding **11d** as a yellow solid.

^1H NMR (400 MHz, CDCl_3) δ 7.43 (dt, $J = 8.6, 2.3$ Hz, 2H, Ar), 7.11 – 7.05 (m, $J = 1.5$ Hz, 2H, Ar), 6.86 (dd, $J = 8.6, 1.4$ Hz, 2H, Ar), 3.53 – 3.38 (m, 2H, $\text{CH}(\text{CH}_3)_2$), 2.86 (dtt, $J = 14.3, 7.1, 3.7$ Hz, 2H, $\text{CH}(\text{CH}_3)_2$), 5.74 (s, 6H, 4-Me), 1.55 – 1.42 (m, 18H, CH_3), 1.35 (q, $J = 7.3$ Hz, 6H, CH_3), 1.00 (t, $J = 4.9$ Hz, 3H, Ir- CH_3).

$^{31}\text{P}\{^1\text{H}\}$ NMR (162 MHz, CDCl_3) δ 23.52 (s).

$^{13}\text{C}\{^1\text{H}\}$ NMR (101 MHz, CDCl_3) δ 172.53 (t, $J = 6.1$ Hz), 159.03 (t, $J = 9.1$ Hz), 132.83 (s), 131.54 (s), 125.30 (t, $J = 3.9$ Hz), 123.23 (t, $J = 24.9$ Hz), 117.75 (t, $J = 5.1$ Hz), 30.01 (t, $J = 16.8$ Hz), 23.26 (t, $J = 14.3$ Hz), 21.36 (s), 20.44 (d, $J = 5.0$ Hz), 20.13 (s), 19.21 (s).

High resolution MS (TOF MS ES+: m/z) 664 $[\text{M}^+][\text{I}^-]$

Elemental analysis

Calculated for $C_{28}H_{43}IrNOP_2$: C, 42.58 H, 5.48 N, 1.77 Found C, 42.16 H, 5.51 N, 1.72

IR $\nu(\text{CO})$ 2011 cm^{-1} (CH_2Cl_2)

Yield: 0.07g, 81%

7.11.56 Synthesis of $[\text{Ir}(\text{Cy-PNP})(\text{CO})(\text{Me})(\text{I})]$ **11e**

Complex **11e** was synthesised according to the general synthetic procedure from **10e** (0.04 g, 0.049 mmol) and excess MeI, yielding **11e** as a yellow solid.

^1H NMR (400 MHz, CDCl_3) δ 7.45 (dt, $J = 8.6, 2.3$ Hz, 2H, Ar), 7.02 (br, 2H, Ar), 6.85 (dd, $J = 8.6, 1.4$ Hz, 2H, Ar), 3.20 (t, $J = 11.4$ Hz, 2H, C-H), 2.54 (t, $J = 12.2$ Hz, 2H, C-H), 2.27 (s, 6H), 2.52 – 1.16 (m, 40H, Cyclohexyl), 0.92 (t, $J = 4.8$ Hz, 3H, Ir- CH_3).

$^{31}\text{P}\{^1\text{H}\}$ NMR (162 MHz, CDCl_3) δ 16.63 (s).

$^{13}\text{C}\{^1\text{H}\}$ NMR (101 MHz, CDCl_3) δ 173.01 (t, $J = 6.1$ Hz), 159.12 (t, $J = 9.3$ Hz), 133.64 (s), 131.36 (s), 124.93 (t, $J = 3.8$ Hz), 122.03 (s), 117.98 (t, $J = 5.1$ Hz), 40.25 (t, $J = 15.3$ Hz), 33.88 (t, $J = 13.5$ Hz), 30.94 (s), 30.11 (s), 29.38 (s), 27.82 (t, $J = 5.6$ Hz), 27.30 (t, $J = 5.7$ Hz), 26.81 (t, $J = 5.6$ Hz), 26.26 (s), 26.13 (s), 20.50 (s).

High resolution MS (TOF MS ES+: m/z) 824 $[\text{M}^+][\text{I}^-]$

Elemental analysis

Calculated for $\text{C}_{40}\text{H}_{59}\text{IrNOP}_2$: C, 50.52 H, 6.25 N, 1.47 Found C, 47.57 H, 6.05 N, 1.27

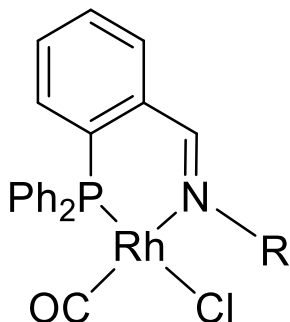
Note consistently low carbon values were obtained during elemental analysis.

IR $\nu(\text{CO})$ 2008 cm^{-1} (CH_2Cl_2)

Yield: 0.033 g, 71%

7.11.57 Synthesis of $[\text{Rh}(\text{R-PN})(\text{CO})\text{Cl}]$ complexes

The synthetic procedure for the synthesis of $[\text{Rh}(\text{^tBu-PN})(\text{CO})\text{Cl}]$ is described below. This procedure is representative of the general synthetic procedure for all complexes of this type $[\text{Ir}(\text{CO})(\text{R-PNP})]$ **14a-g**.



7.11.58 Synthesis of $[\text{Rh}(\text{^tBu-PN})(\text{CO})\text{Cl}]$ **14a**

To a stirred solution of $[\text{RhCl}(\text{CO})_2]_2$ (0.055 g, 0.14 mmol) in toluene (10 ml) the ^tBu-PN ligand (0.1 g 0.28 mmol) was added with the rapid evolution of CO and formation of an orange precipitate. The precipitate was filtered off using a Buchner funnel and allowed to air dry for 1-2 hours to yield **14a** as a fine orange powder.

^1H NMR (250 MHz, CDCl_3) δ 8.04 (t, $J = 2.1$ Hz, 1H, HC=NR), 7.27 - 7.13 (m, 13H, Ar), 6.83 (dd, $J = 9.3, 8.2$ Hz, 1H, Ar), 1.41 (s, 9H, ^tBu).

$^{31}\text{P}\{^1\text{H}\}$ NMR (101 MHz, CDCl_3) δ 52.46 (d, $J = 169.6$ Hz).

$^{13}\text{C}\{^1\text{H}\}$ NMR (101 MHz, CDCl_3) δ 189.62 (dd, $J = 73.5, 14.3$ Hz), 164.32 (d, $J = 7.6$ Hz), 138.26 (d, $J = 14.0$ Hz), 134.44 (d, $J = 8.3$ Hz), 133.68 (s), 132.39 (d, $J = 7.4$ Hz), 131.22 (d,

$J = 2.1$ Hz), 130.75 (d, $J = 1.8$ Hz), 130.56 (s), 130.46 (d, $J = 2.8$ Hz), 130.04 (s), 129.02 (s), 128.69 (d, $J = 10.9$ Hz), 128.21 (s), 125.28 (s), 65.30 (s), 31.45 (s).

High resolution MS (TOF MS ES+ m/z) 476.0626 [M^+][Cl $^-$]

IR $\nu(\text{CO})$ 2005 cm^{-1} (CH_2Cl_2)

Yield 0.117g, 82 %

7.11.59 Synthesis of [Rh(*o*-An-PN)(CO)Cl] **14b**

Complex **14b** was synthesised using the standard method from $[\text{RhCl}(\text{CO})_2]_2$ (0.11 g, 0.28 mmol) and *o*-An-PN (0.22 g, 0.56 mmol) in toluene (10 ml) to yield **14b** as an orange powder.

^1H NMR (400 MHz, CDCl_3) δ 8.11 (d, $J = 2.2$ Hz, 1H, HC=NAr), 7.67 – 7.43 (m, 13H, Ar), 7.28 – 7.19 (m, 1H, Ar), 7.13 – 7.04 (m, 2H, Ar), 6.99 – 6.92 (m, 2H, Ar), 3.84 (s, 3H, 2-OMe).

$^{31}\text{P}\{^1\text{H}\}$ NMR (101 MHz, CDCl_3) δ 46.30 (d, $J = 167.5$ Hz).

^{13}C NMR (101 MHz, CDCl_3) δ 189.09 (dd, $J = 73.8, 15.6$ Hz), 167.93 (d, $J = 8.2$ Hz), 151.55 (s), 140.83 (s), 136.89 (d, $J = 15.6$ Hz), 136.29 (d, $J = 8.3$ Hz), 133.89 (d, $J = 12.7$ Hz), 133.18 (d, $J = 6.8$ Hz), 132.24 (s), 132.03 (s), 131.48 (s), 131.13 (d, $J = 2.3$ Hz), 131.08 (s), 128.67 (d, $J = 11.0$ Hz), 128.23 (s), 127.71 (d, $J = 41.1$ Hz), 124.28 (s), 120.20 (s), 112.48 (s), 56.31 (s).

High resolution MS (TOF MS ES+ m/z) 526.0443 [M^+][Cl $^-$]

IR $\nu(\text{CO})$ 2008 cm^{-1} (CH_2Cl_2)

Yield 0.257g, 82%

7.11.60 Synthesis of [Rh(2,5-(CF $_3$) $_2$ C $_6$ H $_3$ -PN)(CO)Cl] **14c**

Complex **14c** was synthesised using the standard method from $[\text{RhCl}(\text{CO})_2]_2$ (0.05 g, 0.13 mmol), and 3,5-(CF $_3$) $_2$ C $_6$ H $_3$ -PN (0.13 g, 0.26 mmol) in toluene (5 ml) to yield **14c** as an orange powder.

^1H NMR (400 MHz, CDCl_3) δ 8.07 (br, 1H, HC=NAr), 7.75 (d, $J = 7.3$ Hz, 1H, Ar), 7.71 – 7.45 (m, 14H, Ar), 7.04 (dd, $J = 9.7, 7.9$ Hz, 1H, Ar).

$^{31}\text{P}\{^1\text{H}\}$ NMR (162 MHz, CDCl_3) δ 48.12 (d, $J = 161.8$ Hz).

$^{13}\text{C}\{^1\text{H}\}$ NMR (101 MHz, CDCl_3) δ 168.02 (d, $J = 7.8$ Hz), 151.78 (s), 136.54 (d, $J = 7.8$ Hz), 134.25 (d, $J = 7.0$ Hz), 133.84 (d, $J = 12.6$ Hz), 132.05 (s), 131.73 (s), 131.37 (s), 130.39 (d, $J = 53.9$ Hz), 129.06 (d, $J = 11.1$ Hz), 128.22 (s).

High resolution MS (TOF MS ES+ m/z) 632.0085 [M^+][Cl $^-$]

IR $\nu(\text{CO})$ 2011 cm^{-1} (CH_2Cl_2)

Yield 0.125 g, 72 %

7.11.61 Synthesis of $[\text{Rh}(2,6\text{Me}_2\text{-C}_6\text{H}_3\text{-PN})(\text{CO})\text{Cl}]$ **14d**

Complex **14d** was synthesised using the standard method from $[\text{RhCl}(\text{CO})_2]_2$ (0.1 g, 0.25 mmol) and 2,6-Me $_2$ C $_6$ H $_3$ -PN (0.2 g, 0.5 mmol) in toluene (10 ml) to yield **14d** as an orange powder.

^1H NMR (400 MHz, CDCl_3) δ 8.03 (d, $J = 2.5$ Hz, 1H, HC=NAr), 7.75 – 7.40 (m, 13H, Ar), 7.10 – 7.00 (m, 4H, Ar), 2.11 (s, 6H, 2,6(Me) $_2$).

$^{31}\text{P}\{^1\text{H}\}$ NMR (162 MHz, CDCl_3) δ 43.98 (d, $J = 166.5$ Hz).

$^{13}\text{C}\{^1\text{H}\}$ NMR (101 MHz, CDCl_3) δ 168.45 (d, $J = 8.4$ Hz), 150.74 (s), 136.42 (d, $J = 8.5$ Hz), 133.77 – 133.47 (m), 133.31 (s), 132.30 (s), 131.75 (s), 131.46 (d, $J = 2.0$ Hz), 131.11 (d, $J = 2.4$ Hz), 130.04 (s), 128.78 (d, $J = 10.9$ Hz), 127.94 (s), 126.46 (s), 19.49 (s).

High resolution MS (TOF MS ES+ m/z) 524.0651 [M^+][Cl $^-$]

IR $\nu(\text{CO})$ 2009 cm^{-1} (CH_2Cl_2)

Yield 0.22 g, 79 %

7.11.62 Synthesis of $[\text{Rh}(2,6\text{Et}_2\text{-C}_6\text{H}_3\text{-PN})(\text{CO})\text{Cl}]$ **14e**

Complex **14e** was synthesised using the standard method from $[\text{RhCl}(\text{CO})_2]_2$ (0.046 g, 0.12 mmol) and 2,6-Et $_2$ C $_6$ H $_3$ -PN iminophosphine ligand (0.1 g, 0.24 mmol) in toluene (5ml) to yield **14e** as an orange powder.

^1H NMR (400 MHz, CDCl_3) δ 7.96 (d, $J = 2.3$ Hz, 1H, HC=NAr), 7.60 (t, $J = 7.5$ Hz, 1H), 7.55 – 7.30 (m, 12H, Ar), 7.12 – 7.04 (m, 1H, Ar), 7.03 – 6.92 (m, 3H, Ar), 2.57 (dq, $J = 15.1, 7.5$ Hz, 2H), 2.38 (dq, $J = 15.1, 7.5$ Hz, 2H, CH $_2$), 0.85 (t, $J = 7.5$ Hz, 6H, CH $_3$).

$^{31}\text{P}\{^1\text{H}\}$ NMR (162 MHz, CDCl_3) δ 43.37 (d, $J = 166.6$ Hz).

$^{13}\text{C}\{^1\text{H}\}$ NMR (101 MHz, CDCl_3) δ 168.42 (d, $J = 8.6$ Hz), 149.52 (s), 136.64 (d, $J = 8.4$ Hz), 135.61 (s), 133.66 (d, $J = 12.0$ Hz), 133.59 (d, $J = 18.0$ Hz), 132.59 (s), 132.59 (s), 132.06

(s), 131.51 (s), 131.10 (d, $J = 2.3$ Hz), 128.81 (d, $J = 10.9$ Hz), 126.80 (s), 125.49 (s), 25.33 (s), 14.15 (s).

High resolution MS (TOF MS ES+ m/z) 552.0964 [M^+][Cl $^-$]

IR $\nu(\text{CO})$ 2009 cm^{-1} (CH_2Cl_2)

Yield 0.12 g, 85 %

7.11.63 Synthesis of $[\text{Rh}(\text{2,6Et}_2\text{-C}_6\text{H}_3\text{-PN})(\text{CO})\text{Cl}]$ **14f**

Complex **14f** was synthesised using the standard method from $[\text{RhCl}(\text{CO})_2]_2$ (0.13 g, 0.34 mmol) and 2,6- i Pr $_2$ C $_6$ H $_3$ -PN (0.3g, 6.68 mmol) in toluene (10 ml) to yield **14f** as an orange powder.

^1H NMR (400 MHz, CDCl_3) δ 8.09 (d, $J = 2.5$ Hz, 1H, HC=NAr), 7.69 (tt, $J = 7.5, 1.4$ Hz, 1H, Ar), 7.63 – 7.41 (m, 12H, Ar), 7.27 – 7.02 (m, 4H, Ar), 3.06 (septet, $J = 6.7$ Hz, 4H), 1.34 (d, $J = 6.8$ Hz, 3H, CH $_3$), 0.75 (d, $J = 6.8$ Hz, 3H, CH $_3$).

$^{31}\text{P}\{^1\text{H}\}$ NMR (162 MHz, CDCl_3) δ 43.15 (d, $J = 166.2$ Hz).

$^{13}\text{C}\{^1\text{H}\}$ NMR (101 MHz, CDCl_3) δ 167.79 (d, $J = 8.7$ Hz), 148.22 (s), 140.58 (s), 136.59 (d, $J = 8.7$ Hz), 133.72 (s), 133.57 (d, $J = 6.3$ Hz), 132.80 (s), 132.28 (s), 131.50 (d, $J = 1.9$ Hz), 131.07 (d, $J = 2.3$ Hz), 128.81 (d, $J = 10.9$ Hz), 127.11 (s), 123.22 (s), 28.93 (s), 24.34 (s), 23.12 (s).

High resolution MS (TOF MS ES+ m/z) 580.1277 [M^+][Cl $^-$]

IR (CH_2Cl_2) 2009 cm^{-1} (CH_2Cl_2)

Yield 0.294 g, 75 %

7.11.64 Synthesis of $[\text{Rh}(\text{2,4,6,Me}_3\text{-C}_6\text{H}_2\text{-PN})(\text{CO})\text{Cl}]$ **14g**

Complex **14g** was synthesised using the standard method from $[\text{RhCl}(\text{CO})_2]_2$ (0.1 g, 0.27 mmol) and 2,4,6-Me $_3$ C $_6$ H $_2$ -PN (0.22 g, 0.54 mmol) in toluene (10 ml) to yield **14g** as an orange powder.

^1H NMR (400 MHz, CDCl_3) δ 7.90 (d, $J = 2.4$ Hz, 1H, HC=NAr), 7.63 – 7.53 (m, 1H, Ar), 7.52 – 7.31 (m, 12H, Ar), 6.97 – 6.89 (m, 1H, Ar), 6.74 (s, 2H, Ar), 2.17 (s, 3H, 4-CH $_3$), 1.96 (s, 6H, 2,6-CH $_3$).

$^{31}\text{P}\{^1\text{H}\}$ NMR (162 MHz, CDCl_3) δ 44.08 (d, $J = 166.9$ Hz).

$^{13}\text{C}\{^1\text{H}\}$ NMR (101 MHz, CDCl_3) δ 188.68 (dd, $J = 72.6, 16.2$ Hz), 168.46 (d, $J = 8.5$ Hz), 148.55 (s), 136.82 (dd, $J = 16.1, 1.8$ Hz), 136.33 (d, $J = 8.4$ Hz), 135.77 (s), 133.62 (s), 133.61 (d, $J = 12.7$ Hz), 133.25 (s), 132.30 (d, $J = 1.1$ Hz), 131.77 (d, $J = 1.1$ Hz), 131.45 (d, $J = 2.1$ Hz), 131.09 (d, $J = 2.3$ Hz), 129.76 (s), 129.05 (s), 128.78 (d, $J = 10.2$ Hz), 128.67 (d, $J = 9.4$ Hz), 128.24 (s), 125.31 (s), 20.89 (s), 19.40 (s).

High resolution MS (TOF MS ES+ m/z) 538.0807 [M^+][Cl^-]

IR $\nu(\text{CO})$ 2008 cm^{-1} (CH_2Cl_2)

Yield 0.28g, 90 %

7.12 General method for catalytic decarbonylation reactions.

A typical experiment is described below. Quantities of reagents and reaction conditions were adjusted for each experiment as required.

A 10 ml snap cap tube was charged with carboxylic acid (0.5 mmol), additives (acetic anhydride (1.0 mmol) and KI (0.25 mmol) magnetic stirrer and catalyst (0.025 mmol) and placed under a protective atmosphere of nitrogen or argon by purging with a syringe. The vessel was then sealed using the snap cap and placed in an oil bath (pre-heated to 160°C) or a microwave reactor (Discovery Explorer microwave synthesiser). For microwave heating the power rating was set to 200 watts with medium stirring and the temperature was ramped to 160°C and maintained for the duration of the reaction. After the required time, the reaction vessel was allowed to cool to room temperature and the snap cap removed. A sample of the crude reaction mixture was taken for spectroscopic analysis. Isolation of alkene products was achieved using column chromatography on silica, eluting with hexanes. After removal of hexanes under vacuum, the isolated product was weighed to obtain the yield. The product was analysed by ^1H NMR spectroscopy to assess the selectivity for terminal/internal alkenes.

7.12.1 Characterisation of alkene products

Alkene products undecenes ($\text{C}_{11}\text{H}_{22}$), tridecenes ($\text{C}_{13}\text{H}_{26}$), pentadecenes ($\text{C}_{15}\text{H}_{30}$) and heptadecenes ($\text{C}_{17}\text{H}_{34}$) were isolated as inseparable mixture of isomers and were colourless oils. Spectroscopic data for each alkene matched reported literature data.³¹⁻³⁶

7.12.2 Undecenes ($\text{C}_{11}\text{H}_{22}$) mixture of isomers isolated as a clear oil.

1-undecene

$^1\text{H NMR}$ (400 MHz, CDCl_3) δ 5.84 (ddt, $J = 16.9$ Hz, 10.1 Hz, 6.7 Hz 1H, $\text{C}_9\text{H}_{19}\text{CH}=\text{CH}_2$), δ 5.09(m, $\text{C}_9\text{H}_{19}\text{CH}=\text{CH}_2$), δ 2.07-0.9 (m, 19H, aliphatic protons).

Undecenes (internal isomers)

$^1\text{H NMR}$ (400 MHz, CDCl_3) δ 5.5-5.34 (m, 2H olefinic protons), δ 2.07-0.9 (m, 20H, aliphatic protons).

GCMS (TOF MS EI+ m/z) 154.171

7.12.3 Tridecenes ($\text{C}_{13}\text{H}_{26}$) mixture of isomers isolated as a clear oil.

1-tridecenes

$^1\text{H NMR}$ (400 MHz, CDCl_3) δ 5.84 (ddt, $J = 16.9$ Hz, 10.1 Hz, 6.7 Hz 1H, $\text{C}_{13}\text{H}_{23}\text{CH}=\text{CH}_2$), δ 5.09-4.89(m, 2H, $\text{HC}=\text{CH}_2$), δ 2.15-0.84 (m, 23H, aliphatic protons).

tridecenes internal isomers

$^1\text{H NMR}$ (400 MHz, CDCl_3) δ 5.52-5.35 (m, 2H olefinic protons), δ 2.07-0.9 (m, 24H, aliphatic protons).

GCMS (TOF MS EI+ m/z) 182.2031

7.12.4 Pentadecenes ($\text{C}_{15}\text{H}_{30}$) mixture of isomers isolated as a clear oil.

1-pentadecenes

$^1\text{H NMR}$ (400 MHz, CDCl_3) δ 5.81 (ddt, $J = 16.9$ Hz, 10.1 Hz, 6.7 Hz 1H, $\text{C}_{13}\text{H}_{27}\text{CH}=\text{CH}_2$), δ 5.10-4.84(m, 2H, $\text{C}_{13}\text{H}_{27}\text{CH}=\text{CH}_2$), δ 2.19-0.9 (m, 27H, aliphatic protons).

Pentadecenes (internal isomers)

$^1\text{H NMR}$ (400 MHz, CDCl_3) δ 5.5-5.37 (m, 2H olefinic protons), δ 2.07-0.9 (m, 28H, aliphatic protons).

GCMS (TOF MS EI+ m/z) 210.2352

7.12.5 heptadecenes ($\text{C}_{17}\text{H}_{34}$) mixture of isomers isolated as a clear oil.

1-heptadecenes

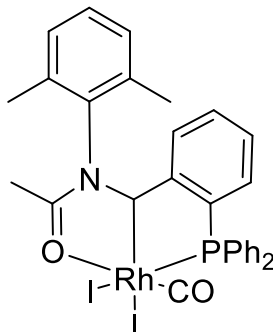
$^1\text{H NMR}$ (400 MHz, CDCl_3) δ 5.84 (ddt, $J = 16.9$ Hz, 10.1 Hz, 6.7 Hz 1H, $\text{C}_{15}\text{H}_{31}\text{CH}=\text{CH}_2$), δ 5.07-4.87(m, 2H, $\text{C}_{15}\text{H}_{31}\text{CH}=\text{CH}_2$), δ 2.13-0.91 (m, 31H, aliphatic protons).

Heptadecenes (internal isomers)

^1H NMR (400 MHz, CDCl_3) δ 5.43-5.4 (m, 2H olefinic protons), δ 2.13-0.91 (m, 32H, aliphatic protons).

GCMS (TOF MS EI+ m/z) 238.26

7.12.6 Synthesis of 15d



The synthetic procedure for the synthesis of **15d** is described below. This procedure is representative of the general synthetic procedure for complexes **15d**, **15f** and **15g**.

A 10 ml snap cap tube charged with myristic acid (0.8 g 3.5mmol), KI (0.3g, 1.75 mmol), Ac_2O (0.7ml, 7 mmol) and **14d** (0.1g 0.178 mmol) was placed under a protective atmosphere of nitrogen or argon. The vessel was then sealed using the snap cap. The sealed tube was then placed in an oil bath pre-heated to 160°C and maintained for the duration of the reaction. The reaction vessel was allowed to cool to room temperature and the reaction mixture taken up in CH_2Cl_2 (100 ml). Deionised water (50 ml) was added and the organic layer was collected. The CH_2Cl_2 was reduced to approximately 20% and hexanes were added with the formation of a brown precipitate. This precipitate was collected and air dried to yield **15d** as a brown solid.

^1H NMR (400 MHz, CDCl_3) δ 8.38 – 8.30 (m, 2H, Ar), 7.73 (t, $J = 7.9$ Hz, 1H, Ar), 7.65 – 7.25 (m, 13H, Ar), 7.20 (t, $J = 7.5$ Hz, 1H, Ar), 6.83 (d, $J = 2.6$ Hz, 1H, Rh-C-H), 6.77 (d, $J = 7.1$ Hz, 1H, Ar), 6.55 (dd, $J = 7.7, 2.6$ Hz, 1H, Ar), 2.71 (s, 3H, N-Acyl), 1.47 (s, 3H, 6-Me), 0.61 (s, 3H, 2-Me).

$^{31}\text{P}\{^1\text{H}\}$ NMR (101 MHz, CDCl_3) δ 53.38 (d, $J = 110.3$ Hz).

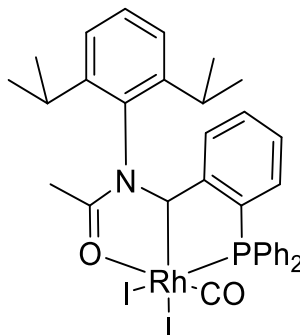
$^{13}\text{C}\{^1\text{H}\}$ NMR (101 MHz, CDCl_3) δ 183.98 (dd, $J = 62.5, 8.5$ Hz), 180.73 (s), 154.09 (d, $J = 31.5$ Hz), 136.61 (s), 136.24 (s), 136.18 (s), 134.99 (d, $J = 9.1$ Hz), 133.43 (s), 132.65 (d, $J = 9.9$ Hz), 132.36 (d, $J = 5.6$ Hz), 132.00 (d, $J = 3.3$ Hz), 131.90 (d, $J = 2.4$ Hz), 130.72 (s), 130.30 (d, $J = 15.0$ Hz), 130.11 (s), 129.48 (s), 128.94 (d, $J = 7.0$ Hz), 128.79 (s), 128.65 (d, $J = 5.9$ Hz), 128.45 (d, $J = 10.5$ Hz), 123.49 (s), 123.01 (s), 79.42 (d, $J = 23.3$ Hz), 20.64 (s), 19.98 (s), 17.03 (s).

High resolution MS (TOF MS ES+ m/z) 843.8822 [M][Na+]

IR 2072, 1560 cm^{-1} (CH_2Cl_2)

Yield 0.12 g, 82 %

7.12.7 Synthesis of **15f**



Complex **15f** was synthesised using the standard method with palmitic acid (1.38 g 4.8 mmol), KI (0.4 g, 2.4 mmol), Ac_2O (1.0 ml, 9.6 mmol) and **14f** (0.15g 2.4 mmol) to yield **15f** as a brown solid.

^1H NMR (400 MHz, CDCl_3) δ 8.39 – 8.27 (m, 2H, Ar), 7.78 – 7.19 (m, 13H, Ar), 6.91 – 6.85 (m, 1H, Ar), 6.79 (d, $J = 2.9$ Hz, 1H, Rh-C-H), 6.57 (dd, $J = 7.5, 2.6$ Hz, 1H, Ar), 4.12 (septet, $J = 6.7$ Hz, 1H, $\text{HC}(\text{CH}_3)_2$), 1.63 (s, 3H, N-Acyl), 1.51 (d, $J = 6.8$ Hz, 3H, CH_3), 1.23 – 1.17 (m, 1H, $\text{CH}(\text{CH}_3)_2$), 1.16 (d, $J = 6.7$ Hz, 3H, CH_3), 0.35 (d, $J = 6.7$ Hz, 3H, CH_3), -0.06 (d, $J = 6.7$ Hz, 3H, CH_3).

$^{31}\text{P}\{^1\text{H}\}$ NMR (162 MHz, CDCl_3) δ 53.03 (d, $J = 110.1$ Hz).

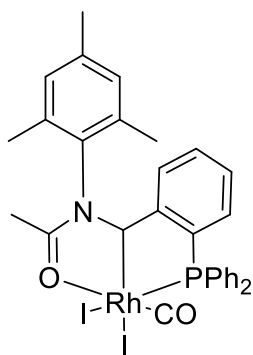
$^{13}\text{C}\{^1\text{H}\}$ NMR (126 MHz, CDCl_3) δ 184.37 – 183.63 (m), 181.72 (s, $J = 37.6$ Hz), 154.08 (d, $J = 27.9$ Hz), 146.99 (s), 145.33 (s), 134.48 (d, $J = 9.2$ Hz), 133.60 (s), 133.52 (s), 132.72 (d, $J = 9.7$ Hz), 132.34 (d, $J = 2.3$ Hz), 132.04 (d, $J = 2.0$ Hz), 131.97 (d, $J = 3.1$ Hz), 130.39 (s), 130.23 (s), 128.84 (d, $J = 10.7$ Hz), 128.52 (d, $J = 12.1$ Hz), 126.15 (s), 124.49 (s), 123.89 (d, $J = 47.4$ Hz), 80.71 (d, $J = 22.9$ Hz), 28.16 (s), 28.03 (s), 24.63 (s), 24.22 (s), 22.41 (s), 21.23 (s).

High resolution MS (TOF MS ES+ m/z) 899.9448 [M][Na⁺]

IR 2072, 1560 cm^{-1} (CH_2Cl_2)

Yield 0.165g, 78 %

A single crystal of **15f** suitable for X-ray crystallography was obtained by slow infusion of hexanes into a concentrated (CH_2Cl_2) solution of the complex.

7.12.8 Synthesis of **15g**

Complex **15g** was synthesised using the standard method with myristic acid (0.58 g 2.5 mmol), KI (0.21 g, 1.22 mmol), Ac₂O (0.52 ml, 5 mmol) and **14g** (0.075g 0.127 mmol) to yield **15g** as a brown solid.

¹H NMR (400 MHz, CDCl₃) δ 8.34 – 8.04 (m, 2H, Ar), 7.62 (t, *J* = 7.8 Hz, 1H, Ar), 7.52 – 7.16 (m, 10H), 6.95 (s, 1H, Ar), 6.71 (d, *J* = 2.7 Hz, 1H, Rh-C-H), 6.49 (dd, *J* = 7.6, 2.5 Hz, 1H, Ar), 6.46 (s, 1H, Ar), 2.55 (s, 3H, N-Acyl), 2.19 (s, 3H, 4-Me), 1.34 (s, 3H, 6-Me), 0.46 (s, 3H, 2-Me).

³¹P{¹H} NMR (162 MHz, CDCl₃) δ 53.54 (d, *J* = 110.1 Hz).

¹³C{¹H} NMR (101 MHz, CDCl₃) δ 184.05 (dd, *J* = 62.5, 8.4 Hz), 180.80 (s), 154.38 (s), 154.07 (s), 139.40 (s), 136.20 (s), 135.74 (s), 134.99 (d, *J* = 9.1 Hz), 133.71 (s), 133.39 (s), 132.65 (d, *J* = 9.9 Hz), 132.33 (d, *J* = 2.7 Hz), 131.97 (d, *J* = 3.4 Hz), 131.91 (d, *J* = 2.5 Hz), 130.82 (s), 130.76 (s), 130.38 (d, *J* = 15.1 Hz), 130.17 (s), 129.03 (s), 128.84 (d, *J* = 7.1 Hz), 128.70 (d, *J* = 10.8 Hz), 128.55 (d, *J* = 12.1 Hz), 123.27 (d, *J* = 47.7 Hz), 79.49 (dd, *J* = 23.0, 1.1 Hz), 20.98 (s), 20.54 (s), 19.95 (s), 16.92 (s).

High resolution MS (TOF MS ES+ *m/z*) 857.8979 [M][Na⁺]

IR 2071, 1560 cm⁻¹ (CH₂Cl₂)

Yield 0.082 g, 77 %

A single crystal of **15g** suitable for X-ray crystallography was obtained by slow infusion of hexanes into a concentrated (CH₂Cl₂) solution of the complex.

7.13 References

- (1) Pangborn, A. B.; Giardello, M. A.; Grubbs, R. H.; Rosen, R. K.; Timmers, F. J. *Organometallics*. **1996**, *15*, 1518.
- (2) Sheldrick, G. *Acta Crystallographica Section A*. **2008**, *64*, 112.
- (3) Wilkinson, J. A. M. G. *Inorg. Syn.*, **1966**, *8*.
- (4) Otto, S.; Roodt, A.; Erasmus, J. J. C.; Swarts, J. C. *Polyhedron*. **1998**, *17*, 2447.
- (5) Pearson, J. M. University of Sheffield, PhD Thesis. **1994**.
- (6) Vickers, P. W. University of Sheffield, PhD Thesis. **1997**.
- (7) Bonati, F.; Ugo, R. *J. Organomet. Chem.* **1967**, *7*, 167.
- (8) Bonati, F.; Ugo, R. *J. Organomet. Chem.* **1968**, *11*, 341.
- (9) Ghaffar, T.; Adams, H.; M. Maitlis, P.; Haynes, A.; J. Sunley, G.; J. Baker, M. *Chem. Commun.* **1998**, 1023.
- (10) Haynes, A.; Maitlis, P. M.; Morris, G. E.; Sunley, G. J.; Adams, H.; Badger, P. W.; Bowers, C. M.; Cook, D. B.; Elliott, P. I. P.; Ghaffar, T.; Green, H.; Griffin, T. R.; Payne, M.; Pearson, J. M.; Taylor, M. J.; Vickers, P. W.; Watt, R. J. *J. Am. Chem. Soc.* **2004**, *126*, 2847.
- (11) Best, J.; Wilson, J. M.; Adams, H.; Gonsalvi, L.; Peruzzini, M.; Haynes, A. *Organometallics*. **2007**, *26*, 1960.
- (12) Crochet, P.; Gimeno, J.; Borge, J.; Garcia-Granda, S. *New J. Chem.* **2003**, *27*, 414.
- (13) Crochet, P.; Gimeno, J.; García-Granda, S.; Borge, J. *Organometallics*. **2001**, *20*, 4369.
- (14) Yoshida, H.; Shirakawa, E.; Kurahashi, T.; Nakao, Y.; Hiyama, T. *Organometallics*. **2000**, *19*, 5671.
- (15) Winter, A. M.; Eichele, K.; Mack, H.-G.; Potuznik, S.; Mayer, H. A.; Kaska, W. C. *J. Organomet. Chem.* **2003**, *682*, 149.
- (16) Wanniarachchi, S.; Liddle, B. J.; Toussaint, J.; Lindeman, S. V.; Bennett, B.; Gardinier, J. R. *Dalton Trans.* **2011**, *40*, 8776.
- (17) Wanniarachchi, S.; Liddle, B. J.; Toussaint, J.; Lindeman, S. V.; Bennett, B.; Gardinier, J. R. *Dalton Trans.* **2010**, *39*, 3167.
- (18) Wanniarachchi, S.; Hewage, J. S.; Lindeman, S. V.; Gardinier, J. R. *Organometallics*. **2013**, *32*, 2885.
- (19) Wanniarachchi, S.; Liddle, B. J.; Lindeman, S. V.; Gardinier, J. R. *J. Organomet. Chem.* **2011**, *696*, 3623.
- (20) Fan, L.; Foxman, B. M.; Ozerov, O. V. *Organometallics*. **2004**, *23*, 326.
- (21) Tilley, D.; Fasulo, M. *Inorg. Chem. Acta* **2010**, *364*, 246.
- (22) Wilson, M. R.; Liu, H.; Prock, A.; Giering, W. P. *Organometallics*. **1993**, *12*, 2044.
- (23) Sanger, A. R. *J. Am. Chem. Soc. Dalton Trans.* **1977**, 120.

-
- (24) Williams, G. L.; Parks, C. M.; Smith, C. R.; Adams, H.; Haynes, A.; Meijer, A. J. H. M.; Sunley, G. J.; Gaemers, S. *Organometallics*. **2011**, *30*, 6166.
- (25) Deb, B.; Dutta, D. K. *J. Mol. Catal.* **2010**, *326*, 21.
- (26) Brink, A.; Roodt, A.; Steyl, G.; Visser, H. G. *Dalton Trans.* **2010**, *39*, 5572.
- (27) Parks, C. PhD Thesis, University of Sheffield. **2015**.
- (28) Gibson, V. C.; V.; Newton, C.; Redshaw, C.; A. Solan, G.; J. P. White, A.; J. Williams, D.; J. Maddox, P. *Chem. Commun.* **1998**, 1651.
- (29) Carabineiro, S. A.; Silva, L. C.; Gomes, P. T.; Pereira, L. C. J.; Veiros, L. F.; Pascu, S. I.; Duarte, M. T.; Namorado, S.; Henriques, R. T. *Inorg. Chem.* **2007**, *46*, 6880.
- (30) Liddle, B. J.; Silva, R. M. *J. Org. Chem.*, **2007**, *72*, 5638.
- (31) Foglia, T. B. P. *J. Am. Oil Chem. Soc.* **1976**, *53*, 737.
- (32) Le Nôtre, J.; Scott, E. L.; Franssen, M. C. R.; Sanders, J. P. M. *Tetrahedron Lett.* **2010**, *51*, 3712.
- (33) Liu, Y.; Kim, K. E.; Herbert, M. B.; Fedorov, A.; Grubbs, R. H.; Stoltz, B. M. *Adv. Synth. Catal.* **2014**, *356*, 130.
- (34) Maetani, S.; Fukuyama, T.; Suzuki, N.; Ishihara, D.; Ryu, I. *Organometallics*. **2011**, *30*, 1389.
- (35) Maetani, S.; Fukuyama, T.; Suzuki, N.; Ishihara, D.; Ryu, I. *Chem. Commun.*, **2012**, *48*, 2552.
- (36) Miller, J. A.; Nelson, J. A.; Byrne, M. P. *J. Org. Chem.*, **1993**, *58*, 20.

Chapter 8

Appendix

8.1 Appendix 1

Crystallographic Data

Crystallographic Data

Table A1 - Crystal data and structure refinement for **3g**

Table A2 - Crystal data and structure refinement for **3k**

Table A3 - Crystal data and structure refinement for **3m**

Table A4 - Crystal data and structure refinement for **4d**

Table A5 - Crystal data and structure refinement for **4k**

Table A6 - Crystal data and structure refinement for **5b**

Table A7 - Crystal data and structure refinement for **6d**

Table A8 - Crystal data and structure refinement for **6e**

Table A9 - Crystal data and structure refinement for **9a**

Table A10 - Crystal data and structure refinement for **9b**

Table A11 - Crystal data and structure refinement for **10b**

Table A12 - Crystal data and structure refinement for **11b**

Table A13 - Crystal data and structure refinement for **11c**

Table A14 - Crystal data and structure refinement for **11c'**

Table A15 - Crystal data and structure refinement for **15f**

Table A16 - Crystal data and structure refinement for **15g**

Table A1: Crystal data and structure refinement for **3g**

Identification code	iah701_0m
Empirical formula	C36 H36 Ir N2 O P
Formula weight	735.84
Temperature	100(2) K
Wavelength	0.71073 Å
Crystal system	Monoclinic
Space group	P 21/n
Unit cell dimensions	
a = 11.3432(8) Å	$\alpha = 90^\circ$.
b = 8.0933(6) Å	$\beta = 96.806(4)^\circ$.
c = 33.517(2) Å	$\gamma = 90^\circ$.
Volume	3055.3(4) Å ³
Z	4
Density (calculated)	1.600 Mg/m ³
Absorption coefficient	4.454 mm ⁻¹
F(000)	1464
Crystal size	0.160 x 0.110 x 0.050 mm ³
Theta range for data collection	1.224 to 26.950°.
Index ranges	-14<=h<=14, -10<=k<=7, -
41<=l<=42	
Reflections collected	25471
Independent reflections	6632 [R(int) = 0.1004]
Completeness to theta = 25.242°	100.0 %
Absorption correction	Semi-empirical from equivalents
Refinement method	Full-matrix least-squares on F ²
Data / restraints / parameters	6632 / 0 / 375
Goodness-of-fit on F ²	0.988
Final R indices [I>2sigma(I)]	R1 = 0.0468, wR2 = 0.0962
R indices (all data)	R1 = 0.0677, wR2 = 0.1077
Extinction coefficient	n/a
Largest diff. peak and hole	1.899 and -1.425 e.Å ⁻³

Table A2: Crystal data and structure refinement for **3k**

Identification code	iah695_0m
Empirical formula	C38 H39 Ir N3 O P
Formula weight	776.89
Temperature	100(2) K
Wavelength	0.71073 Å
Crystal system	Orthorhombic
Space group	Pbca
Unit cell dimensions	
a = 11.657(5) Å	$\alpha = 90^\circ$.
b = 17.027(6) Å	$\beta = 90^\circ$.
c = 33.764(12) Å	$\gamma = 90^\circ$.
Volume	6702(4) Å ³
Z	8
Density (calculated)	1.540 Mg/m ³
Absorption coefficient	4.066 mm ⁻¹
F(000)	3104
Crystal size	0.39 x 0.35 x 0.28 mm ³
Theta range for data collection	1.21 to 27.54°.
Index ranges	-11<=h<=15, -14<=k<=22, -
34<=l<=43	
Reflections collected	28581
Independent reflections	7684 [R(int) = 0.1286]
Completeness to theta = 27.54°	99.5 %
Absorption correction	Semi-empirical from equivalents
Refinement method	Full-matrix least-squares on F ²
Data / restraints / parameters	7684 / 0 / 398
Goodness-of-fit on F ²	0.973
Final R indices [I>2sigma(I)]	R1 = 0.0553, wR2 = 0.1071
R indices (all data)	R1 = 0.1098, wR2 = 0.1289
Largest diff. peak and hole	2.522 and -1.347 e.Å ⁻³

Table A3: Crystal data and structure refinement for **3m**.

Identification code	cocker6_0m_a
Empirical formula	C39 H42 Ir N2 O4 P
Formula weight	825.91
Temperature	97(2) K
Wavelength	0.71073 Å
Crystal system	Triclinic
Space group	P-1
Unit cell dimensions	
a = 9.2184(2) Å	$\alpha = 105.4790(11)^\circ$.
b = 12.3542(3) Å	$\beta = 105.3250(11)^\circ$.
c = 17.1596(4) Å	$\gamma = 98.1370(12)^\circ$.
Volume	1768.47(7) Å ³
Z	2
Density (calculated)	1.551 Mg/m ³
Absorption coefficient	3.863 mm ⁻¹
F(000)	828
Crystal size	0.320 x 0.180 x 0.150 mm ³
Theta range for data collection	1.757 to 27.661°.
Index ranges	-12 ≤ h ≤ 12, -16 ≤ k ≤ 16, -
	22 ≤ l ≤ 22
Reflections collected	26226
Independent reflections	8189 [R(int) = 0.0218]
Completeness to theta = 25.242°	99.8 %
Absorption correction	Semi-empirical from equivalents
Max. and min. transmission	0.76 and 0.43
Refinement method	Full-matrix least-squares on F ²
Data / restraints / parameters	8189 / 0 / 431
Goodness-of-fit on F ²	1.052
Final R indices [I > 2σ(I)]	R1 = 0.0171, wR2 = 0.0405
R indices (all data)	R1 = 0.0187, wR2 = 0.0412
Extinction coefficient	n/a
Largest diff. peak and hole	0.906 and -0.488 e.Å ⁻³

Table A4: Crystal data and structure refinement for **4d**.

Identification code	IAH696_0m
Empirical formula	C34 H33 I Ir N2 O4 P
Formula weight	883.69
Temperature	100(2) K
Wavelength	0.71073 Å
Crystal system	Monoclinic
Space group	P 21/c
Unit cell dimensions	
a = 11.555(2) Å	$\alpha = 90^\circ$.
b = 13.555(3) Å	$\beta = 91.705(13)^\circ$.
c = 19.928(4) Å	$\gamma = 90^\circ$.
Volume	3120.1(11) Å ³
Z	4
Density (calculated)	1.881 Mg/m ³
Absorption coefficient	5.361 mm ⁻¹
F(000)	1712
Crystal size	0.210 x 0.110 x 0.110 mm ³
Theta range for data collection	1.763 to 25.000°.
Index ranges	-13 ≤ h ≤ 13, -16 ≤ k ≤ 16, -
	23 ≤ l ≤ 23
Reflections collected	54321
Independent reflections	5484 [R(int) = 0.1612]
Completeness to theta = 25.000°	99.8 %
Absorption correction	Semi-empirical from equivalents
Max. and min. transmission	0.590 and 0.399
Refinement method	Full-matrix least-squares on F ²
Data / restraints / parameters	5484 / 0 / 392
Goodness-of-fit on F ²	1.041
Final R indices [I > 2σ(I)]	R1 = 0.0528, wR2 = 0.1193
R indices (all data)	R1 = 0.0887, wR2 = 0.1419
Extinction coefficient	n/a
Largest diff. peak and hole	1.908 and -2.260 e.Å ⁻³

Table A5: Crystal data and structure refinement for **4k**.

Identification code	cocker44_0m
Empirical formula	C38 H41 Cl2 I Ir N2 O P
Formula weight	962.70
Temperature	120(2) K
Wavelength	0.71073 Å
Crystal system	Orthorhombic
Space group	Pbca
Unit cell dimensions	
a = 17.0650(10) Å	$\alpha = 90^\circ$.
b = 17.5136(10) Å	$\beta = 90^\circ$.
c = 24.3159(14) Å	$\gamma = 90^\circ$.
Volume	7267.3(7) Å ³
Z	8
Density (calculated)	1.760 Mg/m ³
Absorption coefficient	4.748 mm ⁻¹
F(000)	3760
Crystal size	0.340 x 0.230 x 0.230 mm ³
Theta range for data collection	1.675 to 27.557°.
Index ranges	-22 ≤ h ≤ 21, -22 ≤ k ≤ 22, -
31 ≤ l ≤ 31	
Reflections collected	159627
Independent reflections	8382 [R(int) = 0.0369]
Completeness to theta = 25.242°	100.0 %
Absorption correction	Semi-empirical from equivalents
Max. and min. transmission	0.56 and 0.32
Refinement method	Full-matrix least-squares on F ²
Data / restraints / parameters	8382 / 0 / 420
Goodness-of-fit on F ²	0.997
Final R indices [I > 2σ(I)]	R1 = 0.0166, wR2 = 0.0455
R indices (all data)	R1 = 0.0184, wR2 = 0.0462
Extinction coefficient	n/a
Largest diff. peak and hole	0.521 and -0.998 e.Å ⁻³

Table A6: Crystal data and structure refinement for **5b**

Identification code	cocker26_0m
Empirical formula	C26 H22 N2 O P Rh
Formula weight	512.33
Temperature	100(2) K
Wavelength	1.54178 Å
Crystal system	Monoclinic
Space group	P2 ₁
Unit cell dimensions	
a = 8.8504(2) Å	$\alpha = 90^\circ$.
b = 12.0106(3) Å	$\beta = 92.5080(10)^\circ$.
c = 10.3274(3) Å	$\gamma = 90^\circ$.
Volume	1096.74(5) Å ³
Z	2
Density (calculated)	1.551 Mg/m ³
Absorption coefficient	7.145 mm ⁻¹
F(000)	520
Crystal size	0.060 x 0.030 x 0.030 mm ³
Theta range for data collection	4.285 to 66.604°.
Index ranges	-10 ≤ h ≤ 9, -14 ≤ k ≤ 14, -
12 ≤ l ≤ 12	
Reflections collected	15963
Independent reflections	3805 [R(int) = 0.0276]
Completeness to theta = 67.679°	97.8 %
Absorption correction	Semi-empirical from equivalents
Max. and min. transmission	0.87 and 0.54
Refinement method	Full-matrix least-squares on F ²
Data / restraints / parameters	3805 / 1 / 282
Goodness-of-fit on F ²	0.990
Final R indices [I > 2σ(I)]	R1 = 0.0159, wR2 = 0.0374
R indices (all data)	R1 = 0.0169, wR2 = 0.0378
Absolute structure parameter	0.026(3)
Extinction coefficient	n/a
Largest diff. peak and hole	0.512 and -0.314 e.Å ⁻³

Table A7: Crystal data and structure refinement for **6d**

Identification code	cocker1q_0m
Empirical formula	C17 H16 I N4 O Rh
Formula weight	522.15
Temperature	100(2) K
Wavelength	0.71073 Å
Crystal system	Triclinic
Space group	P-1
Unit cell dimensions	
a = 8.487(3) Å	$\alpha = 85.821(4)^\circ$.
b = 8.604(3) Å	$\beta = 77.046(4)^\circ$.
c = 12.338(4) Å	$\gamma = 81.183(3)^\circ$.
Volume	866.9(5) Å ³
Z	2
Density (calculated)	2.000 Mg/m ³
Absorption coefficient	2.777 mm ⁻¹
F(000)	504
Crystal size	0.300 x 0.200 x 0.200 mm ³
Theta range for data collection	1.695 to 27.401°.
Index ranges	-10<=h<=10, -11<=k<=10, -
15<=l<=15	
Reflections collected	6837
Independent reflections	3464 [R(int) = 0.0251]
Completeness to theta = 25.242°	99.0 %
Absorption correction	Semi-empirical from equivalents
Max. and min. transmission	0.75 and 0.55
Refinement method	Full-matrix least-squares on F ²
Data / restraints / parameters	3464 / 0 / 219
Goodness-of-fit on F ²	1.062
Final R indices [I>2sigma(I)]	R1 = 0.0248, wR2 = 0.0634
R indices (all data)	R1 = 0.0304, wR2 = 0.0670
Extinction coefficient	n/a
Largest diff. peak and hole	0.768 and -0.770 e.Å ⁻³

Table A8: Crystal data and structure refinement for **6e**

Identification code	cocker42_0m_b
Empirical formula	C18 H18 Cl2 I N4 O Rh
Formula weight	607.07
Temperature	446(2) K
Wavelength	0.71073 Å
Crystal system	Monoclinic
Space group	P 21/c
Unit cell dimensions	
a = 17.6765(10) Å	$\alpha = 90^\circ$.
b = 8.1492(5) Å	$\beta = 111.066(2)^\circ$.
c = 15.4483(8) Å	$\gamma = 90^\circ$.
Volume	2076.6(2) Å ³
Z	4
Density (calculated)	1.942 Mg/m ³
Absorption coefficient	2.582 mm ⁻¹
F(000)	1176
Crystal size	0.500 x 0.250 x 0.100 mm ³
Theta range for data collection	2.469 to 27.585°.
Index ranges	-23<=h<=22, -10<=k<=10, -
20<=l<=19	
Reflections collected	18250
Independent reflections	4801 [R(int) = 0.0334]
Completeness to theta = 25.242°	99.7 %
Absorption correction	None
Refinement method	Full-matrix least-squares on F ²
Data / restraints / parameters	4801 / 0 / 246
Goodness-of-fit on F ²	1.171
Final R indices [I>2sigma(I)]	R1 = 0.0556, wR2 = 0.1257
R indices (all data)	R1 = 0.0633, wR2 = 0.1290
Extinction coefficient	n/a
Largest diff. peak and hole	2.441 and -1.657 e.Å ⁻³

Table A9: Crystal data and structure refinement for **9a**

Identification code	frame1redo_a
Empirical formula	C25 H21 I Ir N2 O P
Formula weight	715.51
Temperature	100(2) K
Wavelength	1.54178 Å
Crystal system	Monoclinic
Space group	C2/c
Unit cell dimensions	
a = 23.1950(6) Å	$\alpha = 90^\circ$.
b = 16.9735(5) Å	$\beta = 133.2620(8)^\circ$.
c = 16.1704(4) Å	$\gamma = 90^\circ$.
Volume	4636.1(2) Å ³
Z	8
Density (calculated)	2.050 Mg/m ³
Absorption coefficient	22.414 mm ⁻¹
F(000)	2704
Crystal size	0.040 x 0.040 x 0.010 mm ³
Theta range for data collection	3.692 to 71.374°.
Index ranges	-27<=h<=28, -20<=k<=16, -19<=l<=17
Reflections collected	16290
Independent reflections	4174 [R(int) = 0.0527]
Completeness to theta = 67.700°	99.3 %
Absorption correction	Semi-empirical from equivalents
Max. and min. transmission	0.76 and 0.43
Refinement method	Full-matrix least-squares on F ²
Data / restraints / parameters	4174 / 0 / 281
Goodness-of-fit on F ²	1.041
Final R indices [I>2sigma(I)]	R1 = 0.0355, wR2 = 0.0756
R indices (all data)	R1 = 0.0466, wR2 = 0.0801
Extinction coefficient	n/a
Largest diff. peak and hole	1.460 and -1.333 e.Å ⁻³

Table A10: Crystal data and structure refinement for **9b**

Identification code	cocker20orth
Empirical formula	C27 H25 I Ir N2 O P
Formula weight	743.56
Temperature	100(2) K
Wavelength	0.71073 Å
Crystal system	Orthorhombic
Space group	P2 ₁ 2 ₁ 2 ₁
Unit cell dimensions	
a = 11.1904(3) Å	$\alpha = 90^\circ$.
b = 14.1874(3) Å	$\beta = 90^\circ$.
c = 15.7110(4) Å	$\gamma = 90^\circ$.
Volume	2494.32(11) Å ³
Z	4
Density (calculated)	1.980 Mg/m ³
Absorption coefficient	6.677 mm ⁻¹
F(000)	1416
Crystal size	0.180 x 0.100 x 0.070 mm ³
Theta range for data collection	1.934 to 27.599°.
Index ranges	-13<=h<=14, -18<=k<=18, -20<=l<=16
Reflections collected	33196
Independent reflections	5731 [R(int) = 0.0263]
Completeness to theta = 25.242°	100.0 %
Absorption correction	Semi-empirical from equivalents
Max. and min. transmission	0.56 and 0.32
Refinement method	Full-matrix least-squares on F ²
Data / restraints / parameters	5731 / 0 / 295
Goodness-of-fit on F ²	1.068
Final R indices [I>2sigma(I)]	R1 = 0.0212, wR2 = 0.0481
R indices (all data)	R1 = 0.0222, wR2 = 0.0485
Absolute structure parameter	0.018(3)
Extinction coefficient	n/a
Largest diff. peak and hole	2.862 and -0.643 e.Å ⁻³

Table A11: Crystal data and structure refinement for **10b**

Identification code	COCKER73P21N_a
Empirical formula	C43 H40 Ir N O P2
Formula weight	840.90
Temperature	100(2) K
Wavelength	1.54178 Å
Crystal system	Monoclinic
Space group	P 21/n
Unit cell dimensions	
a = 17.3658(3) Å	$\alpha = 90^\circ$.
b = 19.5087(3) Å	$\beta = 104.0470(10)^\circ$.
c = 21.7368(5) Å	$\gamma = 90^\circ$.
Volume	7143.9(2) Å ³
Z	8
Density (calculated)	1.564 Mg/m ³
Absorption coefficient	8.346 mm ⁻¹
F(000)	3360
Crystal size	0.14 x 0.08 x 0.03 mm ³
Theta range for data collection	2.933 to 66.676°.
Index ranges	-20<=h<=20, -23<=k<=23, -
25<=l<=25	
Reflections collected	115072
Independent reflections	12504 [R(int) = 0.0896]
Completeness to theta = 67.679°	96.8 %
Absorption correction	None
Refinement method	Full-matrix least-squares on F ²
Data / restraints / parameters	12504 / 0 / 877
Goodness-of-fit on F ²	1.058
Final R indices [I>2sigma(I)]	R1 = 0.0297, wR2 = 0.0592
R indices (all data)	R1 = 0.0488, wR2 = 0.0710
Extinction coefficient	n/a
Largest diff. peak and hole	1.019 and -0.780 e.Å ⁻³

Table A12: Crystal data and structure refinement for **11b**

Identification code	cocker50p-1
Empirical formula	C44 H43 I Ir N O P2
Formula weight	982.83
Temperature	100(2) K
Wavelength	0.71073 Å
Crystal system	Triclinic
Space group	P -1
Unit cell dimensions	
a = 10.8295(5) Å	a = 75.917(3)°.
b = 12.9359(6) Å	b = 82.986(3)°.
c = 15.7789(7) Å	g = 72.827(3)°.
Volume	2045.42(17) Å ³
Z	2
Density (calculated)	1.596 Mg/m ³
Absorption coefficient	4.130 mm ⁻¹
F(000)	964
Crystal size	0.200 x 0.200 x 0.100 mm ³
Theta range for data collection	1.689 to 27.682°.
Index ranges	-13<=h<=14, -16<=k<=16, -
20<=l<=20	
Reflections collected	45592
Independent reflections	9400 [R(int) = 0.0658]
Completeness to theta = 25.242°	99.8 %
Absorption correction	Semi-empirical from equivalents
Max. and min. transmission	0.7456 and 0.5380
Refinement method	Full-matrix least-squares on F ²
Data / restraints / parameters	9400 / 2 / 466
Goodness-of-fit on F ²	1.039
Final R indices [I>2sigma(I)]	R1 = 0.0370, wR2 = 0.0756
R indices (all data)	R1 = 0.0551, wR2 = 0.0827
Extinction coefficient	n/a
Largest diff. peak and hole	1.153 and -1.706 e.Å ⁻³

Table A13: Crystal data and structure refinement for **11c**.

Identification code	cocker41_0m
Empirical formula	C96 H104 Cl4 I2 Ir2 N2 O10 P4
Formula weight	2349.69
Temperature	100(2) K
Wavelength	1.54178 Å
Crystal system	Triclinic
Space group	P -1
Unit cell dimensions	
a = 14.5374(4) Å	$\alpha = 63.967(2)^\circ$.
b = 18.5466(5) Å	$\beta = 76.016(2)^\circ$.
c = 20.6022(5) Å	$\gamma = 79.715(2)^\circ$.
Volume	4826.5(2) Å ³
Z	2
Density (calculated)	1.617 Mg/m ³
Absorption coefficient	12.380 mm ⁻¹
F(000)	2324
Crystal size	0.180 x 0.140 x 0.050 mm ³
Theta range for data collection	2.428 to 66.813°.
Index ranges	-17<=h<=17, -22<=k<=21, -
24<=l<=23	
Reflections collected	42733
Independent reflections	16437 [R(int) = 0.0677]
Completeness to theta = 67.679°	93.9 %
Absorption correction	Semi-empirical from equivalents
Max. and min. transmission	0.7528 and 0.4594
Refinement method	Full-matrix least-squares on F ²
Data / restraints / parameters	16437 / 66 / 1030
Goodness-of-fit on F ²	1.028
Final R indices [I>2sigma(I)]	R1 = 0.0660, wR2 = 0.1709
R indices (all data)	R1 = 0.1002, wR2 = 0.1937
Extinction coefficient	n/a
Largest diff. peak and hole	3.610 and -3.298 e.Å ⁻³

Table A14: Crystal structure refinement for **11c'**

Identification code	cocker35_0m
Empirical formula	C44 H42 Cl2 Ir N O5 P2
Formula weight	989.83
Temperature	97(2) K
Wavelength	1.54178 Å
Crystal system	Orthorhombic
Space group	Pbca
Unit cell dimensions	
a = 13.4401(6) Å	$\alpha = 90^\circ$.
b = 19.6813(8) Å	$\beta = 90^\circ$.
c = 32.6758(14) Å	$\gamma = 90^\circ$.
Volume	8643.4(6) Å ³
Z	8
Density (calculated)	1.521 Mg/m ³
Absorption coefficient	8.174 mm ⁻¹
F(000)	3952
Crystal size	0.18 x 0.14 x 0.08 mm ³
Theta range for data collection	2.70 to 66.69°.
Index ranges	-16<=h<=16, -23<=k<=23, -
38<=l<=38	
Reflections collected	125730
Independent reflections	7645 [R(int) = 0.0429]
Completeness to theta = 66.69°	99.9 %
Absorption correction	None
Max. and min. transmission	0.5608 and 0.3208
Refinement method	Full-matrix least-squares on F ²
Data / restraints / parameters	7645 / 0 / 502
Goodness-of-fit on F ²	1.107
Final R indices [I>2sigma(I)]	R1 = 0.0266, wR2 = 0.0636
R indices (all data)	R1 = 0.0312, wR2 = 0.0658
Largest diff. peak and hole	1.293 and -0.700 e.Å ⁻³

Table A15; Crystal structure refinement for **15f**

Identification code	iah710_0m_a
Empirical formula	C34 H35 I2 N O2 P Rh
Formula weight	877.31
Temperature	100(2) K
Wavelength	0.71073 Å
Crystal system	Triclinic
Space group	P-1
Unit cell dimensions	
a = 11.1887(5) Å	$\alpha = 96.326(2)^\circ$.
b = 11.9954(5) Å	$\beta = 108.212(2)^\circ$.
c = 14.6987(6) Å	$\gamma = 112.425(2)^\circ$.
Volume	1672.06(13) Å ³
Z	2
Density (calculated)	1.743 Mg/m ³
Absorption coefficient	2.435 mm ⁻¹
F(000)	856
Crystal size	0.340 x 0.280 x 0.160 mm ³
Theta range for data collection	1.511 to 27.630°.
Index ranges	-14<=h<=14, -15<=k<=15, -19<=l<=19
Reflections collected	35954
Independent reflections	7714 [R(int) = 0.0293]
Completeness to theta = 25.242°	99.8 %
Absorption correction	Semi-empirical from equivalents
Max. and min. transmission	0.74 and 0.39
Refinement method	Full-matrix least-squares on F ²
Data / restraints / parameters	7714 / 0 / 375
Goodness-of-fit on F ²	1.027
Final R indices [I>2sigma(I)]	R1 = 0.0195, wR2 = 0.0390
R indices (all data)	R1 = 0.0239, wR2 = 0.0408
Extinction coefficient	n/a
Largest diff. peak and hole	0.562 and -0.672 e.Å ⁻³

Table A16: Crystal structure refinement for **15g**

Identification code	iah711p21c_a
Empirical formula	C31 H31 I2 N O3 P Rh
Formula weight	853.25
Temperature	100(2) K
Wavelength	0.71073 Å
Crystal system	Monoclinic
Space group	P2 ₁ /c
Unit cell dimensions	
a = 19.398(2) Å	a = 90°.
b = 9.8529(11) Å	b = 94.590(3)°.
c = 16.929(2) Å	g = 90°.
Volume	3225.2(6) Å ³
Z	4
Density (calculated)	1.757 Mg/m ³
Absorption coefficient	2.524 mm ⁻¹
F(000)	1656
Crystal size	0.320 x 0.280 x 0.180 mm ³
Theta range for data collection	1.053 to 27.496°.
Index ranges	-25<=h<=22, -12<=k<=6, -19<=l<=21
Reflections collected	17613
Independent reflections	7357 [R(int) = 0.0678]
Completeness to theta = 25.000°	99.7 %
Absorption correction	Semi-empirical from equivalents
Max. and min. transmission	0.69 and 0.32
Refinement method	Full-matrix least-squares on F ²
Data / restraints / parameters	7357 / 0 / 355
Goodness-of-fit on F ²	1.043
Final R indices [I>2sigma(I)]	R1 = 0.0735, wR2 = 0.1695
R indices (all data)	R1 = 0.1389, wR2 = 0.2024
Extinction coefficient	n/a
Largest diff. peak and hole	2.767 and -1.547 e.Å ⁻³

8.2 Appendix 2

Tabulated rate constants

Table A2.1: Values of k_{obs} for reaction of $[\text{Ir}(\text{Ph-NN})(\text{CO})_2]$ (**1a**) with MeI at 23°C in CH_2Cl_2

Table A2.2: Values of k_{obs} for reaction of $[\text{Ir}(\text{Ph-NN})(\text{CO})(\text{PPh}_3)]$ (**3a**) with MeI at 23°C in CH_2Cl_2 .

Table A2.3: Values of k_{obs} for reaction of $[\text{Ir}(\text{Ph-NN})(\text{CO})(\text{P-}o\text{-Tol}_3)]$ (**3b**) with MeI at 23°C in CH_2Cl_2 .

Table A2.4: Values of k_{obs} for reaction of $[\text{Ir}(\text{Ph-NN})(\text{CO})(\text{P-}P\text{-Tol}_3)]$ (**3c**) with MeI at 23°C in CH_2Cl_2 .

Table A2.5: Values of k_{obs} for reaction of $[\text{Ir}(\text{Ph-NN})(\text{CO})(\text{P-}o\text{-An}_3)]$ (**3d**) with MeI at 23°C in CH_2Cl_2 .

Table A2.6: Values of k_{obs} for reaction of $[\text{Ir}(\text{Ph-NN})(\text{CO})(\text{P}(\text{-}F\text{-C}_6\text{H}_4)_3)]$ (**3e**) with MeI at 23°C in CH_2Cl_2 .

Table A2.7: Values of k_{obs} for reaction of $[\text{Ir}(2\text{-}i\text{PrC}_6\text{H}_4\text{-NN})(\text{CO})(\text{PPh}_3)]$ (**3f**) with MeI at 23°C in CH_2Cl_2 .

Table A2.8: Values of k_{obs} for reaction of $[\text{Ir}(2\text{-}i\text{PrC}_6\text{H}_4\text{-NN})(\text{CO})(\text{P-}o\text{-Tol}_3)]$ (**3g**) with MeI at 23°C in CH_2Cl_2 .

Table A2.9: Values of k_{obs} for reaction of $[\text{Ir}(2\text{-}i\text{PrC}_6\text{H}_4\text{-NN})(\text{CO})(\text{P-}o\text{-AnPh}_2)]$ (**3h**) with MeI at 23°C in CH_2Cl_2 .

Table A2.10: Values of k_{obs} for reaction of $[\text{Ir}(2\text{-}i\text{PrC}_6\text{H}_4\text{-NN})(\text{CO})(\text{P-}o\text{-An}_2\text{Ph}_1)]$ (**3i**) with MeI at 23°C in CH_2Cl_2 .

Table A2.11: Values of k_{obs} for reaction of $[\text{Ir}(2\text{-}i\text{PrC}_6\text{H}_4\text{-NN})(\text{CO})(\text{P-}o\text{-An}_3)]$ (**3j**) with MeI at 23°C in CH_2Cl_2 .

Table A2.12: Values of k_{obs} for reaction of $[\text{Ir}(2,6\text{-}i\text{Pr}_2\text{C}_6\text{H}_3\text{-NN})(\text{CO})(\text{PPh}_3)]$ (**3k**) with MeI at 23°C in CH_2Cl_2 .

Table A2.13: Values of k_{obs} for reaction of $[\text{Ir}(2,6\text{-}i\text{Pr}_2\text{C}_6\text{H}_3\text{-NN})(\text{CO})(\text{P-}o\text{-An}_3)]$ (**3m**) with MeI at 23°C in CH_2Cl_2 .

Table A2.14: Values of k_{obs} for reaction of $[\text{Rh}(\text{CO})\text{Ph}_2\text{NN}]$ (**5a**) with MeI at 23°C in CH_2Cl_2 .

Table A2.15: Values of k_{obs} for reaction of $[\text{Rh}(\text{CO})\text{-}o\text{-Tol}_2\text{PNN}]$ (**5b**) with MeI at 23°C in

CH₂Cl₂.

Table A2.16: Values of k_{obs} for reaction of [Rh(CO)H-NNN] (**5c**) with MeI at 23°C in CH₂Cl₂.

Table A2.17: Values of k_{obs} for reaction of [Rh(CO)Me-NNN] (**5d**) with MeI at 23°C in CH₂Cl₂.

Table A2.18: Values of k_{obs} for reaction of [Rh(CO)Me-CNN] (**5e**) with MeI at 23°C in CH₂Cl₂.

Table A2.19: Values of k_{obs} for reaction of [Rh(CO)Et-CNN] (**5f**) with MeI at 23°C in CH₂Cl₂.

Table A2.20: Values of k_{obs} for reaction of [Ir(CO)Ph₂NN] (**8a**) with MeI at 23°C in CH₂Cl₂.

Table A2.21: Values of k_{obs} for reaction of [Ir(CO)*o*-Tol₂PNN] (**8b**) with MeI at 23°C in CH₂Cl₂.

Table A2.22: Values of k_{obs} for reaction of [Ir(CO)(Ph-PNP)] (**10a**) with MeI at 23°C in CH₂Cl₂.

Table A2.23: Values of k_{obs} for reaction of [Ir(CO)(*o*-Tol-PNP)] (**10b**) with MeI at 23°C in CH₂Cl₂.

Table A2.24: Values of k_{obs} for reaction of [Ir(CO)(*o*-An-PNP)] (**10c**) with MeI at 23°C in CH₂Cl₂.

Table A2.25: Values of k_{obs} for reaction of [Ir(CO)(*i*Pr-PNP)] (**10d**) with MeI at 23°C in CH₂Cl₂.

Table A2.26: Values of k_{obs} for reaction of [Ir(CO)(Cy-PNP)] (**10e**) with MeI at 23°C in CH₂Cl₂.

Table A2.27: Values of k_{obs} for reaction of [Rh(CO)(H-NNN)] (**12a**) with MeI at 23°C in CH₂Cl₂.

Table A2.28: Values of k_{obs} for reaction of [Rh(CO)(Me-NNN)] (**12b**) with MeI at 23°C in CH₂Cl₂.

Table A2.1: Values of k_{obs} for reaction of $[\text{Ir}(\text{Ph-NN})(\text{CO})_2]$ (**1a**) with MeI at 23°C in CH_2Cl_2 .

[MeI]/mol dm ⁻³	$k_{\text{obs}} / \text{s}^{-1}$
1.6	0.00058
2.4	0.00079
3.2	0.00092
4.8	0.00135

Table A2.2: Values of k_{obs} for reaction of $[\text{Ir}(\text{Ph-NN})(\text{CO})(\text{PPh}_3)]$ (**3a**) with MeI at 23°C in CH_2Cl_2 .

[MeI]/mol dm ⁻³	$k_{\text{obs}} / \text{s}^{-1}$
0.004	0.0017
0.008	0.00453
0.012	0.00583
0.016	0.0083

Table A2.3: Values of k_{obs} for reaction of $[\text{Ir}(\text{Ph-NN})(\text{CO})(\text{P-}o\text{-Tol}_3)]$ (**3b**) with MeI at 23°C in CH_2Cl_2 .

[MeI]/mol dm ⁻³	$k_{\text{obs}} / \text{s}^{-1}$
0.04	0.00266
0.056	0.00313
0.072	0.00366
0.088	0.00416

Table A2.4: Values of k_{obs} for reaction of $[\text{Ir}(\text{Ph-NN})(\text{CO})(\text{P-}p\text{-Tol}_3)]$ (**3c**) with MeI at 23°C in CH_2Cl_2 .

[MeI]/mol dm ⁻³	$k_{\text{obs}} / \text{s}^{-1}$
0.004	0.00477
0.008	0.00837
0.012	0.01
0.016	0.0128

Table A2.5: Values of k_{obs} for reaction of $[\text{Ir}(\text{Ph-NN})(\text{CO})(\text{P-}o\text{-An}_3)]$ (**3d**) with MeI at 23°C in CH_2Cl_2 .

[MeI]/mol dm ⁻³	$k_{\text{obs}} / \text{s}^{-1}$
0.000768	0.0434
0.001152	0.0567
0.001536	0.0681
0.00192	0.0810

Table A2.6: Values of k_{obs} for reaction of $[\text{Ir}(\text{Ph-NN})(\text{CO})(\text{P}(\text{P-F-C}_6\text{H}_4)_3)]$ (**3e**) with MeI at 23°C in CH_2Cl_2 .

[MeI]/mol dm ⁻³	$k_{\text{obs}} / \text{s}^{-1}$
0.032	0.00406
0.048	0.00655
0.064	0.0083
0.08	0.0108

Table A2.7: Values of k_{obs} for reaction of $[\text{Ir}(2\text{-}^i\text{PrC}_6\text{H}_4\text{-NN})(\text{CO})(\text{PPh}_3)]$ (**3f**) with MeI at 23°C in CH_2Cl_2 .

[MeI]/mol dm ⁻³	$k_{\text{obs}} / \text{s}^{-1}$
0.0096	0.00294
0.0128	0.00386
0.0151	0.00483
0.0192	0.00591

Table A2.8: Values of k_{obs} for reaction of $[\text{Ir}(2\text{-}^i\text{PrC}_6\text{H}_4\text{-NN})(\text{CO})(\text{P-}o\text{-Tol}_3)]$ (**3g**) with MeI at 23°C in CH_2Cl_2 .

[MeI]/mol dm ⁻³	$k_{\text{obs}} / \text{s}^{-1}$
0.032	0.00186
0.048	0.00247
0.064	0.00355
0.08	0.00449

Table A2.9: Values of k_{obs} for reaction of $[\text{Ir}(2\text{-}^i\text{PrC}_6\text{H}_4\text{-NN})(\text{CO})(\text{P}o\text{-AnPh}_2)]$ (**3h**) with MeI at 23°C in CH_2Cl_2 .

[MeI]/mol dm ⁻³	$k_{\text{obs}} / \text{s}^{-1}$
0.00128	0.0044
0.00192	0.0120
0.00256	0.0163
0.0032	0.0225

Table A2.10: Values of k_{obs} for reaction of $[\text{Ir}(2\text{-}^i\text{PrC}_6\text{H}_4\text{-NN})(\text{CO})(\text{P}o\text{-An}_2\text{Ph}_1)]$ (**3i**) with MeI at 23°C in CH_2Cl_2 .

[MeI]/mol dm ⁻³	$k_{\text{obs}} / \text{s}^{-1}$
0.000512	0.0124
0.001024	0.0256
0.001536	0.0391
0.002048	0.0513

Table A2.11: Values of k_{obs} for reaction of $[\text{Ir}(2\text{-}^i\text{PrC}_6\text{H}_4\text{-NN})(\text{CO})(\text{P}o\text{-An}_3)]$ (**3j**) with MeI at 23°C in CH_2Cl_2 .

[MeI]/mol dm ⁻³	$k_{\text{obs}} / \text{s}^{-1}$
0.000512	0.0196
0.001024	0.0336
0.001536	0.0570
0.002048	0.0838

Table A2.12: Values of k_{obs} for reaction of $[\text{Ir}(2,6\text{-}^i\text{Pr}_2\text{C}_6\text{H}_3\text{-NN})(\text{CO})(\text{PPh}_3)]$ (**3k**) with MeI at 23°C in CH_2Cl_2 .

[MeI]/mol dm ⁻³	$k_{\text{obs}} / \text{s}^{-1}$
0.0016	0.00453
0.0032	0.00846
0.0048	0.0140
0.0064	0.0194

Table A2.13: Values of k_{obs} for reaction of $[\text{Ir}(2,6\text{-}^i\text{Pr}_2\text{C}_6\text{H}_3\text{-NN})(\text{CO})(\text{P}o\text{-An}_3)]$ (**3m**) with MeI at 23°C in CH_2Cl_2 .

[MeI]/mol dm ⁻³	$k_{\text{obs}} / \text{s}^{-1}$
0.0016	0.00453
0.0032	0.00846
0.0048	0.0140
0.0064	0.0194

Table A2.14: Values of k_{obs} for reaction of $[\text{Rh}(\text{CO})\text{Ph}_2\text{NN}]$ (**5a**) with MeI at 23°C in CH_2Cl_2 .

[MeI]/mol dm ⁻³	$k_{\text{obs}} / \text{s}^{-1}$
0.008	0.00178
0.016	0.00344
0.024	0.00542
0.032	0.00706

Table A2.15: Values of k_{obs} for reaction of $[\text{Rh}(\text{CO})o\text{-Tol}_2\text{PNN}]$ (**5b**) with MeI at 23°C in CH_2Cl_2 .

[MeI]/mol dm ⁻³	$k_{\text{obs}} / \text{s}^{-1}$
0.032	0.00811
0.048	0.0119
0.064	0.0163
0.08	0.0200

Table A2.16: Values of k_{obs} for reaction of $[\text{Rh}(\text{CO})\text{H-NNN}]$ (**5c**) with MeI at 23°C in CH_2Cl_2 .

[MeI]/mol dm ⁻³	$k_{\text{obs}} / \text{s}^{-1}$
0.0016	0.00330
0.0024	0.00517
0.0032	0.00710
0.004	0.00882

Table A2.17: Values of k_{obs} for reaction of [Rh(CO)Me-NNN] (**5d**) with MeI at 23°C in CH₂Cl₂.

[MeI]/mol dm ⁻³	$k_{\text{obs}} / \text{s}^{-1}$
0.0032	0.00859
0.0064	0.0168
0.008	0.0202
0.0096	0.0254
0.0048	0.0122

Table A2.18: Values of k_{obs} for reaction of [Rh(CO)Me-CNN] (**5e**) with MeI at 23°C in CH₂Cl₂.

[MeI]/mol dm ⁻³	$k_{\text{obs}} / \text{s}^{-1}$
0.0016	0.00831
0.0024	0.0126
0.0032	0.0178
0.004	0.0217

Table A2.19: Values of k_{obs} for reaction of [Rh(CO)Et-CNN] (**5f**) with MeI at 23°C in CH₂Cl₂.

[MeI]/mol dm ⁻³	$k_{\text{obs}} / \text{s}^{-1}$
0.0032	0.0135
0.0064	0.0276
0.0096	0.0419
0.0128	0.0522

Table A2.20: Values of k_{obs} for reaction of [Ir(CO)Ph₂NN] (**8a**) with MeI at 23°C in CH₂Cl₂.

[MeI]/mol dm ⁻³	$k_{\text{obs}} / \text{s}^{-1}$
0.00064	0.00319
0.00128	0.00627
0.00192	0.00897
0.00256	0.0115
0.0032	0.0144

Table A2.21: Values of k_{obs} for reaction of [Ir(CO)-*o*-Tol₂PNN] (**8b**) with MeI at 23°C in CH₂Cl₂.

[MeI]/mol dm ⁻³	$k_{\text{obs}} / \text{s}^{-1}$
0.00096	0.00591
0.00192	0.0110
0.002888	0.0168
0.00384	0.0214

Table A2.22: Values of k_{obs} for reaction of [Ir(CO)(Ph-PNP)] (**10a**) with MeI at 23°C in CH₂Cl₂.

[MeI]/mol dm ⁻³	$k_{\text{obs}} / \text{s}^{-1}$
0.00064	0.00146
0.00128	0.00294
0.00192	0.00475
0.00256	0.00587
0.0032	0.00789

Table A2.23: Values of k_{obs} for reaction of [Ir(CO)(*o*-Tol-PNP)] (**10b**) with MeI at 23°C in CH₂Cl₂.

[MeI]/mol dm ⁻³	$k_{\text{obs}} / \text{s}^{-1}$
0.0016	0.00233
0.0032	0.00313
0.0048	0.00384
0.0064	0.00485

Table A2.24: Values of k_{obs} for reaction of [Ir(CO)(*o*-An-PNP)] (**10c**) with MeI at 23°C in CH₂Cl₂.

[MeI]/mol dm ⁻³	$k_{\text{obs}} / \text{s}^{-1}$
0.00032	0.0600
0.00064	0.184
0.00096	0.313
0.0016	0.567

Table A2.25: Values of k_{obs} for reaction of $[\text{Ir}(\text{CO})(i\text{Pr-PNP})]$ (**10d**) with MeI at 23°C in CH_2Cl_2 .

$[\text{MeI}]/\text{mol dm}^{-3}$	$k_{\text{obs}} / \text{s}^{-1}$
0.032	0.00590
0.04	0.00772
0.048	0.00943
0.056	0.0110

Table A2.26: Values of k_{obs} for reaction of $[\text{Ir}(\text{CO})(\text{Cy-PNP})]$ (**10e**) with MeI at 23°C in CH_2Cl_2 .

$[\text{MeI}]/\text{mol dm}^{-3}$	$k_{\text{obs}} / \text{s}^{-1}$
0.0032	0.00150
0.00384	0.00165
0.00512	0.00214
0.0064	0.00265

Table A2.27: Values of k_{obs} for reaction of $[\text{Rh}(\text{CO})(\text{H-NNN})]$ (**12a**) with MeI at 23°C in CH_2Cl_2 .

$[\text{MeI}]/\text{mol dm}^{-3}$	$k_{\text{obs}} / \text{s}^{-1}$
0.00128	0.00675
0.00192	0.00911
0.00256	0.0124
0.0032	0.0164

Table A2.28: Values of k_{obs} for reaction of $[\text{Rh}(\text{CO})(\text{Me-NNN})]$ (**12b**) with MeI at 23°C in CH_2Cl_2 .

$[\text{MeI}]/\text{mol dm}^{-3}$	$k_{\text{obs}} / \text{s}^{-1}$
0.00064	0.00131
0.00128	0.00201
0.00192	0.00255
0.00256	0.00292
0.0032	0.00318

8.3 Appendix 3

Additional Spectroscopic characterisation and information

Figure A3.1: ^1H NMR spectrum of $[\text{Ir}(\text{CO})(\text{Ph-PNP})(\text{Me})(\text{I})]$ at -50°C .

Figure A3.2: Variable temperature ^1H NMR spectra of $[\text{Ir}(\text{CO})(o\text{-An-PNP})(\text{Me})(\text{I})]$.

Figure A3.3: Variable temperature $^{31}\text{P}\{^1\text{H}\}$ NMR spectra of $[\text{Ir}(\text{CO})(o\text{-An-PNP})(\text{Me})(\text{I})]$ from 20°C (purple) to -50°C (red) in 10°C increments.

Figure A3.4: ^1H NMR of $\text{C}_{15}\text{H}_{30}$ alkenes obtained after catalysis along with an example selectivity calculation.

Figure A3.5: ^1H NMR of deuterated C_{15} chain length alkenes obtained after catalysis.

Figure A3.6: ^2H NMR of deuterated C_{15} chain length alkenes obtained after catalysis.

Table A3.1: Results from preliminary studies using $[\text{IrCl}(\text{CO})(\text{PPh}_3)_2]$.

Table A3.2: Results from duration studies using $[\text{IrCl}(\text{CO})(\text{PPh}_3)_2]$.

Table A3.3: Results from temperature study using $[\text{IrCl}(\text{CO})(\text{PPh}_3)_2]$.

Table A3.4: Results from additive study using $[\text{IrCl}(\text{CO})(\text{PPh}_3)_2]$.

Table A3.5: Results from study using $[\text{Rh}(\text{acac})(\text{CO})(\text{L})]$ complexes.

Table A3.6: Results from study using $[\text{IrCl}(\text{CO})(\text{L})_2]$ complexes.

Table A3.7: Results from study using $[\text{RhCl}(\text{CO})\text{P-P}]$ bidentate phosphine complexes.

Table A3.8: Results from study using $[\text{Ir}(\text{Ar-NN})(\text{CO})(\text{L})]$ complexes.

Table A3.9: Results from study using $[\text{Ir}(\text{R-PNP})(\text{CO})]$ complexes.

Table A3.10: Results from study using rhodium pincer complexes.

Table A3.11: Results from study using $[\text{Rh}(\text{NNX})(\text{CO})]$ pincer complexes.

Table A3.12: Results from study using $[\text{Rh}(\text{Cl})(\text{NN-R})(\text{CO})]$ iminophosphine complexes.

Table A3.13: Results from study using $[\text{RhI}_2(\text{CO})(\text{PCO-Ar})]$ complexes.

Jan28
Dean Cocker Sample ref. [Ir(CO)(Ph-PNP)I(Me)] in CDCl₃ at -50 deg

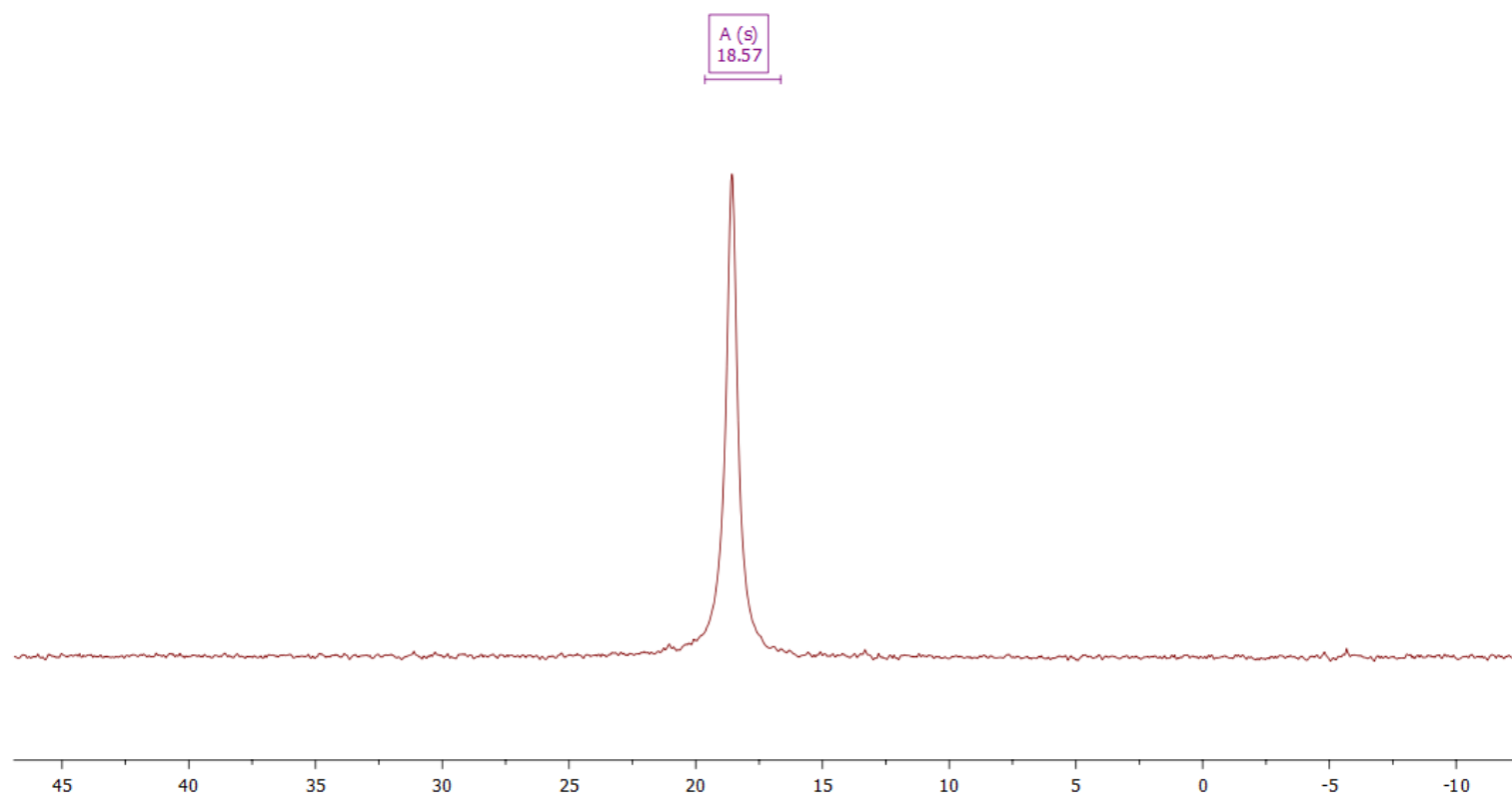


Figure A3.1: ¹H NMR spectrum of [Ir(CO)(Ph-PNP)(Me)(I)] at -50°C (CDCl₃).

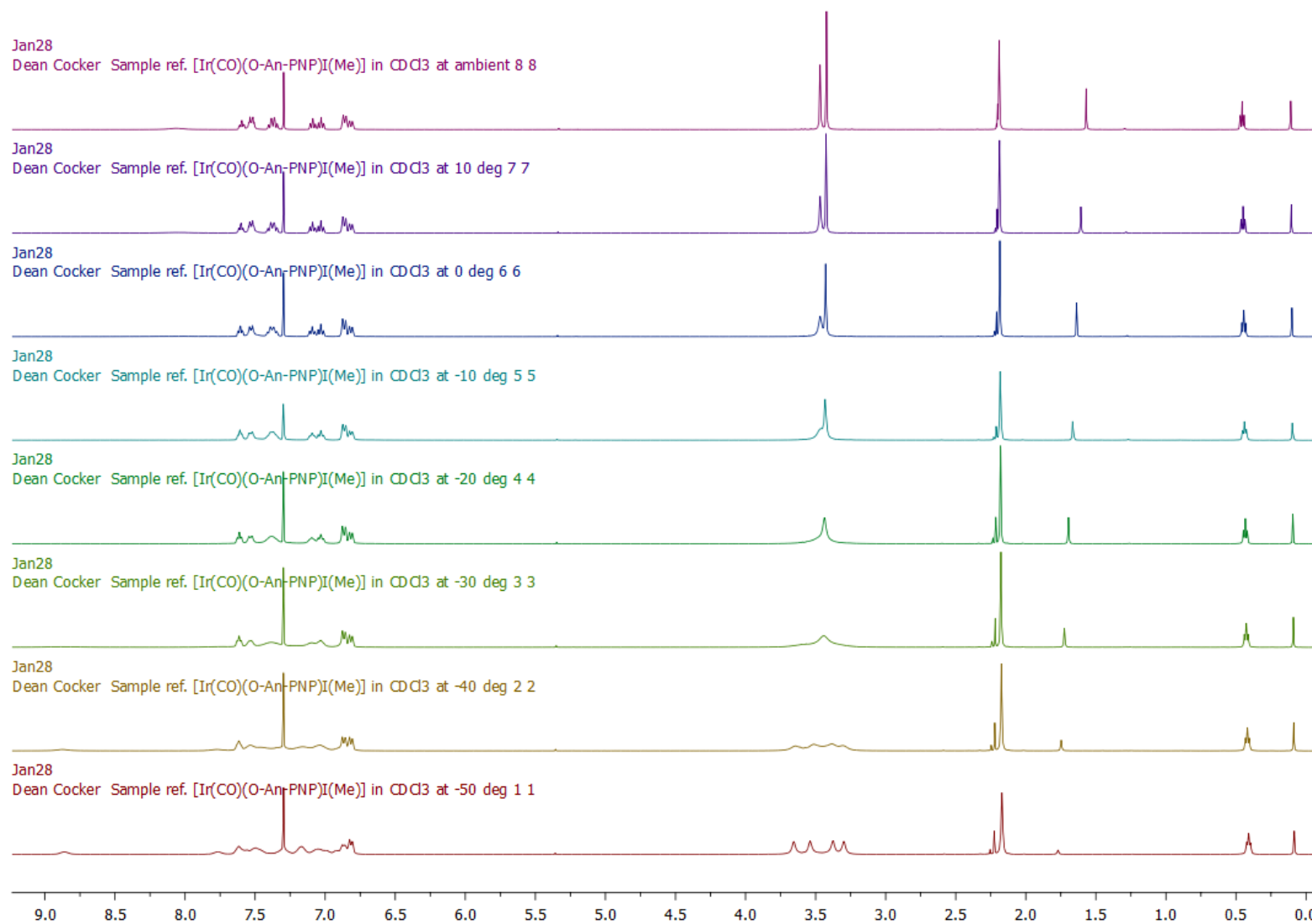


Figure A3.2: Variable temperature ¹H NMR spectra of [Ir(CO)(*o*-An-PNP)(Me)(I)](CDCl₃).

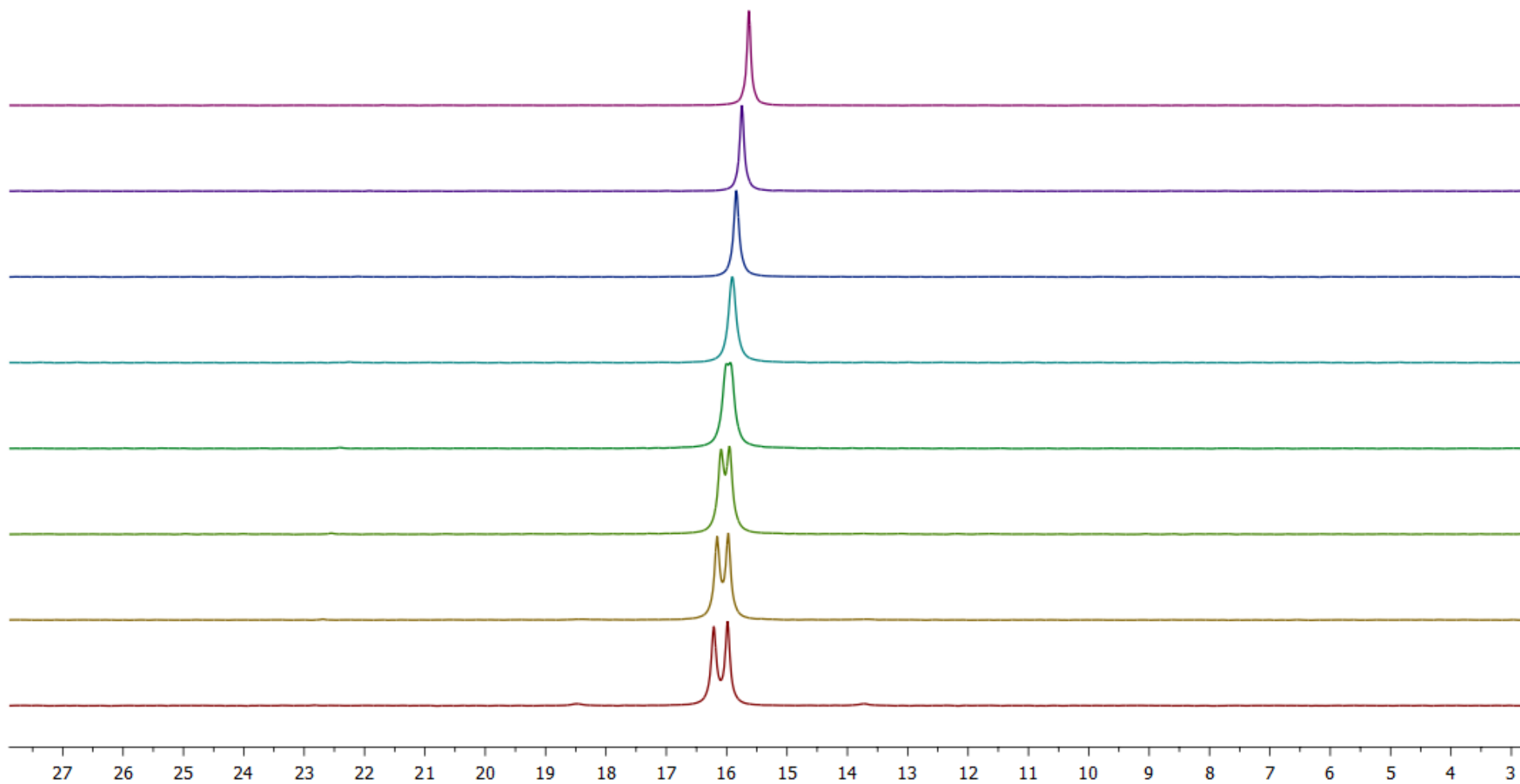


Figure A3.3: Variable temperature $^{31}\text{P}\{^1\text{H}\}$ NMR spectra of $[\text{Ir}(\text{CO})(o\text{-An-PNP})(\text{Me})(\text{I})]$ from 20°C (purple) to -50°C (red) in 10°C increments (CDCl_3).

Selectivity Calculation

Integration value of 1-alkene peak: 2.0

Integration value of internal alkene peaks 1.08

Both correspond to two olefinic hydrogens and can therefore be used to compare as a percentage.

Thus $(2.0/3.08) * 100 = 65\%$ terminal alkenes

$100\% - 65\% = 35\%$ internal alkenes

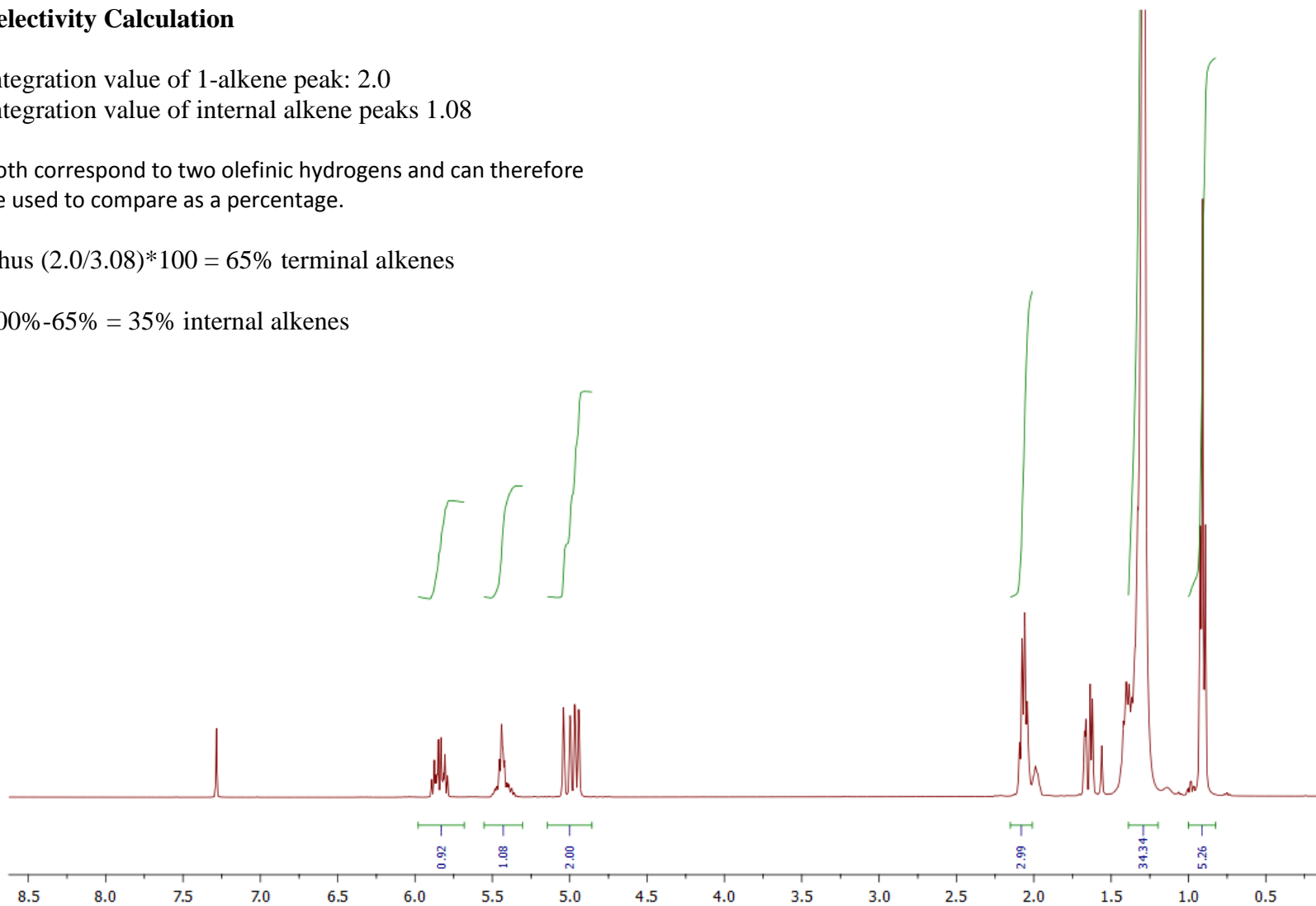


Figure A3.4: ¹H NMR of C₁₅H₃₀ alkenes obtained after catalysis along with an example selectivity calculation (CDCl₃).

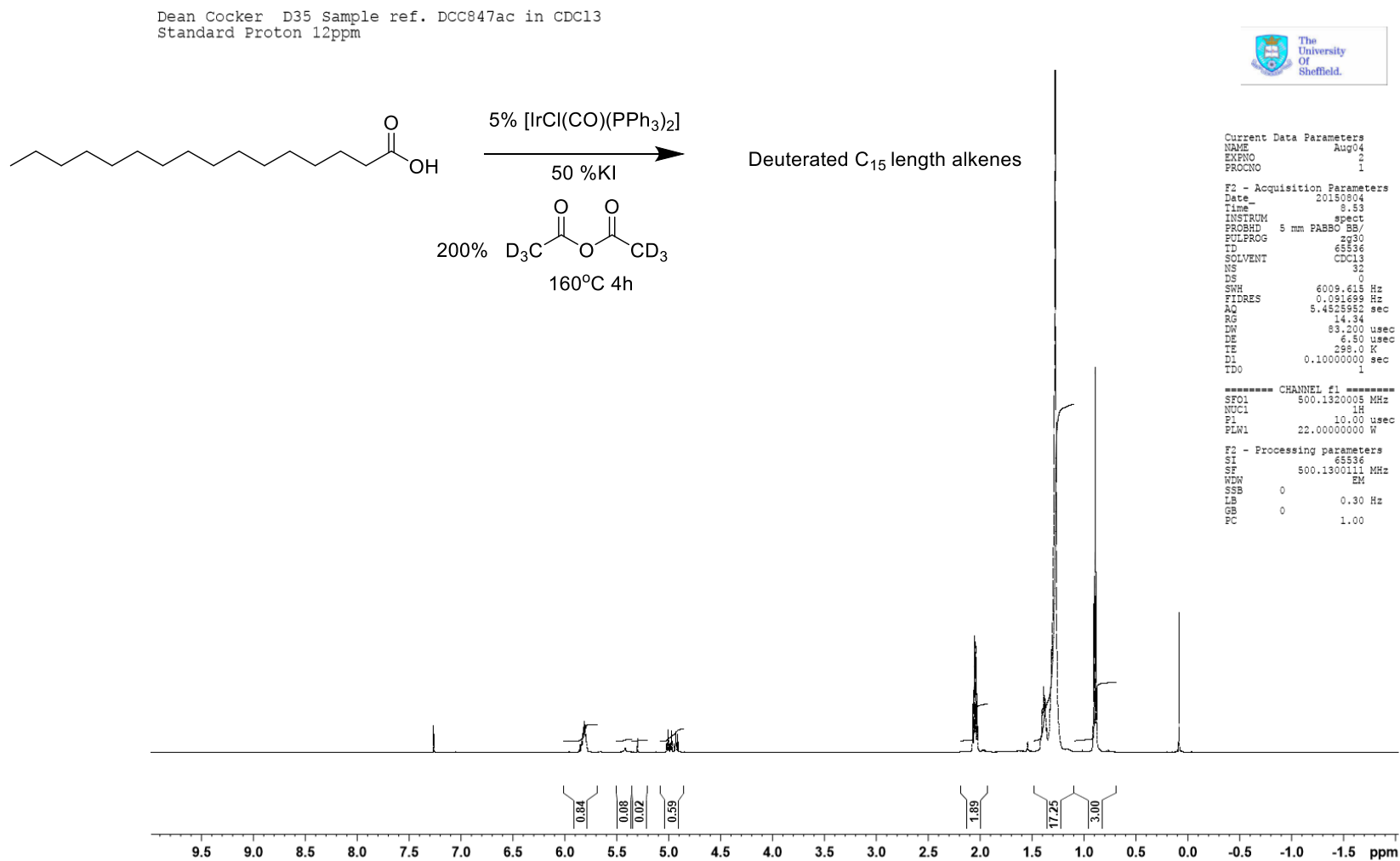


Figure A3.5: ¹H NMR of deuterated C₁₅ chain length alkenes obtained after catalysis (CDCl₃).

Dean Cocker D35 Sample ref. DCC847ac in CDCl₃
2H through lock channel

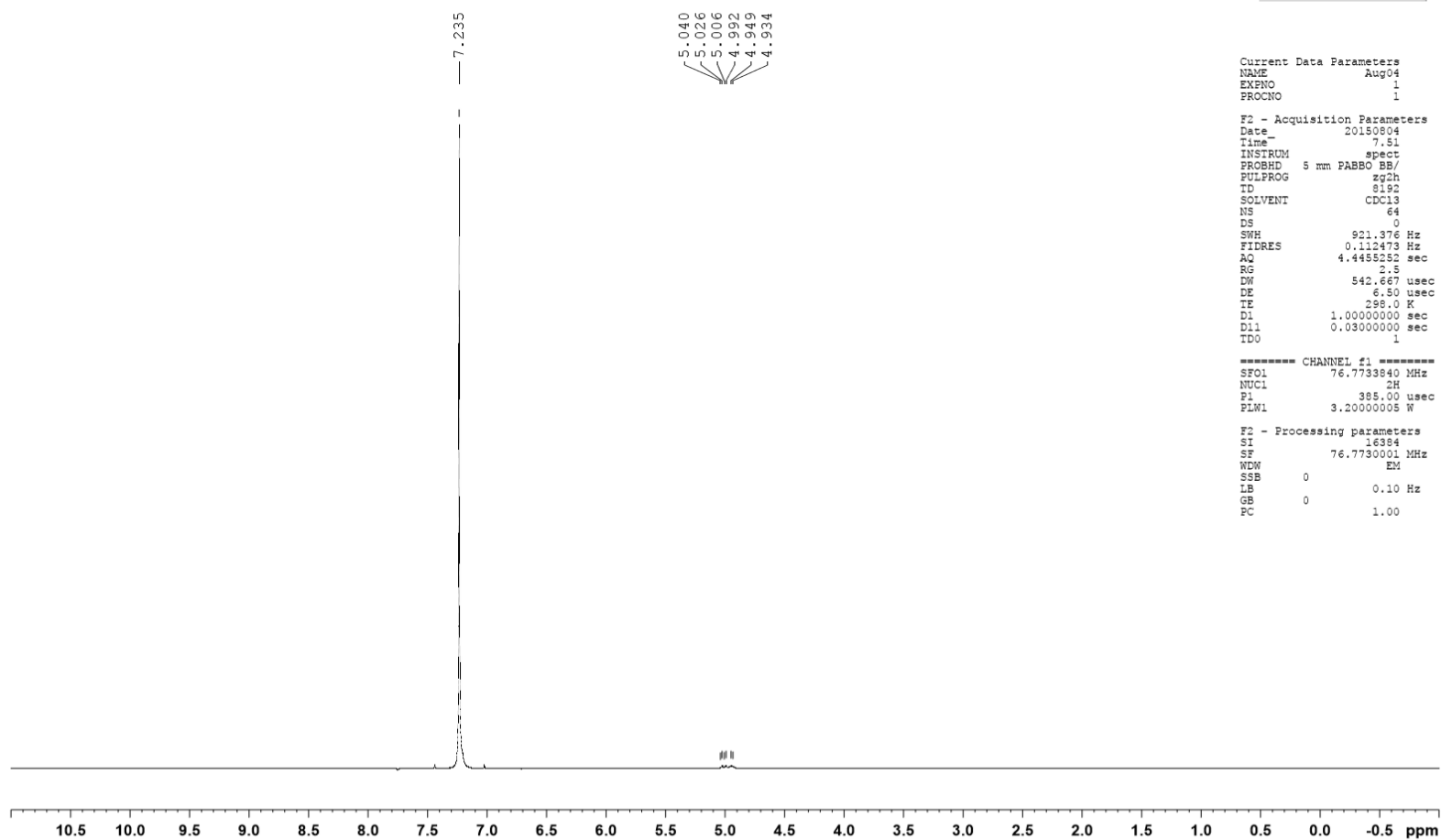


Figure A3.6: ²H NMR of deuterated C₁₅ chain length alkenes obtained after catalysis (CDCl₃)(same conditions as Figure A.3.5).

Reaction	Acid	Catalyst (%)	Additives (%)	Temperature (°C)	Time (h)	Yield (%)	Terminal (%)	Internal (%)
337	Stearic acid (C ₁₈)	5% [IrCl(CO)(PPh ₃) ₂]	KI 50% Ac ₂ O 200%	160	4	55	70	30
338	Dodecanoic acid (C ₁₂)	5% [IrCl(CO)(PPh ₃) ₂]	KI 50% Ac ₂ O 200%	160	4	43	64	36
342	Myristic acid (C ₁₄)	5% [IrCl(CO)(PPh ₃) ₂]	KI 50% Ac ₂ O 200%	160	4	95	85	15
343	Palmitic acid (C ₁₆)	5% [IrCl(CO)(PPh ₃) ₂]	KI 50% Ac ₂ O 200%	160	4	99	82	18
348	Stearic acid (C ₁₈)	5% [IrCl(CO)(PPh ₃) ₂]	KI 50% Ac ₂ O 200%	160	4	95	93	7
349	Dodecanoic acid (C ₁₂)	5% [IrCl(CO)(PPh ₃) ₂]	KI 50% Ac ₂ O 200%	160	4	53	79	21
352	Palmitic acid (C ₁₆)	5% [IrCl(CO)(PPh ₃) ₂]	KI 50% Ac ₂ O 200%	160	1	80	93	7
353	Palmitic acid (C ₁₆)	5% [IrCl(CO)(PPh ₃) ₂]	KI 50% Ac ₂ O 200%	160	2	89	89	11
354	Palmitic acid (C ₁₆)	5% [IrCl(CO)(PPh ₃) ₂]	KI 50% Ac ₂ O 200%	160	3	81	81	19

Table A3.1: Results from preliminary studies using [IrCl(CO)(PPh₃)₂].

Reaction	Acid	Catalyst (%)	Additives (%)	Temperature (°C)	Time (h)	Yield (%)	Terminal (%)	Internal (%)
356	Palmitic acid (C ₁₆)	5% [IrCl(CO)(PPh ₃) ₂]	KI 50% Ac ₂ O 200%	160	0.25	50	93	7
373	Palmitic acid (C ₁₆)	5% [IrCl(CO)(PPh ₃) ₂]	KI 50% Ac ₂ O 200%	160	0.5	90	94	6
357	Palmitic acid (C ₁₆)	5% [IrCl(CO)(PPh ₃) ₂]	KI 50% Ac ₂ O 200%	160	0.5	44	86	14
361	Palmitic acid (C ₁₆)	5% [IrCl(CO)(PPh ₃) ₂]	KI 50% Ac ₂ O 200%	160	0.5	83	93	7
358	Palmitic acid (C ₁₆)	5% [IrCl(CO)(PPh ₃) ₂]	KI 50% Ac ₂ O 200%	160	0.75	64	92	8
352	Palmitic acid (C ₁₆)	5% [IrCl(CO)(PPh ₃) ₂]	KI 50% Ac ₂ O 200%	160	1	80	93	7
353	Palmitic acid (C ₁₆)	5% [IrCl(CO)(PPh ₃) ₂]	KI 50% Ac ₂ O 200%	160	2	89	89	11
354	Palmitic acid (C ₁₆)	5% [IrCl(CO)(PPh ₃) ₂]	KI 50% Ac ₂ O 200%	160	3	81	81	19
343	Palmitic acid (C ₁₆)	5% [IrCl(CO)(PPh ₃) ₂]	KI 50% Ac ₂ O 200%	160	4	99	82	18

Table A3.2: Results from duration studies using [IrCl(CO)(PPh₃)₂].

Reaction	Acid	Catalyst (%)	Additives (%)	Temperature (°C)	Time (h)	Yield (%)	Terminal (%)	Internal (%)
343	Palmitic acid (C ₁₆)	5% [IrCl(CO)(PPh ₃) ₂]	KI 50% Ac ₂ O 200%	160	4	99	82	18
363	Palmitic acid (C ₁₆)	5% [IrCl(CO)(PPh ₃) ₂]	KI 50% Ac ₂ O 200%	140	4	80	93	7
364	Palmitic acid (C ₁₆)	5% [IrCl(CO)(PPh ₃) ₂]	KI 50% Ac ₂ O 200%	120	4	18	92	8
365	Palmitic acid (C ₁₆)	5% [IrCl(CO)(PPh ₃) ₂]	KI 50% Ac ₂ O 200%	100	4	0	0	0

Table A3.3: Results from temperature study using [IrCl(CO)(PPh₃)₂].

Reaction	Acid	Catalyst (%)	Additives (%)	Temperature (°C)	Time (h)	Yield (%)	Terminal (%)	Internal (%)
343	Palmitic acid (C ₁₆)	5% [IrCl(CO)(PPh ₃) ₂]	KI 50% Ac ₂ O 200%	160	4	99	82	18
366	Palmitic acid (C ₁₆)	5% [IrCl(CO)(PPh ₃) ₂]	KI 25% Ac ₂ O 200%	160	4	81	85	15
367	Palmitic acid (C ₁₆)	5% [IrCl(CO)(PPh ₃) ₂]	KI 5% Ac ₂ O 200%	160	4	23	80	20
368	Palmitic acid (C ₁₆)	5% [IrCl(CO)(PPh ₃) ₂]	KBr 50% Ac ₂ O 200%	160	4	14	77	23
369	Palmitic acid (C ₁₆)	5% [IrCl(CO)(PPh ₃) ₂]	KCl 50% Ac ₂ O 200%	160	4	8	79	21
374	Palmitic acid (C ₁₆)	5% [IrCl(CO)(PPh ₃) ₂]	KI 50% TFAA 200%	160	4	0	0	0

Table A3.4: Results from additive study using [IrCl(CO)(PPh₃)₂].

Reaction	Acid	Catalyst (%)	Additives (%)	Temperature (°C)	Time (h)	Yield (%)	Terminal (%)	Internal (%)
375	Palmitic acid (C ₁₆)	5% [Rh(acac)(CO)(P <i>p</i> -An ₃)]	KI 50% Ac ₂ O 200%	160	4	96	56	44
379	Palmitic acid (C ₁₆)	5% [Rh(acac)(CO)(PCy ₃)]	KI 50% Ac ₂ O 200%	160	4	92	70	30
380	Palmitic acid (C ₁₆)	5% [Rh(acac)(CO)(P <i>o</i> -An ₃)]	KI 50% Ac ₂ O 200%	160	4	92	55	46
382	Palmitic acid (C ₁₆)	5% [Rh(acac)(CO)(P(4-Cl-C ₆ H ₄) ₃)]	KI 50% Ac ₂ O 200%	160	4	94	56	44
386	Palmitic acid (C ₁₆)	5% [Rh(acac)(CO)(P <i>o</i> -Tol ₃)]	KI 50% Ac ₂ O 200%	160	4	98	62	38
387	Palmitic acid (C ₁₆)	5% [Rh(acac)(CO)(PPh ₃)]	KI 50% Ac ₂ O 200%	160	4	89	58	42
388	Palmitic acid (C ₁₆)	5% [Rh(acac)(CO) ₂]	KI 50% Ac ₂ O 200%	160	4	94	52	48

Table A3.5: Results from study using [Rh(acac)(CO)(L)] complexes.

Reaction	Acid	Catalyst (%)	Additives (%)	Temperature (°C)	Time (h)	Yield (%)	Terminal (%)	Internal (%)
343	Palmitic acid (C ₁₆)	5% [IrCl(CO)(PPh ₃) ₂]	KI 50% Ac ₂ O 200%	160	4	99	82	18
391	Palmitic acid (C ₁₆)	5% [IrCl(CO)(PCy ₃) ₂]	KI 50% Ac ₂ O 200%	160	4	93	7	93
392	Palmitic acid (C ₁₆)	5% [IrCl(CO)(PPh ₂ Et) ₂]	KI 50% Ac ₂ O 200%	160	4	92	56	44
393	Palmitic acid (C ₁₆)	5% [IrCl(CO)(PPhEt ₂) ₂]	KI 50% Ac ₂ O 200%	160	4	90	40	60
396	Palmitic acid (C ₁₆)	5% [IrCl(CO)(P <i>o</i> -Tol ₃) ₂]	KI 50% Ac ₂ O 200%	160	4	Na	Na	Na
397	Palmitic acid (C ₁₆)	5% [IrCl(CO)(P <i>o</i> -An ₃) ₂]	KI 50% Ac ₂ O 200%	160	4	Na	Na	Na
404	Palmitic acid (C ₁₆)	5% [RhCl(CO)(PPh ₃) ₂]	KI 50% Ac ₂ O 200%	160	2	79	61	39

Table A3.6: Results from study using [IrCl(CO)(L)₂] complexes.

Reaction	Acid	Catalyst (%)	Additives (%)	Temperature (°C)	Time (h)	Yield (%)	Terminal (%)	Internal (%)
507	Stearic acid (C ₁₈)	5 % [RhCl(CO)(dppe)]	KI 50% Ac ₂ O 200%	160	4	76	76	24
508	Palmitic acid (C ₁₆)	5% [RhCl(CO)(dppe)]	KI 50% Ac ₂ O 200%	160	4	82	76	24
509	Myristic acid (C ₁₄)	5 % [RhCl(CO)(dppe)]	KI 50% Ac ₂ O 200%	160	4	85	88	12
630	Myristic acid (C ₁₄)	5% [RhCl(CO)(xantphos)]	KI 50% Ac ₂ O 200%	160	4	95	50	50
631	Myristic acid (C ₁₄)	5% [RhCl(CO)(dpephos)]	KI 50% Ac ₂ O 200%	160	4	85	65	35

Table A3.7: Results from study using [RhCl(CO)P-P]bidentate phosphine complexes.

Reaction	Acid	Catalyst (%)	Additives (%)	Temperature (°C)	Time (h)	Yield (%)	Terminal (%)	Internal (%)
769	Myristic acid (C ₁₄)	5% 1a	KI 50% Ac ₂ O 200%	160	4h	0	0	0
770	Palmitic acid (C ₁₆)	5% 1a	KI 50% Ac ₂ O 200%	160	4h	0	0	0
771	Stearic acid (C ₁₈)	5% 1a	KI 50% Ac ₂ O 200%	160	4h	0	0	0
772	Myristic acid (C ₁₄)	5% 1a	Ac ₂ O 200%	160	4h	0	0	0
773	Myristic acid (C ₁₄)	5% 3d	Ac ₂ O 200%	160	4h	0	0	0
777	Myristic acid (C ₁₄)	5% 3h	KI 50% Ac ₂ O 200%	160	4h	0	0	0
778	Myristic acid (C ₁₄)	5% 3f	KI 50% Ac ₂ O 200%	160	4h	0	0	0
779	Myristic acid (C ₁₄)	5% 3b	KI 50% Ac ₂ O 200%	160	4h	0	0	0
783	Myristic acid (C ₁₄)	5% 3e	KI 50% Ac ₂ O 200%	160	4h	0	0	0
784	Myristic acid (C ₁₄)	5% 3d	KI 50% Ac ₂ O 200%	160	4h	0	0	0

Table A3.8: Results from study using [Ir(Ar-NN)(CO)(L)] complexes.

Reaction	Acid	Catalyst (%)	Additives (%)	Temperature (°C)	Time (h)	Yield (%)	Terminal (%)	Internal (%)
500	Palmitic acid (C ₁₆)	5% 10a	KI 50% Ac ₂ O 200%	160	4	0	0	0
501	Palmitic acid (C ₁₆)	5% 10b	KI 50% Ac ₂ O 200%	160	4	0	0	0
502	Palmitic acid (C ₁₆)	5% 10e	KI 50% Ac ₂ O 200%	160	4	0	0	0
787	Myristic acid (C ₁₄)	5% 10b	KI 50% Ac ₂ O 200%	160	4	0	0	0
788	Myristic acid (C ₁₄)	5% 10a	KI 50% Ac ₂ O 200%	160	4	0	0	0
789	Myristic acid (C ₁₄)	5% 10e	KI 50% Ac ₂ O 200%	160	4	0	0	0
790	Myristic acid (C ₁₄)	5% 10d	KI 50% Ac ₂ O 200%	160	4	0	0	0
791	Myristic acid (C ₁₄)	5% 10c	KI 50% Ac ₂ O 200%	160	4	0	0	0
801	Myristic acid (C ₁₄)	5% 10a	Ac ₂ O 200%	160	4	0	0	0
802	Myristic acid (C ₁₄)	5% 10b	Ac ₂ O 200%	160	4	0	0	0
803	Myristic acid (C ₁₄)	5% 10e	Ac ₂ O 200%	160	4	0	0	0

Table A3.9: Results from study using [Ir(R-PNP)(CO)] complexes.

Reaction	Acid	Catalyst (%)	Additives (%)	Temperature (°C)	Time (h)	Yield (%)	Terminal (%)	Internal (%)
411	Palmitic acid (C ₁₆)	5% [tBuRh(CO) PCP]	KI 50% Ac ₂ O 200%	160	4	0	0	0
412	Palmitic acid (C ₁₆)	5% [tBuRh(CO) POCOP]	KI 50% Ac ₂ O 200%	160	4	0	0	0
414	Palmitic acid (C ₁₆)	5% [tBuRh(CO) PNCNP]	KI 50% Ac ₂ O 200%	160	4	0	0	0
423	Palmitic acid (C ₁₆)	5% [Rh(ⁱ Pr-PNP)(CO)]	KI 50% Ac ₂ O 200%	160	4	74	65	35
424	Palmitic acid (C ₁₆)	5% [Rh(<i>o</i> -tol-PNP)(CO)]	KI 50% Ac ₂ O 200%	160	4	0	0	0
427	Palmitic acid (C ₁₆)	5% [Rh(2- ⁱ PrOC ₆ H ₄ -PNP)(CO)]	KI 50% Ac ₂ O 200%	160	4	41	74	26
428	Palmitic acid (C ₁₆)	5% [Rh(^t BuPh-PNP)(CO)]	KI 50% Ac ₂ O 200%	160	4	59	68	32
433	Palmitic acid (C ₁₆)	5% [Rh(Ph-PNP)(CO)]	KI 50% Ac ₂ O 200%	160	4	75	82	18

Table A3.10: Results from study using rhodium pincer complexes.

Reaction	Acid	Catalyst (%)	Additives (%)	Temperature (°C)	Time (h)	Yield (%)	Terminal (%)	Internal (%)
793	Myristic acid (C ₁₄)	5% 12a	KI 50% Ac ₂ O 200%	160	4	28	81	19
795	Stearic acid (C ₁₈)	5% 12a	KI 50% Ac ₂ O 200%	160	4	59	78	22
796	Myristic acid (C ₁₄)	5% 12a	Ac ₂ O 200%	160	4	0	0	0
797	Stearic acid (C ₁₈)	5% 12a	Ac ₂ O 200%	160	4	0	0	0
798	Myristic acid (C ₁₄)	5% 5b	KI 50% Ac ₂ O 200%	160	4	66	77	23
799	Palmitic acid (C ₁₆)	5% 5b	KI 50% Ac ₂ O 200%	160	4	49	72	28
808	Myristic acid (C ₁₄)	5% 5a	KI 50% Ac ₂ O 200%	160	4	70	75	25
810	Stearic acid (C ₁₈)	5% 5a	KI 50% Ac ₂ O 200%	160	4	27	70	30
816	Myristic acid (C ₁₄)	5% 5a	Ac ₂ O 200%	160	4	0	0	0
817	Palmitic acid (C ₁₆)	5% 5a	Ac ₂ O 200%	160	4	0	0	0
818	Stearic acid (C ₁₈)	5% 5a	Ac ₂ O 200%	160	4	0	0	0
821	Dodecanoic acid (C ₁₂)	5% 5c	KI 50% Ac ₂ O 200%	160	4	95	64	36
822	Myristic acid (C ₁₄)	5% 5c	KI 50% Ac ₂ O 200%	160	4	78	67	33
823	Palmitic acid (C ₁₆)	5% 5c	KI 50% Ac ₂ O 200%	160	4	62	66	34
825	Myristic acid (C ₁₄)	5% 5d	KI 50% Ac ₂ O 200%	160	4	72	69	31
826	Palmitic acid (C ₁₆)	5% 5d	KI 50% Ac ₂ O 200%	160	4	83	70	30
827	Stearic acid (C ₁₈)	5% 5d	KI 50% Ac ₂ O 200%	160	4	42	75	25
804	Dodecanoic acid (C ₁₂)	5% 5f	KI 50% Ac ₂ O 200%	160	4	97	60	40
805	Myristic acid (C ₁₄)	5% 5f	KI 50% Ac ₂ O 200%	160	4	98	61	39
806	Stearic acid (C ₁₈)	5% 5f	KI 50% Ac ₂ O 200%	160	4	60	80	20
813	Myristic acid (C ₁₄)	5% 5f	Ac ₂ O 200%	160	4	0	0	0
814	Palmitic acid (C ₁₆)	5% 5f	Ac ₂ O 200%	160	4	0	0	0
815	Stearic acid (C ₁₈)	5% 5f	Ac ₂ O 200%	160	4	0	0	0

Table A3.11: Results from study using [Rh(NNX)(CO)] pincer complexes.

Reaction	Acid	Catalyst (%)	Additives (%)	Temperature (°C)	Time (h)	Yield (%)	Terminal (%)	Internal (%)
512	Stearic acid (C ₁₈)	5% 14a	KI 50% Ac ₂ O 200%	160	4	97	59	41
513	Palmitic acid (C ₁₆)	5% 14a	KI 50% Ac ₂ O 200%	160	4	99	61	39
514	Myristic acid (C ₁₄)	5% 14a	KI 50% Ac ₂ O 200%	160	4	80	63	37
515	Stearic acid (C ₁₈)	5% 14f	KI 50% Ac ₂ O 200%	160	4	73	70	30
516	Palmitic acid (C ₁₆)	5% 14f	KI 50% Ac ₂ O 200%	160	4	81	60	40
836	Palmitic acid (C ₁₆)	5% 14f	KI 0% Ac ₂ O 200%	160	4	0	0	0
517	Myristic acid (C ₁₄)	5% 14f	KI 50% Ac ₂ O 200%	160	4	90	72	28
520	Stearic acid (C ₁₈)	5% 14b	KI 50% Ac ₂ O 200%	160	4	96	66	34
521	Palmitic acid (C ₁₆)	5% 14b	KI 50% Ac ₂ O 200%	160	4	92	66	34
522	Myristic acid (C ₁₄)	5% 14b	KI 50% Ac ₂ O 200%	160	4	95	66	34
531	Myristic acid (C ₁₄)	5% 14c	KI 50% Ac ₂ O 200%	160	4	94	49	51
532	Palmitic acid (C ₁₆)	5% 14c	KI 50% Ac ₂ O 200%	160	4	93	52	48
527	Stearic acid (C ₁₈)	5% 14d	KI 50% Ac ₂ O 200%	160	4	97	68	32
528	Palmitic acid (C ₁₆)	5% 14d	KI 50% Ac ₂ O 200%	160	4	95	68	32
529	Myristic acid (C ₁₄)	5% 14d	KI 50% Ac ₂ O 200%	160	4	89	70	30
684	Palmitic acid (C ₁₆)	5% 14e	KI 50% Ac ₂ O 200%	160	4	93	64	36
685	Stearic acid (C ₁₈)	5% 14e	KI 50% Ac ₂ O 200%	160	4	87	72	28
690	Myristic acid (C ₁₄)	5% 14g	KI 50% Ac ₂ O 200%	160	4	66	66	34
691	Palmitic acid (C ₁₆)	5% 14g	KI 50% Ac ₂ O 200%	160	4	69	63	37
692	Stearic acid (C ₁₈)	5% 14g	KI 50% Ac ₂ O 200%	160	4	61	72	28

Table A3.12: Results from study using [Rh(Cl)(NN-R)(CO)] iminophosphine complexes.

Reaction	Acid	Catalyst (%)	Additives (%)	Temperature (°C)	Time (h)	Yield (%)	Terminal (%)	Internal (%)
829	Palmitic acid (C ₁₆)	5% 15g	KI 50% Ac ₂ O 200%	160	4	73	60	40
828	Palmitic acid (C ₁₆)	5% 15d	KI 50% Ac ₂ O 200%	160	4	0	0	0
533	Palmitic acid (C ₁₆)	5% 15f	KI 50% Ac ₂ O 200%	160	4	84	70	30
661	Myristic acid (C ₁₄)	5% 15f	KI 0% Ac ₂ O 200%	160	4	0	0	0
533	Palmitic acid (C ₁₆)	5% 15f	KI 50% Ac ₂ O 200%	160	4	84	70	30
837	myristic acid (C ₁₄)	5% 15f	KI 50% Ac ₂ O 200%	160	4	85	69	31
836	dodecanoic acid(C ₁₂)	5% 15f	KI 50% Ac ₂ O 200%	160	4	94	76	24
839	myristic acid (C ₁₄)	1% 15f	KI 50% Ac ₂ O 200%	160	4	65	70	30
840	myristic acid (C ₁₄)	1% 15f	KI 50% Ac ₂ O 200%	160	8	75	72	28

Table A3.13: Results from study using [RhI₂(CO)(PCO-Ar)] complexes.